UNIVERSITY OF SOUTHAMPTON

Faculty of Natural and Environmental Sciences
School of Ocean and Earth Science

Shear Enhanced Nutrient Supply at the Mesoscale.

by

Alexander Forryan

A thesis submitted in partial fulfillment for the degree of Doctor of Philosophy

August 17, 2011

UNIVERSITY OF SOUTHAMPTON

ABSTRACT

FACULTY OF NATURAL AND ENVIRONMENTAL SCIENCES
SCHOOL OF OCEAN AND EARTH SCIENCE

Doctor of Philosophy

SHEAR ENHANCED NUTRIENT SUPPLY AT THE MESOSCALE.

by Alexander Forryan

Phytoplankton live almost exclusively in the sunlit waters of the euphotic zone. However, in addition to sunlight, phytoplankton require a regular supply of nutrients to grow. In the open ocean such nutrients are abundant in the dark waters below the euphotic zone. Hence, to a large extent it is the physical mechanisms driving the transfer of nutrient rich water into the euphotic zone which dictate patterns of phytoplankton growth. Using a combination of observation and high resolution computer modelling this thesis investigates whether shear associated with mesoscale features leads to locally enhanced turbulent mixing and a shear-enhanced nutrient supply. Measurements of turbulent diffusivity and nutrient concentrations have been made in a region containing an eddy dipole, a strong mesoscale feature, consisting of a cyclonic eddy and an anti-cyclonically rotating mode-water eddy. The effect of this strong mesoscale feature on vertical turbulent mixing is assessed by investigating whether variations in vertical shear associated with the mesoscale feature enhance the observed vertical turbulent mixing. Using these observations of turbulent diffusivity, augmented by further measurements from two other ocean regions, a new parametrization of shear-enhanced vertical turbulent mixing is developed. The new shear-enhanced mixing parametrization is implemented in a high-resolution computer model of a mode-water eddy. This model is then used to examine the effect of interactions between the eddy and the wind on vertical nutrient fluxes. The shear enhancement to nutrient supply by mesoscale circulation is found to be potentially of much greater significance than has previously been considered. Modelling suggests that when forced by high variability winds mode-water eddies appear to be capable of locally enhancing the vertical turbulent nutrient flux by up to an order of magnitude. The work in this thesis suggests that vertical turbulent flux may well be underestimated as a stimulus to new production.

Contents

List of Figures

List of Tables

Acknowledgements

I would like to acknowledge, with gratitude, the assistance of my three supervisors, Dr. Adrian P. Martin, Dr Katya Popova and Professor Meric Srokosz, in the preparation of this thesis. Without the patient guidance of my supervisors none of this would have been possible.

List of symbols

C	A scalar property
t	Time
K	Turbulent diffusion coefficient (m^2 s^{-1})
K_o	Turbulent diffusion coefficient under neutral conditions
K_v	Turbulent viscosity
K_t	Turbulent diffusivity
K_{bs}	Background turbulent diffusivity
K_{shap}	The effective diffusivity from a Shapiro filter application
x, y, z	The coordinate axes
u, v, w	Velocity in the x, y, z directions respectively (m s^{-1})
N	Buoyancy frequency (s^{-1})
ε	The dissipation rate of turbulent kinetic energy (W kg^{-1})
Γ	Mixing efficiency
Ri	The gradient Richardson number
Ri_{crit}	The critical gradient Richardson number
S_h	Vertical shear (s^{-1})
g	Acceleration due to gravity (m s^{-2})
ρ	Potential density (km m^{-3})
σ_0	Potential density calculated with reference to 0 dbar pressure - 1000 (km m^{-3})
α, n	Positive constants
ν	The molecular viscosity of water
P_{shear}	Pseudo shear
k	Wavenumber
k_c	The Kolmogorov wavenumber
k_l	The lower wavenumber limit of equilibrium range
L_o	The Ozmidov length scale (m)
L_t	The Thorpe length scale (m)
Φ(k)	The vertical shear power spectrum
Φ_{Nas}(k)	The Naysmith universal turbulence spectrum

T_1	Inert tracer 1
T_2	Inert tracer 2
$V(r)$	Azimuthal velocity at radius r (m s^{-1})
V_o	Maximum constant azimuthal velocity
V_{max}, V_{min}	The maximum and minimum azimuthal velocity when azimuthal velocity varies
R	Radius of maximum azimuthal velocity
r	Distance from eddy centre (radius km)
θ_o	The bearing of the maximum azimuthal velocity V_{max}
θ	The bearing of $V(r)$
s_e	A standard estimate of error
D_{stripe}	The depth of the inert tracer stripe (m)
U_E, V_E	Ekman volume transports
ε^2	The ratio of the densities for ocean and atmosphere
τ	Wind stress
C_d	The drag coefficient
f	Coriolis or planetary vorticity
p	Pressure (dbar)
Ω	The rotation rate of the earth
Φ	Latitude
T_o, T_i	Temperature (°C)
S_o, S_i	Salinity
R^2	The correlation of determination
s_e	Standard estimate of error

To Mr. T.
Always listening.

Chapter 1

Introduction

Phytoplankton, the myriad tiny single-celled plants that comprise the vast majority of life in the oceans, live exclusively in the sunlit waters of the upper 100 to 200 m of the water column. This sunlit region of the ocean, where there is sufficient light for phytoplankton to photosynthesise, is known as the euphotic zone (e.g. Sarmiento et al. 2006). In addition to sunlight phytoplankton require a regular supply of macro-nutrients - carbon, nitrate, phosphate and, silicate - as well as trace elements, such as iron, to grow. Carbon is absorbed directly into the surface ocean from the atmosphere. However, with the exception of some phytoplankton that can fix nitrogen, the principle source of the remaining macro-nutrients and trace elements is from the remineralisation of decaying organic matter (e.g. Sarmiento et al. 2006). Gravity ensures that decaying organic matter sinks, and so this remineralisation occurs almost exclusively in the dark waters below the eupotic zone (e.g. Sarmiento et al. 2006). Consequently, for phytoplankton to grow nutrient-laden water must pass from the deeper, dark sections of the water column up into the euphotic zone. To a large extent, it is the physical mechanisms driving this transfer of water into the euphotic zone which dictates patterns of phytoplankton growth (primary production) within the ocean (e.g. Sarmiento et al. 2006; Williams and Follows 2003). Primary production itself can be considered to be the sum of 'new' production and 'regenerated' production. Broadly speaking new production is fuelled by the input of nutrient from outside the euphotic zone while regenerated production is from the re-cycling of nutrients within the euphotic zone (Dugdake and Goering, 1967).

Of the many physical mechanisms that bring deeper waters up to the surface, three that have received the most attention are deep winter convective mixing (Williams et al., 2000), turbulent mixing (Jickells et al., 2008; Law et al., 2001; Lewis et al.,

1986) and mesoscale up-welling (Klein and Lapeyre, 2009; Allen et al., 2005; McGillicuddy et al., 2003; Martin and Pondaven, 2003; Oschlies, 2002*b*; Martin and Richards, 2001; Lévy et al., 2001; McGillicuddy et al., 1999; Oschlies and Garcon, 1998; McGillicuddy et al., 1998; Lévy et al., 1998). The relative contribution of each of these three physical mechanisms to the total flux of nutrients into the euphotic zone for a given region of the ocean depends in part upon the location (latitude) and time of year (Williams and Follows, 2003).

1.1 Deep winter convective mixing

On an annual timescale, deep winter convective mixing, which occurs when the colder temperatures and higher wind speeds of winter deepen the surface wind-mixed layer by tens to hundreds of meters, provides the largest single source of nutrients into the euphotic zone in both the sub-tropical and sub-polar gyres (Williams and Follows, 2003; Williams et al., 2000; McGillicuddy et al., 1998). In the North Atlantic sub-polar gyre, seasonal re-stratification and increasing levels of irradiance lead to a major phytoplankton bloom event in spring when the nutrients brought to the surface by deep winter mixing are largely consumed (Allen et al., 2005; Sanders et al., 2005; Williams and Follows, 2003). However, there are often residual nitrate and phosphate concentrations found post bloom (Sanders et al., 2005). Why there is a residual nutrient concentration following the spring bloom in the sub-polar gyre is subject to debate and several reasons have been advanced (Nielsdóttir et al., 2009; Sanders et al., 2005; Popova et al., 2002). Nutrient levels supplied through deep winter mixing topped up with the occasional injection of fresh nutrient through summer storms may supply more nutrient than can be used by phytoplankton in the high latitude light regime of the sub-polar gyre (Popova et al., 2002). Heavy grazing by zooplankton and species succession as the bloom progresses may result in the dominant phytoplankton groups at the end of the bloom primarily utilizing re-cycled nitrogen, such as ammonium, and unable to utilize fully the remaining 'fresh' nitrate pool (Sanders et al., 2005). Light levels at high latitudes may be insufficient to allow nitrate uptake by non-siliceous phytoplankton, hence the bloom comes to an end when silicate is exhausted due to light limitation (Sanders et al., 2005); Up-welling of silicate at the Iceland-Faeroes front has been observed to prolong the duration of the bloom in proximity to the front (Allen et al., 2005). Iron limitation has also been suggested as contributing to the residual post-bloom macro-nutrient concentrations in the Iceland Basin (Nielsdóttir et al., 2009). Iron is an essential trace element for all phytoplankton and a lack of iron has been demonstrated to result in low production despite high concentrations of surface macro-nutrients in the Southern Ocean and sub-polar Pacific ocean (Boyd et al., 2007). Explanations postulating a limiting nutrient, either silicate or iron, also depend on the ratio of limiting nutrient to nitrate being lower than required for phytoplankton growth in the up-welled waters.

In the sub-tropical gyre the magnitude of the deep winter mixing supply of nutrients is not as large as in the sub-polar regions. The deep winter mixing supply of nutrient in the sub-tropical gyre is rapidly consumed by the wintertime bloom and for large periods of the year the waters of the sub-tropical gyre are oligotrophic, that is in a state of nutrient limitation. (Williams and Follows, 2003; Williams et al., 2000).

1.2 Vertical turbulent mixing

Vertical turbulent mixing, in the open ocean, is thought to be responsible for the stability of the observed abyssal density structure, the magnitude of the polewards transport of heat in the ocean's meridional overturning circulation (Munk, 1966; Munk and Wunsch, 1998) and, more contentiously, to be the major contributor to the fluxes of nutrients which fuel primary production in the oligotrophic ocean (Lewis et al., 1986). Nevertheless, neither the magnitude nor the distribution of vertical turbulent mixing in the open ocean are accurately known, particularly at the mesoscale.

1.2.1 Background to turbulence

Turbulence is an energetic, eddying, and highly dissipative state of motion which results in the transfer of properties such as heat, salinity, and momentum at much greater rates than molecular diffusion alone (Tennekes and Lumley, 1972). Turbulence occurs as a result of instability in fluid flows. It acts to disperse scalar properties such as heat, salinity, and other tracers such as nutrients, and requires a steady supply of energy to maintain the turbulent motion (Tennekes and Lumley, 1972). Turbulent diffusivity (K), which is analogous to molecular diffusivity, has been used to describe how scalar properties disperse as a result of turbulent motions such that

$$\frac{\partial C}{\partial t} = K\frac{\partial^2 C}{\partial z^2}$$

(Tennekes and Lumley, 1972) where C is a scalar property, t is time and z the vertical distance.

Energy in turbulent flow cascades from large turbulent eddies, at the scale of the instability generating the turbulence, to small turbulent eddies and is finally dissipated by molecular viscosity (Thorpe, 2005; Tennekes and Lumley, 1972). Dissipation in turbulent flow occurs at eddy scales smaller than the Kolmogorov microscale η, which is defined as the smallest scale of turbulent motion unaffected by molecular processes

$$\eta = \left(\frac{\nu^3}{\varepsilon}\right)^{\frac{1}{4}}$$

(Tennekes and Lumley, 1972) where υ is molecular viscosity and ε is the turbulent kinetic energy dissipation rate. Or as as L.F. Richardson elegantly phrased it,

> "Big whirls have little whirls that feed on their velocity.
> And little whirls have lesser whirls and so on to viscosity
> – in a molecular sense"

(Thorpe, 2005).

1.2.2 Turbulence in the ocean

On the scale of an ocean basin a bulk estimate for the vertical turbulent diffusivity has been calculated from consideration of the vertical profiles of conserved tracers such as temperature, salinity, and ^{14}C distributions in the ocean interior. For the Pacific Ocean basin the bulk estimate of vertical turbulent diffusivity is approximately 1.3 x10^{-4} m^2 s^{-1} (Munk, 1966). This vertical turbulent diffusion is considered to be a product of the wave-wave interactions of the internal wave field which is generated by the actions of the wind and tide (Munk and Wunsch, 1998).

However, vertical turbulent diffusivity calculated from observed internal wave shear in the Sargasso Sea, using an empirical relationship between internal wave shear and turbulent kinetic energy dissipation (Gregg, 1989), was found to be 0.1 x10^{-4} m^2 s^{-1} (Kunze and Sanford, 1996). This is consistent with observations of vertical turbulent diffusivity of between 0.12 ± 0.02 x10^{-4} m^2 s^{-1} and 0.17 ± 0.02 x10^{-4} m^2 s^{-1} for the south eastern part of the North Atlantic subtropical gyre at a depth of $\sim$ 300 m in a location away from topographical influence (Ledwell et al., 1998).

It may be possible to reconcile the direct observations, calculations from internal wave shear, and bulk calculations of vertical turbulent diffusivity by proposing that elevated ocean mixing is confined to boundary layers with localised hot spots over rough topography (Kunze and Sanford, 1996; Polzin et al., 1997), or in straits and overflows across deep sills (Bryden and Nurser, 2003). Intense localised turbulent mixing over rough topography in the Southern Ocean has been suggested to be sufficient to close the budget for the ocean's meridional overturning circulation (Naveira Garabato et al., 2004).

1.2.3 Turbulence measurement techniques

The measurement of turbulence presents some unique challenges in that turbulence fluctuates in both time and space and is often weak and difficult to measure. Turbulent diffusivity can be measured using several different techniques, each with advantages and disadvantages.

1.2.3.1 Intermittency and instantaneous measurements of turbulence

The spatial and temporal distribution of turbulence in the ocean is highly intermittent. The intermittent nature of turbulent mixing in the ocean can be characterised by an intermittency factor. This factor is defined as the variance of the log of the turbulent kinetic energy dissipation rate. In stratified layers analysis of observation data suggests that the distribution functions for turbulent kinetic energy dissipation and temperature dissipation are approximately lognormal with a large intermittency factor in the range of 3 to 7. Statistical analysis of such lognormal distributions implies that to achieve a 95 % confidence in estimates of a mean to $\pm$10 % accuracy requires between 2,600 and 10,000 measurements for intermittency of 3 and 7 respectively (Baker and Gibson, 1987).

The intermittency and statistical distribution of turbulence in the ocean has significant implications for 'instantaneous' turbulence measurement techniques, such as those made using Thorpe scales and microstructure shear profilers (see below). The small number of measurements that can be made, compared to the number required for a $\pm$10 % accuracy, implies that estimates of mean turbulent quantities from instantaneous measurements are always associated with a high degree of uncertainty. In general, as many measurements as are reasonably practicable are taken and where a data set is determined to be lognormal, statistical analyses appropriate to lognormal distributions are used which reflect the uncertainty associated with the calculations. Estimates of uncertainty for microstructure measurements are usually in the region of ± 50 % (Thorpe, 2004; Rippeth et al., 2003).

1.2.3.2 Microstructure shear profilers

A microstructure shear profiler comprises a shear probe deployed on a vibration free platform designed to move with a steady velocity through the water. A shear probe makes direct measurements of cross-axial velocity fluctuations using a piezoceramic beam which, similar to a gramophone pickup, generates voltages in response to cross-axial fluctuating forces (Prandke, 2008*a*; Lueck et al., 2002). Microstructure profilers are commonly deployed as free-fall instruments, though profilers have also been towed, mounted on autonomous vehicles, and deployed on moorings (Thorpe, 2004; Lueck et al., 2002; Gregg, 1999). These direct measurements of microstructure shear can then be used to calculate turbulent kinetic energy dissipation rates and consequently turbulent diffusivity (Chapter 2).

1.2.3.3 Acoustic Doppler Current Profiler (ADCP)

Unlike microstructure shear probes which estimate the turbulent kinetic energy dissipation rates directly, ADCP data is used to calculate production rates of turbulent kinetic energy. However, for a steady homogeneous flow the production rate of turbulent kinetic energy can be assumed to equal the dissipation rate (Tennekes and Lumley, 1972). ADCP transmits sound pulses in an acoustic 'beam' and estimates water velocity by measuring the change in frequency (doppler shift) between transmitted and received sound pulses. Fluctuations in the average along-beam velocity for ADCP data can be used to estimate Reynolds stress profiles from which the production rates of turbulent kinetic energy can be calculated (Howarth and Souza, 2005; Lu and Lueck, 1999). Estimates of Reynolds stress can be contaminated by waves, either surface or internal, by statistical errors relating to the time intervals chosen for the average beam velocity fluctuations, and by Doppler noise (Lu and Lueck, 1999). Simultaneous measurement of turbulent kinetic energy dissipation rates using microstructure profiler and kinetic energy production using a sea bed mounted ADCP, found a mean ratio of production to dissipation of 0.63 ± 0.17, which is within the range of observational uncertainty for measurements of dissipation (Rippeth et al., 2003).

At present ADCP measurement of turbulence has only been made in shallow coastal waters using bed-mounted ADCP (Rippeth et al., 2003). The technique is yet to be validated for ship-mounted ADCP in the open ocean.

1.2.3.4 Thorpe scales

The Thorpe scale is defined as the root mean square of the vertical displacements required to reorder a measured profile of potential density so that it is gravitationally stable (Johnson and Garrett, 2004; Stansfield et al., 2001; Thorpe, 1977). Turbulent kinetic energy dissipation can be estimated by analysis of the length scale of density overturns (Thorpe, 1977). Problems with instrument resolution, slow sensor response time, and instrument noise can limit the application of this technique to areas of strong mixing with strong density gradients (Stansfield et al., 2001). Application of the technique may also be limited by effects such as ship motion causing the CTD (conductivity, temperature, depth) sensors to oscillate vertically (Johnson and Garrett, 2004).

1.2.3.5 Tracer release

In tracer release experiments, vertical turbulent diffusivity is estimated by monitoring the vertical spread of a passive tracer over a period of weeks to months (Ledwell et al., 1998). Sulphur hexafluoride (SF_6) was commonly used as a tracer (Kim et al., 2005; Ledwell et al., 2000; Law et al., 2001, 1998; Ledwell et al., 1998) as it is detectable at low concentrations (10^{-17} mol L^{-1}) by electron capture, is non-reactive, non-harmful to marine organisms, and, due to low solubility, only occurs in low concentrations (order 10^{-15} mol L^{-1}) in the ocean (Ledwell et al., 2000). Unfortunately SF_6 is a potent greenhouse gas and is now rarely used.

Tracer is injected on a selected constant density surface (Ledwell et al., 2000), or across a density range (Law et al., 2001). Tracer concentrations are sampled using a towed water sampling array and analysed using standard techniques (Kim et al., 2005; Ledwell et al., 2000; Law et al., 2001, 1998; Ledwell et al., 1998). The calculation of vertical turbulent diffusivity involves fitting the observed evolution in tracer distributions to a model of tracer diffusivity which allows for variation in density surfaces (Ledwell et al., 1998; Law et al., 1998). Errors in the estimates of vertical turbulent diffusivity arise from observational error in the variation of density surfaces, sampling error, distortion of tracer distribution due to persistent shear, and variation in SF_6 background concentration over long timescales (Ledwell et al., 1998). Error can also occur due to event driven vertical advection, for example storms, and due to sampling resolution (Law et al., 2001).

The advantage of this technique is that it provides a time integrated turbulent diffusivity measurement for a region, which eliminates the variability errors associated with averaging instantaneous measurements of turbulent kinetic energy dissipation. Hence the intermittency problem faced when using instantaneous measurement techniques, as described above, is removed. The technique integrates spatially so does not provide an accurate, fine scale, method of determining the spatial distribution of turbulent energy dissipation. Hence this technique cannot be used to isolate high mixing regions. Nevertheless, turbulent diffusivity measured by tracer release compares favourably with that calculated using microstructure profilers (Ledwell et al., 2000; Polzin et al., 1997).

1.2.4 Turbulent nutrient supply

Due to the dominance of deep winter mixing as a source of nutrient supply to the surface ocean in the sub-polar gyre, the turbulent supply of nutrients in the region is traditionally considered to be a minor source of nutrients into the surface ocean (Williams and Follows, 2003). However, if as has been suggested, either iron or silicate is limiting in the sub-polar gyre post spring bloom then the small but constant supply of limiting nutrient from turbulent mixing may still have a strong influence on levels of production in the post bloom period.

For large periods of the year in the sub-tropical gyre primary production is restricted by the availability of surface nutrient. Following the winter bloom, the turbulent supply of nutrients has been suggested to be one of the primary sources of nutrient (Lewis et al., 1986). However, in much the same way that basin scale estimates of vertical turbulent diffusivity are difficult to reconcile with direct observations, long-timescale integrated estimates of nutrient supply for the open ocean differ from local estimates based on turbulent diffusivity measurements. In the oligotrophic eastern Atlantic the vertical turbulent nitrate flux of 0.14 (95 % confidence interval: 0.002 to 0.89) mmol m^{-2} day^{-1}, estimated using microstructure measurements of turbulent diffusivity, matched within error limits the integrated rate of nitrate uptake

0.807 ± 0.17 mmol m^{-2} day^{-1} measured, in situ, by ^{15}N-labelled nitrate incorporation (Lewis et al., 1986). However, nitrate flux into the euphotic zone near Bermuda has been estimated as 1.64 ± 0.5 mmol m^{-2} day^{-1}, from the ^{3}He budget (Jenkins, 1988). Though it may be possible to reconcile these two figures through their relative spatial location within the sub-tropical gyre (Oschlies, 2002*b*), other longer term geochemical estimates of new production are still an order of magnitude greater than estimates of new production based on turbulent diffusivity measurement. Measurements can account for 0.33 (95 % confidence interval: 0.003 to 2) mol C m^{-2} year^{-1} of new production (Lewis et al., 1986), which is approximately an order of magnitude lower than estimates of 2 to 4 mol C m^{-2} year^{-1} from geochemical tracers such as oxygen, argon, and helium (Carlson et al., 1994).

1.3 The effect of the mesoscale

Within the basin scale and seasonal patterns of nutrient supply, time varying circulations at the mesoscale, order 10 to 100 km, have a strong influence on the local supply of nutrient (Klein and Lapeyre, 2009; Allen et al., 2005; McGillicuddy et al., 2003; Martin and Pondaven, 2003; Oschlies, 2002*b*; Martin and Richards, 2001; Lévy et al., 2001; McGillicuddy et al., 1999; Oschlies and Garcon, 1998; McGillicuddy et al., 1998; Lévy et al., 1998).

Mesoscale circulations can create patches of locally high, or low, nutrient concentration which contributes to the observed patchy horizontal distribution of phytoplankton (e.g. Martin 2005). The influence of the mesoscale circulation is responsible for the swirls, streaks and, patches in surface chlorophyll concentration which can be seen in satellite images of ocean colour. High chlorophyll concentrations indicate regions of high phytoplankton concentration (figure 1.1).

Of more relevance to this thesis, mesoscale circulation, in the form of mesoscale eddies, has been suggested as a mechanism capable of closing the nutrient budget in the Sargasso Sea, though this is still subject to considerable debate (McGillicuddy and Robinson, 1997; Oschlies and Garcon, 1998; McGillicuddy et al., 1998, 1999; Oschlies, 2001, 2002*a*,*b*; McGillicuddy et al., 2003; Martin and Pondaven, 2003).

1.3.1 Mesoscale eddies

Mesoscale eddies are a ubiquitous and persistent feature of the ocean (e.g. Richardson 1993; Martin et al. 1998; McDowell and Rossby 1978). They can be generated through a variety of processes including barotropic and baroclinic instability of large scale flows (Richardson, 1993), intense short duration wind events (Willett et al., 2006) and deep winter mixing (Marshall and Schott, 1999). Three types of mesoscale eddy have received the most attention; surface cyclones, surface anticyclones and mode-water eddies. Surface cyclones elevate isopycnal surfaces and depress the sea-surface height while surface anticyclones depress isopycnal surfaces and elevate sea-surface height. Mode-water eddies comprise a thick (up to 1000 m) lens of water displacing isopycnals above and below it and elevating sea-surface height. Mode-water eddies rotate anti-cyclonically (Richardson, 1993; McWilliams, 1985).

1.3.2 Eddy driven vertical nutrient transport mechanisms

Mesoscale eddies are thought to influence vertical nutrient transport through a number of different processes. Two of the processes that have received the most attention are eddy-pumping and Ekman suction.

1.3.2.1 Eddy-pumping

Eddy-pumping is a term used to describe when the presence of an eddy, for example a cyclone or mode-water eddy, causes the doming up of isopycnals which then brings deeper potentially nutrient rich waters into the euphotic zone (McGillicuddy and Robinson, 1997).

Estimates of enhanced nutrient fluxes due to eddy pumping typically make three major assumptions. i) The eddies propagate as linear features, i.e. do not trap significant amounts of water for long time periods. ii) The biological production is fast enough to consume all of the up-welled nutrients within the time the passage of an eddy raises nutrients into the euphotic zone. iii) The rate that nutrients are regenerated below the euphotic zone is fast compared to the rate at which eddies raise the isopycnals (McGillicuddy et al., 2003, 1999, 1998; McGillicuddy and Robinson, 1997).

Consider the three assumptions in turn. i) Analysis of float data from the Sargasso Sea indicates that some eddies exhibit strongly non-linear behaviour and trap water within them for periods up to several months (Richardson, 1993). ii) Assuming the linear propagation of eddies, biological production is unlikely to be fast enough to utilize more than ~ 44 % of the available nutrients (Martin and Pondaven, 2003). iii) Finally, at the basin scale, maintaining the two assumptions that eddies are linear and biological production is fast enough to utilize 100 % of the available nutrients, modelling the regeneration process of nutrients below the euphotic zone rather that relaxing the sub-euphotic depth nutrient concentration back to climatological values over a fixed time period suggests that eddy pumping has little or no effect on basin scale production (Oschlies, 2002*b*,*a*, 2001; Oschlies and Garcon, 1998).

On balance, previous studies would suggest that eddy pumping alone is unlikely to be capable of closing the nutrient budget in the oligotrophic sub-tropical gyre (McGillicuddy and Robinson, 1997; Oschlies and Garcon, 1998; McGillicuddy et al., 1998, 1999; Oschlies, 2001, 2002*a*,*b*; McGillicuddy et al., 2003; Martin and Pondaven, 2003).

1.3.2.2 Ekman suction

Traditionally parametrizations for wind stress applied in ocean models (e.g McGillicuddy et al. 2003; Oschlies 2002*a*) neglect the effects of the water speed (Large and Pond, 1981). However, including the water speed in parametrizing wind stress, when considering an anti-cyclonic eddy, can result in upwelling in the eddy core (Ledwell et al., 2008; McGillicuddy et al., 2007; Martin and Richards, 2001). If we consider an anti-cyclonic eddy in the northern hemisphere subject to an westerly wind stress, (figure 1.2), there will be a southward Ekman transport (because of the circular geometry of the eddy, there will be an Ekman transport regardless of wind direction, though the direction of the transport will vary with the wind direction) given by

$$\tau_x = \rho(\frac{\partial U_E}{\partial t} - fV_E)$$

for the x-component of wind stress (τ_{x}) and

$$\tau_y = \rho(\frac{\partial V_E}{\partial t} + fU_E)$$

for the y-component of wind stress (τ_{y}) (Gill, 1982) where U_E, V_E are the Ekman volume transports in the x and y directions respectively and ρ is the density. The wind stress is parametrized using a formulation based on the relative speed of the water and wind

$$\boldsymbol{\tau} = \frac{\rho_a C_d}{(1+\varepsilon)^2} \left| \boldsymbol{u_a} - \boldsymbol{u_o} \right| (\boldsymbol{u_a} - \boldsymbol{u_o})$$

(Bye, 1986) where, ρ_a is the density of air (taken as a constant 1.2 kg m^{-3}), ε^2 is the ratio of the densities for atmosphere and ocean ($\varepsilon \approx 0.034$, Martin and Richards (2001)), C_d the drag coefficient, and $|\boldsymbol{u_a}|$, $|\boldsymbol{u_o}|$ are the absolute speeds of the air and the water respectively. This results in lower wind stress when the wind blows in the same direction as the water current (position A in figure 1.2). This difference in wind stress on opposing sides of the eddy results in a divergence in Ekman transport, with consequent up-welling, in the eddy core (figure 1.2).

1.3.2.3 The relative importance of eddy driven vertical nutrient transport mechanisms

Of the three types of eddy described above, anti-cyclonic mode-water eddies are often observed to be associated with high production in the Sargasso Sea (McGillicuddy et al., 2007; Sweeney et al., 2003; McNeil et al., 1999). One such anti-cyclonic mode-water eddy was sampled on six occasions during June to Sept 2005 in the sub-tropical gyre near Bermuda. Within the mode-water eddy core primary production was observed in a sub-surface chlorophyll maximum between 60 to 80 m deep on the second occupation that was much higher than is normally observed in the region (McGillicuddy et al., 2007).

Two potential mechanisms associated with a mode-water eddy have been suggested that may generate enhanced upwelling of nutrients in the eddy core; wind-induced Ekman suction and non-linear sub-mesoscale instability (Martin and Richards, 2001). Tracer release, within the high production mode-water eddy, described above, combined with numerical modelling of the mode-water eddy have been used to suggest that the dominant mechanism is the wind-induced Ekman suction (Ledwell et al., 2008). However, there is some debate about this interpretation of the observations. Sub-mesoscale physical processes, acting around the edge of the eddy have also been suggested as a possible source of the observed tracer flux (Mahadevan et al., 2008; McGillicuddy et al., 2008; Martin and Richards, 2001).

1.3.2.4 Physical characteristics of mode-water eddies in the North Atlantic

Mode-water eddies in the northern North Atlantic are formed by winter convection (Kasajima et al., 2006; Lilly and Rhines, 2002; Martin et al., 1998; Brundage and Dugan, 1986). Convective mixing forms a column of weakly stratified water with low potential vorticity (close to zero) compared to the surrounding water (Legg and Marshall, 1993; Marshall and Schott, 1999). This potential vorticity anomaly is resolved by the formation of a rim current around the convective column which is strongly cyclonic at the surface and weakly anti-cyclonic at depth. Isopycnals at the edge of the column arch upwards towards the centre and the deep anti-cyclonic circulation decays away from the centre of the column on the scale of the Rossby radius of deformation (Legg and Marshall, 1993; Marshall and Schott, 1999). Instability causes the cyclonic and anti-cyclonic parts of the convective column to split forming a baroclinic dipole (Oliver et al., 2008). The baroclinic dipole then propagates in the direction of the flow between the cyclone and anti-cyclone parts. Interaction with topography causes the dipole to separate forming separate cyclonic and mode-water eddies (Oliver et al., 2008).

Eddies similar to mode-water eddies, consisting of a lens of homogeneous water, can also be formed by instabilities in slope currents (Pingree and le Cann, 1992; Schultz Tokos and Rossby, 1991). Examples of eddies formed through slope current instabilities are 'swoddies' formed by the slope current off northern Spain in the Southern Bay of Biscay and 'meddies' formed by the overflow of Mediterranean water into the North Atlantic (Schultz Tokos and Rossby, 1991).

Mode-water eddies appear to be long lived, with observed lifetimes of months to years (Martin et al., 1998; McDowell and Rossby, 1978). Mode-water eddies propagate following gradients in potential vorticity (β), which can be potentially planetary, topographic, or caused by surrounding currents (McWilliams, 1985). Mode-water eddies generally propagate west-southwestwards when under the influence of planetary β (McWilliams, 1985). However, topography can act as barrier to mode-water eddies resulting in the mode-water eddies becoming diverted or trapped near oceanic ridges where they can remain stationary for many months (e.g. Martin et al. 1998; Kasajima et al. 2006).

Mode-water eddies formed through convection appear to have greater core thickness and smaller solid body core radii the further north their formation. For example, Greenland and Labrador Seas eddy cores' (above 70^o N) thickness are $\sim$ 2000 m with solid body radii less than 15 km (Kasajima et al., 2006; Lilly and Rhines, 2002), while Iceland Basin eddy cores ($\sim 60^o$ N Latitude) are ~ 1000 m thick with solid body core radius ~ 20 km (Jickells et al., 2008; Martin et al., 1998) and BATS and POMME eddy cores (between 30^o to 50^o N) are ~ 500 m thick, radius ~ 20 to 30 km (Reverdin et al., 2009; Brundage and Dugan, 1986). A close linear relationship between first baroclinic Rossby radius of deformation and eddy radius is observed for all eddies forming north of 30^o N (Eden, 2007), while the depth of the eddy core is possibly related to the depth of winter convection at the latitude of formation (See table 1.1 for a summary of observed mode-water eddy properties).

1.3.3 Sub-mesoscale processes

Sub-mesoscale physical processes associated with small scale, of order 10 km gradients in density and vorticity, have been associated with potentially high vertical velocities which may have a locally positive effect on nutrient flux (Klein and Lapeyre, 2009; Lapeyre and Klein, 2006; Lévy et al., 2001).

A horizontal gradient in density, such as occurs at the edge of a cyclonic or mode-water eddy, will have an associated geostrophic flow along the density gradient (Gill, 1982). For simplicity we consider the case of a horizontal density gradient (front) with a constant planetary vorticity (f). The along front geostrophic velocity will reduce with lateral distance from the front creating a horizontal shear. The horizontal shear results in a horizontal gradient in relative vorticity on either side of the front, one side of the front with cyclonic relative vorticity and the other with anticyclonic relative vorticity (figure 1.3).

Strain driven frontogenesis is where horizontal strain in the direction of the along front flow causes a convergence (Hoskins and Bretherton, 1972). Water converging on the front experiences a change in relative vorticity. Preservation of potential vorticity then results in the thickness of the isopycnals on either side of the front changing in response to the change in relative vorticity. Isopycnal separation on the cyclonic side of the front is increased and isopycnal separation on the anticyclonic side decreased. The non-symmetric changes in isopycnal thickness on either side of the front cause an ageostrophic circulation to be established with upwelling on the anticyclonic side and downwelling on the cyclonic side which intensifies the density gradient and works to re-establish geostrophic balance (Mahadevan and Tandon, 2006; Pollard and Regier, 1992).

As described above in the previous sub-section, winds blowing over water results in an Ekman transport. If the wind blows along a front that is orientated such that the Ekman transport results in higher density water being transported over lower density water, this will result in an intense mixing event. The intense mixing event induces a cross frontal ageostrophic secondary circulation that accelerates the down wind frontal flow resulting in subduction on the dense side of the front and upwelling along the frontal interface (Thomas and Lee, 2005).

Other upper ocean sub-mesoscale physical processes include mixed layer instability where lateral gradients in mixed layer density slump from the horizontal to the vertical resulting in the re-stratification of the surface mixed layer (Boccaletti et al., 2007) and ageostrophic baroclinic instability where a spontaneous loss of balance for a balanced geostrophic flow results in a large vertical velocity (Molemaker et al., 2005).

1.4 Shear-enhanced nutrient supply and the aims of this thesis

Studies in the laboratory suggest that vertical shear flow in a stratified medium has the potential to produce vertical turbulent mixing which is driven by instabilities in the shear flow (Turner, 1973; Monin and Yaglom, 1971). Mesoscale features, such as eddies, western boundary currents and fronts with their observed strong variation in local horizontal current velocities are also sites of vertical shear which may in turn produce shear enhanced mixing. However, mesoscale circulation in the ocean is traditionally not considered to be responsible for any local increases in vertical turbulent mixing.

To date, direct measurements of turbulent diffusivity around strong mesoscale features such as the Gulf Stream have only recorded moderate levels of turbulent diffusivity of a similar magnitude to what is observed in the open ocean (Gregg and Sanford, 1980). Mesoscale shear flow, associated with strong currents, has only been observed to produce mixing at magnitudes above open ocean values for parts of the Florida Current (Winkel et al., 2002) and for the Equatorial Undercurrent (Peters et al., 1995, 1988). Nevertheless, geostrophically stable shear flow associated with mesoscale features may set up conditions for vertical turbulent mixing which is then triggered by other processes (Van Gastel and Pelegri, 2004) such as tropical instability waves (Moum et al., 2009) and tide/wind interactions (Rippeth et al., 2009). Enhanced vertical shear associated with sub-mesoscale physical processes occurring at density fronts, such as frontogenesis (Section 1.3.3) may also result in episodic mixing events (Nagai et al., 2009; Van Gastel and Pelegri, 2004; Pelegri and Csanady, 1994).

In this thesis it is proposed to investigate how mesoscale circulation might influence nutrient supply into the euphotic zone through shear enhanced vertical turbulent mixing. The investigation will be carried out using a combination of observation and high resolution computer modelling.

Measurements of turbulent diffusivity and nutrient concentrations have been made around an eddy dipole, a strong mesoscale feature, consisting of a cyclonic eddy and an anti-cyclonically rotating mode-water eddy, as part of UK RSS Discovery cruise D321 (Chapter 2). Production in the sub-polar gyre, of which the Iceland Basin is a part, is not typically considered to be limited by nutrient availability. However, these measurements were made post-bloom when lack of a key trace element, such as iron, may be limiting production (Section 1.1). Under limiting conditions the magnitude of vertical turbulent mixing is potentially of great significance to production (Section 1.2.4). The effect of the presence of a strong mesoscale feature on vertical turbulent mixing is assessed by considering whether mesoscale variations in shear associated with the mesoscale feature enhances the observed vertical turbulent mixing. The potential significance of the turbulent flux of iron to post-bloom production in the region is also considered.

Using the observations of turbulent diffusivity made in the Iceland Basin, combined with observations made in two other ocean regions, a parametrization of shear enhanced vertical turbulent mixing is calibrated (Chapter 3). The shear enhanced mixing parametrization of Pacanowski and Philander (1981) was originally developed to improve modelling of the Equatorial Undercurrent and shear enhanced mixing parametrizations are usually applied to models with vertical resolution of order 25 m to stabilise overflows and jets (Large et al., 1994; Pacanowski and Philander, 1981). To date, little consideration has been given as to how mesoscale shear might stimulate vertical turbulent turbulent mixing for model flows where the vertical resolution is of order 10 m. The parametrisation developed in this thesis will be both appropriate for mesoscale flow and suitable for use in a high-resolution ocean model.

Eddies are potentially of most significance to the vertical supply of nutrient in the oligotrophic sub-tropical gyre and mode-water eddies are often observed to be associated with high production in the Sargasso Sea (Section 1.3.1). Previous studies investigating vertical fluxes associated with mode-water eddies focussed on an isolated eddy to enable a clearer diagnosis of the vertical fluxes, specifically of the processes driving any vertical flux (Martin and Richards, 2001; Ledwell et al., 2008). For consistency with previous studies and to include potential Ekman-suction effects (Section 1.3.2), a high resolution computer model of a mode-water eddy is constructed (Chapter 4).

The mode-water eddy model is constructed using observations from the Iceland Basin of the mode-water component of the eddy dipole. The observations from the Iceland Basin contain not only measurements of turbulent diffusivity but also high spatial resolution data for hydrography and circulation using both CTD and ADCP. These measurements allow the construction of an eddy model with a representative density and velocity structure and the subsequent comparison of model effective turbulent diffusivity with observation.

Despite eddies not being of the same potential significance to nutrient supply in the Iceland Basin as in the sub-tropical gyre, the physical characteristics of mode-water eddies in the Iceland Basin appear to be similar to the physical characteristics of mode-water eddies found elsewhere in the North-Atlantic (Section 1.3.2.4). Hence the conclusions of this thesis are potentially applicable in all areas of the North-Atlantic.

The new shear enhanced mixing parametrization is implemented in the eddy model and the eddy model is then used to examine the effect of interactions between the eddy and the wind on vertical nutrient fluxes. The vertical flux is quantified and the contribution of vertical diffusive flux to total vertical flux is investigated (Chapter 5).

Location	Rotation	Water properties of core	Core	Notes	Reference
Greenland Sea (~75°N 0°W)	Geostrophic velocity ~20 cm s^{-1} at 1500 to 2000 m. Radius ~8 to 15 km, in solid body rotation.	-0.96°C / 34.88 salinity (σ_o 28.1 kg m^{-3})	~2000 m thick below 500 m depth	Formed by local convection, potentially a persistent feature of Greenland sea	Kasajima et al. (2006) Oliver et al. (2008)
Iceland Basin (~60° N 20°W)	Max rotational speed ~40 cm s^{-1} at 40 km radius. At 700 m depth in solid body rotation to ~20 km. ~3.5 days rotational period at 20 km radius	7.8 °C / 35.18 salinity (σ_o 27.45 kg m^{-3})	~1000 m thick centred on 700 m depth	Source deep winter mixing of water from Rockall region	Martin et al. (1998) (PRIME)
	Max rotational speed 35 cm s^{-1} at 25 km radius, 3 to 3.5 day rotational period	$<$ 9 °C / 35.3 salinity (σ_o 27.4 kg m^{-3})	Similar to PRIME eddy	Similar to PRIME eddy	Jickells et al. (2008) (ACSOE)
Labrador Sea (~57°N 52°W)	Peak rotation speeds 10 to15 cm s^{-1}, 10 to 15 km solid body radius	2.6 to 2.7 °C / 34.8 to 38.8 salinity (0.1°C lower than surrounding waters)	Between ~250 to ~1250 m thick centre at ~500 to ~750 m depth	Formed by deep winter convection in Labrador Sea	Lilly and Rhines (2002)

Location	Rotation	Water properties of core	Core	Notes	Reference
NE Atlantic (45°N 11°30'W)	Maximum rotational speed 15 to 20 cm s^{-1} at 15 km radius ~60 km diameter zonal 45 km diameter meridional, rotational period ~5 days.	11.5 °C / 36.17 Salinity (nr 1000 m depth) (2.5 °C / 0.5 > surroundings) (σ_o 27.6 kg m^{-3})	Between 600 to 1600 m thick centred at 1200 m depth	'Meddy' northern variety generated between Cape Finisterre and Cape Ortegal. Not formed by convection	Paillet et al. (2002)
NE Atlantic (Southern Bay of Biscay) ~45 °N	Maximum rotational speed 30 cm s^{-1} at 30 km radius, 50 to 60 km radius, rotation period ~3 days	12.95 °C / 35.74 salinity (σ_o 27.8 kg m^{-3})	Between ~70 to ~280 m thick	'Swoddy' - not formed by convection but by mixing of slope water near Cap Ferat.	Garcia-Soto et al. (2002) Pingree and le Cann (1992) Paillet (1999)
NE Atlantic (43.5°N 15 to 19°W)	Rotational speed ~20 cm s^{-1} (between 8 to 17 km from centre at 400 m depth), solid body radius ~30 km, ~5 days rotational period at 15 km radius.	11 to 12.7 °C / 35.5 to 35.7 salinity (σ_o 27.175 kg m^{-3})	~600 m thick below 150 m depth	Formed by convection at Northern end of Bay of Biscay ~North of 47 °N. 3 year lifetime	Reverdin et al. (2009) (POMME)

Location	Rotation	Water properties of core	Core	Notes	Reference
NE Atlantic (south of 40°N)	Peak speeds 18 cm s^{-1} at 16 km radius and 25 ms^{-1} at 24 km radius, 48 km diameter ~6 day rotation period.	12°C / 36.2 salinity (σ_o 27.5 kg m^{-3})	500 m thick centred at 1000m depth decaying to 350 m thick	'Meddy' - not formed by convection	Schultz Tokos and Rossby (1991)
Sargasso Sea BATS (~30°N 64°W)	Peak rotational speed ~30cm s^{-1}, Solid body rotation to ~20 km. Rotation period ~6.3 days at 20 km.	σ_o 26.25 to 26.5 kg m^{-3}	~500m thick below 100 m depth	Angular velocity decreases from 20 km radius by 0.1 rad day^{-1} out to 100 km	Ledwell et al. (2008)
	Rotational speed ~30 cm s^{-1} at 250 to 500 m depth. Solid body rotation to ~20 km. ~5 days rotation period at 20 km	10 °C / 36.5 salinity (σ_o 26.4 kg m^{-3})	~500 m thick centred on ~350 depth	Convective formation between 35 to 38°N Eastern coast of US	McGillicuddy et al. (1999) Brundage and Dugan (1986)

Location	Rotation	Water properties of core	Core	Notes	Reference
Sargasso Sea (Antilles current region ~20 to 30 °N 70°W)	Peak rotational speed 4 to 5 cm s^{-1} (Radius not recorded.)	σ_o 26.5 to 27.3 kg m^{-3}. Lens core is 1 g cm^{-2} more salt in the core than surrounding waters.	~80 m thick below 654 m depth	Estimated to be 3 to 4 years old. Origin near the Gulf of Cadiz	Zantopp and Leaman (1982)
	Maxumum rotation speed 30 cm s^{-1} at 50 km radius. Maximum radius 100km.	σ_o 27.3 to 27.55 kg m^{-3}. Lens core is saltier than surrounding waters	~400 m thick below 800 m depth	Meddy	McDowell and Rossby (1978)
NE Atlantic (25° N)	Maximum rotational speed 16 cm s^{-1} at 175 m depth, 100 km diameter, ~5 to 8 day rotation period.	19.9 °C / 37.06 salinity (σ_o 26.4 kg m^{-3})	190 m depth vertical decay scale ~250 m aspect ratio ~0.14 %	'Swesty' formation at approx 27 °N 22 °W	Pingree (1996)

TABLE 1.1: A summary of the physical properties of mode-water eddies observed in the North Atlantic.

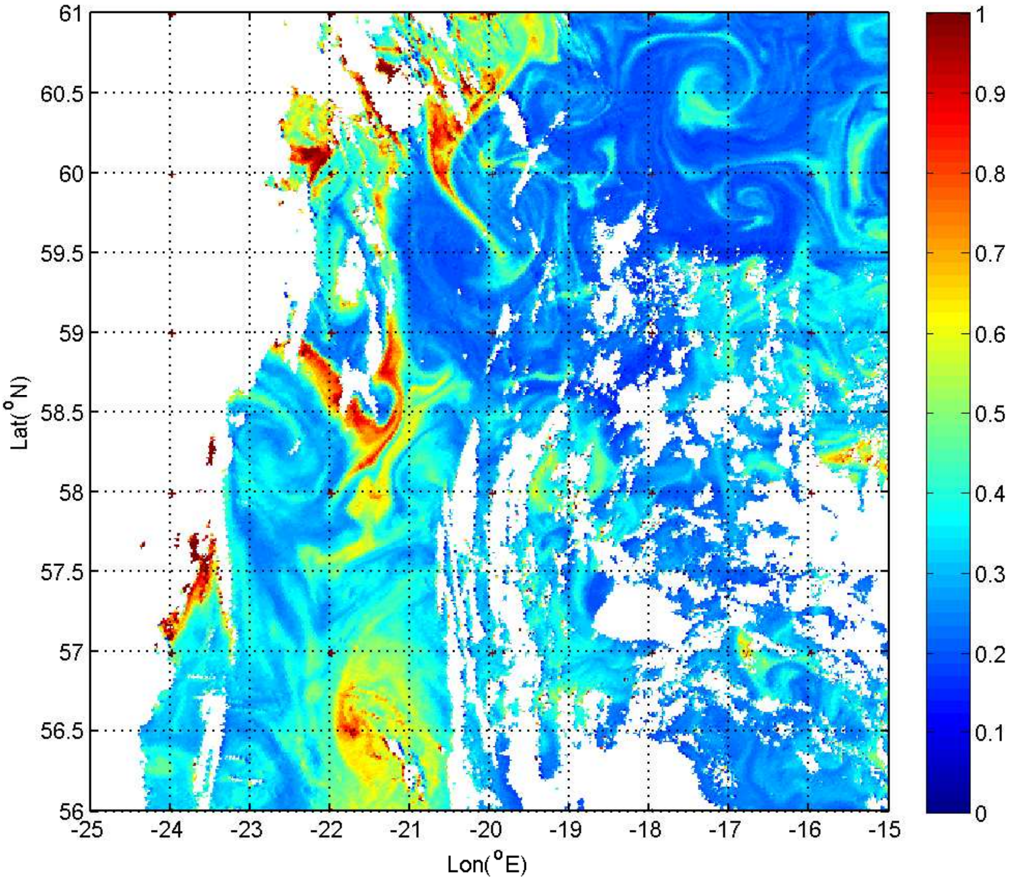

FIGURE 1.1: Satellite images of MODIS chlorophyll concentration (mg m^{-3}) from the 6th July 2007 for the Iceland Basin. This images shows a typically patchy distribution of surface chlorophyll potentially due to mesoscale circulations. Processed satellite image data for chlorophyll concentration from 1 km resolution MODIS data were downloaded from the NERC Earth Observation Data Acquisition and Analysis Service (NEODAAS). The white areas are cloud.

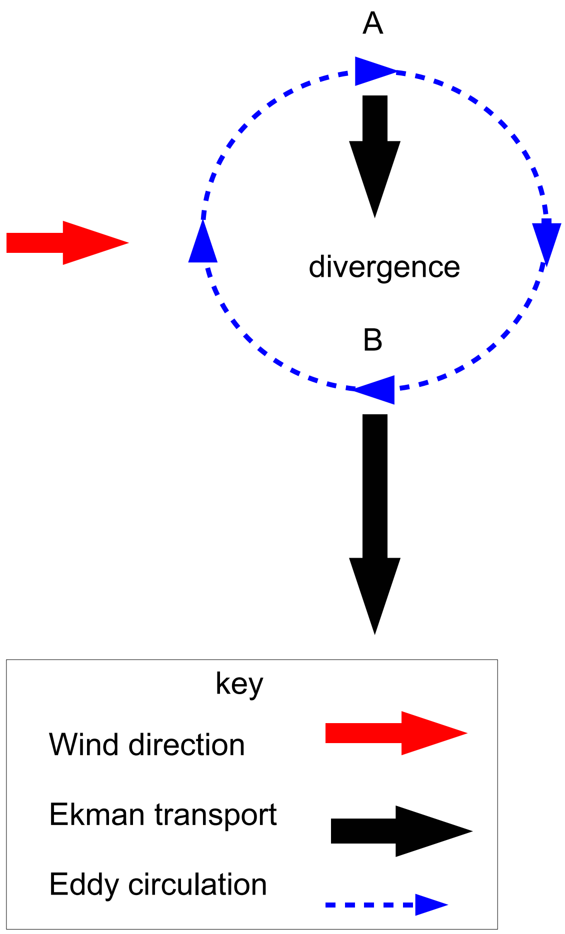

FIGURE 1.2: Cartoon of an anti-cyclonic eddy (Northern Hemisphere) showing how wind stress can lead to a divergence and up-welling in the eddy core. The length of the transport arrows indicates the magnitude of the transport.

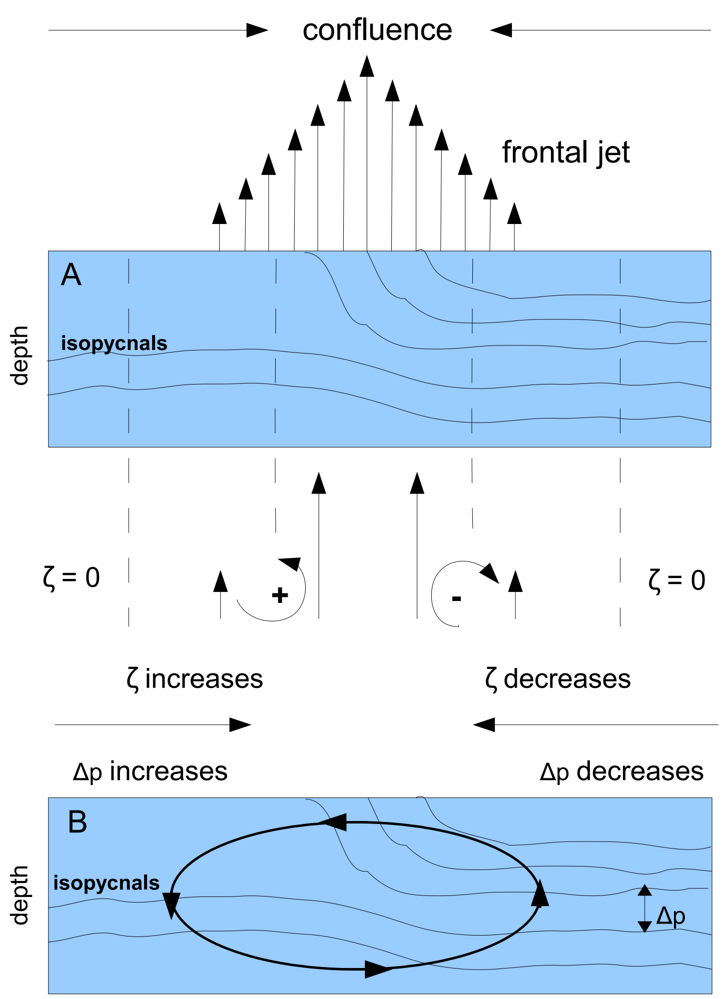

FIGURE 1.3: Cartoon of a density front initially in geostrophic balance on an f-plane. Horizontal strain, in the direction of the frontal jet creates a confluence (panel A). Water drawn laterally towards the frontal jet experiences a gradient in relative vorticity (ζ), increasing on the cyclonic side of the jet and decreasing on the anticyclonic side of the jet. Conserving potential vorticity, the distance between the isopycnals (Δp) increases on the cyclonic side of the jet and decreases on the anticyclonic. This change in isopycnal thickness establishes an ageostrophic secondary circulation (panel B) which acts to restore geostrophic balance.

Chapter 2

Observations of vertical turbulent nutrient flux.

2.1 Introduction

In the north Atlantic sub-polar gyre, of which the Iceland Basin is a part, the primary source of nutrients to the surface ocean is deep winter convection (Williams et al., 2000). In contrast to the seasonal supply of nutrients from deep winter mixing, vertical turbulent mixing is a constant flux. Nevertheless, in the Iceland Basin vertical turbulent mixing is considered to be a minor source of nutrients into the surface ocean (Williams et al., 2000).

In the Iceland Basin, seasonal stratification and increased levels of irradiance lead to a major bloom event in spring (Sanders et al., 2005; Nielsdóttir et al., 2009). However, significant nitrate and phosphate concentrations can persist post bloom (Sanders et al., 2005). One possible explanation of this pool of residual nutrient is iron limitation (Nielsdóttir et al., 2009). Where nutrients are limiting the small but constant supply of limiting nutrient from turbulent mixing may control levels of primary production. For example, in the oligotrophic eastern Atlantic the vertical nitrate flux, associated with vertical turbulent transport from deeper waters matches, within error limits, the integrated rate of nitrate uptake measured, in situ, by ^{15}N-labelled nitrate incorporation (Lewis et al., 1986).

Vertical turbulent mixing in the interior of the stably stratified ocean is often associated with shear instability (Polzin, 1996). Shear instability occurs over a range of time and space scales, from the finescale (vertical resolution $\leq$ 10 m) to the measoscale. At the finescale, shear instability is generated by the breaking of internal waves (Polzin, 1996; Toole and Schmitt, 1987). The sources of internal waves include interaction of the internal tides with topography and wind forcing (Garrett and St. Laurent, 2002; Garrett, 2001; Munk and Wunsch, 1998). At larger scales vertical turbulent mixing can be generated by breaking inertial waves (Marmorino, 1987; Gregg et al., 1986), the shear flow from wind generated inertial currents (D'Asaro, 1985) and instabilities in the shear flow associated with mesoscale features such as boundary currents and fronts (Winkel et al., 2002; Pelegri and Csanady, 1994; Peters et al., 1988).

The objective of this chapter is to estimate vertical nutrient fluxes due to turbulent mixing in the Iceland Basin in the presence of a strong mesoscale feature. The vertical turbulent mixing is to be calculated from a series of velocity shear measurements taken using a free-fall microstructure profiler. The effect of the presence of a strong mesoscale feature on vertical turbulent mixing will be assessed, specifically addressing the question of whether mesoscale variations in shear associated with the mesoscale feature enhances the observed vertical turbulent mixing. Whether the dominant mixing processes are finescale internal wave shear or large scale instability in stratified shear flow, will be explored.

2.1.1 Survey site

The observations processed in this thesis were taken as part of Discovery cruise D321 to the Iceland Basin in August 2007 (Figure 2.1). The overall purpose of this cruise was to examine controls on export production in the region.

On arrival at the survey site it was found that within the survey area was an eddy dipole, consisting of a cyclonic eddy and an anti-cyclonically rotating mode-water eddy (Figure 2.2). The cyclonic eddy is characterised by doming up of isopycnals, displacing the seasonal thermocline upwards, which causes cyclonic rotation and a reduction in sea-surface height. The cyclonic eddy has an elevated sea-surface temperature compared to the surrounding waters (Figure 2.2). The water column profile of the mode-water eddy is characterised by a lens-shaped water mass at mid depth ($\sim$ 550 m) displacing the seasonal thermocline upwards and the permanent thermocline downwards resulting in anti-cyclonic rotation and elevated sea-surface height (Chapter 1). The mode-water eddy exhibits a reduced sea-surface temperature compared to the surrounding waters (Figure 2.2). Within the eddy dipole the two eddies interact producing a region of high current speed ($\sim$ 0.7 m s^{-1}) between the eddy cores. The influence of this high speed region between the eddy cores is apparent where high chlorophyll concentration water has been drawn in from north of the survey region forming a filament of high chlorophyll concentration (Figure 2.2).

During the three week survey small scale turbulent mixing was measured at fifteen stations in various locations in and around the eddy dipole structure (Table 2.1, Figure 2.3).

2.1.2 Turbulent mixing

The magnitude of turbulent mixing can be characterised as a turbulent diffusivity (K), which is analogous to molecular diffusivity, and describes the rate at which scalar properties disperse as a result of turbulent motions (Chapter 1). Turbulent diffusivity can be related to the dissipation of turbulent kinetic energy (ε), using the relationship,

$$\varepsilon = \frac{KN^2}{\Gamma} \tag{2.1}$$

(Osborn, 1980) where Γ is a constant mixing efficiency, the ratio of buoyancy flux to turbulent production, and N is the buoyancy frequency.

$$N^2 = -\frac{g}{\rho}\frac{d\rho}{dz}$$

(Gill, 1982) where g is acceleration due to gravity and ρ potential density.

The level of vertical mixing from non-inertial, tide generated internal wave interactions is generally low. Interactions between internal waves of the Garret & Munk spectrum (Garrett and Munk, 1979) are calculated to give rise to vertical turbulent diffusivity of order 7 x 10^{-6} m^2 s^{-1} (Polzin et al., 1995). However, vertical turbulent diffusivity is observed to be enhanced when tidally generated internal waves interact with topography (Ledwell et al., 2000; Polzin et al., 1997). The levels of vertical mixing from internal wave interactions can also be enhanced by the breaking of near-inertial, wind generated internal waves (Gregg et al., 1986). The level of turbulent dissipation from the breaking of near-inertial internal waves is observed to be higher than the level of turbulent dissipation predicted from interactions of non-inertial internal waves (Gregg et al., 1986). However, the breaking of near-inertial internal waves and any associated mixing is intermittent (Gregg et al., 1986). Mixing patches associated with finescale shear instabilities from the breaking of non-inertial internal waves occur on vertical scales of 2 to 3 m (Alford and Pinkel, 2000; Polzin, 1996) while the mixing patches associated with finescale shear instabilities from the breaking of near-inertial internal waves are between 5 to 10 m thick (Marmorino, 1987; Gregg et al., 1986). The resultant dissipation of turbulent kinetic energy arising from the breaking of internal waves is observed to scale with the buoyancy frequency (N) $\varepsilon \propto N^2$(Polzin et al., 1995; Gregg and Sanford, 1988).

At larger vertical scales turbulent mixing can be generated by instabilities in the shear flow, associated with mesoscale features such as boundary currents, fronts, and jets (Winkel et al., 2002; Pelegri and Csanady, 1994; Peters et al., 1988) or with the vertical shear arising from wind generated inertial currents (D'Asaro, 1985). Persistent instability in stratified shear flow, associated with strong currents, has to date only been observed to be the dominant process driving mixing for parts of the Florida Current (Winkel et al., 2002) and, occasionally, for the Pacific Equatorial Undercurrent (Peters et al., 1995, 1988). However, geostrophically stable shear flow, associated with features such as the Gulf Stream or the Equatorial Undercurrent, may set up conditions for vertical mixing which is then triggered by other processes (Van Gastel and Pelegri, 2004), e.g. tropical instability waves (Moum et al., 2009), tides and wind (Rippeth et al., 2009). Instability in shear flows associated with fronts, e.g. during frontogenic meanders, and time variation associated with shears from wind generated inertial motions can also result in episodic mixing events (Pelegri and Csanady, 1994; D'Asaro, 1985). The vertical shear generating mixing events in the Gulf Stream are observed to occur on vertical scales of $>$ 25 m (Van Gastel and Pelegri, 2004).

Turbulent diffusivity of any scalar quantity (such as momentum or tracer concentration) in a stably stratified shear flow is often related to gradient Richardson number (Ri) defined as the ratio of buoyancy frequency squared to vertical shear (S_h) squared,

$$Ri = \frac{N^2}{{S_h}^2}$$

$${S_h}^2 = (\frac{du}{dz})^2 + (\frac{dv}{dz})^2$$

(Gill, 1982) where u, v are velocities in the x, y direction respectively through an equation of the form

$$K = K_o(1 + \alpha Ri)^{-n} \tag{2.2}$$

where K_o is the turbulent diffusion under neutral conditions and α, n are positive constants (Peters et al., 1988; Monin and Yaglom, 1971; Munk and Anderson, 1948). See Chapter 3 for further discussion of equation 2.2.

2.2 Methods

2.2.1 Turbulence measurement techniques

The measurement of turbulent phenomena presents some unique challenges. Turbulence fluctuates in both time and space and is often weak and difficult to measure. The construction of the measuring instrument, the deployment procedure, and the method of calculation can all potentially introduce errors and biases into the results.

2.2.1.1 The microstructure profiler

The microstructure profiler used in this study was an MSS90L free-fall microstructure profiler (serial number 35) produced by Sea and Sun Technology GmbH and ISS Wassermesstechnik. The profiler is cylindrical in shape with two PNS shear probes (Section 2.2.1.2) and several other sensors (Table 2.2 and 2.3) mounted at the descending end, protected by a guard ring. The two shear probes are on slim shafts approximately 150 mm in front of the CTD (conductivity, temperature, depth) sensors (Figure 2.4).

The profiler has buoyant foam rings at the opposite end from the sensor array where a light tether is attached for data and power transmission. On deployment the profiler free-falls vertically through the water, the sensor array downwards, with the shear probes measuring velocity fluctuations in the 'clean', undisturbed, water in advance of the other sensors. The guard ring is wrapped in string and tassels are attached to the buoyancy end of the profiler to reduce the turbulent 'noise' generated as the profiler passes through the water. Data from the sensors are recorded continuously while the profiler is falling by a P.C., connected via the tether, using software provided by Sea and Sun Technology GmbH (Prandke, 2008*c*).

2.2.1.2 The PNS shear probe

The PNS shear probe, fitted to the MSS profiler, consists of a small aerofoil shaped bead attached by cantilever to a piezoceramic beam which, similar to a gramophone pickup, generates voltages in response to cross-axial fluctuating forces (Prandke, 2008*a*; Lueck et al., 2002). The cantilever and the piezoceramic beam are both protected by a metallic cap (Figure 2.5). The cantilever increases the sensitivity of the piezoceramic beam and the metal cap provides some protection against excessive sideways forces (Lueck et al., 2002).

Shear probes are unable to distinguish between velocity fluctuations resulting from turbulent motion and those arising from profiler movement (pseudo-shear). Pseudo-shear is generated as a result of the construction of the profiler, interactions of the profiler and probe with the surrounding water, and errors in deployment (Prandke, 2007). Pseudo-shear manifests itself as both permanent broad and narrow band signals, intermittent signals, and spikes in the shear profiles.

2.2.1.3 Profiler deployment

Deployment of a microstructure profiler requires careful handling by the operator to minimise the generation of pseudo-shear. Permanent broad band and narrow band pseudo-shear, arising from the construction of the profiler and interactions of the profiler and probe with the surrounding water, can be minimised through tuning of the profiler's drop speed (Prandke and Stips, 1998).

Intermittent pseudo-shear arising from transitory effects of the water on the profiler and cable, and the influence of the operator and ship, can be minimised by ensuring that sufficient slack is maintained in the tether, to allow the profiler to sink in free-fall, isolating the profiler from external vibrations (Prandke, 2007). Intermittent pseudo-shear can occur where the profiler passes through the base of the seasonal thermocline ($\sim$ 30 m Figure 2.6). The abrupt change in density causes the profiler to wobble and results in a spike in the pseudo-shear (Figure 2.6). The operator can also cause intermittent pseudo-shear by rough handling the cable during deployments.

Spikes in the shear profiles arising from collisions with particles, for example marine snow or jellyfish (Stips, 2005), can only be compensated for when processing the shear data (Section 2.2.2).

2.2.1.4 Profiler drop speed

The selection of the profiler drop speed is constrained by both the design of the shear probe, and the properties of the turbulence being measured. The frequency (f_{ex}) of the velocity fluctuations imposed upon the shear probe depends on the vertical scale of the cross-stream component of the turbulence measured (L_v) and the drop speed (V) where

$$f_{ex} = \frac{V}{L_v} \tag{2.3}$$

(Prandke and Stips, 1998). The smallest L_v that can be resolved depends on the spatial response of the shear probe aerofoil, calculated for the PNS shear probe as 5.25 mm (Prandke and Stips, 1998).

The voltages generated by the piezoceramic beam in response to velocity fluctuations at any natural resonant frequency of the shear probe will be erroneously high. Hence the drop speed is determined such that f_{ex} is away from any shear probe natural resonance frequencies. The frequency response curve of the PNS shear probe has a resonance peak at about 315 Hz and is flat below approximately 270 Hz (Prandke and Stips, 1998). Using equation 2.3 the drop speed of the profiler should be below 1.4 m s^{-1}.

Shear probes measure velocity fluctuations as a time-series. Conversion of the time-series measurements into a “space-series” for the calculation of shear (Section 2.2.2) requires Taylor's 'frozen' turbulence hypothesis to be valid, where the turbulent water current velocity measured is much smaller in magnitude than the speed of the probe (Tennekes and Lumley, 1972). Hence the shear probe must be able to traverse the largest scales of microstructures within the time scale of eddies dissipating. The length and time scales for the microstructures are given by the Kolmogorov microscales $(\frac{\nu^3}{\varepsilon})^{\frac{1}{4}}$ for length and $(\frac{\nu}{\varepsilon})^{\frac{1}{2}}$ for time where $\nu = 1$ x10^{-6} m^2 s^{-1} is the molecular viscosity of water (Tennekes and Lumley, 1972). With 90 % of dissipation observed to occur at length scales between 1.5 to 70 times the Kolmogorov length scale (Lueck et al., 2002), the minimum speed required of the probe, applying these constraints, is given by

$$V > 70(\nu\varepsilon)^{\frac{1}{4}} \tag{2.4}$$

(Lueck et al., 2002). Using equation 2.4 for dissipation rates of $\sim 10^{-4}$ W kg^{-1}, the upper limit of detection for the PNS probe (Prandke and Stips, 1998), the profiler drop speed must exceed 0.2 m s^{-1}.

The drop speed, combined with the depth of profiling, also affects the time taken to record a profile, which has implications for the number of measurements that can be taken during a deployment. Higher profiler drop speeds increase the internal vibration of the profiler, leading to higher levels of pseudo-shear. For a drop speed of 0.8 m s^{-1}, the dissipation rate resulting from the instrument pseudo-shear (pseudo-dissipation) is $\sim 10^{-11}$ W kg^{-1} (Prandke and Stips, 1998). The manufacturers' recommended drop speed of approximately 0.5 m s^{-1} is a compromise which allows profiles to be taken as rapidly as possible while minimising the instrument generated pseudo-shear.

2.2.1.5 The number of measurements

Turbulence in the ocean has pronounced spatial and temporal variation which is typically not best characterised by Gaussian distributions (Baker and Gibson, 1987). Consequently, to obtain robust estimates of dissipation rates, multiple measurements need to be combined and each profiler deployment should consist of as many profiles as reasonably practicable. As a rule of thumb, robust estimates of dissipation can be made with measurements from 5 to 10 consecutive profiles (Prandke, 2007).

The distribution of the turbulent diffusivity and turbulent kinetic energy dissipation data for each station was tested using the Kolmogorov-Smirnov test (Press et al., 1989) over the depth intervals used in calculating vertical shears (8 m Section 2.2.6). For each station, each cast was processed individually in 0.5 m depth intervals. The data from all individual casts was collected together into 8 m depth intervals and then compared to both a normal and lognormal distribution using a Kolmogorov-Smirnov test. Each cast was processed individually and the results considered together in order to ensure that there were a sufficient number of data points at each depth interval for the Kolmogorov-Smirnov test to distinguish between different distributions (the number of data points should be > 20, Press et al. 1989). In all cases, for both turbulent diffusivity and turbulent kinetic energy dissipation measurements, the Kolmogorov-Smirnov test returned a higher significance when the data was compared to a lognormal distribution than when the data was compared to a normal distribution.

Consequently the method of Baker and Gibson (1987) was used when averaging station profiles of turbulent diffusivity and turbulent kinetic energy dissipation vertically into 8 m depth intervals. The method of Baker and Gibson (1987) defines the mean (M) for lognormally distributed data as

$$M = \exp(\mu + \frac{\sigma^2}{2}) \tag{2.5}$$

where μ and σ^2 are the arithmetic mean and variance of the log transformed data. The 95 % confidence intervals are then given by,

$$M * \exp(\pm 1.96 * \eta_b)$$

where

$$\eta_b = \sqrt{[\sigma^2/n + \sigma^4/2(n-1)]}$$

and n is the number of data points (Baker and Gibson, 1987).

2.2.2 Calculation of microstructure shear

The voltage generated by the piezoceramic beam (E_p), in response to a cross-axial velocity fluctuation (u'), when the probe is travelling at a constant speed (V) (Figure 2.7), is given by

$$E_p = \hat{s}\, V u' \tag{2.6}$$

where $\hat{s}$ is a probe calibration factor (Prandke, 2007). The shear probe calibration factor is determined by imposing a flow of known velocity on to the probe, whilst it is rotating axially at a fixed angle to the flow, and measuring the output voltage. The shear probes on the MSS90L profiler were calibrated by ISS Wassermesstechnik to an accuracy of approximately ± 5 % for angles of attack (α) less than 15° (Prandke, 2007). The probe calibration factor is affected by both angle of attack, and temperature. The angle of attack is measured by tilt sensors on the profiler and corrections for temperature and in situ angle of attack, are applied when the shear is calculated (Prandke, 2007). Due to the hydrodynamic properties of the profiler and cable, the profiler does not fall perfectly vertically through the water but maintains a constant tilt in the x-direction (Figure 2.6). For a typical deployment the mean angle of attack for the probe is 2.69 ± 0.74^{o} in the x direction and 0.14 ± 0.46^{o} in the y direction.

Differentiating 2.6 with respect to time gives

$$\frac{\partial E_p}{\partial t} = \hat{s}V\frac{\partial u'}{\partial t}$$

If the probe is travelling vertically downwards (z), with a constant sinking velocity (V), the rate of change of cross-axial velocity with distance, assuming 'frozen' flow, can be expressed as

$$\frac{\partial u'}{\partial z} = \frac{1}{V}\frac{\partial u'}{\partial t}$$

Hence

$$\frac{\partial u'}{\partial z} = \frac{1}{\hat{s}V^2}\frac{\partial E_p}{\partial t}$$

(Prandke, 2007).

2.2.2.1 Error correction of microstructure shear calculations

Permanent broadband pseudo-shear (P_{shear}) arises from vibrations of the profiler components and housing. The magnitude of the permanent broadband pseudo-shear generated by the profiler determines the lower limit of the shear the probe can detect (Prandke and Stips, 1998). An estimate of P_{shear} can be made from the horizontal acceleration (a), measured by the profiler acceleration sensors, and the drop speed of the profiler

$$P_{shear} = \frac{a}{V}$$

(Prandke and Stips, 1998). Permanent narrow-band pseudo-shear, which can be seen in Figure 2.8 as peaks at approximately 50 to 60 cpm (cycles per meter) and 110 cpm, arises from eddy generation and vortex shedding as the profiler passes through the water. Such peaks in the shear spectrum are removed by band-pass filtering the shear spectrum before the dissipation rate calculation (Prandke, 2007).

Spikes in shear profiles arising from collision of the probes with solid material are removed by de-spiking the profile prior to estimations of dissipation rate. Profiles are de-spiked by breaking the shear profile into a series of small windows and considering each window in turn, replacing by interpolation shear values that are greater than an empirically determined threshold. In this thesis, profiles are de-spiked following the method of Stips (2005) and Prandke (2008*c*), where the standard deviation of the shear is calculated over a window of 40 sample lines and values of the shear, within the window, that exceed 2.7 times the calculated standard deviation are replaced by linear interpolation between adjacent acceptable values.

The spatial response of the shear probe imposes a minimum wavelength for velocity fluctuations that the probe can resolve. As the wavelength of the velocity fluctuations decreases the response of the shear probe attenuates (Prandke, 2007; Rippeth et al., 2003; Moum et al., 1995; Oakey, 1982). The degree of attenuation can be estimated in the laboratory by measurement of controlled mechanically generated turbulent dissipation. A transfer function can then be derived which is used to correct for probe attenuation (Prandke, 2007; Prandke and Stips, 1998). In this thesis a transfer function empirically derived in this manner by the manufacturer for the PNS shear probe (Prandke, 2007) was used to correct for shear probe attenuation.

The quality of the resultant processed shear profiles was checked by visual comparison of the power spectrum of the measurements with the Naysmith form of the universal turbulence spectrum (Prandke, 2007; Stips, 2005). In Figure 2.8 the two profiles show good agreement with the universal spectrum between 2 to 30 cpm (See Section 2.2.3.2 for an explanation of the limits chosen). Above 30 cpm the measured spectrum differs from the universal spectrum due to pseudo-shear and the attenuation of the shear probe.

2.2.3 Calculation of turbulent kinetic energy dissipation

2.2.3.1 Theory and assumptions

The rate of turbulent kinetic energy dissipation can be calculated from the variance of the vertical shear

$$\varepsilon = \frac{15}{2}v\overline{\left(\frac{du'}{dz}\right)^2} \tag{2.7}$$

where the overbar indicates a spatial or temporal mean value and *u'* is the turbulent velocity fluctuation (Lueck et al., 2002). This estimation depends on the underlying assumption of isotropy of turbulence. Turbulence is locally isotropic only within the 'equilibrium range', from the wavenumber (k_l) where the strain rate of the turbulent eddies becomes large compared to the mean strain rate, to the Kolmogorov wavenumber (k_c) (Tennekes and Lumley, 1972). The Kolmogorov wavenumber, the reciprocal of the Kolmogorov microscale, is given by

$$k_c = \left(\frac{\varepsilon}{\upsilon^3}\right)^{\frac{1}{4}} \tag{2.8}$$

The Kolmogorov microscale represents the smallest scale of turbulent motions unaffected by the dissipative effects of molecular viscosity. At length scales smaller than the Kolmogorov microscale, energy from turbulent motions is dissipated as heat through the action of molecular viscosity (Tennekes and Lumley, 1972). The lower limit of the equilibrium range (k_l) is less well defined. There is no sharp boundary between isotropic and non-isotropic turbulence. The lower limit has to be set empirically (Stips, 2005). In this thesis a value of $k_l = 2$ cpm has been used (see Section 2.2.3.2).

The largest scale of turbulent motions in stratified water is given by the Ozmidov length scale

$$L_o = \left(\frac{\varepsilon}{N^2}\right)^{\frac{1}{2}}$$

(Tennekes and Lumley, 1972). If the ratio between the Kolmogorov and Ozmidov length scales is large then the length scales of the smallest and largest turbulent motions are well separated. In this case the smallest turbulent motions may have isotropic properties (Thorpe, 2005). From observation, equation 2.7 can be used to calculate accurately the rate of turbulent kinetic energy dissipation if the critical ratio

$$I = \frac{\varepsilon}{\upsilon N^2}$$

is greater than 20 (Prandke, 2007; Yamazaki and Osborn, 1990). As the value of I decreases the error in the calculations of ε increases up to a maximum of 35 % (Prandke, 2007; Yamazaki and Osborn, 1990). For the data in this thesis, taking the molecular viscosity for seawater to be 1.2 x10^{-6} m^2 s^{-1}, I is greater than the critical value of 20 for 92 % of the measurements, only dropping below 20 in the seasonal thermocline ($\sim$ 30 m depth Section 2.3.1.1).

The variance of the vertical shear ($\overline{\left(\frac{du'}{dz}\right)^2}$ Equation 2.7), over a given depth interval, is usually calculated as the 'total power' of the vertical shear power spectrum ($\Phi(k)$), between the limits k_l to k_c, calculated for the same depth interval. For a function c sampled N times to give values $c_0, \ldots, c_{N-1}$

$$TotalPower = \frac{1}{N}\sum_{j=0}^{N-1}|c_j|^2 \qquad (2.9)$$

where j is the index of the jth sample of c (Press et al., 1989). Determination of shear variance from the shear power spectrum allows filtering of the power spectrum to eliminate measured shear that is not associated with turbulent dissipation and the application of corrections for shear probe spatial response (Stips, 2005; Rippeth et al., 2003; Moum et al., 1995).

The vertical shear power spectrum is calculated from the discrete Fourier transform of the vertical shear fluctuations ($\mathbb{S}_h(k)$). If we consider N samples of $S_h'(z)$, ${S_h}'_0, \ldots, {S_h}'_{N-1}$, evenly spaced within a given depth interval where $S_h'(z)$ is the vertical gradient in velocity fluctuations. The corresponding Fourier transformed values, $\mathbb{S}_{h0}, \ldots, \mathbb{S}_{hN-1}$, are given by

$$\mathbb{S}_{hj} = \sum_{m=0}^{N-1} S'_{hm} e^{2\pi imj/N} \qquad j = 0, \ldots, N-1$$

where m and j are indexes to the mth and jth samples of $S_h'(z)$ and $\mathbb{S}_h(k)$ respectively (Press et al., 1989). The periodogram method of power spectrum estimation is defined for the first $N/2$ values of $\mathbb{S}_h(k)$ up the the critical (Nyquist) wavenumber k_n (Press et al., 1989). The critical wavenumber is the largest wavenumber that can be resolved for the given sampling interval

$$k_n = \frac{1}{2\Delta}$$

(Press et al., 1989) where Δ is the sampling interval. For a shear probe with a sampling frequency of 1024 Hz and a drop speed of 0.5 ms^{-1} the sampling interval is 4.8 x10^{-4} m and the critical wavenumber is 1024 cpm. Hence from Equation 2.8 the highest dissipation rate that can be measured is 1.32 x10^6 Wkg^{-1}. Using the periodogram method of power spectrum integration

$$\Phi(k) = \frac{1}{N^2}\left[|\mathbb{S}_{hj}|^2 + |\mathbb{S}_{hN-j}|^2\right] \quad j = 1, 2 \ldots, \left(\frac{N}{2} - 1\right)$$

$$k = \frac{j}{N\Delta}$$

where j is the index of the jth sample of $\mathbb{S}_h(k)$ (Press et al., 1989). $\Phi(k)$ is a normalised power spectrum (Press et al., 1989). Hence, the sum of $\Phi(k)$ between k_l to k_c is equal to the total power between those limits. By Parseval's theorem (Press et al., 1989) the total power of $\Phi(k)$ is equal to the total power of $S_h'(z)$ which from Equation 2.9 is equivalent to the variance of the vertical shear.

2.2.3.2 Methods of estimating turbulent kinetic energy dissipation

There are two approaches, both described below, for calculating the dissipation rate by integration of the power spectrum of the vertical shear variance. One method is to integrate the measured spectrum (Oakey, 1982; Rippeth et al., 2003; Prandke, 2007) and the other is to integrate the universal turbulence spectrum, dimensionalised and scaled to match the measurements (Moum et al., 1995).

Integrating the measured turbulence spectrum Integration of the measured spectrum is either by integration of a segment of the power spectrum and applying corrections for lost variance (Rippeth et al., 2003; Prandke, 2007), or by subtraction of an estimated noise spectrum followed by integration across the whole spectrum (Oakey, 1982). In both cases, corrections for sensor attenuation are applied to the measurements, either as a scaling to the dissipation estimates (Prandke, 2007), or to the shear power spectrum prior to integration (Oakey, 1982; Rippeth et al., 2003).

Using the first method, where a segment of the measured power spectrum is to be integrated, the upper and lower wavenumber limits of integration are determined heuristically such that pseudo-shear is at a minimum in the spectrum segment (Rippeth et al., 2003; Prandke, 2007). The correction factor for lost variance is estimated based upon the fraction of the total spectrum energy contained within the integrated segment (Rippeth et al., 2003; Prandke, 2007). The fraction of total spectrum energy contained within the integrated segment is estimated from consideration of the fraction of total spectrum energy contained within the universal spectrum integrated within the same limits (Rippeth et al., 2003; Prandke, 2007). For example, at a dissipation rate of 1 x 10^{-8} W kg^{-1} integration between 2 to 30 cpm accounts for ∼ 90 % of the total dissipation and the measured dissipation estimated by integration between 2 and 30 cpm would be ∼9 x 10^{-9} W kg^{-1} (Figure 2.9). However, at a dissipation rate of 1 x 10^{-5} W kg^{-1} integration between 2 to 30 cpm accounts for ∼ 20 % of the total dissipation and the measured dissipation estimated by integration between 2 and 30 cpm would be ∼2 x 10^{-6} W kg^{-1} (Figure 2.9). Using this process, estimates of the dissipation that would be measured between finite integration limits can be used to calculate correction factors for lost variance at different measured dissipation rates and integration limits. The appropriate correction factors are then applied to the results of integrating the segment of the measured power spectrum to give an estimate of the true dissipation rate (Rippeth et al., 2003; Prandke, 2007).

Using the second method, when integrating the whole of the measurement spectrum, the noise power spectrum is typically approximated as being equal to the power spectrum calculated for regions within the measurements where uncorrected dissipation rates are lowest. This estimated noise spectrum, assumed to be constant for all dissipation rates, is subtracted from measurements after correction for the probe spatial response (Oakey, 1982). True dissipation rates are then calculated by integration of the whole spectrum for the corrected measurements (Oakey, 1982).

Scaling a universal turbulence spectrum Dimensionalising and scaling the universal spectrum using the measurements can be done in two ways. The first involves an iterative procedure. The universal spectrum is initially scaled and dimentionalised based on the dissipation rate estimated by integrating a restricted segment of the measurement power spectrum. The upper and lower wavenumber limits for the integration of the restricted power spectrum segment are determined heuristically. Initially a dissipation rate is estimated by integration of the power spectrum between 2 and 10 cpm. This initial dissipation rate is then used to select suitable upper and lower wavenumber limits for a second integration of the power spectrum. The dissipation rate estimated from the second integration of the measured power spectrum is then compared to the dissipation rate calculated from integrating the scaled universal spectrum between the same limits. If the two estimates do not agree to within 5 %, then the initial estimate of the dissipation rate is increased by multiplying by the ratio of the measured dissipation to the dissipation calculated from the universal spectrum. The integration limits are re-calculated and the procedure is repeated until the two dissipation values differ by less than 5 %, when the total dissipation is calculated by integration of the scaled universal spectrum up to k_c (Moum et al., 1995).

The second method for calculating dissipation, and the one used in this thesis, is by integration of a scaled and dimensionalised universal turbulence spectrum. The universal spectrum was scaled by curve fitting an analytical form of the universal spectrum to a segment of the measured vertical shear power spectrum using a least squares fit. The least squares fit minimises the square of the difference between the log of the analytical universal shear power spectrum and the log of the observed shear power spectrum for all points between fixed wave number limits (2 to 30 or k_c cpm, whichever is lower, see below).

One of the advantages of using the second method over the previously described methods is that it allows data from multiple profiles to be used in calculating a single estimate of dissipation for a station. The segment of the power spectrum considered, in all methods of calculating dissipation, is a small fraction of the total power spectrum. For a high dissipation rate of $\sim 10^{-7}$ W kg^{-1}, a value typical above the seasonal thermocline (Lueck et al., 2002), k_c is $\sim$560 cpm. The range 2 to 30 cpm is less than 5 % of the total spectrum and the wavenumber for the peak dissipation rate, given by $0.125 k_c$ (Gregg, 1999), is outside this range at 70 cpm. Only for lower rates of dissipation $\sim 10^{-9}$ W kg^{-1} does the peak dissipation rate fall within the range of 2 to 30 cpm. Even in this case the segment only represents $\sim$ 20 % of the total spectrum's energy. Direct integration using extrapolation from such a small range of the power spectrum is sensitive to any outlying values which may occur within the segment and skew the estimate of dissipation. Curve fitting, to data pooled from a number of casts, is more robust to outlying values. Considering the spectra from all profiles of a deployment together increases the number of points available for the curve fit by typically a factor of ten, thereby improving the quality of the curve fit and the robustness of the calculated dissipation rate.

The power spectrum of the measurements was calculated for each 1 s of data in each profile (1024 data points, $\sim$ 0.5 m) using the Welch method, with a Bartlett window of size 512 points, and a 50 % window overlap. The Welch method of power spectrum estimation calculates the power spectrum of a record by averaging the periodogram in sections of the record, modified by application of a window function, to minimise power 'leakage' from one frequency to another (Welch, 1967). The choice of time interval for power spectrum integration is determined by the scale of the turbulent velocity structures being measured and the profiler drop speed (Stips, 2005). The time interval needs to be sufficiently long such that the distance travelled by the probe is in excess of the wavelength of the largest of the turbulent velocity structures in the equilibrium range. For the MSS profiler the standard depth interval is 0.5 m (Stips, 2005).

For each station, the power spectrum was calculated, for each individual cast, for each depth interval. For each depth interval an analytical form for the empirical Naysmith spectrum

$$\Phi_{Nas}(k) = \frac{8.05k^{\frac{1}{3}}}{1 + (20k)^{3.7}} \tag{2.10}$$

(Roget et al., 2006) was fitted simultaneously to the power spectra from all casts using a least squares fit between the limits 2 to 30 cpm (or k_c whichever was lower) . The lower limit wavenumber of 2 cpm was selected as this represents the wavenumber of the maximum possible wavelength of turbulent velocity fluctuation resolvable within a depth interval of 0.5 m. This lower limit also eliminates low frequency noise from the probe wobbling during descent (Prandke, 2007). The maximum upper limit of the integration, 30 cpm, was selected to be below the resonant frequency of the shear probe guard ring, which is visible as the spike at between 50 to 60 cpm in Figure 2.8 (Prandke and Stips, 1998). As discussed above, a correction for shear probe spatial response was then applied to the dissipation estimate, using the empirical polynomial function for the PNS probe (Prandke, 2007).

As a check on the calculated dissipation rates, dissipation was also calculated by taking the geometric mean of the power spectra for each station, integrating between limits, and applying the empirical polynomial correction for lost variance (Prandke, 2007). The values of dissipation calculated by this method were then compared with those from the curve fitting to give an independent estimate of goodness of fit. This estimate was used as an indicator for which sections of a station profile should be manually checked. Deviations of greater than 1 order of magnitude were investigated by qualitative comparison of the shape of the combined shear power spectra for that segment with the universal spectrum (Stips, 2005; Prandke, 2008*c*). Individual profiles, within the segments, exhibiting significant deviation from the universal spectrum (where the shape of the power spectrum did not conform to the shape of the universal spectrum within the limits of integration defined above), were removed from the calculation. All sections of profiles where the tilt angle, as recorded by the profiler, exceeded 15°(Section 2.2.2) were discarded. All results for depths shallower than 14 m (approximately three times the draft of the ship) were also discarded to ensure there was no contamination of the results by the turbulent wake of the ship and for compatibility with data from ship mounted ADCP. Calculated dissipation rates were also compared with values calculated from the estimated pseudo-shear (pseudo-dissipation). In this case profiles were not discarded unless dissipations were below pseudo-dissipation rates for eight consecutive segments, representing a 4 m depth interval, comparable to the resolution of the ship mounted ADCP.

Combining independent estimates of turbulent kinetic energy dissipation rate The microstructure profiler has two independent shear sensors (Section 2.2.1.1). The data from the two independent shear sensors were used to calculate two estimates of the dissipation rate for a station using the method described above. The two estimates of the dissipation rate were then combined to provide a single estimate of the dissipation rate for the station. Following the method described in Prandke (2008*c*), the geometric mean of the two values was taken unless the value from one sensor exceeded the other by a factor of 5, in which case the lower of the two values was used.

2.2.3.3 Estimating the error in the calculation of turbulent kinetic energy dissipation

Errors in calculating estimates of the dissipation rate arise from a number of sources. Calibration of the shear sensors (Section 2.2.2) is to within ±5 %, and the influence of non-isotropic turbulence is estimated to add up to 35 % error to calculations (Section 2.2.3.1). In addition to these, uncertainties in the flow speed past the shear probe, estimated to be $\sim \pm 5$ %, adds an additional ~ 20 % error to the calculation (Oakey, 1982; Moum et al., 1995), as the calculated dissipation depends on the variance of flow shear squared (equation 2.7). Lesser (< 10 % Dewey and Crawford (1988) errors arise from drift in shear probe calibration and uncertainties in the estimates of viscosity. Combining all the estimates of error together gives a generally accepted estimate of ±50 % error in the calculation of turbulent dissipation (Oakey, 1982; Moum et al., 1995; Rippeth et al., 2003).

2.2.3.4 Verification of turbulent kinetic energy dissipation rates

As an independent check, the results for each station, calculated as described above, were compared with dissipation rates calculated using the standard MSSpro software (Prandke, 2008*c*). The MSSpro software is supplied with the MSS90L profiler by ISS

Wassermesstechnik and calculates dissipation by integration of the shear spectrum measurements between 2 and 30 cpm followed by the application of corrections for shear probe attenuation and lost variance (Prandke, 2008*c*).

For all stations, the maximum difference between the two methods of calculating dissipation is less than the 50 % estimate of error for the calculation of dissipation rates (Section 2.2.3.3), with a mean per station difference of less than 30 % in all cases (for example station 16222, Figure 2.10). Scatter plotting the results against each other showed no systematic bias in the calculation of dissipation at dissipation rates below 10^{-6} W kg^{-1}, the highest dissipation rate recorded in this thesis (for example station 16222, Figure 2.10).

2.2.4 Calculating turbulent diffusivity

Turbulent diffusivity was calculated from the measured dissipation of turbulent kinetic energy using equation 2.1. The mixing efficiency (Γ) has been estimated to be 0.2 by theoretical consideration of the critical flux Richardson number (Osborn, 1980) and calculated to be 0.235 ± 0.14 from measurements of temperature dissipation rate (Oakey, 1982). In this study a value of 0.2 was used, in line with previous studies (Prandke, 2007; Stips, 2005; Rippeth et al., 2003; Moum et al., 1995).

2.2.5 ADCP and hydrographic measurements

Current velocity down to approximately 300 m was measured using a ship-mounted 150 kHz RDI Acoustic Doppler Current Profiler (ADCP) and logged using RD Instruments data acquisition software (DAS version 2.48 with profiler firmware 17.10). The instrument was configured to sample over 120 second intervals with 96 depth intervals of 4 m thickness starting at 14 m depth using pulse length 4 m and blank beyond transmit of 4 m. Calibration of the ADCP was carried out over the continental shelf on route to the survey site. Values of misalignment angle (14.4^{o}), which corrects for the rotational position of the ADCP on the ship's hull relative to the ship's axis, and the amplitude factor (0.9683), which corrects for the fore-aft tilt of the instrument relative to the horizontal plane, were derived. ADCP data was collected and processed by Stuart Painter, Steven Alderson, and Roz. Pidcock (Allen, 2007).

2.2.6 Calculating shear from ADCP data

Vertical shear was calculated from the ADCP data recorded while the microstructure profiler was being deployed. The individual ADCP velocity components recorded while the station was in progress were averaged in time, using a depth interval of 8 m, to produce a station mean velocity profile. An 8 m depth interval is used for consistency with the shear calculation method described in Chapter 3. The gradient in velocity was calculated, between successive depth intervals, for the individual velocity components. The gradients in velocity component were then combined by taking the root of the sum of the components squared to give the vertical shear at the mid point of each depth interval. The resultant shear profile was smoothed in the vertical by taking a running average over 7 ADCP depth intervals (56 m), to reduce the small scale variability and to emphasise any large scale variations. For a full description of the calculation of vertical shear see Chapter 3.

2.2.7 Calculation of mixed layer and euphotic depths

Measurements of temperature and salinity from the microstructure profiler were combined, for each station, to calculate the station density profile and the depth of the mixed layer. Density was calculated (with respect to 0 dbar pressure) using the UNESCO equation of state (UNESCO, 1980). Following the method of Kara et al. (2000) mixed layer depths for each profile were calculated using a density change criteria. A temperature change of 0.2^{o} from the temperature measured at 10 m depth was used to calculate a density change criterion of the difference in density between the seawater at 10 m and the seawater at 10 m cooled by the temperature change (Kara et al., 2000). Temperature changes of 0.1^{o} and 0.2^{o} and 0.8^{o}, which have been used previously (Kara et al., 2000), were evaluated by comparison of the calculated mixed layer depth with the depth of the homogeneous sections of the calculated density profiles. The density change criteria resulting from a temperature change of 0.2^{o} was selected as best representing the depth of the homogeneous sections.

The euphotic depth was calculated as 1 % of surface irradiance, where irradiance was measured using a 4π downwelling Photosynthetically Available Radiation (PAR) sensor attached to the main shipboard CTD frame. A mean euphotic depth was calculated using PAR data from all CTD casts taken during the D321 cruise.

2.2.8 Nutrient concentration measurements and calculating nutrient fluxes

2.2.8.1 Macro-nutrient concentrations

Analysis for micro-molar concentrations of nitrate and nitrite (referred to hereafter cumulatively as nitrate), phosphate, and silicate was carried out using a scalar Sanplus autoanalyser. Samples were analysed within 24 hours of being taken and were kept refrigerated at approximately 4^o C until analysed. An artificial seawater matrix (ASW) of 40 g L^{-1} sodium chloride was used as the inter-sample wash and standard matrix. The nutrient free status of the ACW solution was checked by running Ocean Scientific International (OSI) nutrient free seawater on every run of the autoanalyser. Data processing was done using Skalar proprietary software and was carried out within 72 hours of the sample analysis run being finished. The performance of the autoanalyser was monitored by compiling time series of baseline, instrument sensitivity, calibration curve correlation coefficient, nitrate reduction efficiency and sample duplicate difference for each sample run (Allen, 2007).

The duplicate difference for each sample run was calculated by comparing the values of the first two drift samples analysed on each run for each macro-nutrient. All except seven runs had less than a 3 % difference. Silicate concentrations always had less than a 3 % difference. Nitrate concentrations had three runs that were above a 3 % difference with a maximum difference of 14 % and phosphate concentrations had four runs above 3 % difference with a maximum difference of 9.5 %. Macro-nutrient samples were collected and analysed by Mark Stinchcombe and Richard Sanders (Allen, 2007).

2.2.8.2 Iron concentrations

Seawater samples to be analysed for dissolved iron (dFe) were collected using a titanium frame CTD with designated "iron-clean" sample bottles. Samples were pressure filtered using nitrogen free oxygen through 0.4 µm and 0.2 µm filters and acidified to a pH ~1.8 with ultra pure HCl. Dissolved iron concentration was measured using flow-injection chemiluminescence methods where samples are buffered with ammonium acetate to pH 4 and pre-concentrated on a resin column during analysis. Each sample was run in triplicate. Iron samples were collected and analysed by Maria Nielsdóttir, Eric Achterberg and Mark Moore and are published in Nielsdóttir et al. (2009).

2.2.8.3 Calculating nutrient flux

Nutrient flux is conventionally modelled by analogy with molecular diffusion, hence the changes in distribution of an inert tracer (C) undergoing turbulent mixing can be represented as

$$\frac{\partial C}{\partial t} = \frac{\partial}{\partial z}\left(K(z)\frac{\partial C}{\partial z}\right)$$

where t is time, z is depth and K is the turbulent diffusivity. The vertical flux of nutrient into the waters above a depth z is therfore given by the product of the turbulent diffusivity and the nutrient gradient at depth z,

$$F(z) = K(z)\frac{\partial C}{\partial z} \qquad (2.11)$$

Vertical nutrient gradients were calculated by first order differencing. For the stations where nutrient measurements were taken on CTDs before or following turbulence stations the calculated turbulent diffusivity for the sample depth interval was combined with the nutrient gradient for the station to give an estimate of turbulent nutrient flux.

2.2.9 Estimating the horizontal distribution of mixing

In an attempt to characterise the spatial variation of turbulent diffusivity due to the influence of the eddy dipole, the location of each of the stations was grouped according to their relationship to the dipole (Figure 2.3). The positions and core diameters of the two eddies were estimated using the ADCP data from three surveys made during cruise D321 by least squares fitting of the ADCP data, recorded at 63 m depth (the closest ADCP depth interval to the euphotic depth), to velocity profiles of the form

$$V(r) = V_0\left(\frac{r}{R}\right)\exp\left[\frac{1}{2}\left(1-\frac{r^2}{R^2}\right)\right]$$

(Martin and Richards, 2001) where $V(r)$ is the azimuthal velocity at radius r from the eddy centre, V_0 is the maximum azimuthal velocity, and R is the radius of maximum azimuthal velocity. For each ADCP survey, values of V_0 and R for both eddies centred at positions x_1, y_1 and x_2, y_2 were fitted to the ADCP velocity data for 63 m depth by minimising the root mean square difference between the calculated velocity field and the ADCP velocity data.

Four distinct regions were identified: the jet region between the two eddy cores, the eddy cores, regions around the eddy core but not between the two eddies, and the background waters (Figure 2.3 and Table 2.4). Once assigned the location of the stations was checked by consideration of both the current magnitude and direction during the station, taken from the shipboard ADCP (Figure 2.11).

For station 16283, the identification of appropriate region is difficult. The station is sited away from the estimated positions of the known eddy dipole cores (Figure 2.3). The magnitude of the current velocity while station 16283 was in progress, showed water movement consistent with either known background stations or with station 16285, known to be within the cyclone eddy core (Figure 2.11). The mixed layer depth of 46 m for station 16283 is greater than observed for known background stations and most closely compares to station 16285 in the cyclonic eddy core (52 m, Figure 2.12). This would suggest that the station 16283 was in the core of a third unidentified eddy within the survey region. However, current direction on arriving and leaving the station remained constant which is not consistent with the expected changes in current direction on entering and exiting an eddy as observed for station 16285 (Figure 2.11). As a result of the uncertainty in the location of this station it has not been included in subsequent comparisons of mixing distribution between the four regions.

Profiles from all stations within each region were first averaged into 8 m depth intervals for consistency with the depth intervals used in calculating vertical shear from the ship ADCP data. Station profiles of buoyancy, originally calculated from microstructure profiler CTD data at 0.5 m depth intervals, were averaged into 8 m depth intervals by taking a mean for each depth interval. Station profiles of turbulent kinetic energy dissipation and turbulent diffusivity were averaged into 8 m depth intervals using equation 2.5.

The 8 m depth interval station profiles of shear and buoyancy were combined into regional profiles by taking a mean, and an estimate of standard error, at each depth interval. For turbulent kinetic energy dissipation and turbulent diffusivity, the 8 m depth interval station profiles were combined into regional profiles by taking a mean of the log transformed data at each depth interval and then reversing the log transform. Confidence intervals to the regional profiles were calculated by taking a mean of the log transformed upper and lower confidence limits for the individual station profiles at each depth interval.

Regional mean nutrient profiles were estimated, for each nutrient, by linearly interpolating individual nutrient profiles onto a common depth profile and averaging over all profiles at each depth of the common profile. Common depth profiles, for each nutrient, were chosen to minimise the differences in depth between the original sample depths and the nearest common profile depth. Depths used in the common depth profile for all macro-nutrients were 14, 25, 32, 37, 52, and 81 m. Depths used in the common depth profile for iron were 12, 22, 29, 34, 49, and 78 m. The interpolated profiles for each nutrient at each station were checked for accuracy by visually comparing to the original nutrient profiles.

2.3 Results

2.3.1 Individual profiles

2.3.1.1 Mixed layer, euphotic depth, buoyancy, shear and, Richardson number

Throughout the survey area, for the duration of the survey, density profiles show a strong seasonal thermocline, the mixed layer depth varying between 18 m and 52 m (Figure 2.12). The shallowest mixed layer depths are associated with measurements taken in the area between the two eddies (23 ± 3 m, mean ± standard deviation stations 16286, 16288, 16289, 16292, 16295, 16296, Figure 2.12) and the deepest (52 m) in the core of the cyclonic eddy (station 16285, Figure 2.12). The mixed layer depth away from observed mesoscale features, was 30 m (30 ± 8 m, mean ± standard deviation stations 16260 16232, 16226, 16222, Figure 2.12). The mean depth of the euphotic zone across the whole D321 survey area, for the duration of the survey, was 64 ± 10 m (mean ± standard deviation).

Buoyancy frequency, for all stations, shows a peak just below the mixed layer in the seasonal thermocline where the density gradients are steepest, with N^2 between 1 to 10 x10^{-4} s^{-2}. The maximum N^2 observed is for station 16247 and the minimum N^2 observed is for station 16241 (Figure 2.13). N^2 reduces with depth to between 1 and 2 x10^{-5} s^{-2} at the euphotic depth and below for all stations except 16285 ($N^2 = 5$ x10^{-5} s^{-2}, Figure 2.13).

For stations 16222, 16226, 16232, 16242, 16247, 16260 and 16269 un-smoothed shear shows spikes just below the mixed layer where the observed shear is at least three times greater than in the waters directly above and below. The maximum value of the shear observed just below the mixed layer is 2 $x10^{-2}$ s^{-1} for station 16222 (Figure 2.14). At the euphotic depth and below, un-smoothed shear is between 1 $x10^{-4}$ and 4 $x10^{-3}$ s^{-1} in all cases except for station 16286, in the jet, where shear exceeds 4 $x10^{-3}$ s^{-1} above 73 m depth (Figure 2.14). Applying a smoothing window to the vertical shear (Section 2.2.6) removes the peaks just below the mixed layer and reduces vertical shear to between 1 and 3 $x10^{-3}$ s^{-1} at the euphotic depth and below (Figure 2.14).

The Richardson number, calculated from shear and buoyancy with a 56 m smoothing window applied, is between 1 and 20 at the euphotic depth and below in all cases except station 16285, in the cyclone, where the Richardson number is above 20 between 40 to 97 m depth (Figure 2.15).

2.3.1.2 Turbulent mixing

For all stations, turbulent kinetic energy dissipation in the mixed layer is between 1 $x10^{-9}$ and 1 $x10^{-6}$ W kg^{-1}. The mean turbulent kinetic energy dissipation in the mixed layer for all stations is 1 ± 4 $x10^{-7}$ W kg^{-1}. There is a peak in turbulent kinetic energy dissipation at the mixed layer base (maximum 3 $x10^{-6}$ W kg^{-1} station 16296, in the jet, Figure 2.16). At the euphotic depth and below, turbulent kinetic energy dissipation is almost constant, between 1 and 3 $x10^{-9}$ W kg^{-1}. The exception is station 16285, in the cyclone core, where turbulent kinetic energy dissipation peaks at 3 $x10^{-8}$ W kg^{-1} just below the euphotic zone, reducing to between 1 to 2 $x10^{-9}$ W kg^{-1} below 80 m (Figure 2.16).

For all stations turbulent diffusivity is above 1 $x10^{-5}$ m^2 s^{-1} in the mixed layer. There is a minimum in turbulent diffusivity at the mixed layer base (minimum 1 $x10^{-6}$ m^2 s^{-1} for station 16247, on the edge of the cyclone, Figure 2.17). At the euphotic depth and below, turbulent diffusivity is below 1 $x10^{-4}$ m^2 s^{-1} for all stations (Figure 2.17).

2.3.1.3 Nutrient profiles

Vertical profiles for macro-nutrients, nitrate, phosphate and silicate, all exhibit typical nutrient type profiles, with relatively low concentrations in the surface waters and concentrations increasing with depth (Figure 2.18, Table 2.5). Average concentrations of macro-nutrients at the first sample depth below the base of the euphotic zone ($\sim$ 80 m) are in all cases greater than 65 % of the average concentrations at 200 m depth and average macro-nutrient concentrations at 200 m depth are at least three times the surface concentrations for all nutrients (Table 2.5). In all cases, the concentrations of nutrients in the mixed layer, as represented by the shallowest sample depth, are above detection limit(Table 2.5). Where there is a measurable nutrient concentration gradient across the euphotic depth, the gradient is positive (concentration lower above and higher below). For stations 16232 and 16247 the nutrient concentrations at the sample depth below the euphotic depth are within the 3 % of the nutrient concentrations at the sample depth above the euphotic zone, suggesting the concentrations of the nutrients are constant, within the limits of measurement accuracy, and that there is no measurable gradient (figure 2.18). The sharpest gradients in nutrient concentrations in all cases are between the base of the mixed layer and the euphotic depth (Figure 2.18). Station 16285, in the cyclone core, shows a spike in nutrient concentrations at a depth just above the base of the mixed layer which is almost an order of magnitude higher than observed for other mixed layer samples. This may be caused by a sampling error. Consequently this observation has been omitted from any subsequent processing of nutrient data. This chapter focuses on fluxes at the euphotic depth. Nutrient concentration gradients across the euphotic depth for station 16285 are comparable to the other stations so have been included in the results and subsequent analysis.

The vertical profiles for dissolved iron (dFe) were more variable than macro-nutrient profiles across the survey region (Figure 2.19). However, all profiles showed an increase in concentration from surface to depth with all station average dFe concentrations at 400 m three times mixed layer concentrations (Table 2.5). Gradients in iron concentration across the base of the euphotic zone vary from positive (stations 16282 and IB16) to negative (stations 16236, 16260 and 16286, Figure 2.19).

2.3.1.4 Turbulent nutrient fluxes

Calculating turbulent nutrient fluxes for the individual stations where there are both turbulence measurements and nutrient observations using equation 2.11, the highest fluxes for all three macro-nutrients were recorded for station 16285 and the lowest for station 16247 (Table 2.6). Fluxes of nitrate at the base of the euphotic zone (64 m) vary between zero and 0.34 (95 % confidence interval: 0.241 to 0.469) mmol m^2 day^{-1}. Fluxes of silicate at the base of the euphotic zone vary between 0.21 (95 % confidence interval: 0.018 to 0.023) and 0.094 (95 % confidence interval: 0.067 to 0.131) mmol m^2 day^{-1}. Fluxes of phosphate at the base of the euphotic zone vary between zero and 0.035 (95 % confidence interval 0.025 to 0.050) mmol m^2 day^{-1} (Table 2.6).

There are only two turbulence stations with accompanying measurements of dissolved iron (stations 16260 and 16286). For both of these stations the dissolved iron flux at the base of the euphotic zone (64 m) is negative, i.e. downwards, with the fluxes for each station -5.2 (95 % confidence interval: -4.75 to -5.70) $x10^{-7}$ mmol Fe m^2 day^{-1} and -1.2 (95 % confidence interval -9.0 to -1.5) $x10^{-5}$ mmol Fe m^2 day^{-1} respectively (Table 2.7).

2.3.2 The horizontal distribution of mixing

In order to see if there is any observable horizontal variability in properties across the different regions of the eddy dipole (Table 2.4), profiles of shear, buoyancy, turbulent kinetic energy dissipation and, turbulent diffusivity were combined into mean regional profiles.

2.3.2.1 Buoyancy, shear and Richardson number

The profiles of buoyancy for the background, jet, and edge regions are very similar. All three differ from the profile for the core region (represented by station 16285). However, the regional profiles of buoyancy all follow the same trend with a peak in buoyancy below the mixed layer, where N^2 is between 3 to 5 x 10^{-4} s^{-2} and a reduction in buoyancy with depth (Figure 2.20). For all regions except the core N^2 is between 1 and 2 $x10^{-5}$ s^{-2} at the euphotic depth and below (Figure 2.20). Below the sub mixed layer peak buoyancy for the core region is higher than for the other regions throughout the depth range, with N^2 between 3 $x10^{-4}$ and 2 $x10^{-5}$ s^{-2} at the euphotic depth and below (Figure 2.20).

The regional profiles of shear all appear distinct (Figure 2.21). All regions except the core, follow a similar trend with higher shears in the mixed layer and a reduction of shear with depth, while the shear in the core region appears to be constant (1.7 ± 0.8 $x10^{-3}$ s^{-1} mean ± standard deviation). Shear at the euphotic depth is lowest in the edge and highest in the background and jet regions, varying between 1.2 and 2.5 $x10^{-3}$ s^{-1} at the euphotic depth and below (Figure 2.21).

Regional profiles of the Richardson number show distinct variation across the four regions (Figure 2.22). Profiles for the jet and background regions are similar with Richardson number between 7 and 9 at the euphotic depth. The Richardson number in the edge region is consistently higher throughout the whole depth range than for the background and jet regions and is 18 at the euphotic depth (Figure 2.22). Nevertheless, the profiles of Richardson number for the edge, background and jet regions show a similar trend of higher Richardson number in the mixed layer which reduces with depth (Figure 2.22). As might be expected from the regional profiles of buoyancy and shear, the profile of Richardson number in the core region is different in both magnitude and shape from the other three regions. The Richardson number is 38 in the core at the euphotic depth (Figure 2.22).

2.3.2.2 Turbulent mixing

Considering the regional profiles of turbulent kinetic energy dissipation, with the exception of the core region (station 16285), the 95 % confidence limits for the regions overlap at all depths below the mixed layer (Figure 2.23). Turbulent kinetic energy dissipation for the jet, background, and edge regions is between 1 to 3 x10^{-9} W kg^{-1} at the euphotic depth. Turbulent kinetic energy dissipation in the core region is higher than the other regions (above 3 x10^{-9} W kg^{-1}) and outside the 95 % confidence limits of the other regions at all depths above 100 m (Figure 2.23). At the euphotic depth the core region turbulent kinetic energy dissipation is 1.1 (95 % confidence interval 0.9 to 1.3) x10^{-8} W kg^{-1}. For the core region, represented by a single station, the confidence limits quoted are for averaging the station into 8 m vertical depth intervals.

Regional profiles of turbulent diffusivity all show the same trend of a minimum in turbulent diffusivity just below the mixed layer (Figure 2.24). The turbulent diffusivity for all regions is of similar magnitude at the euphotic depth and below, with turbulent diffusivity between 0.9 to 3 x10^{-5} m^2 s^{-1} at the euphotic depth (Figure 2.24). The core region has the lowest turbulent diffusivity at the euphotic depth, 8.8 (95 % confidence interval: 7 to 11) x10^{-6} m^2 s^{-1}, which may be due to the close proximity of the mixed layer base to the euphotic depth in the core region (Figure 2.24). For the core region, represented by a single station, the confidence limits quoted are for averaging the station into 8 m vertical depth intervals.

2.3.2.3 Nutrient profiles and turbulent fluxes

For all three macro-nutrients the regional mean concentration for the jet region is higher at all depths than the concentrations in the other regions (Figure 2.25, 2.26 and 2.27). Concentrations in the jet region are $\sim$ 13 mmol m^{-3} for nitrate, $\sim$ 4 mmol m^{-3} for silicate and $\sim$ 0.8 mmol m^{-3} for phosphate at the euphotic depth. Concentrations in the background and edge regions are broadly similar throughout the depth range (Figure 2.25, 2.26 and 2.27). Concentrations in the edge and background regions are $\sim$ 11 mmol m^{-3} for nitrate, $\sim$ 3 mmol m^{-3} for silicate and $\sim$ 0.7 mmol m^{-3} for phosphate at the euphotic depth. Below the mixed layer, concentrations in the core region are consistently lower than for the other three regions (Figure 2.25, 2.26 and 2.27). Concentrations in the core are $\sim$ 4 mmol m^{-3} for nitrate, $\sim$ 1 mmol m^{-3} for silicate and $\sim$ 0.4 mmol m^{-3} for phosphate at the euphotic depth. However the core and edge regions are represented by single stations (stations 16285 and 16247 respectively) so any comparisons should be treated with caution.

Regional mean fluxes at the euphotic depth, were calculated from the regional mean macro-nutrient profiles and the regional mean turbulent diffusivity. Fluxes of all three macro-nutrients appear to be similar in all four regions at the euphotic depth (Table 2.8). Macro-nutrient fluxes at the euphotic depth for the background and jet regions are comparable with fluxes of 0.1 mmol m^{-2} day $^{-1}$ for nitrate and silicate and 0.005 mmol m^{-2} day $^{-1}$ for phosphate (Table 2.8). Fluxes in the edge region are lower for all three macro nutrients 0.002 mmol m^{-2} day $^{-1}$ for nitrate, 0.02 mmol m^{-2} day $^{-1}$ for silicate and, zero mmol m^{-2} day $^{-1}$ for phosphate (Table 2.8). This reflects the small gradients in nutrient concentrations observed (Figure 2.25, 2.26 and 2.27). Differences in flux between the edge and the other regions may be exaggerated by the edge region being represented by a single station and should be treated with caution. Macro-nutrient fluxes at the euphotic depth in the core region are comparable to the jet and background regions for nitrate (0.1 mmol m^{-2} day $^{-1}$, Table 2.8) but smaller than the jet and background regions for silicate (0.03 mmol m^{-2} day $^{-1}$, Table 2.8) and larger for phosphate (0.01 mmol m^{-2} day $^{-1}$, Table 2.8). Again differences in flux between the core and the other regions may be exaggerated by the core region being represented by a single station and should be treated with caution.

2.3.3 Area mean profiles

2.3.3.1 Turbulent mixing

Combining the results of all turbulence stations, as described in Section 2.2.9, the area mean turbulent diffusivity for 65 m (just below mean euphotic depth) is 0.21 (95 % confidence interval: 0.17 to 0.26) x10^{-4} m^2 s^{-1}, while at the base of the mixed layer (33 m), the area mean turbulent diffusivity is 0.14 (95 % confidence interval: 0.1 to 0.2) x10^{-4} m^2 s^{-1}. The area mean turbulent kinetic energy dissipation at 65 m is 2.0 (95 % confidence interval: 1.79 to 2.4) x10^{-9} W kg^{-1} (Figure 2.28).

2.3.3.2 Nutrient profiles and fluxes

Area mean profiles for macro-nutrients were constructed by linear interpolation of all the individual station results as described in Section 2.2.9 (Figure 2.29). An area mean nutrient flux was then calculated for the base of the euphotic zone from the area mean nutrient profiles and the area mean turbulent diffusivity using equation 2.11. The nitrate flux is 0.13 (95 % confidence interval 0.08 to 0.22) mmol m^{-2} day^{-1}, the silicate flux is 0.08 (95 % confidence interval 0.05 to 0.12) mmol m^{-2} day^{-1} and, the phosphate flux is 8.6 (95 % confidence interval 13.0 to 5.2) x10^{-3} mmol m^{-2} day^{-1}.

An area mean profile of dissolved iron was constructed by linear interpolation of the individual station results for all the published iron measurements (Nielsdóttir et al., 2009) for the cruise as described in Section 2.2.9 (Figure 2.30). An area mean dissolved iron flux was then calculated for the base of the euphotic zone using equation 2.11. The flux is 2.6 (95 % confidence interval 4.3 to 1.3) x10^{-6} mmol m^{-2} day^{-1}.

2.4 Discussion

2.4.1 Turbulent mixing

There appears to be little, if any, measurable variation in horizontal turbulent diffusivity between the four regions identified around the eddy dipole at all depths. However, the horizontal resolution of the turbulence measurements is coarse, with a mean station separation of $\sim$ 51 $\pm$42 km, and an irregular sampling pattern. Such a crude horizontal survey is unlikely to be sufficient to resolve mesoscale horizontal variations in mixing where changes in water properties occur on horizontal scales of order 10 km. Of the four regions sampled, only the core of the cyclonic eddy shows any consistent deviations outside the 95 % confidence interval of the area mean values with higher turbulent kinetic energy dissipation and higher buoyancy frequency. However, the resultant turbulent diffusivity in the cyclonic eddy core is of similar magnitude to the area mean due to the greater dampening effect of the elevated buoyancy frequency. This would suggest that the area mean profile of turbulent diffusivity, being consistent with both the regional profiles and the individual station profiles, is likely to be representative of the area as a whole within the confidence limits.

The value of the area mean turbulent diffusivity reported here for the base of the euphotic zone of 0.14 (95 % confidence interval: 0.1 to 0.2) x10^{-4} m^2 s^{-1} is lower than recorded in previous studies from the Iceland basin, where turbulent diffusivity has been reported to be between 0.97 ± 0.3 x 10^{-4} m^2 s^{-2} (Jickells et al., 2008) and 1.51 ± 0.29 x 10^{-4} m^2 s^{-2} (Law et al., 2001). In both cases the turbulent diffusivity was measured by tracer release at the base of the mixed layer, ~15 m depth, within the core of mode-water eddies located near the survey site for this thesis (59° 10' N, 20° 15' W, (Law et al., 2001); 60° N, 21° W, (Jickells et al., 2008)). Nevertheless, the measurements reported in this thesis are comparable to those reported within a mode-water eddy core in the Sargasso Sea of 0.35 ± 0.05 x10^{-4} m^2 s^{-1} (Ledwell et al., 2008), measured by tracer release at the base of euphotic zone, and consistent with values reported elsewhere for the open ocean of between 0.12 ± 0.02 x10^{-4} m^2 s^{-1} and 0.17 ± 0.02 x10^{-4} m^2 s^{-1} (Ledwell et al., 1998), measured using tracer release at 300 m depth for the south eastern part of the subtropical gyre in the North Atlantic.

The tracer release technique allows the calculation of time and space integrated estimates of mixing which can reduce the statistical uncertainties of instantaneous measurements. Diffusivity measured by tracer release compares favourably with diffusivity calculated using microprofilers (Ledwell et al., 2000; Polzin et al., 1997). Unfortunately during this study no measurements of turbulent diffusivity were taken within the core of the mode-water eddy part of the dipole. The density profile calculated from CTD station 16286 taken on 19th July 2008 at 59° 16' N 19° 43' W suggests that this station ought to be within the mode-water eddy core. However, analysis of the ADCP data recorded while the subsequent turbulent diffusivity measurements were taken shows a near constant water velocity of a magnitude comparable to that recorded during stations known to be in the jet region (Figure 2.11). This would suggest that the ship had, by this time, drifted out of the core towards the edge of the eddy. As a result, direct comparison with previous studies can not be made.

Previous observations of a mode-water eddy record a low buoyancy frequency within the mode-water eddy core (Martin et al., 1998). Hence, it is possible that turbulent diffusivity within the mode-water eddy core is higher than area mean levels due to reduced buoyancy frequency (equation 2.1). The buoyancy frequency calculated from cruise D321 CTD station 16286 at 64 m is 4.8 x 10^{-3} s^{-1}. This figure combined with the area mean turbulent kinetic energy dissipation would give a turbulent diffusivity of 0.2 x 10^{-4} m^2 s^{-1} within the mode-water eddy core which is still within the 95 % confidence interval for the area mean turbulent diffusivity. However, the levels of turbulent kinetic energy dissipation within the mode-water eddy core may be higher than the area mean due to dissipation of internal waves at near inertial frequency trapped within the mode-water eddy core (Kunze, 1985).

Measurements of turbulent diffusivity in this study show an area-wide trend of a minimum directly below the mixed layer, despite a peak in turbulent kinetic energy dissipation at the same depth, due to the strong seasonal thermocline suppressing mixing. As a result, the area mean figure for turbulent mixing at the base of the mixed layer is lower that that recorded at the base of the euphotic zone. This would suggest, assuming similar seasonal stratification in previous studies, that for the turbulent diffusivities here to approach those of the previous studies, turbulent kinetic energy dissipation in the mode-water eddy core would need to be approximately an order of magnitude higher than the area mean $\sim$ 1x10^{-8} W kg^{-1}. This would be comparable to the observed turbulent kinetic energy dissipation in the cyclone core above 80 m depth.

The mixed layer and the region directly below (up to 20 m deeper) can be subject to wind generated inertial motions resulting in high, time varying, vertical shears (D'Asaro, 1985). Such time varying vertical shears may likewise result in time varying levels of turbulent diffusivity at the base of the mixed layer. Near-inertial internal waves can break in the high buoyancy region below the mixed layer generating enhanced regions of time-variant turbulent kinetic energy dissipation and potentially enhanced mixing (Gregg et al., 1986). The enhanced mixing generated by inertial features can persist for several days, but is limited spatially to the regions near the inertial feature (Gregg et al., 1986; D'Asaro, 1985).

In the presence of order 10 km horizontal gradients in density and vorticity, the surface mixed layer can be subject to a range of sub-mesoscale physical processes. Sub-mesoscale physical processes such as strain driven frontogenesis (Hoskins and

Bretherton, 1972), mixed layer instability (Boccaletti et al., 2007), loss of geostrophic balance (Molemaker et al., 2005), and wind-frontal interactions (Thomas and Lee, 2005) may result in potentially high vertical velocities at the base of the mixed layer and enhanced convective mixing. Such sub-mesoscale physical processes are both temporally and spatially highly heterogeneous.

The inertial period for the Iceland Basin is $\sim$ 14 h. The near instantaneous (station duration $\sim$ 1 h) measurement technique used in this thesis is capable of detecting enhanced mixing due to inertial features and sub-mesoscale processes if deployed where the mixing is occurring. However, it is unlikely that the coarse temporal and spatial resolution of the D321 turbulence measurements would be able to adequately resolve any enhanced mixing due to inertial or sub-mesoscale processes over an inertial period. Some, though not all, of the individual shear profiles show peaks just below the mixed layer which are suggestive of shear resulting from inertial motions. Hence it is possible that the increased levels of turbulent diffusivity reported previously for the Iceland Basin (Jickells et al., 2008; Law et al., 2001) are as a result of the effects of wind driven inertial motions or sub-mesoscale processes in the surface layer.

The Richardson number in the cyclonic eddy core is up to five times higher than for the other regions yet the turbulent diffusivity is similar. Within the cyclonic eddy core there appears to be a qualitative relationship between the observed turbulent kinetic energy dissipation and buoyancy frequency. Below the mixed layer turbulent dissipation appears to decrease as N^2 decreases (Figure 2.20 and 2.23). This would suggest the possibility of an $\varepsilon \propto N^2$ type relationship which is characteristic of turbulent dissipation caused through internal wave field interactions (Polzin et al., 1995; Gregg and Sanford, 1988). However, scatter-plotting measured turbulent kinetic energy dissipation against the square of the buoyancy frequency for observations from all stations shows no consistent relationship for the area as a whole (Figure 2.31).

For all the regions except the cyclonic eddy core region there appears to be a qualitative relationship between turbulent diffusivity and Richardson number. Increased Richardson number appears to correspond to a decrease in turbulent diffusivity. For example, in the edge region Richardson number is consistently higher than in the background and jet regions while the turbulent diffusivity in the edge region is consistently lower than in the background and jet regions (Figure 2.22, and 2.24). Scatter-plotting turbulent diffusivity against Richardson number for all observations, including the core, appears to show a relationship consistent with equation 2.2 (Figure 2.32, Chapter 3). This suggests that in the regions outside the cyclonic eddy core region instabilities in stratified shear flow contribute to the observed diffusivity.

2.4.2 Nutrient fluxes

The turbulent macro-nutrient fluxes calculated here, of 0.13 (95 % confidence interval 0.08 to 0.22) mmol m^{-2} day^{-1} for nitrate, 0.08 (95 % confidence interval 0.05 to 0.12) mmol m^{-2} day^{-1} for silicate and 8.6 $x10^{-3}$ (95 % confidence interval 13.0 to 5.2) mmol m^{-2} day^{-1} for phosphate are approximately an order of magnitude lower that those previously reported for the Iceland Basin. Previous studies have recorded nitrate fluxes of 1.8 (Law et al., 2001) and 1.5 mmol m^{-2} day^{-1} (Jickells et al., 2008), silicate fluxes of 0.9 mmol m^{-2} day^{-1} (Jickells et al., 2008) and phosphate fluxes of 1.25 mmol m^{-2} day^{-1} (Law et al., 2001). This may reflect both the order of magnitude lower value of the turbulent diffusivity calculated during this study and the depth at which the nutrient gradients were calculated. Previous studies have estimated macro-nutrient fluxes at the base of the mixed layer, reporting nutrient gradients of 107.2 μmol m^{-4} for nitrate, 34.3 μmol m^{-4} for silicate and 7.41 μmol m^{-4} for phosphate (Law et al., 2001). These gradients are of the same magnitude as the area mean nutrient gradients observed at the euphotic depth in this thesis of 70 μmol m^{-4} for nitrate, 41.2 μmol m^{-4} for silicate and 4.6 μmol m^{-4} for phosphate (Figure 2.29). This would suggest that the order magnitude differences in the nutrient fluxes are due to the difference in the observed turbulent diffusivity.

New production, that is production from fresh inorganic nutrients rather than from recycled organic nutrients such as ammonium, in the Irminger Basin (approximately 2^{o} North of the D321 survey site) is considered to be negligible after August (Sanders et al., 2005) which is typical of post-bloom conditions. The steepest nutrient gradients are associated with post-bloom conditions when the surface nutrient concentrations are at their lowest (Sanders et al., 2005). Hence, the turbulent supply of nutrients into the Iceland Basin euphotic zone is potentially at its largest at the time of the survey. This would suggest, from the fluxes measured in this thesis, a maximum annual turbulent nutrient supply into the euphotic zone in the Iceland Basin of the order of 48 mmol m^{-2} $year^{-1}$ for nitrate, 28 mmol m^{-2} $year^{-1}$ for silicate and, 3 mmol m^{-2} $year^{-1}$ for phosphate.

Modelling the supply of nutrients from deep wintertime mixing in the North Atlantic sub-polar gyre gives an estimate of 1.4 $\pm$ 0.2 mol m^{-2} for the annual supply of nitrate (Williams et al., 2000).

We can be more specific for the Iceland Basin. Wintertime mixing in the North Atlantic can penetrate to depths of $\sim$ 400 to 600 m (Williams et al., 2000). Hence, waters at depths of $\sim$ 400 to 600 m, with a nitrate concentration of $\sim$12 mmol m^{-3}, are representative of the end of winter surface waters (Nielsdóttir et al., 2009). A summertime mixed layer of between 30 to 40 m depth with an initial nitrate concentration of $\sim$12 mmol m^{-3} contains a volume integrated total of between 360 to 480 mmol m^{-2} of nitrate supplied by deep wintertime mixing (Nielsdóttir et al., 2009). This would suggest that turbulent mixing in the Iceland Basin provides a supply of nitrate equivalent to between 3 to 13 % of the convective nitrate supply.

Complete utilization by phytoplankton of 360 to 480 mmol m^{-2} year^{-1} of nitrate is calculated to require between 18 to 24 μmol m^{-2} year^{-1} of iron (Nielsdóttir et al., 2009). Deep winter mixing in the Iceland Basin is estimated to supply between 12 to 16 μmol m^{-2} year^{-1} of dissolved iron and atmospheric deposition a further $\sim$ 5 μmol m^{-2} year^{-1} of iron (Nielsdóttir et al., 2009). Using the combined area mean dissolved iron profile and the area mean estimate of turbulent diffusivity, turbulent mixing in the Iceland Basin is estimated to supply 1 μmol Fe m^{-2} year^{-1} (95 % confidence interval 0.2 to 2) of dissolved iron into the euphotic zone. This is consistent with an estimate of a dissolved iron flux of 0.5 μmol Fe m^{-2} year^{-1} calculated from the nitrate flux presented in this thesis and a dissolved Fe:NO_3 concentration ratio of 1x10^{-5}:1 for water depths below the mixed layer in the North Atlantic $\sim$ 45^o to 60^o N (Fung et al., 2000).

Turbulent mixing in the iceland Basin is estimated to provide a supply of iron that is equivalent to between 6 to 8 % of the convective iron supply. Combining the estimate of turbulent supply of dissolved iron from this thesis with deep winter mixing and atmospheric deposition estimates is approximately enough, at the higher end of the confidence limit, to balance the estimated iron requirements of new production. However, there is a larger uncertainty associated with this flux than for the macro-nutrient fluxes due to an uncertainty of $\sim$ $\pm$ 40 % associated with the gradient in iron concentration (figure 2.30).

There is a large amount of variability in the observed vertical profiles for dissolved iron. Gradients in iron concentration across the euphotic depth are both positive and negative for different profiles (Figure 2.19). The area mean vertical profile for dissolved iron suggests a concentration minima between the mixed layer and the euphotic depth (Figure 2.30), though this region is poorly resolved in the iron concentration measurements. Dissolved iron profiles are considered to be constant at depth with dissolved iron concentrations of ~ 0.6 nM below 500 m in all ocean waters away from the continental shelf (Johnson et al., 1997). However, there is potentially greater variability in surface concentrations of dissolved iron where the resultant surface concentration of iron is a balance between supply and utilization (Luther III and Wu, 1997). The major supply route for iron into the surface waters is considered to be through aeolean deposition (Fung et al., 2000). Between 12 to 14 % of dissolved iron in surface waters is expected to be the more reactive Fe(II) ion which is produced from insoluble Fe(III) in sunlit surface waters, but oxidises rapidly (in times of seconds to hours) back to Fe(III) in oxygenated seawater (Hansard et al., 2009). This would suggest that a combination of production of dissolved iron in the sunlit upper mixed layer combined with aeolean deposition might result in locally higher concentrations of dissolved iron in the mixed layer compared to those immediately below the euphotic depth. The presence of poorly resolved concentration minima in the iron profiles above the euphotic depth may well be the cause of the negative concentration gradients for some of the iron stations which contributes to the high levels of uncertainty associated with the turbulent iron flux.

2.5 Conclusions

When compared to the convective supply of nutrient from deep winter mixing observations of turbulent nutrient flux reported in this thesis would tend to support the view that, for the Iceland Basin, vertical turbulent flux is a minor source of nutrient into the surface waters (Williams and Follows, 2003; Williams et al., 2000). The magnitude of turbulent macro-nutrient flux is estimated to be at most 13 % of the estimated supply of macro-nutrient by deep winter mixing in the region. Turbulent macro-nutrient fluxes calculated here are an order of magnitude lower than previous estimates for the region. This is due to the order of magnitude lower estimate of turbulent diffusivity reported in this thesis.

Observations of the vertical turbulent flux of iron into the surface waters of the Iceland Basin are, at best, inconclusive. Directly calculated dissolved iron fluxes are consistent with estimates of dissolved iron flux based on nitrate flux. The magnitude of the observed dissolved iron flux is consistent with the size of the discrepancy between estimated new production requirements for dissolved iron and the supply of dissolved iron by deep winter mixing and aeolean deposition. However profiles of dissolved iron are highly variable leading to an order magnitude 95 % confidence limit on dissolved iron fluxes.

The area mean turbulent diffusivity reported in this thesis for the D321 survey area is comparable to expected open ocean background levels (Ledwell et al., 1998) and turbulent diffusivity reported for a mode-water eddy core in the Sargasso Sea (Ledwell et al., 2008), but lower than the values reported for mode-water eddy cores in the same area measured using tracer release techniques (Law et al., 2001; Jickells et al., 2008). The discrepancy between the results reported in this thesis and previous studies in the same area is potentially due either to enhanced dissipation within the mode-water eddy core, due to the dissipation of trapped near-inertial internal waves (Kunze, 1985), or due to time variant mixing events caused by processes in the upper mixed layer which were not captured in measurements taken using a microstructure profiler.

Investigation of the spatial distribution of turbulent diffusivity shows an almost uniform horizontal distribution of diffusivity across the survey area. This observation is quite surprising given the strong horizontal gradients in water velocity and density observed between the different regions. However, with the exception of the cyclonic eddy core region, vertical variation in the observed mixing and Richardson number would suggest that mesoscale shear flow may still be contributing towards the observed mixing.

Within the core of the cyclonic eddy levels of turbulent kinetic energy dissipation and buoyancy frequency are elevated in comparison to the other regions around the eddies. However, due to the compensating effect of the increased buoyancy, the elevated turbulent kinetic energy dissipation does not lead to significantly increased turbulent diffusivity within the core. The weak relationship between buoyancy and turbulent kinetic energy dissipation within the cyclonic eddy core is suggestive of finescale shear from internal waves contributing to the observed mixing within the cyclonic eddy core.

Station No.	Date	Position (deg. min.)	No. of casts	Max. depth of profile (m)	Macro-nutrients	Dissolved Iron	ADCP
16222	02/08/07	58° 50N 19° 51W	10	141			Y
16226	05/08/07	58° 50N 21° 00W	10	152	Y		Y
16232	06/08/07	59° 01N 21° 00W	10	139	Y		Y
16241	09/08/07	59° 52N 19° 37W	10	135			Y
16242	09/08/07	59° 52N 20° 07W	12	130			Y
16247	10/08/07	59° 56N 20° 26W	10	138	Y		Y
16260	12/08/07	59° 10N 19° 08W	10	134	Y	Y	Y
16269	13/08/07	59° 12N 19° 28W	9	133	Y		Y
16283	16/08/07	59° 36N 20° 38W	10	139	Y		Y
16285	18/07/07	59° 41N 18° 42W	11	134	Y		Y
16286	19/08/07	59° 17N 19° 47W	10	129	Y	Y	Y
16288	20/08/07	59° 30N 19° 02W	10	204			Y
16289	20/08/07	59° 26N 19° 16W	10	138			Y
16292	20/08/07	59° 22N 19° 26W	10	133			Y
16295	20/08/07	59° 18N 19° 40W	10	130			Y

Table 2.1: The position, date and number of casts taken for each turbulence measurement station for cruise D321.

Profiler	MSS90L
Depth limit	500 m
Weight in air	15 kg
Length of housing (see Figure 2.4)	1.25 m
Sensor s fitted	Pressure, Temperature, Conductivity, 2 x Shear, Tilt (2-axis), NTC[1], NTCHP[2], ACC[3],
Data channels	16
Sampling Rate	1024 per sec
Resolution	16 Bit
[1]Temperature microstructure sensor FP07 [2]Temperature microstructure sensor with pre-emphasized amplification [3]Acceleration sensor for measuring the profiler vibration	

Table 2.2: MSS90L microstructure profiler size and sensor inventory. Taken from the published specification of MSS90L (Prandke, 2008*b*).

Sensor	Range	Accuracy	Resolution
Microstructure shear (Airfoil lift force sensor)	0 to 6 s^{-1} (Dissipation rate 10^{-2} to 10^{-10} W kg^{-1})	not specified	$\sim 10^{-3}$ s^{-1}
Microstructure temperature (FP07)	-2 to +30 °C	± 0.02 °C	500 µC (linear)
Pressure	1 to 50 bar	± 0.1 % fs[1]	0.002 % fs[1]
Temperature	-2 to +30 °C	± 0.01 °C	0.0005 °C
Conductivity	0 to 6 mS cm^{-1}	± 0.005 mS cm^{-1}	0.0001 mS cm^{-1}
Acceleration	-1 to +1 m s^2	0.02 m s^2	0.005 m s^2
[1]Full scale pressure range			

Table 2.3: Sensor range, accuracy, and resolution for MSS90L microstructure profiler. Taken from the published specification of MSS90L (Prandke, 2008*b*).

Region	Jet	Core	Edges	Background
Station number	16286 16288 (cyclone) 16289 16292 16295 16269 (mode-water)	16283 (uncertain see Section 2.2.9) 16285 (cyclone)	16241 (cyclone) 16242 (cyclone) 16247 (cyclone)	16222 16226 16232 16260

Table 2.4: Turbulence measurement stations for cruise D321 grouped according to location with respect to the eddy dipole structure.

Mixed layer nutrient concentrations.			
NO_3 (mmol m^{-3})	PO_4 (mmol m^{-3})	SiO_3 (mmol m^{-3})	dFe (mmol m^{-3})
3.28 ± 1.1	0.3 ± 0.11	0.74 ± 0.8	0.1 ± 0.08 x10^{-3}
80 m sample depth nutrient concentrations			
NO_3 (mmol m^{-3})	PO_4 (mmol m^{-3})	SiO_3 (mmol m^{-3})	dFe (mmol m^{-3})
11.3 ± 2.3	0.8 ± 0.07	3.5 ± 1.2	0.1 ± 0.06 x10^{-3}
200 m sample depth nutrient concentrations.(400m for dFe)			
NO_3 (mmol m^{-3})	PO_4 (mmol m^{-3})	SiO_3 (mmol m^{-3})	dFe (mmol m^{-3})
13.5 ± 0.9	0.9 ± 0.05	5.4 ± 0.7	0.34 ± 0.19 x10^{-3}

TABLE 2.5: Mean (± standard deviation) of all stations nutrient concentrations at selected depths. The sample depth of 80 m is the closest sample depth to the base of the euphotic zone (64 m).

Press. dbar	NO_3 (mmol m^{-2} day $^{-1}$)	PO_4 (mmol m^{-2} day $^{-1}$)	SiO_3 (mmol m^{-2} day $^{-1}$)
Background station 16226 flux (95 % confidence interval)			
20	-12.367 (-29.237 : -5.232)	0.000 (0.000 : 0.000)	-4.122 (-9.746 : -1.744)
28.5	5.575 (36.296 : 0.856)	0.115 (0.748 : 0.018)	1.379 (8.980 : 0.212)
34.5	0.177 (0.242 : 0.130)	0.013 (0.017 : 0.009)	0.030 (0.041 : 0.022)
44.5	0.840 (1.402 : 0.504)	0.056 (0.093 : 0.033)	0.245 (0.409 : 0.147)
66	0.111 (0.127 : 0.097)	0.003 (0.004 : 0.003)	0.126 (0.145 : 0.110)
105.5	0.067 (0.073 : 0.061)	0.004 (0.005 : 0.004)	0.119 (0.130 : 0.109)
Background station 16232 (95 % confidence interval)			
17	0.085 (0.110 : 0.066)	-0.014 (-0.018 : -0.011)	0.007 (0.009 : 0.005)
25.5	0.143 (0.172 : 0.119)	0.038 (0.046 : 0.032)	0.005 (0.007 : 0.005)
31.5	0.063 (0.083 : 0.048)	-0.012 (-0.016 : -0.009)	0.020 (0.026 : 0.015)
41.5	0.864 (1.564 : 0.477)	0.060 (0.108 : 0.033)	0.243 (0.440 : 0.134)
63	0.171 (0.199 : 0.147)	0.003 (0.004 : 0.003)	0.091 (0.106 : 0.078)
102.5	0.088 (0.096 : 0.080)	0.005 (0.005 : 0.004)	0.095 (0.104 : 0.087)
Edge station 16247 (95 % confidence interval)			
18	0.037 (0.049 : 0.028)	-0.024 (-0.032 : -0.018)	-0.016 (-0.021 : -0.012)
26.5	0.182 (0.220 : 0.150)	0.016 (0.020 : 0.013)	0.000 (0.000 : 0.000)
32.5	0.145 (0.346 : 0.061)	0.012 (0.028 : 0.005)	0.025 (0.061 : 0.011)
42.5	0.225 (0.298 : 0.170)	0.013 (0.018 : 0.010)	0.083 (0.109 : 0.062)
64.5	-0.003 (-0.003 : -0.003)	-0.000 (-0.000 : -0.000)	0.021 (0.023 : 0.018)
104	0.119 (0.129 : 0.110)	0.009 (0.010 : 0.008)	0.111 (0.120 : 0.103)
Background station 16260 (95 % confidence interval)			
19	0.156 (0.212 : 0.115)	-0.020 (-0.027 : -0.015)	-0.232 (-0.314 : -0.171)
27.5	0.132 (0.284 : 0.061)	0.009 (0.020 : 0.004)	0.034 (0.074 : 0.016)
33.5	0.049 (0.079 : 0.030)	0.003 (0.005 : 0.002)	0.021 (0.035 : 0.013)
44	0.085 (0.100 : 0.073)	0.003 (0.004 : 0.003)	0.053 (0.063 : 0.046)
66	0.145 (0.159 : 0.132)	0.007 (0.007 : 0.006)	0.113 (0.124 : 0.104)
105.5	0.077 (0.083 : 0.072)	0.008 (0.009 : 0.008)	0.046 (0.049 : 0.042)
Jet station 16269 (95 % confidence interval)			
17.5	16.078 (157.999 : 1.636)	1.128 (11.088 : 0.115)	4.795 (47.123 : 0.488)
26	0.068 (0.097 : 0.048)	0.005 (0.008 : 0.004)	0.024 (0.033 : 0.017)
32	0.064 (0.085 : 0.048)	0.004 (0.005 : 0.003)	0.024 (0.032 : 0.018)
42.5	0.147 (0.213 : 0.102)	0.010 (0.014 : 0.007)	0.058 (0.083 : 0.040)
64	0.088 (0.100 : 0.078)	0.006 (0.007 : 0.005)	0.069 (0.078 : 0.060)
103	0.053 (0.060 : 0.047)	0.002 (0.003 : 0.002)	0.049 (0.056 : 0.044)
Uncertain location station 16283 (95 % confidence interval)			

Press. dbar	NO_3 (mmol m^{-2} day $^{-1}$)	PO_4 (mmol m^{-2} day $^{-1}$)	SiO_3 (mmol m^{-2} day $^{-1}$)
19.5	0.132 (0.267 : 0.065)	0.117 (0.237 : 0.058)	0.000 (0.000 : 0.000)
28.5	-0.119 (-0.154 : -0.093)	-0.119 (-0.154 : -0.093)	0.013 (0.017 : 0.010)
34.5	0.181 (0.220 : 0.148)	0.000 (0.000 : 0.000)	0.000 (0.000 : 0.000)
44.5	0.700 (1.817 : 0.270)	0.073 (0.189 : 0.028)	0.107 (0.277 : 0.041)
66.5	0.083 (0.111 : 0.061)	0.006 (0.008 : 0.005)	0.036 (0.048 : 0.027)
106	0.108 (0.117 : 0.100)	0.000 (0.000 : 0.000)	0.034 (0.037 : 0.031)
Cyclone eddy core station 16285 (95 % confidence interval)			
19	173.602 (223.198 : 135.027)	37.200 (47.828 : 28.934)	-37.200 (-47.828 : -28.934)
27.5	-79.535 (-96.670 : -65.437)	-9.357 (-11.373 : -7.698)	-4.679 (-5.686 : -3.849)
65	0.336 (0.469 : 0.241)	0.035 (0.050 : 0.025)	0.094 (0.131 : 0.067)
104.5	0.161 (0.182 : 0.143)	0.003 (0.004 : 0.003)	0.028 (0.032 : 0.025)
Jet station 16286 (95 % confidence interval)			
19	6.381 (14.090 : 2.890)	0.347 (0.766 : 0.157)	2.324 (5.130 : 1.052)
30	0.252 (0.352 : 0.180)	0.016 (0.022 : 0.011)	0.099 (0.138 : 0.071)
43.5	0.119 (0.174 : 0.081)	0.008 (0.012 : 0.006)	0.080 (0.118 : 0.055)
65	0.059 (0.073 : 0.047)	0.003 (0.004 : 0.002)	0.065 (0.081 : 0.052)
104.5	0.027 (0.031 : 0.024)	0.002 (0.002 : 0.001)	0.040 (0.045 : 0.035)

TABLE 2.6: Turbulent macro-nutrient fluxes for all turbulence stations with adjacent macro-nutrient measurements from cruise D321.

Press. dbar	dFe (mmol m^{-2} day $^{-1}$)
Station 16260 (95 % confidence interval)	
17	-1.7×10^{-6} (-2.3×10^{-6} : -1.3×10^{-6})
26	7.5×10^{-6} (1.9×10^{-5} : 3.0×10^{-6})
32	-1.2×10^{-6} (-1.4×10^{-6} : -1.0×10^{-6})
42	-7.0×10^{-7} (-9.0×10^{-7} : -5.4×10^{-7})
64	-5.2×10^{-7} (-5.7×10^{-7} : -4.7×10^{-7})
103	6.0×10^{-6} (6.4×10^{-6} : 5.6×10^{-6})
Station 16286 (95 % confidence interval)	
17	7.7×10^{-4} (1.7×10^{-3} : 3.4×10^{-4})
25.5	-5.2×10^{-5} (-9.6×10^{-5} : -2.9×10^{-5})
31.5	2.8×10^{-5} (4.5×10^{-5} : 1.8×10^{-5})
56	-1.2×10^{-5} (-1.5×10^{-5} : -9.0×10^{-6})
103	2.0×10^{-5} (2.3×10^{-5} : 1.8×10^{-5})

Table 2.7: Turbulent macro-nutrient fluxes for turbulence stations with adjacent iron measurements.

NO_3 (mmol m^{-2} day $^{-1}$)			
Background (3 stations)	Edge (1 station)	Core (1 station)	Jet (2 stations)
0.12 (0.09 : 0.17)	0.002 (0.002 : 0.003)	0.12 (0.09 : 0.15)	0.09 (0.02 : 0.19)
SiO_3 (mmol m^{-2} day $^{-1}$)			
Background (3 stations)	Edge (1 station)	Core (1 station)	Jet (2 stations)
0.1 (0.07 : 0.13)	0.02 (0.017 : 0.025)	0.03 (0.02 : 0.04)	0.08 (0.02 : 1.64)
PO_4 (mmol m^{-2} day $^{-1}$)			
Background (3 stations)	Edge (1 station)	Core (1 station)	Jet (2 stations)
0.004 (0.003 : 0.005)	0	0.01 (0.009 : 0.015)	0.005 (0.003 : 0.01)

TABLE 2.8: Mean (95% confidence interval) nutrient fluxes for the four regions calculated at 65 m (just below the mean euphotic depth) using regional mean turbulent diffusivity and regional mean nutrient concentrations. Note the edge and core regions are represented by single stations (stations 16247 and 16285 respectively).

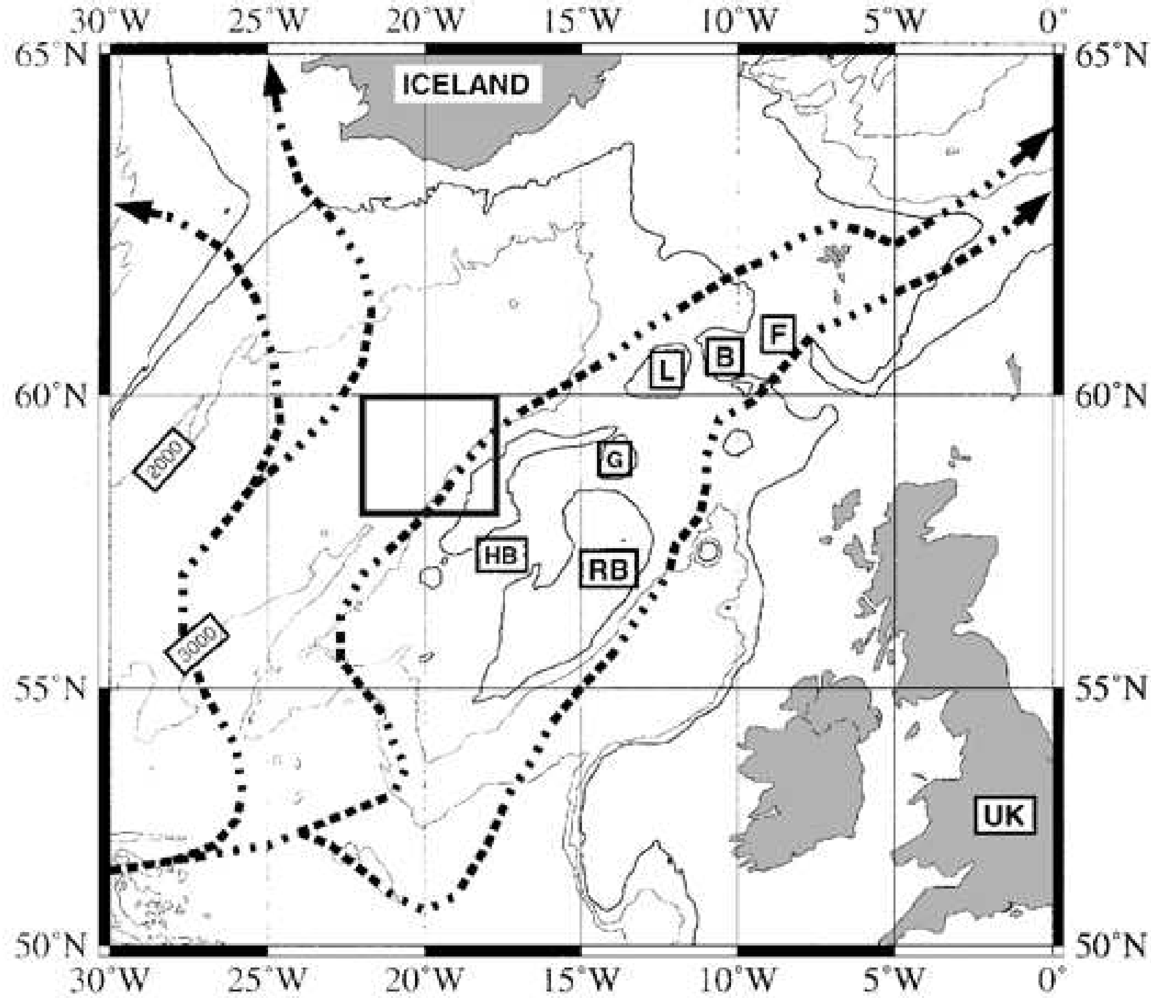

FIGURE 2.1: Bathymetry of the Iceland Basin, with large scale circulation (branches of the North Atlantic Current) shown as bold dashed lines. The initials denote Bill Bailey's Bank (B), Faeroe Bank (F), George Bligh Bank (G), Hatton Bank (HB), Lousy Bank (L) and Rockall Bank (RB) (Reproduced with permission of Martin et al. (1998)). The rectangle marks the location of the survey area and the two satellite images in figure 2.2.

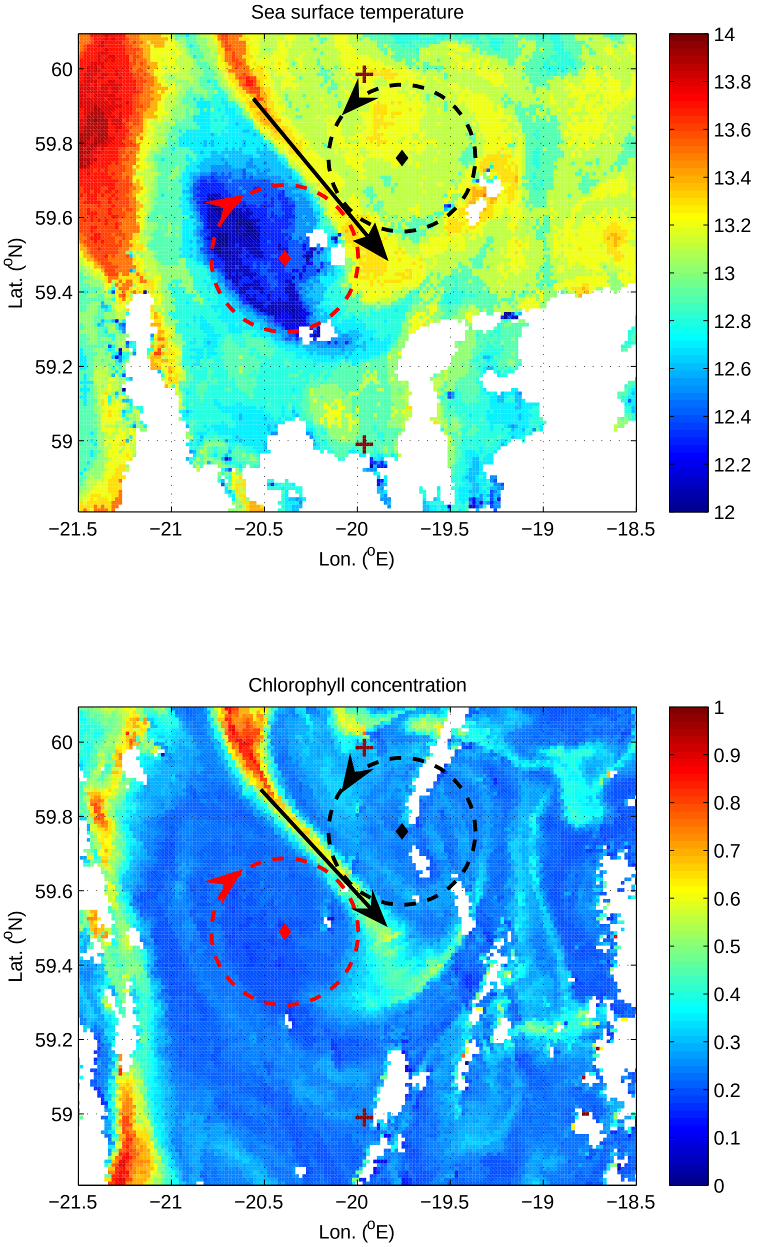

FIGURE 2.2: Satellite images of AVHRR sea surface temperature (°C upper panel) and MODIS chlorophyll concentration (mg m^{-3} lower panel) from the 5th and 6th August 2007 respectively for the D321 survey site. Processed satellite image data for sea surface temperature from $\tilde{1}$ km resolution AVHRR data and chlorophyll concentration from 1 km resolution MODIS data were downloaded from the NERC Earth Observation Data Acquisition and Analysis Service (NEODAAS). Estimated positions, and flow direction for the eddy dipole and jet regions are marked. The warm and cold sea-surface temperature signals of the cyclone and mode-water eddies respectively can be seen, with the cyclone centred approximately at 59.8 °N 19.8 °W and the mode-water centred approximately at 59.5 °N, 20.4 °W. The white areas are cloud.

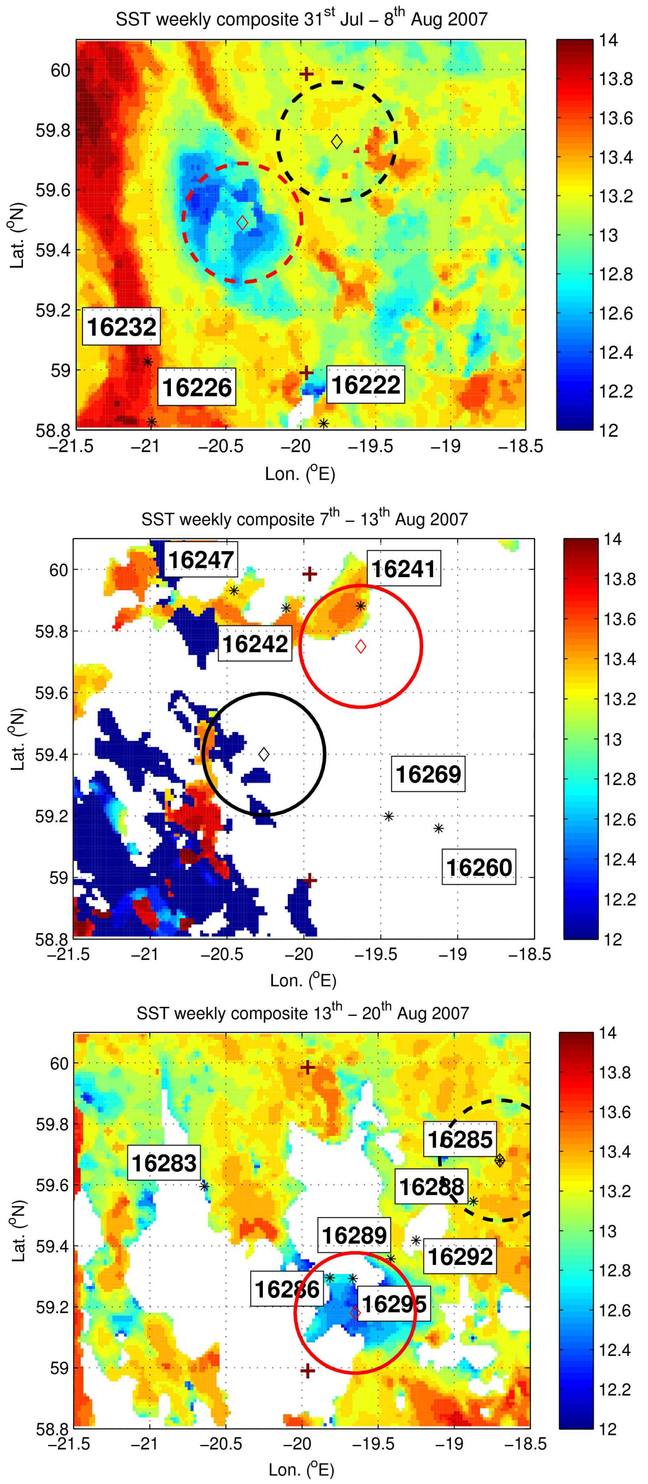

FIGURE 2.3: Weekly composite satellite images of AVHRR sea surface temperature (°C) for the D321 survey area showing the location of the turbulence measurement stations. Stations are plotted on the image corresponding to the week including the date of the station. The date of the individual stations is given in Table 2.1. Approximate positions of the two eddies (cyclone in black, mode-water in red) are marked as dashed lines, solid lines denote eddy positions calculated from contemporaneous ADCP data.

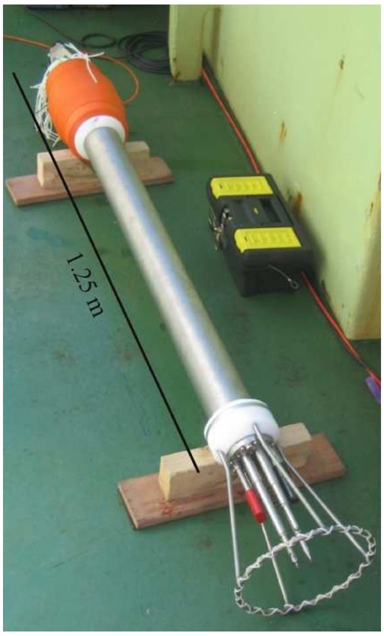

Figure 2.4: The MSS microstructure profiler. The length of the profiler housing is marked. Buoyant foam rings are in orange with the sensor array and guard ring in the bottom right of the picture. The tether can be seen (orange cable) in the top left of the picture. Note the tassles on the top of the profiler and the cord wrapped round the guard ring to reduce interference on passage through the water. (Photo M. Srokosz).

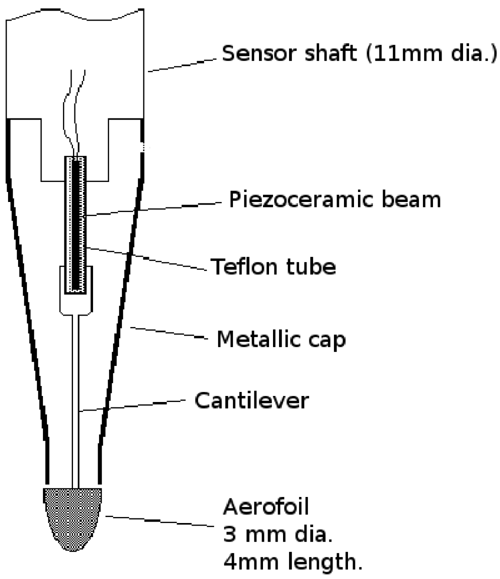

FIGURE 2.5: A diagram of a PNS-type aerofoil shear probe, showing the piezoceramic beam, cantilever, aerofoil bead, and protective metallic cap.

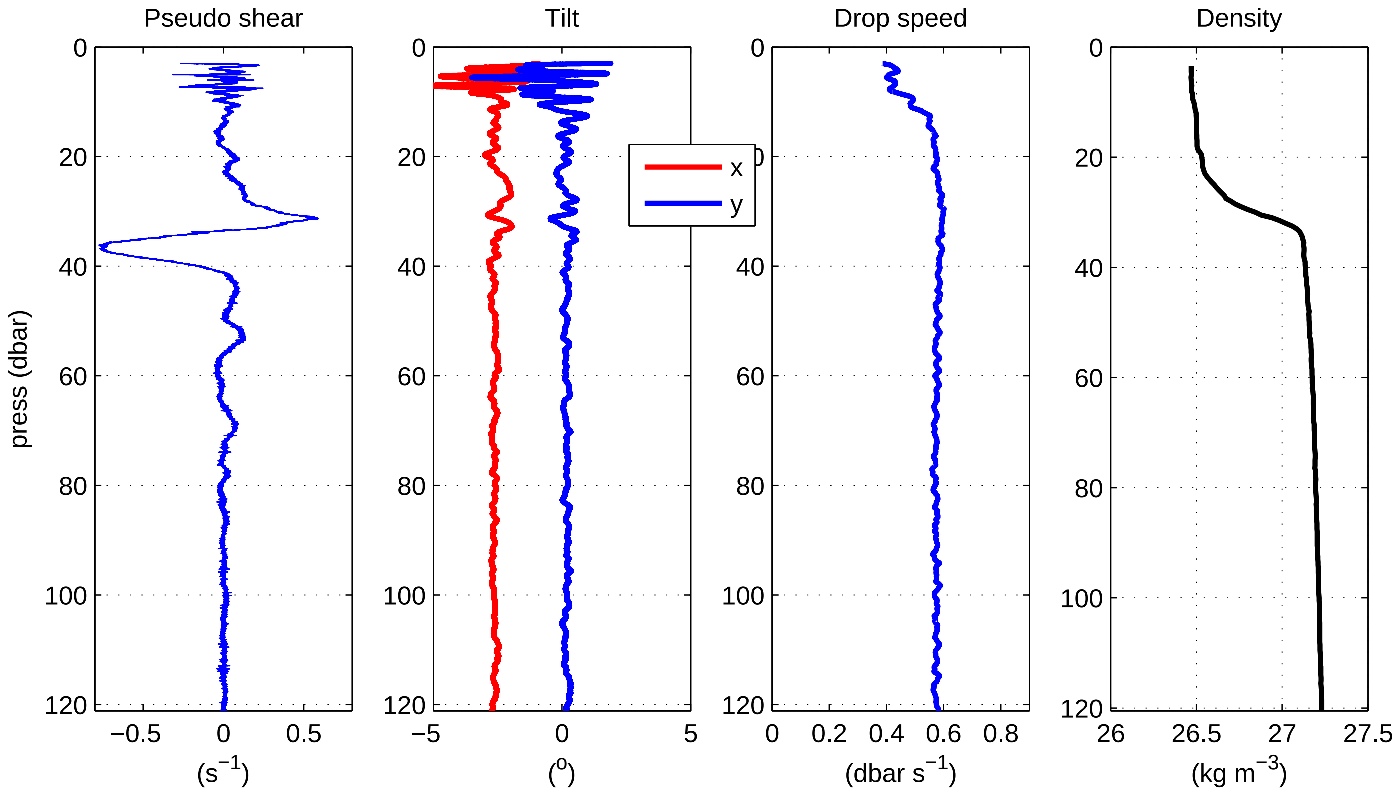

FIGURE 2.6: An example of the deployment characteristics of the MSS profiler, showing pseudo-shear (left hand panel), profiler tilt, profiler drop speed, and water density calculated from measurements of temperature and salinity taken by the profiler (right hand panel).

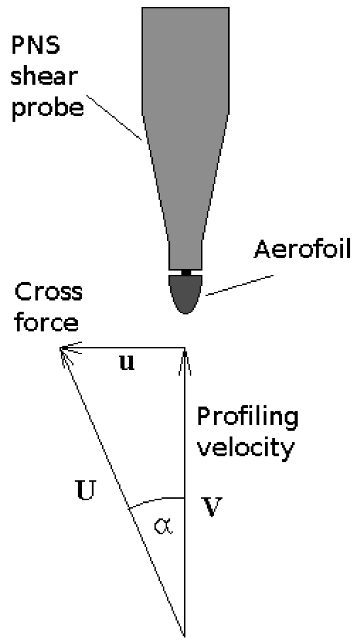

FIGURE 2.7: Schematic of PNS shear probe moving with constant velocity V with respect to the water experiencing an instantaneous water velocity U at angle α to the direction of shear probe travel, resulting in axial velocity u at the probe.

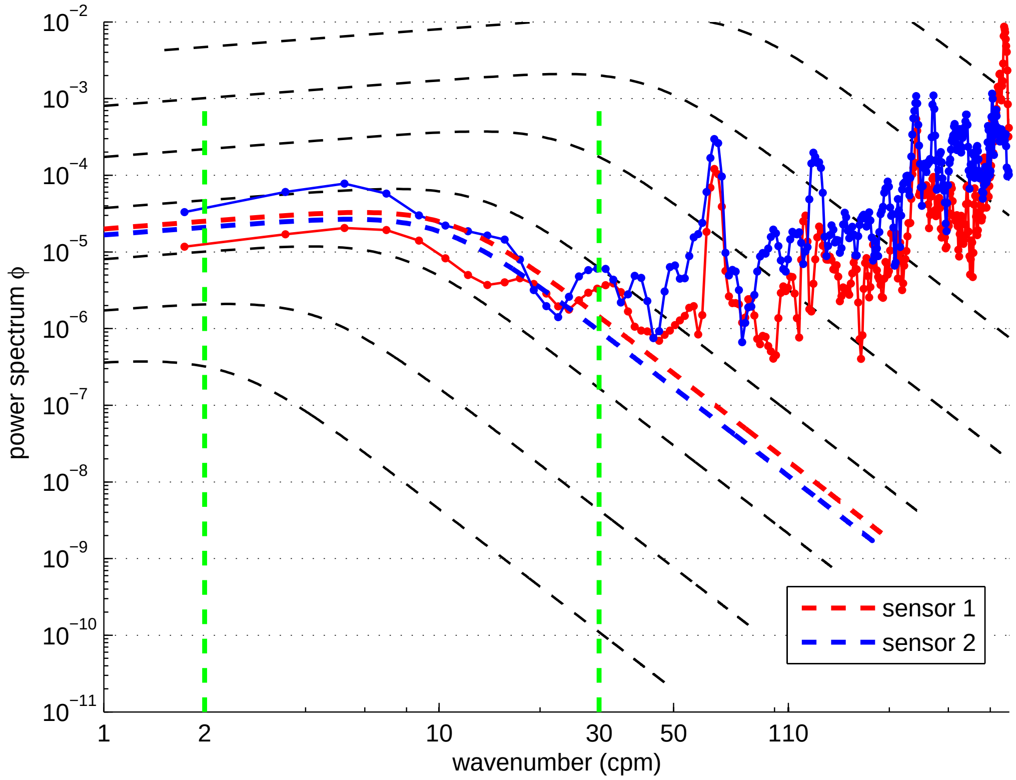

FIGURE 2.8: Example shear spectrum for a single cast (sensor 1 in red, sensor 2 in blue) plotted with Naysmith theoretical universal spectra (dashed black lines, equation 8). Examples of permanent narrow band pseudo-shear can be seen at between 50 and 110 cpm. The observations approximate to the shape of the universal spectrum between the marked limits (2 and 30 wavenumbers). The universal spectrum for each sensor, estimated from integration between 2 and 30 wavenumbers, is shown as dashed red lines for sensor 1 and dashed blue lines for sensor 2.

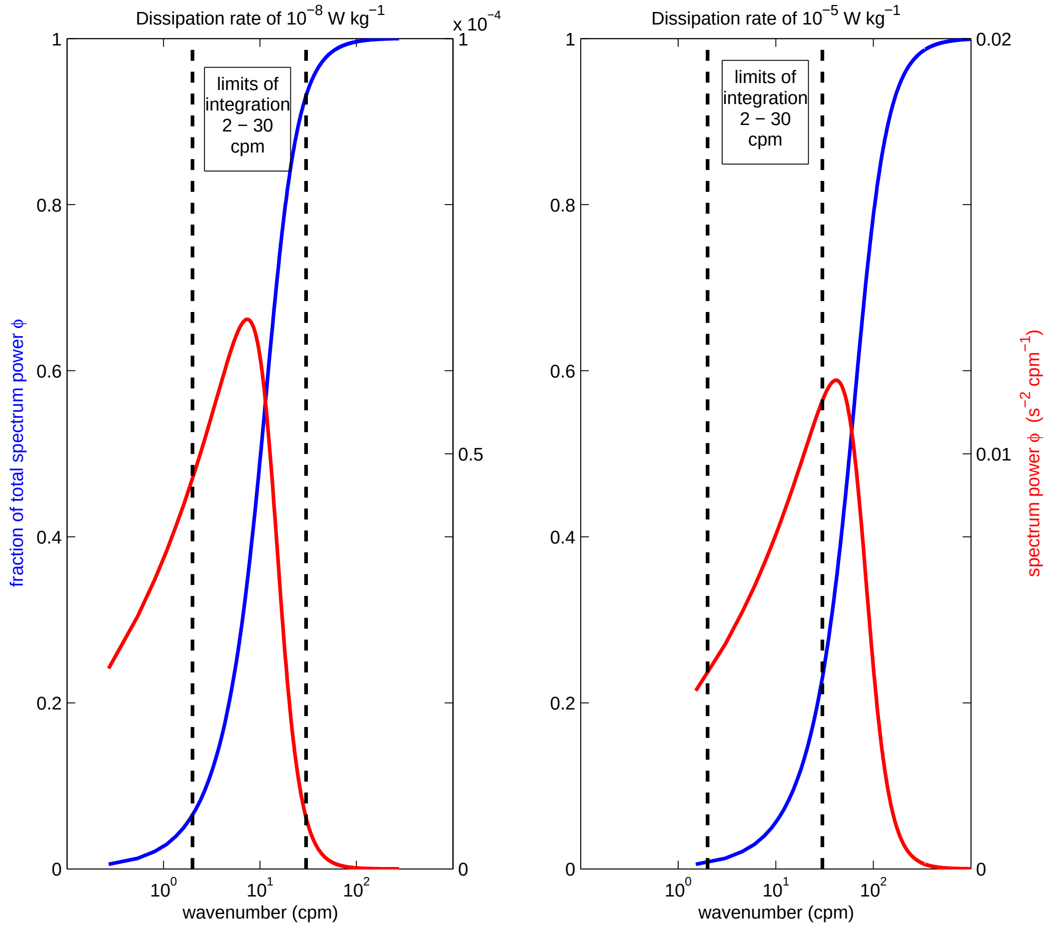

FIGURE 2.9: The fraction of total dissipation that is measured between integration limits of 2 and 30 cpm for two different dissipation rates calculated using the Naysmith form of the universal spectrum (equation 2.10). The fraction of total dissipation is shown in blue, and corresponds to the left hand axis. The power spectrum is shown in red and corresponds to the right hand axis. Integration limits are marked in black. When the dissipation rate is 1x10^{-8} W kg^{-1} 90 % of the total dissipation is contained within the integration limits (left hand panel). When the dissipation rate is 1x10^{-5} W kg^{-1} 20 % of the total dissipation is contained within the integration limits (right hand panel).

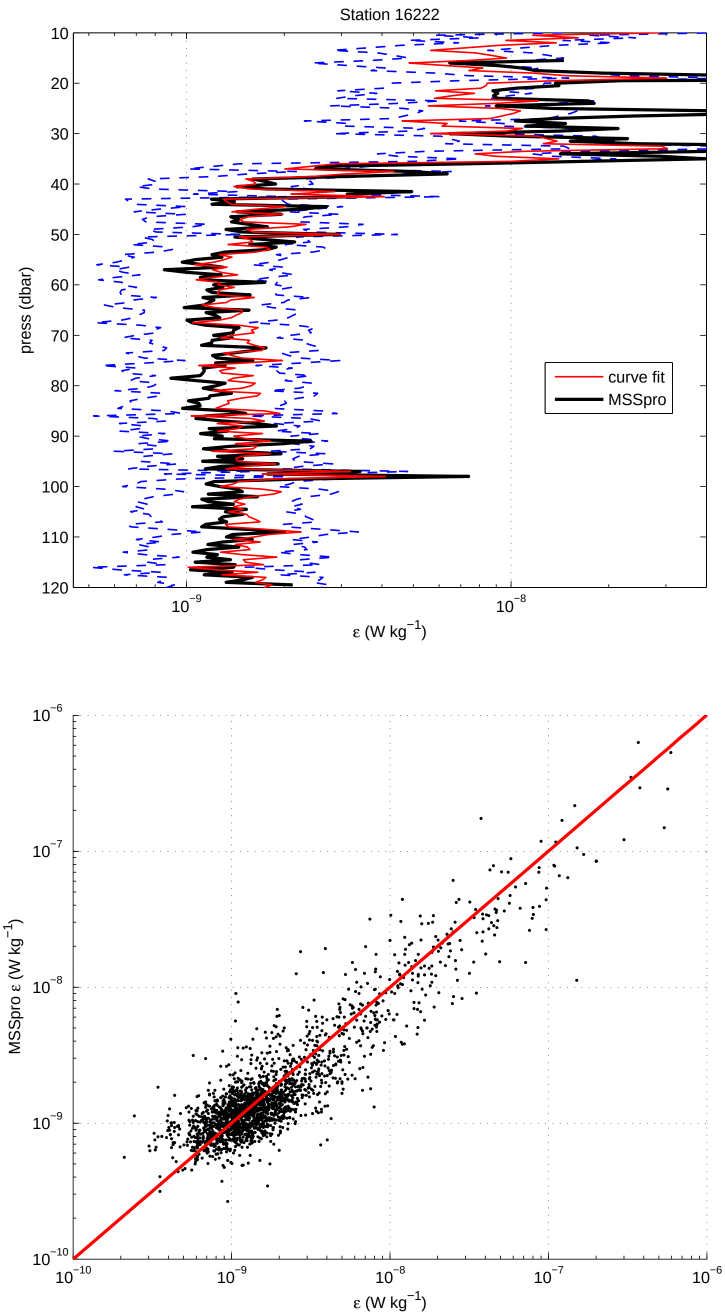

FIGURE 2.10: Comparison of results for dissipation calculated by curve fitting, as described in Section 2.2.3.2, with those calculated using MSSpro standard software for an example station (station 16222). In the upper panel the red line shows the values calculated by curve fitting (in 0.5 m depth intervals). The dashed blue lines show the ± 50 % estimated calculation uncertainty to the curve fit value. The black lines show the values for the station calculated using MSSpro standard software. The lower panel shows a scatter plot of curve fitting vs. MSSpro for the full dataset (0.5 dbar depth intervals) from the 10 casts comprising the station.

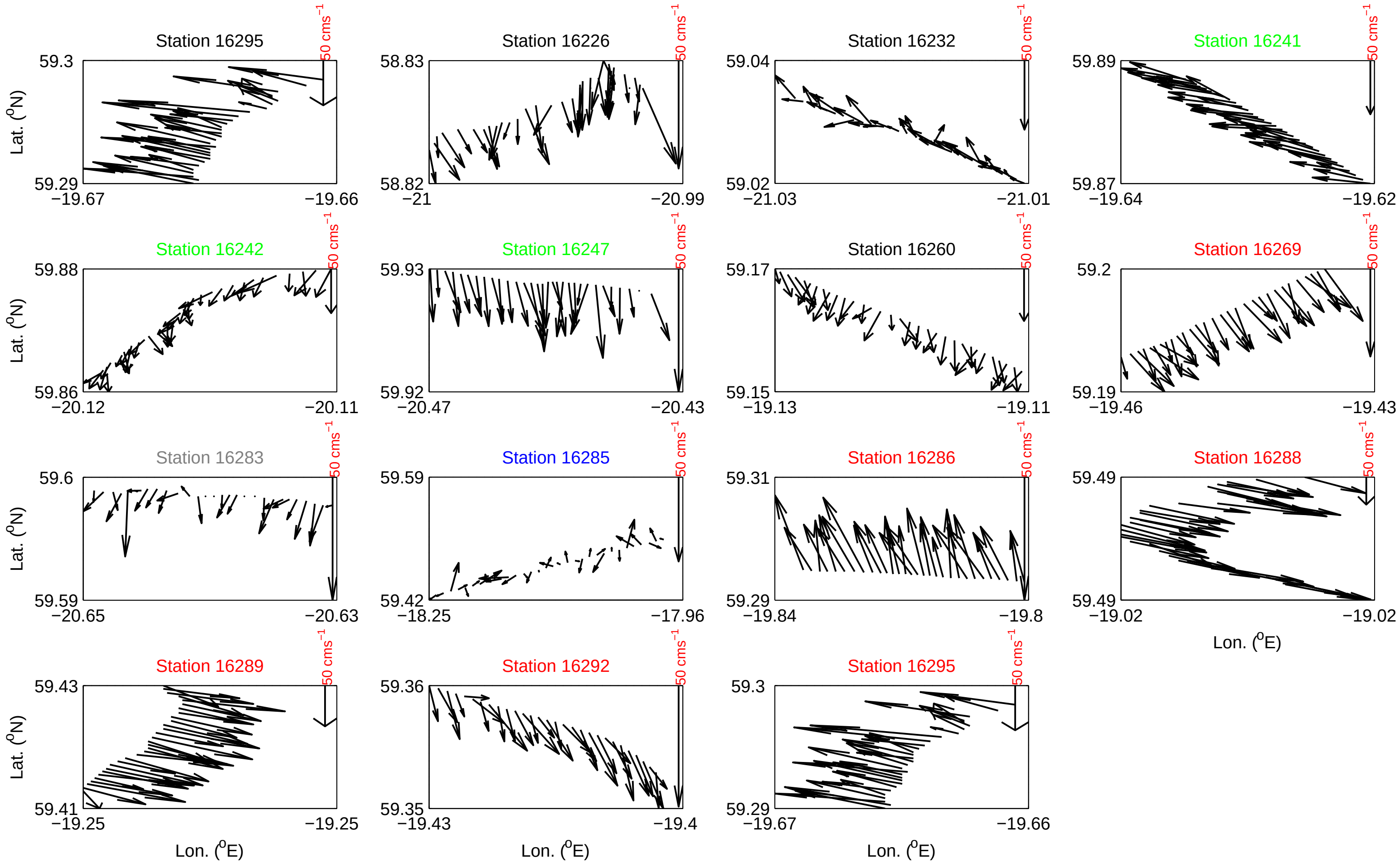

FIGURE 2.11: Current vectors for 63 m depth (the closest ADCP measurement to the euphotic depth of 64 m), showing the direction and strength of the water movements while turbulence stations were in progress. For location of stations relative to eddy dipole see figure 2.3. An arrow of a length indicating a water speed of 50 cm s^{-1} is shown in the top right hand corner of each plot. The colour of the figure title indicates the region that the station is in. Blue is the core region, black the background region, red the jet region and green the edge region (Table 2.4).

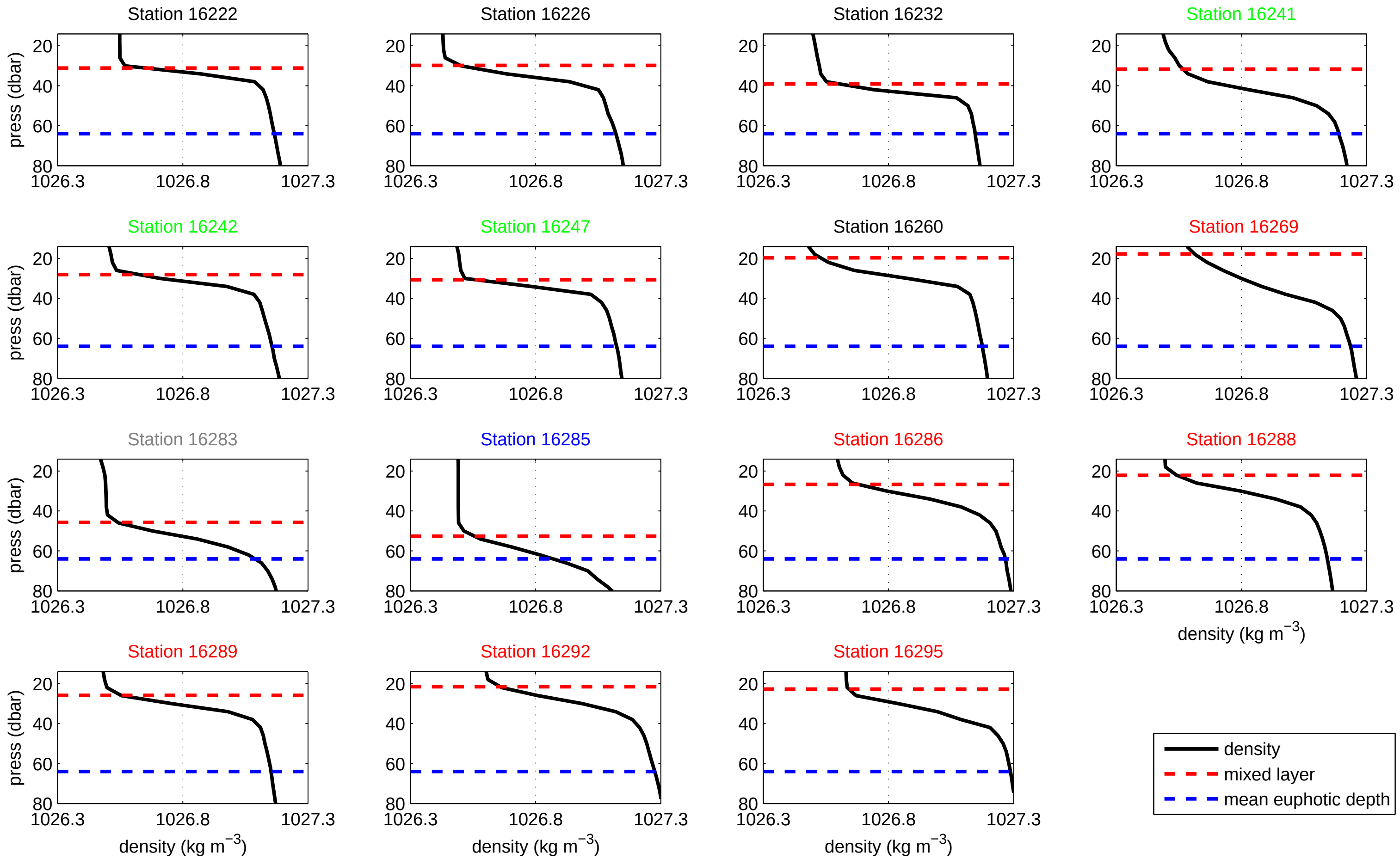

FIGURE 2.12: Profiles of density calculated from CTD measurements from the turbulence profiler. The depth of euphotic zone (64 m) is marked in blue and the mixed layer depth, calculated as described in Section 2.2.7, in red. For the location of stations relative to the eddy dipole see Figure 2.3. The colour of the figure title indicates the region that the station is in. Blue is the core region, black the background region, red the jet region and green the edge region (Table 2.4).

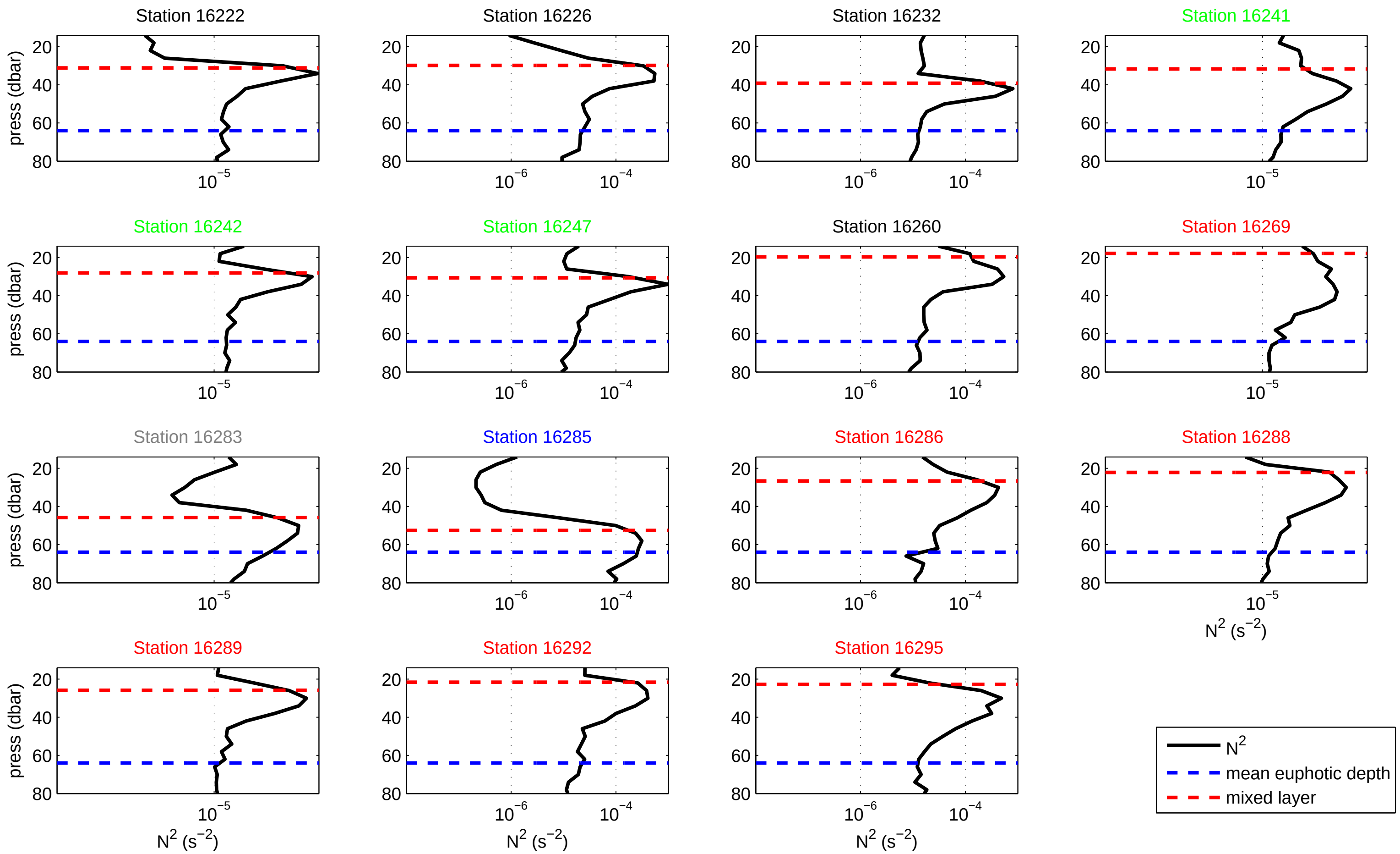

FIGURE 2.13: Profiles of the square of the buoyancy frequency, N^2, calculated from CTD measurements from the turbulence profiler. The depth of euphotic zone (64 m) is marked in blue and the mixed layer depth, calculated as described in Section 2.2.7, in red. For the location of stations relative to the eddy dipole see Figure 2.3. The colour of the figure title indicates the region that the station is in. Blue is the core region, black the background region, red the jet region and green the edge region (Table 2.4).

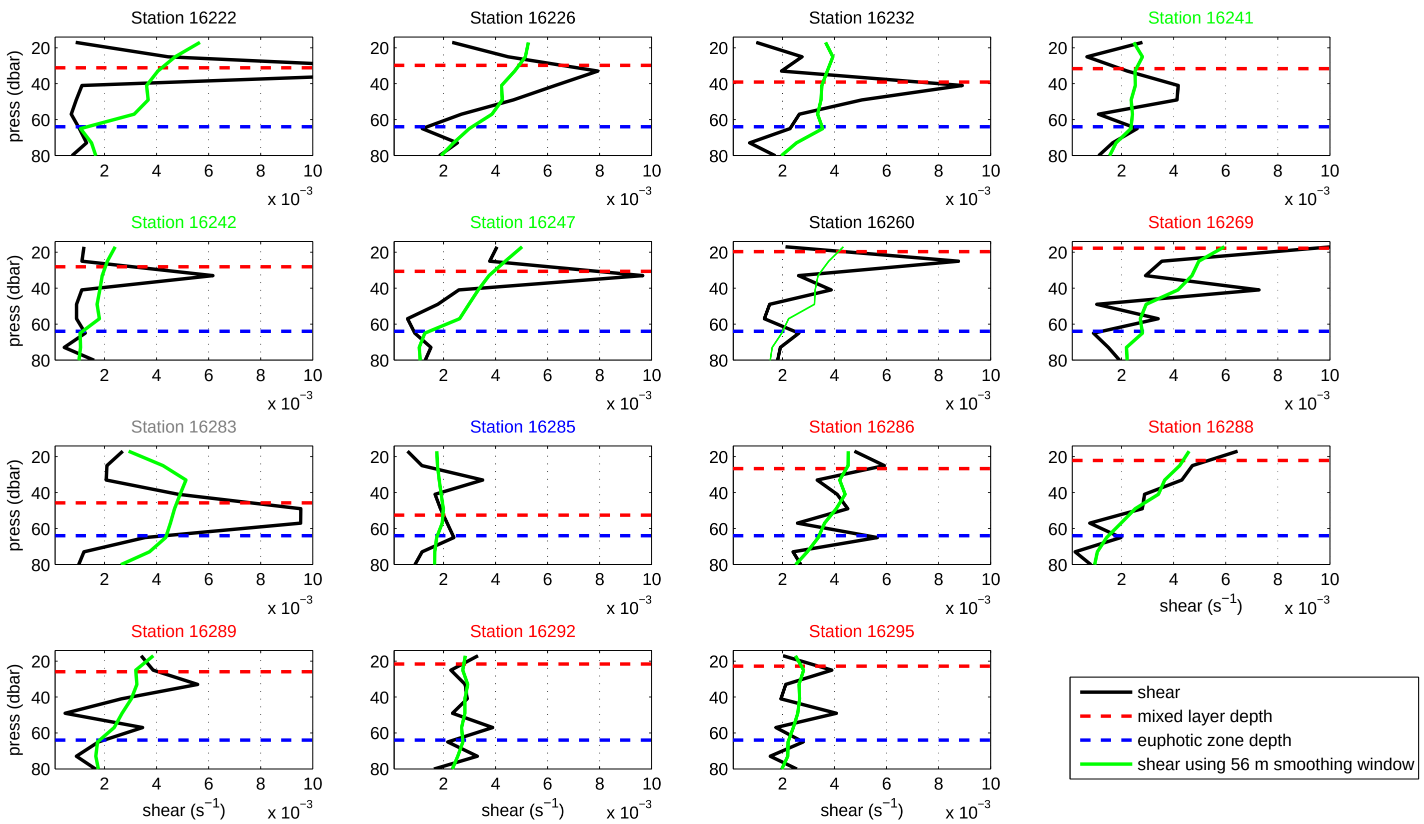

FIGURE 2.14: Profiles of mean vertical shear calculated from ADCP data recorded while turbulence stations were in progress. Raw, unsmoothed, shear is shown in black, and shear smoothed using a 56 m window in green.. The depth of euphotic zone (64 m) is marked in blue and the mixed layer depth, calculated as described in Section 2.2.7, in red. For the location of stations relative to the eddy dipole see Figure 2.3. The colour of the figure title indicates the region that the station is in. Blue is the core region, black the background region, red the jet region and green the edge region (Table 2.4).

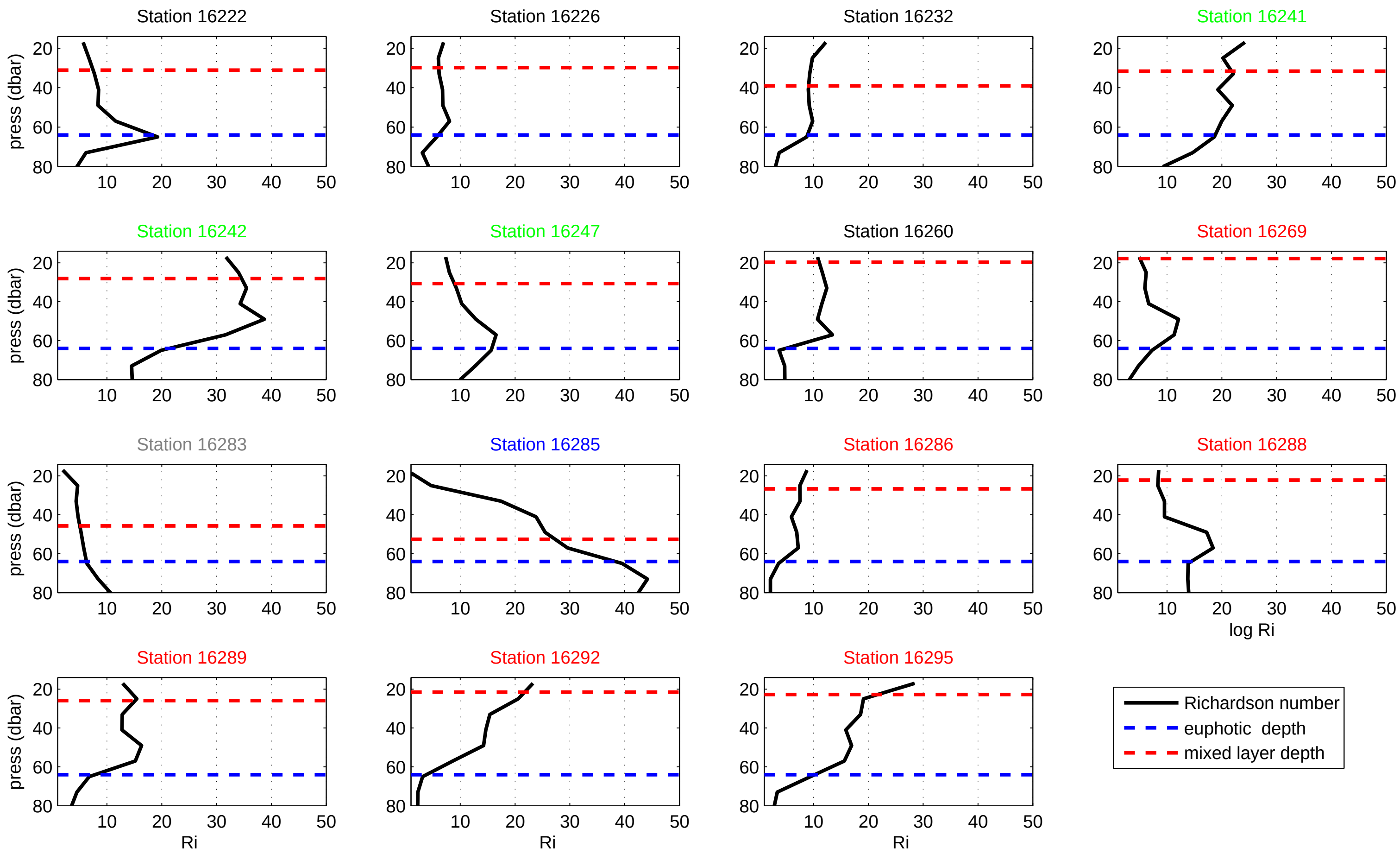

FIGURE 2.15: Profiles of Richardson number calculated from ADCP (shear) and turbulence profiler CTD (buoyancy frequency) data (see Section 2.1.2). Both shear and buoyancy were smoothed using a 56 m window before calculation. The depth of euphotic zone (64 m) is marked in blue and the mixed layer depth, calculated as described in Section 2.2.7, in red. For the location of stations relative to the eddy dipole see Figure 2.3. The colour of the figure title indicates the region that the station is in. Blue is the core region, black the background region, red the jet region and green the edge region (Table 2.4).

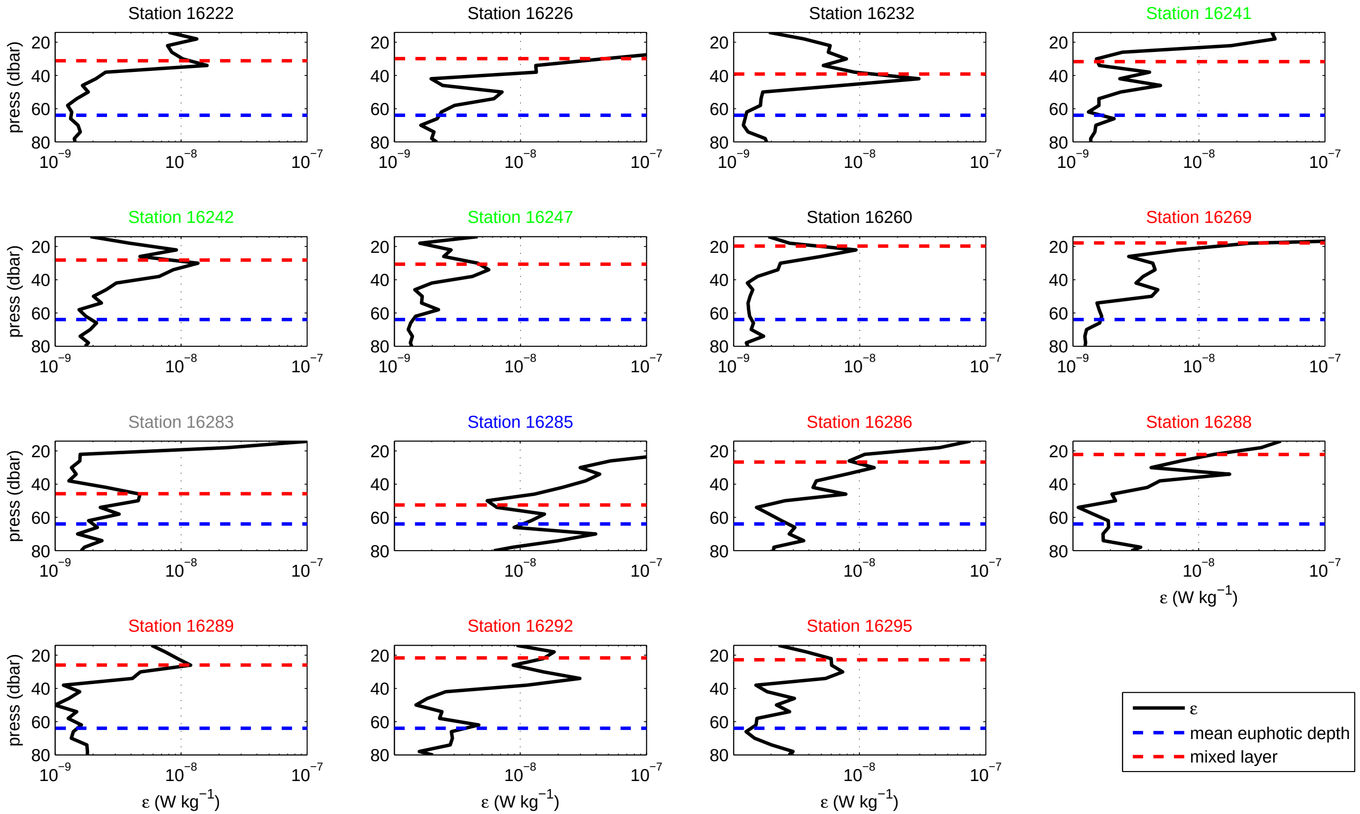

FIGURE 2.16: Profiles of turbulent kinetic energy dissipation (ε). Note the log scale on the x-axis. The depth of euphotic zone (64 m) is marked in blue and the mixed layer depth, calculated as described in Section 2.2.7, in red. For the location of turbulence stations relative to the eddy dipole see Figure 2.3. The colour of the figure title indicates the region that the station is in. Blue is the core region, black the background region, red the jet region and green the edge region (Table 2.4).

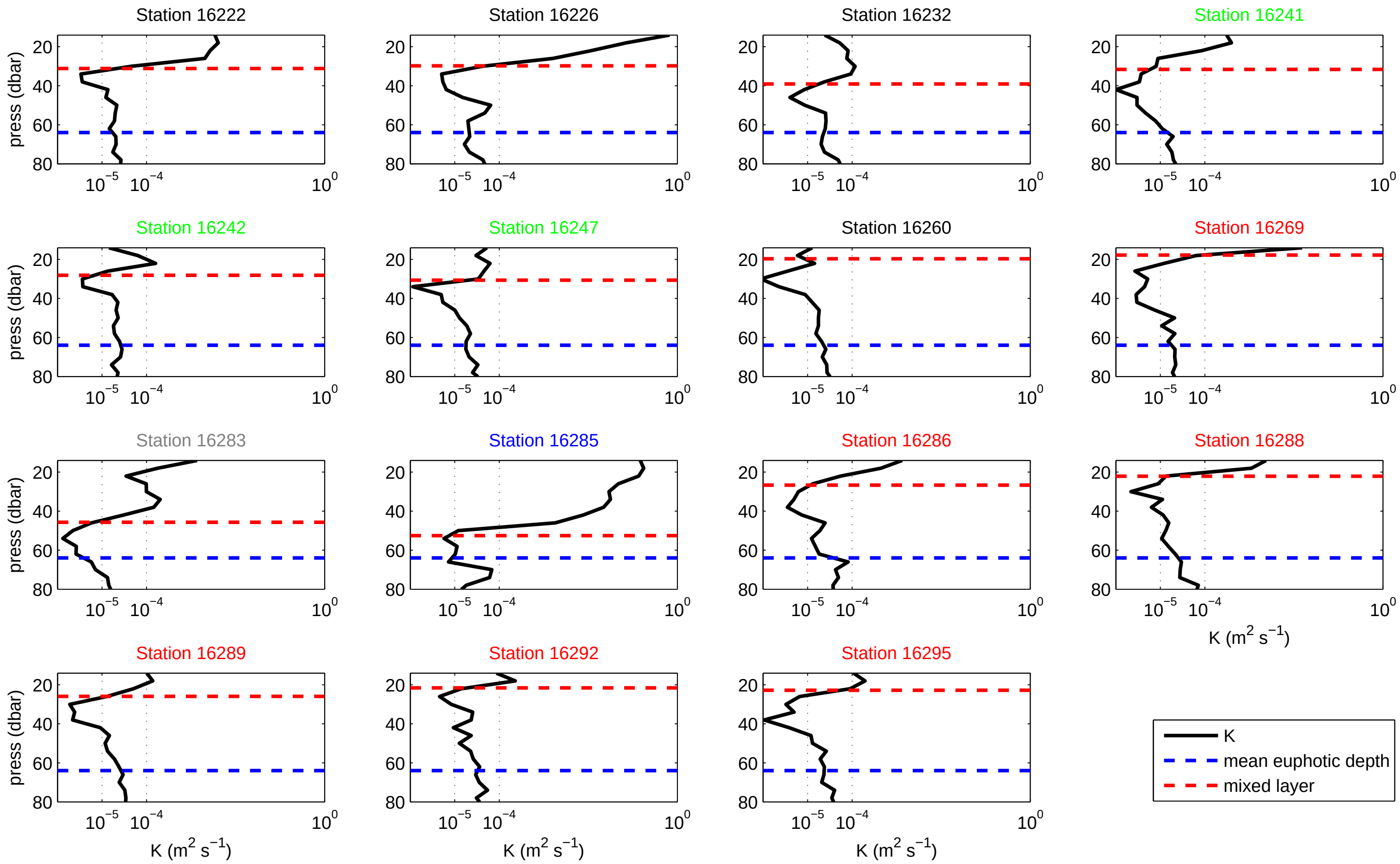

FIGURE 2.17: Profiles of turbulent diffusivity (K). Note the log scale on the x-axis. The depth of euphotic zone (64 m) is marked in blue and the mixed layer depth, calculated as described in Section 2.2.7, in red. For the location of turbulence stations relative to the eddy dipole see Figure 2.3. The colour of the figure title indicates the region that the station is in. Blue is the core region, black the background region, red the jet region and green the edge region (Table 2.4).

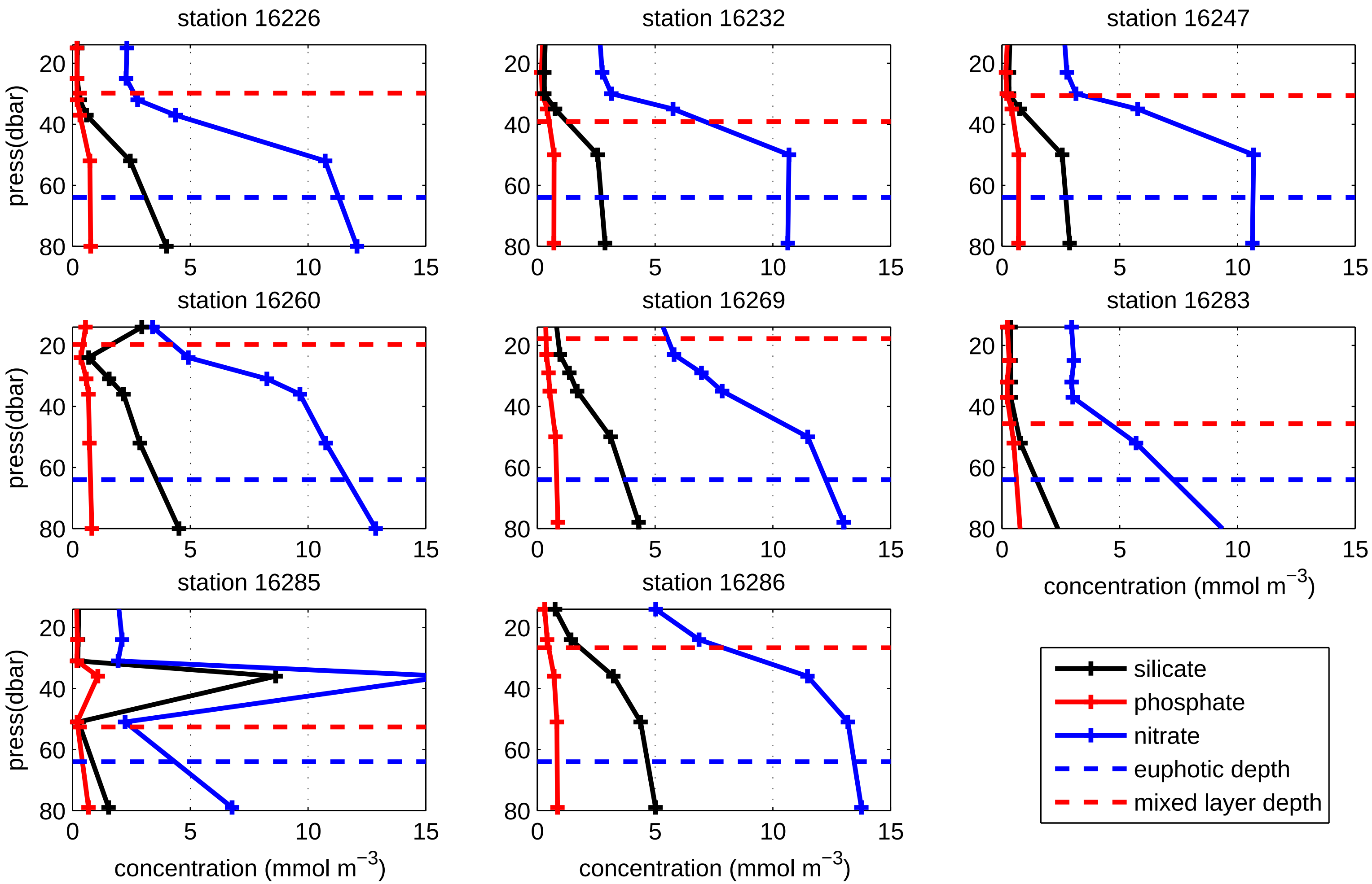

FIGURE 2.18: Profiles of macro-nutrient concentrations for all stations where contemporary turbulence measurements were taken. Measurement error is estimated at 3 %. The depth of euphotic zone (64 m) is marked in blue and the mixed layer depth, calculated as described in Section 2.2.7, in red. For the location of stations relative to the eddy dipole see Figure 2.3.

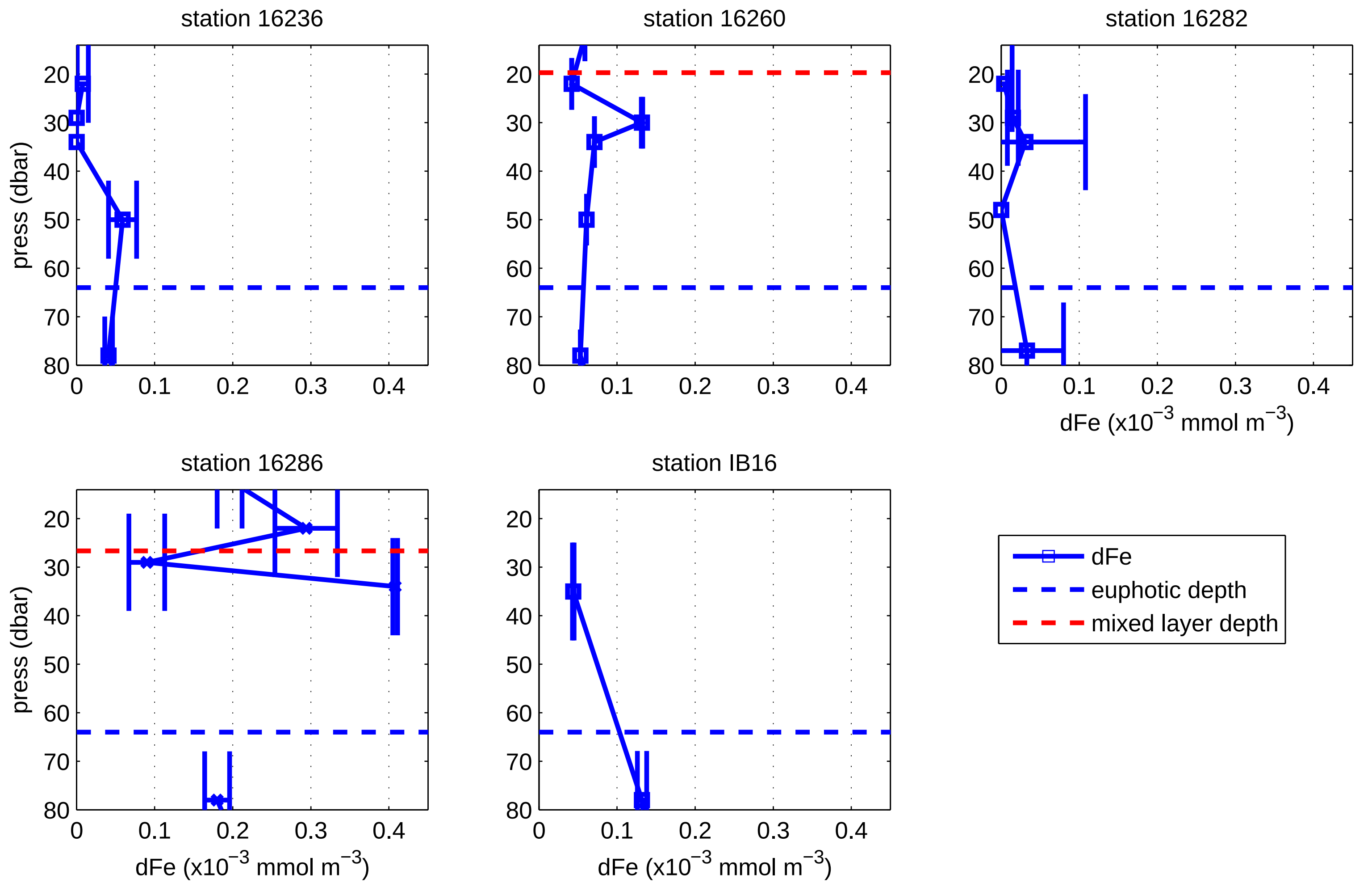

FIGURE 2.19: Profiles of dissolved iron (dFe) concentrations using data from all published stations in Nielsdóttir et al. (2009). Stations 16260 and 16286 have adjacent turbulence measurements. Each sample was analysed in triplicate and the error bars show standard error for the analysis. The depth of euphotic zone (64 m) is marked in blue and the mixed layer depth, calculated as described in Section 2.2.7, for stations 16260 and 16286 in red. For the location of turbulence stations relative to the eddy dipole see Figure 2.3.

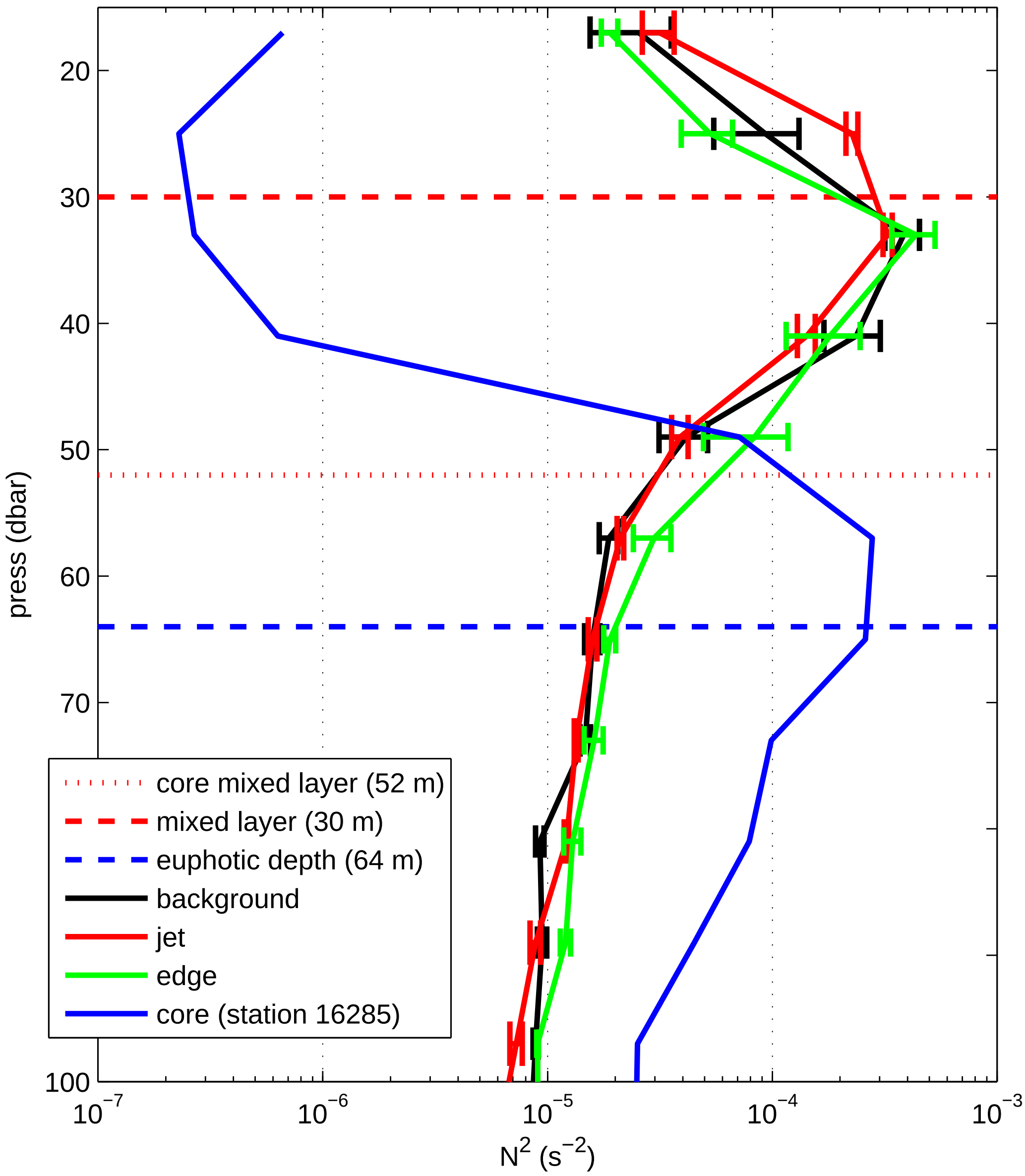

FIGURE 2.20: Profiles of N^2 for the four regions. Note the core region is represented by a single station (16285). Error bars mark standard errors for the combined regional values. The depth of mixed layer is marked as a dashed red line (52 m for core, 30 m for the remaining regions). The euphotic depth is marked as a blue dashed line (64 m).

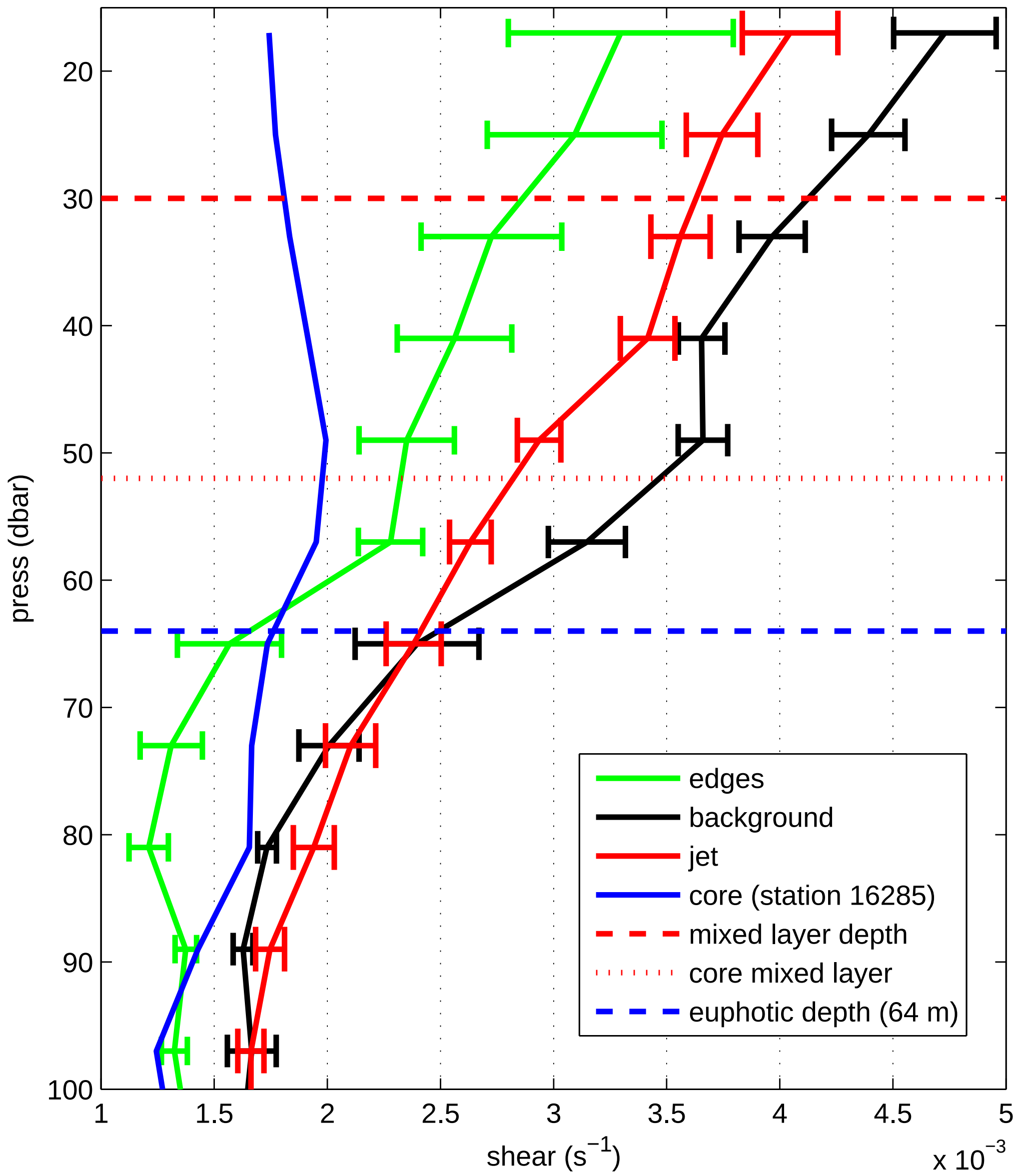

FIGURE 2.21: Profiles of shear for the four regions with a 56 m smoothing window applied. Note the core region is represented by a single station (16285). Error bars mark standard errors for the combined regional values. The depth of mixed layer is marked as a dashed red line (52 m for core, 30 m for the remaining regions). The euphotic depth is marked as a blue dashed line (64 m).

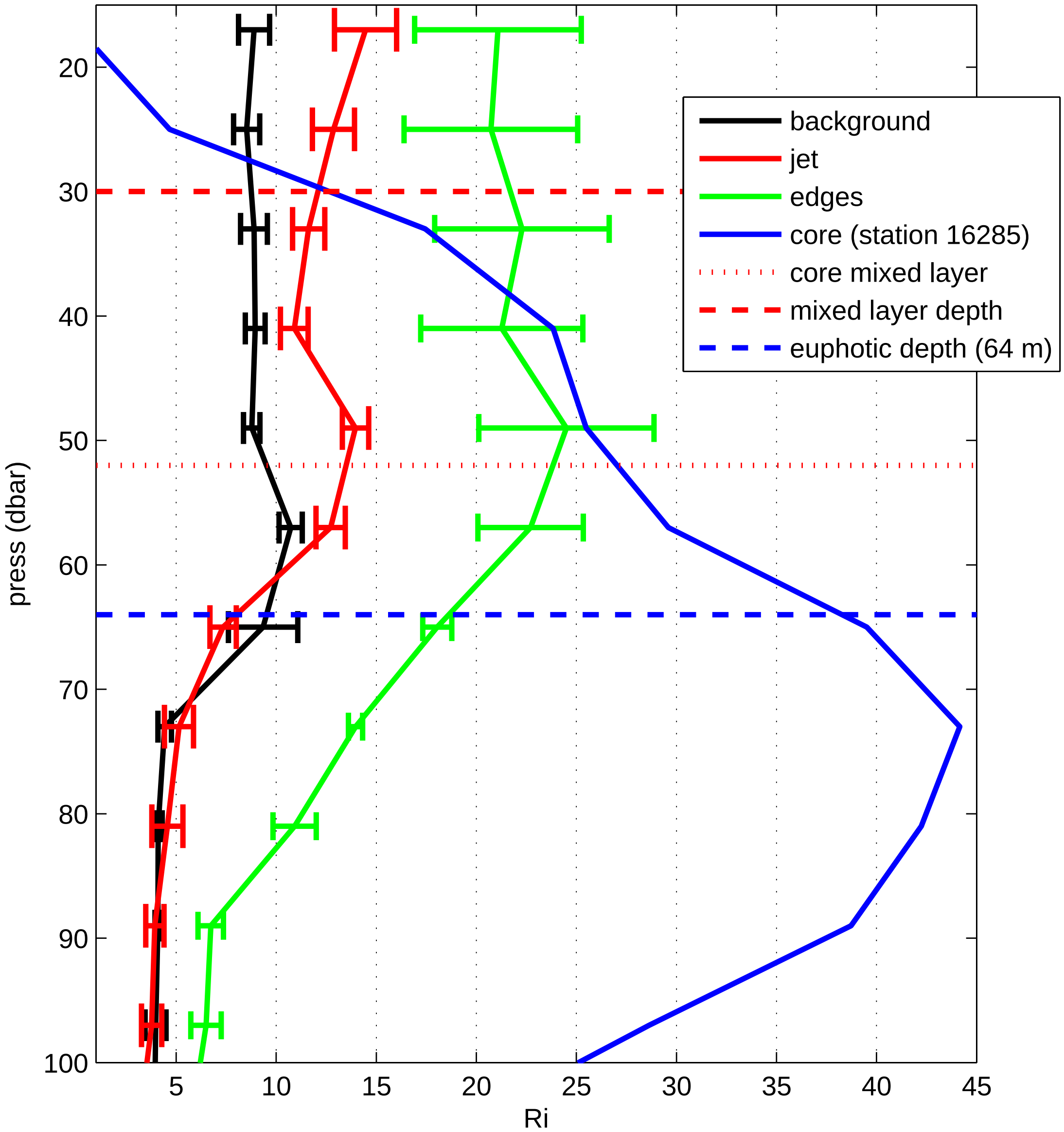

FIGURE 2.22: Profiles of Richardson number calculated from ADCP (shear) and turbulence profiler CTD (buoyancy frequency) data (see Section 2.1.2) for the four regions. Both shear and buoyancy were smoothed using a 56 m window before calculation. Note the core region is represented by a single station (16285). Error bars mark standard errors for the combined regional values. The depth of mixed layer is marked as a dashed red line (52 m for core, 30 m for the remaining regions). The euphotic depth is marked as a blue dashed line (64 m).

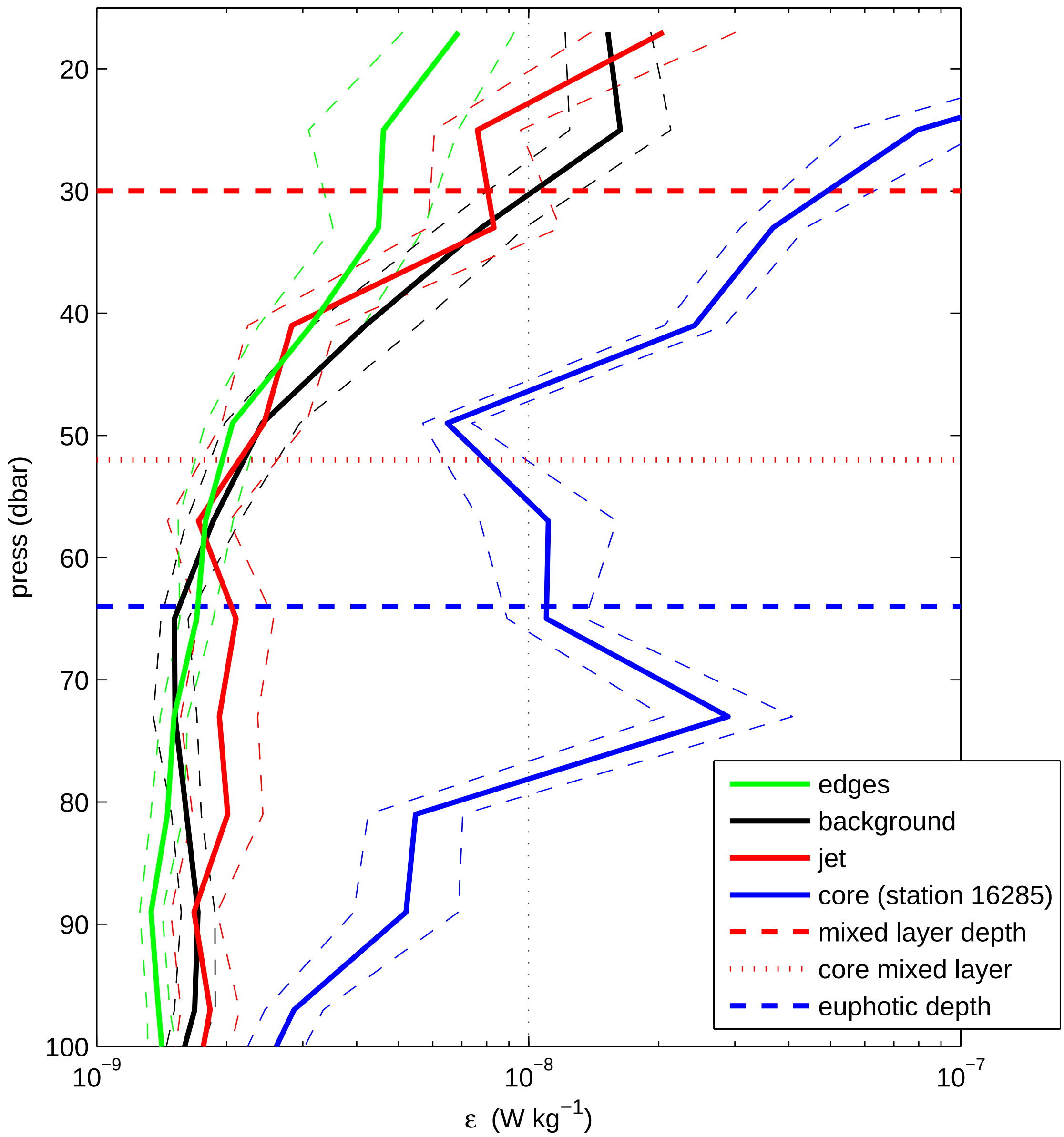

FIGURE 2.23: Profiles of turbulent kinetic energy dissipation (ε) for the four regions. Note the core region is represented by a single station (16285). Dashed lines mark the upper and lower 95 % confidence limits for each regional profile. The depth of mixed layer is marked as a dashed red line (52 m for core, 30 m for the remaining regions). The euphotic depth is marked as a blue dashed line (64 m).

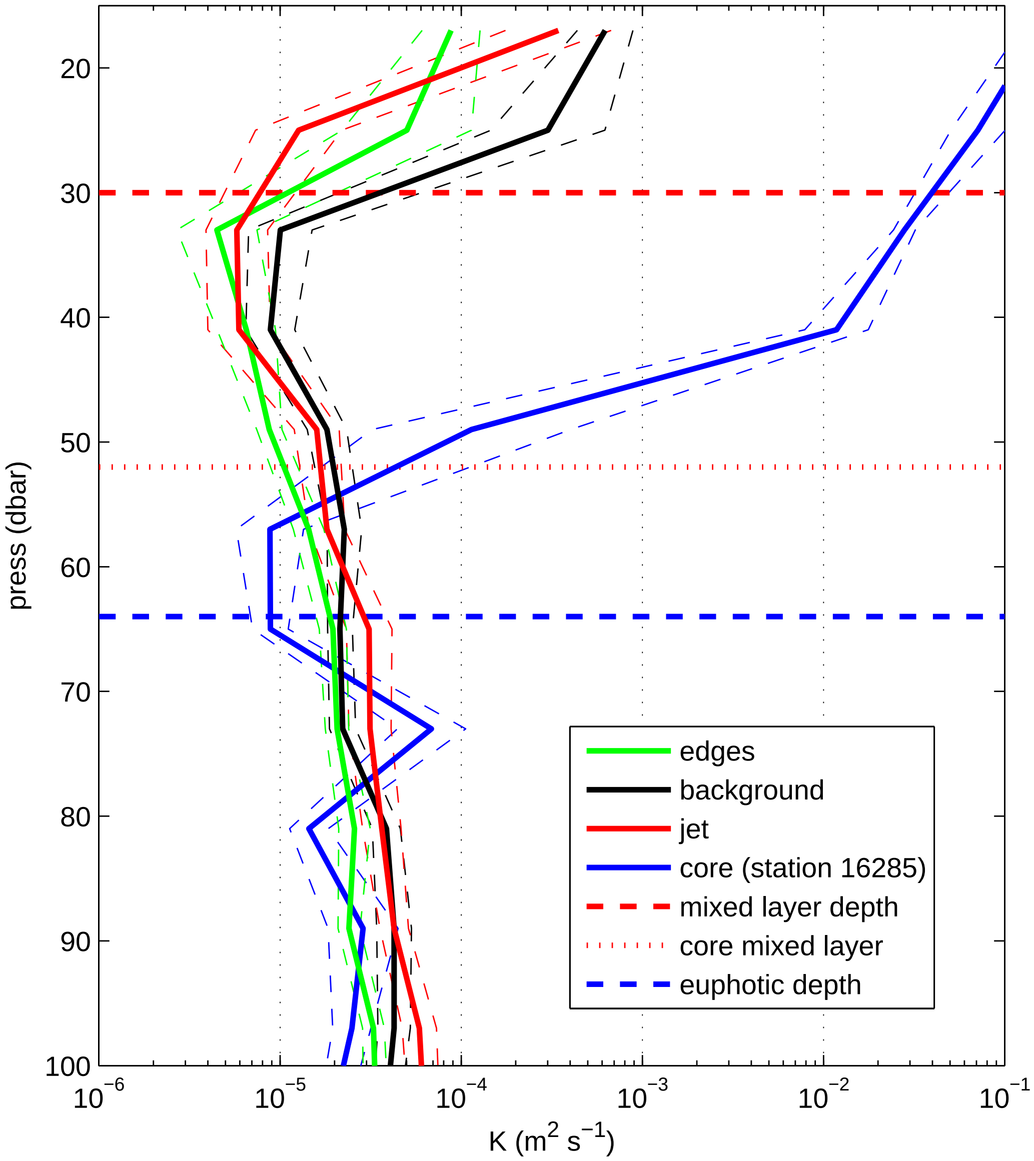

FIGURE 2.24: Profiles of turbulent diffusivity (K) for the four regions (note the core region is represented by a single station 16285). Dashed lines mark the upper and lower 95 % confidence limits for the regional profile. The depth of mixed layer is marked as a dashed red line (52 m for core, 30 m for the remaining regions). The euphotic depth is marked as a blue dashed line (64 m).

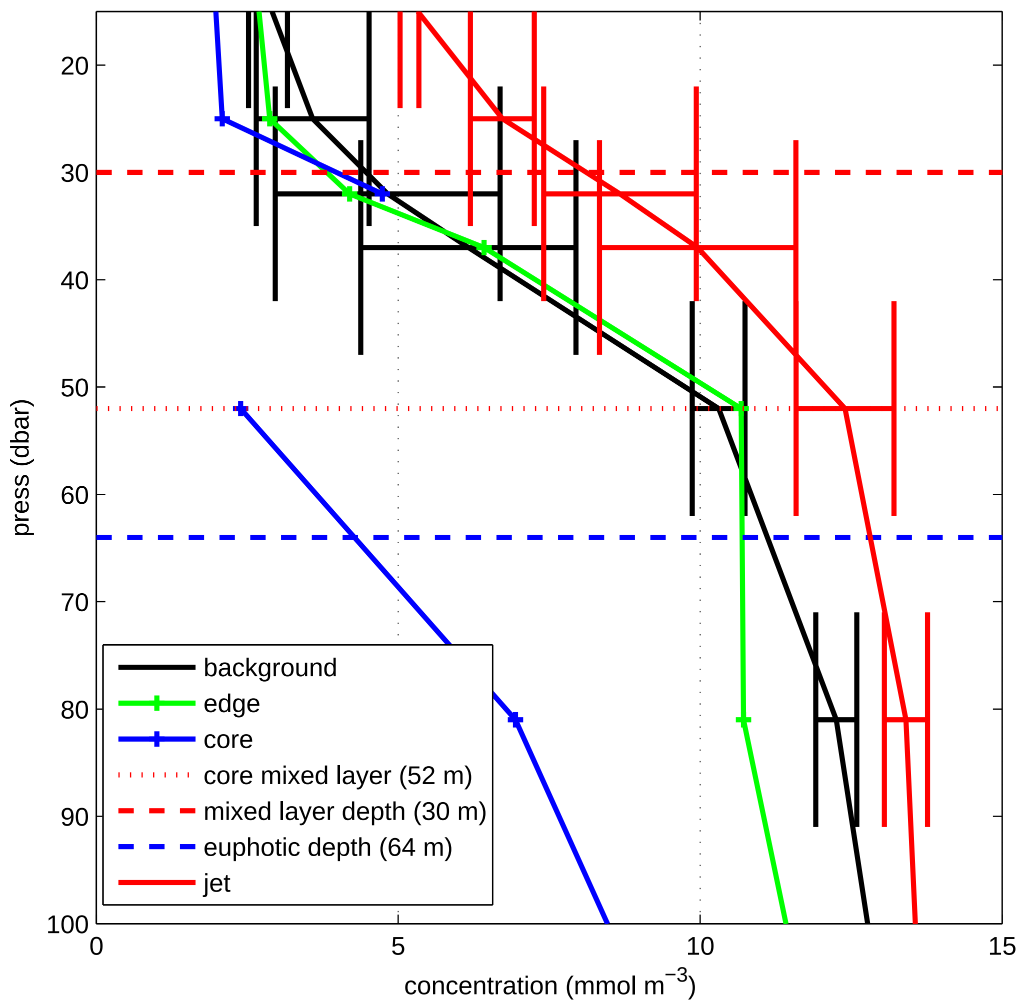

FIGURE 2.25: Profiles of nitrate concentration for the four regions Note the core and edge regions are represented by a single stations (16285 and 16247 respectively). Error bars mark standard errors for the combined regional values. The depth of mixed layer is marked as a dashed red line (52 m for core, 30 m for the remaining regions). The euphotic depth is marked as a blue dashed line (64 m).

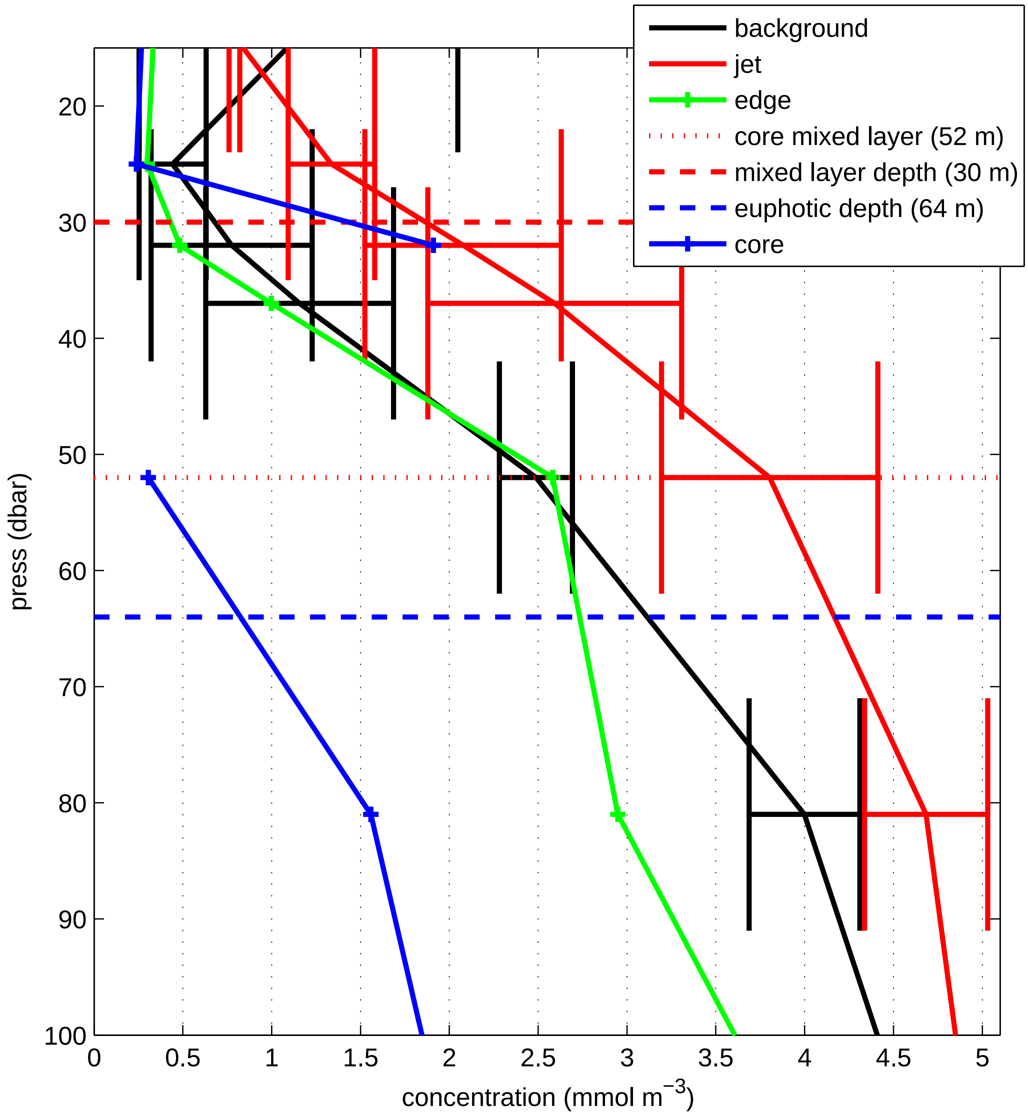

FIGURE 2.26: Profiles of silicate concentration for the four regions. Note the core and edge regions are represented by a single stations (16285 and 16247 respectively). Error bars mark standard errors for the combined regional values. The depth of mixed layer is marked as a dashed red line (52 m for core, 30 m for the remaining regions). The euphotic depth is marked as a blue dashed line (64 m).

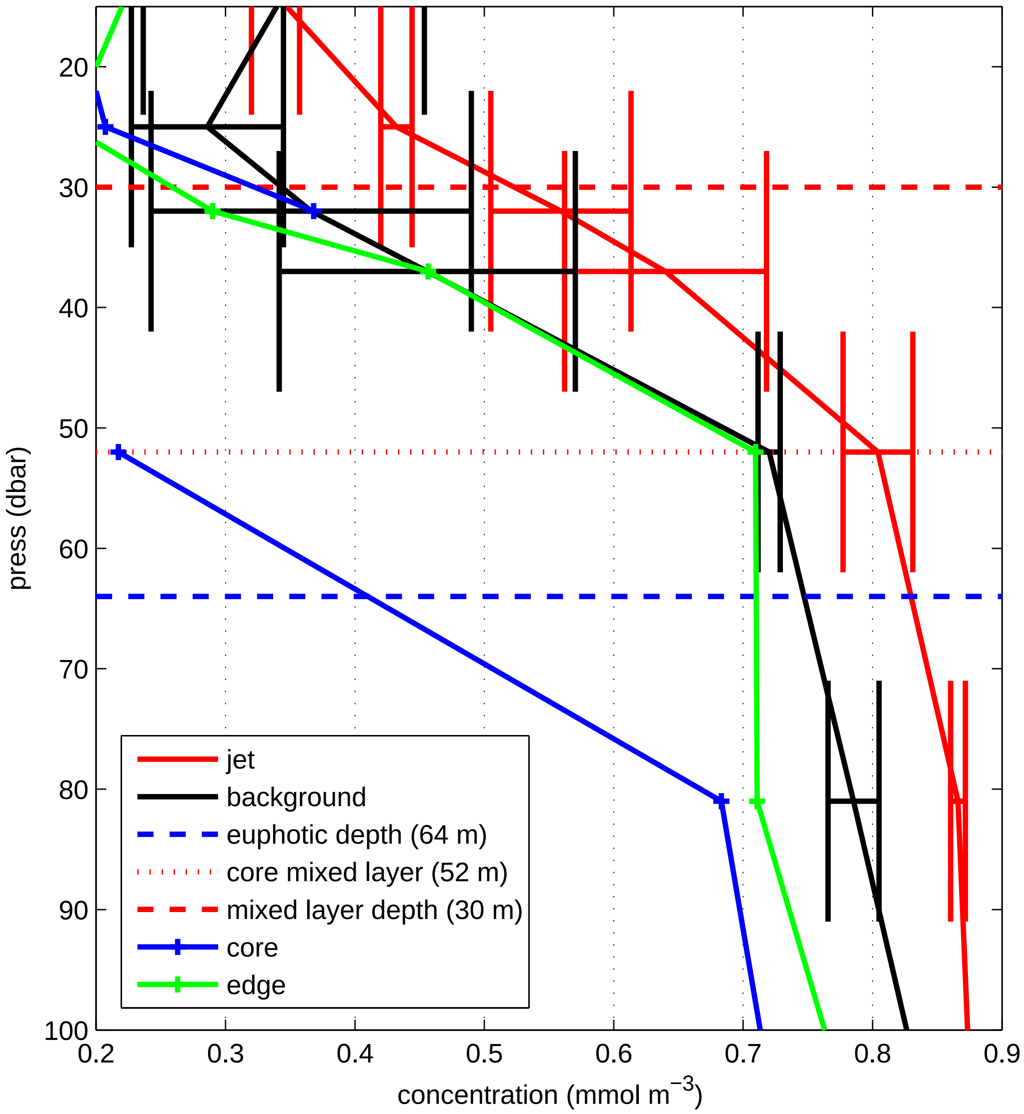

FIGURE 2.27: Profiles of phosphate concentration for the four regions. Note the core and edge regions are represented by a single stations (16285 and 16247 respectively). Error bars mark standard errors for the combined regional values. The depth of mixed layer is marked as a dashed red line (52 m for core, 30 m for the remaining regions). The euphotic depth is marked as a blue dashed line (64 m).

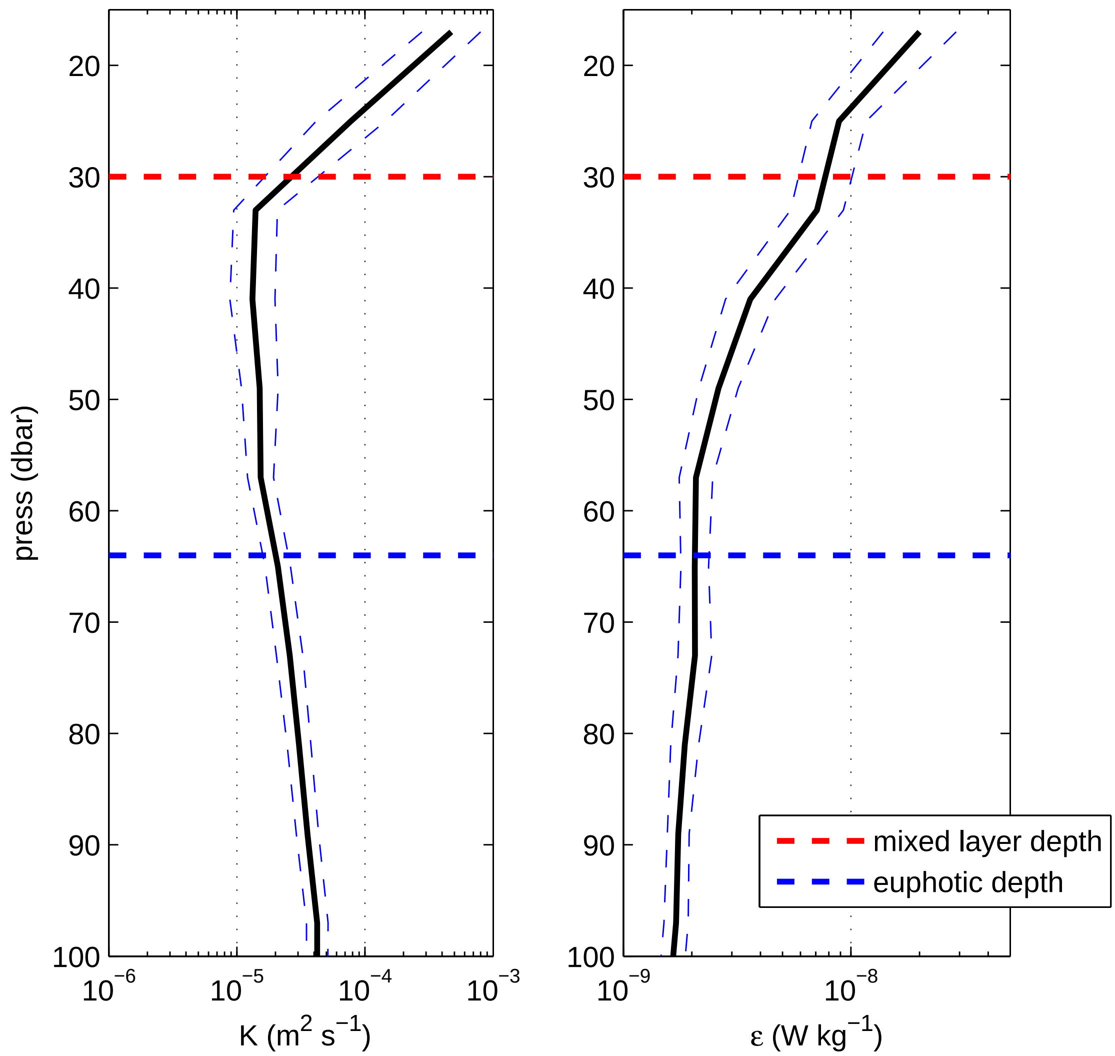

FIGURE 2.28: Area mean profiles of turbulent diffusivity (K) and turbulent kinetic energy dissipation (ε). Dashed lines mark the upper and lower 95 % confidence limits for the regional profile. The depth of mixed layer (30 m) is marked in red and the euphotic depth (64 m) in blue.

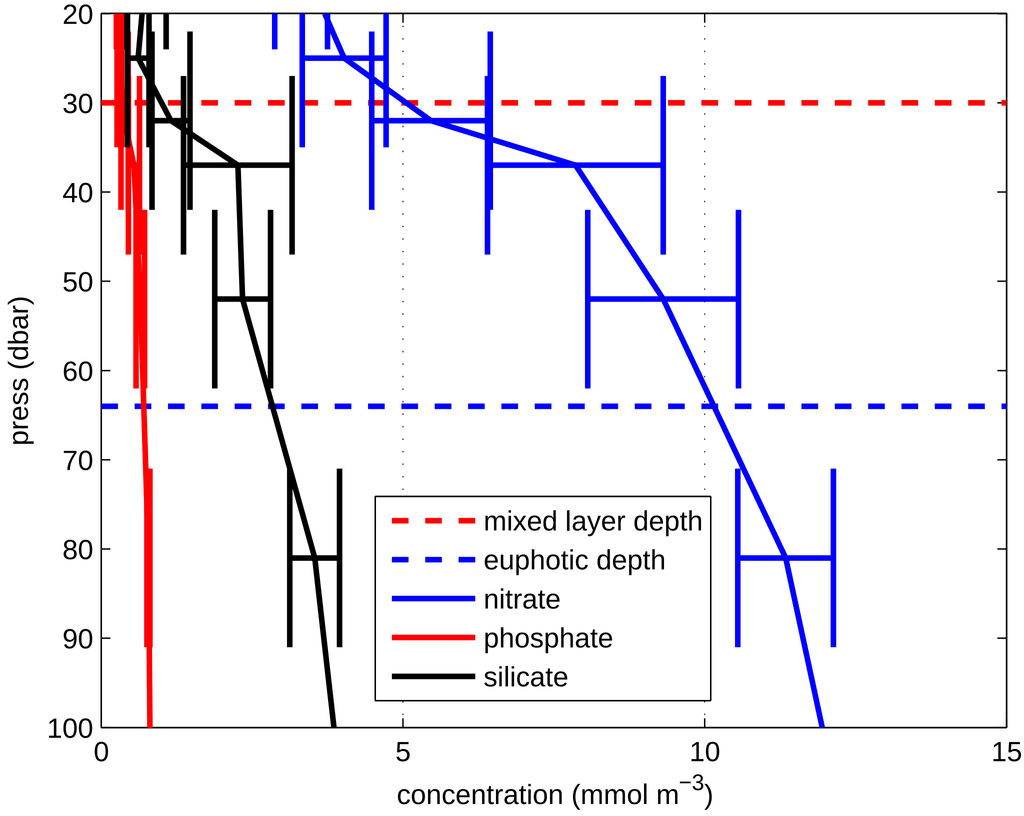

FIGURE 2.29: Area mean profiles of macro-nutrient concentrations. Error bars show standard errors for the means. The depth of mixed layer (30 m) is marked in red and the euphotic depth (64 m) in blue.

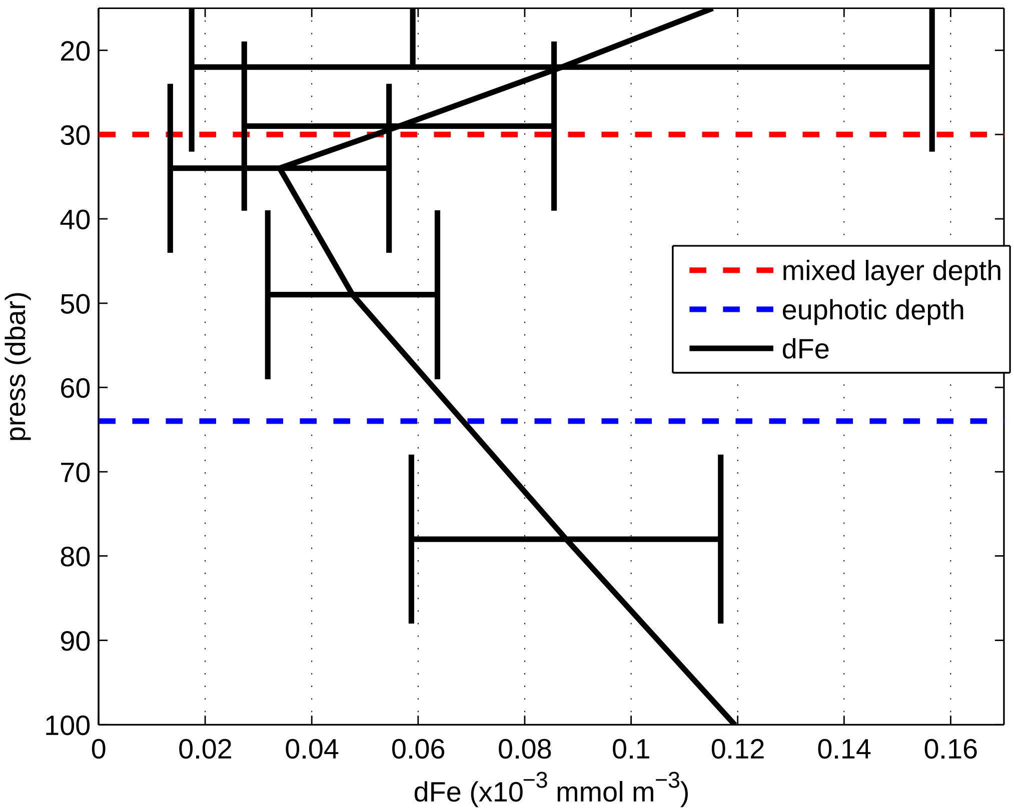

FIGURE 2.30: Area mean profiles of dissolved iron concentration (dFe). Error bars show standard error for the mean. The depth of mixed layer (30 m) is marked in red and the euphotic depth (64 m) in blue.

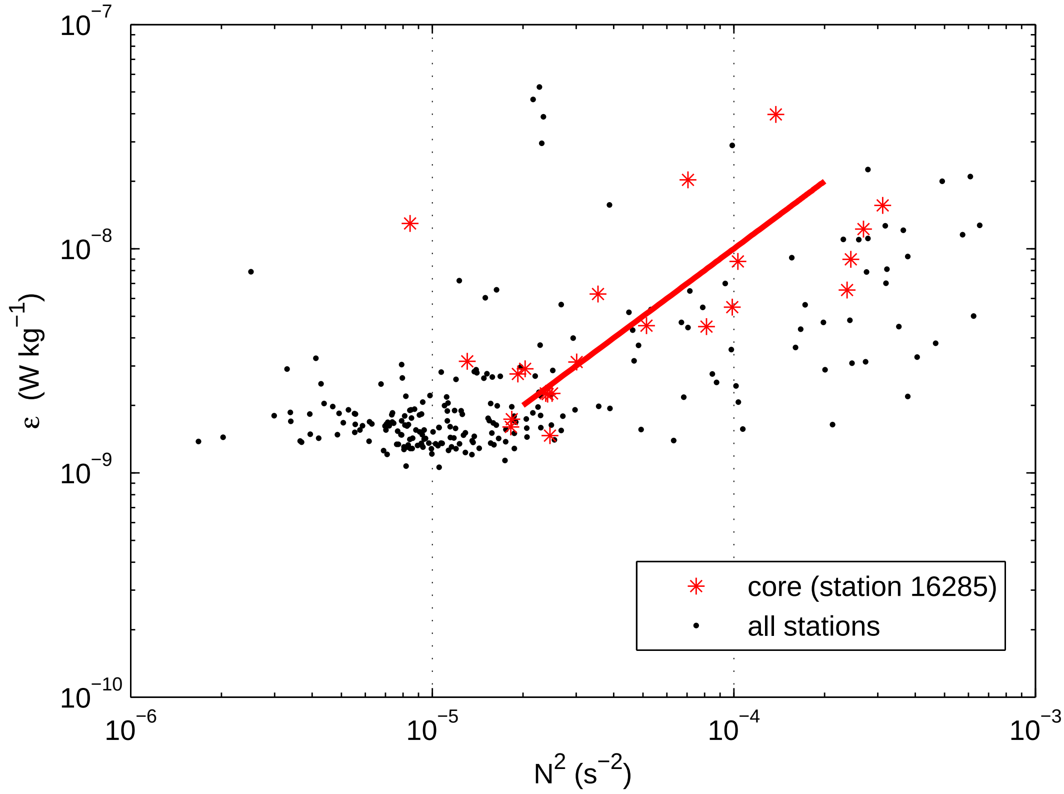

FIGURE 2.31: Scatter plot of N^2 vs turbulent kinetic energy dissipation (ε) for all observations. Observations for station 16285 (the eddy core) are shown in red. The red line indicates $\varepsilon \ \propto \ N^2$

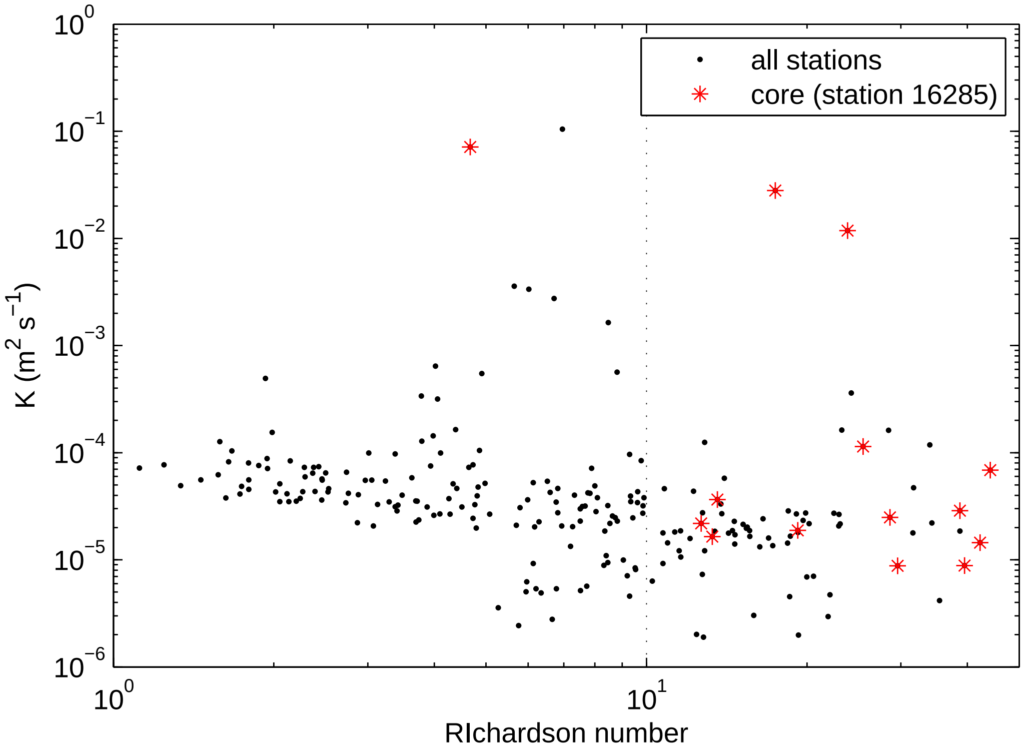

FIGURE 2.32: Scatter plot of Richardson number vs turbulent diffusivity for all observations. The Richardson number is calculated from ADCP (shear) and turbulence profiler CTD (buoyancy frequency) data (see Section 2.1.2). Both shear and buoyancy were smoothed using a 56 m window before calculation.

Chapter 3

Calibration of a Richardson number based mixing parametrization

3.1 Introduction

Vertical turbulent mixing processes in the ocean occur on a wide range of time and space scales. Ocean models, with limited spatial and temporal resolution, are capable of explicitly resolving only a subset of these processes and hence require suitable subgrid-scale parametrizations of vertical mixing in terms of an easily diagnosable quantity such as the Richardson number (Jackson et al., 2008; Yu and Schopf, 1997). Shear enhanced mixing parametrisations have been developed for application in global scale climate models with large scale ($\sim 1^o$) horizontal resolution. The aim of these shear enhanced mixing parametrisations has been to improve the representation of large scale ocean features that are significant to climate using the vertical shear resolvable by the model (Large et al., 1994; Pacanowski and Philander, 1981).

Previous shear enhanced mixing parametrisations have been focussed specifically on improving the representation of the Equatorial Under Current (Large et al., 1994; Pacanowski and Philander, 1981). The tuning of previous parametrisations to the Equatorial Under Current potentially compromises the representation of other ocean features where shear enhanced mixing is important, for example gravity driven overflow currents (Chang et al., 2005; Jackson et al., 2008). However, some ocean features, such as near surface currents are insensitive to the form of the shear enhanced mixing parametrisation used (Yu and Schopf, 1997).

Mesoscale resolving models have a much higher horizontal resolution than climate models, typically of order 0.1°, and can resolve ocean features of a much smaller scale at $\sim$ 10 to 100 km horizontal resolution. Mesoscale features do not typically generate the low Richardson number (Ri) events associated with the enhanced mixing observed for the Equatorial Under Current. Direct observations of the Equatorial Under Current report a range of Richardson number between 0.1 to $\sim$ 14, with a large proportion of the observations being for Richardson numbers less than one (Peters et al., 1988). While previous studies of strong mesoscale features report Ri in the range 3 to 40 for the Gulf Stream (Pelegri and Csanady, 1994) and 2 to 20 for the Florida current (Winkel et al., 2002). Hence the use of existing parametrisations of shear enhanced mixing, tuned for the Equatorial Under Current, in mesoscale resolving ocean models is unlikely to result in any increase in effective vertical turbulent nutrient flux.

Observations in Chapter 2 suggest that there may be a relationship between the Richardson number of mesoscale flows and observed vertical mixing around a strong mesoscale feature. To date, little consideration has been given as to how such mesoscale shear might stimulate vertical turbulent nutrient flux for model flows where the Richardson number is greater than one and the horizontal resolution is sufficient to resolve mesoscale flow. The objective of this chapter is to calibrate a Richardson number based parametrization of vertical mixing, using observations of vertical turbulent mixing from three separate ocean regions, which is suitable for use in such a high resolution ocean model.

3.2 Parametrizing vertical mixing

3.2.1 Shear enhanced mixing and the Richardson number

From theoretical analysis the stability of a stratified shear flow is often described by a single dimensionless parameter such as the gradient Richardson number (Ri) defined as the ratio of buoyancy frequency (N) squared to vertical shear (S_h) squared (Monin and Yaglom, 1971)

$$Ri = \frac{N^2}{{S_h}^2} \tag{3.1}$$

$$S_h{}^2 = (\frac{du}{dz})^2 + (\frac{dv}{dz})^2 \tag{3.2}$$

$$N^2 = -\frac{g}{\rho}\frac{d\rho}{dz} \tag{3.3}$$

(Gill, 1982) where g is acceleration due to gravity ρ is potential density and u, v are velocities in the x, y directions respectively. Hereafter Richardson number (Ri) refers to the gradient Richardson number as defined above (equation 3.1). A low Richardson number, below a critical value (Ri_{crit}), is a necessary (but not sufficient) condition for instabilities in the flow to grow, sustaining vertical turbulent mixing (Thorpe, 2005; De Silva et al., 1999). The critical value of the Richardson number is typically less than one and is often considered to be 0.25 from laboratory studies (Thorpe, 2005; Peters et al., 1988), though values as high as 0.7 have been used in mixing parametrizations (Large et al., 1994). Vertical turbulent mixing has been observed to be enhanced in regions of low Richardson number, both in the laboratory (Thorpe, 2005; Turner, 1973) and in the ocean (Peters et al., 1988; Toole and Schmitt, 1987).

The magnitude of vertical turbulent mixing can be characterised as a turbulent diffusivity (K). The turbulent diffusivity of any scalar quantity (such as momentum or tracer concentration) resulting from shear flow in stable stratification (i.e. buoyancy frequency > 0) is often related to the Richardson number (for $Ri > Ri_{crit}$)through an equation of the form

$$K_s = K_{os}(1 + \alpha_s Ri)^{-n_s} \tag{3.4}$$

where K_s is the turbulent diffusion coefficient for the scalar quantity s, K_{os} is the turbulent diffusion under neutral stability, and α_s, n_s are constants (Peters et al., 1988; Monin and Yaglom, 1971; Munk and Anderson, 1948). The form of equation 3.4 has been chosen to satisfy the known limiting conditions $K_s \to K_{os}$ as $Ri \to 0$ and $K_s \to 0$ as $Ri \to \infty$ (Monin and Yaglom, 1971; Munk and Anderson, 1948). Neutral stability is the condition for a fluid flow when the buoyancy frequency and consequently, from equation 3.1, the Richardson number are zero. Under these conditions, from equation 3.4, the turbulent diffusion coefficient is equal to K_{os}

The diffusion coefficients for tracers are usually considered to be equal and different from the diffusion coefficient for momentum (Peters et al., 1988; Munk and

Anderson, 1948). Typically the turbulent diffusion coefficient for momentum is referred to as the turbulent viscosity (K_v), while the turbulent diffusion coefficient for tracers is referred to as the turbulent diffusivity (K_t). As formulated in equation 3.4 turbulent diffusivity and turbulent viscosity are independent. However, empirical relationships have been proposed relating the constants α_s and n_s for turbulent diffusivity and turbulent viscosity (Munk and Anderson, 1948), and theoretical arguments used to determine the ratio of turbulent diffusivity to turbulent viscosity (Monin and Yaglom, 1971). Lacking direct observations of K_v and K_t to estimate the parameters in equation 3.4, previous studies have proposed various values for the constants K_{os}, α_s and, n_s. Only one set of extant parameters has been estimated from simultaneous calibration of equation 3.4 to direct observation, though the authors do not state which of the parameters were fixed a priori and which were fitted to observation (Peters et al., 1988).

Turbulent diffusion under neutral stability is typically considered to be a constant for flows in the ocean interior below the surface mixed layer (Yu and Schopf, 1997; Peters et al., 1988; Pelegri and Csanady, 1994). In previous studies values ranging from 5 to 50 x10^{-4} m^2s^{-1} have been used for K_{os} (Table 3.1). Where the region of neutral stability is bounded by a surface, for example in the upper mixed layer which is bounded by the atmosphere, K_{os} is considered to be a function of distance from the bounding surface and surface stress (Soloview et al., 2001; Monin and Yaglom, 1971; Robinson, 1966; Munk and Anderson, 1948).

From consideration of atmospheric data α_s was originally assumed to equal 10 when estimating K_v (Munk and Anderson, 1948) and 3.333 (Munk and Anderson, 1948) when estimating K_t, though the value for estimating K_t was changed to 10 in later studies (Pelegri and Csanady, 1994). Most commonly α_s has been assumed to equal 5 when calculating both K_v and K_t based on laboratory experimental data (Yu and Schopf, 1997; Peters et al., 1988; Pacanowski and Philander, 1981; Jones, 1973; Robinson, 1966).

Laboratory studies have suggested that that $K \propto Ri^{-1.5}$ (Turner, 1973) and $n_s =$ -1.5 has been used in some previous studies when estimating K_v (Peters et al., 1988) and K_t (Pelegri and Csanady, 1994; Munk and Anderson, 1948). However, values of $n_s =$ -0.5 (Munk and Anderson, 1948), and $n_s =$ -1 (Jones, 1973; Robinson, 1966) have also been used when estimating K_v. and values of $n_s =$ -2.5 (Peters et al., 1988), and $n_s =$ -3 (Yu and Schopf, 1997) used when estimating K_t. For a summary of the constants most commonly used in Richardson number mixing parametrizations see Table 3.1.

The form of the relationship between turbulent mixing coefficients and Richardson number as presented in equation 3.4 is only considered to be valid for Richardson numbers above Ri_{crit} (Lozovatsky et al., 2006; Peters et al., 1988). Several forms for the sub-critical Richardson number relationship and values for the critical Richardson number have been proposed (Lozovatsky et al., 2006; Soloview et al., 2001; Large et al., 1994; Peters et al., 1988). From direct observations of the Pacific Equatorial Undercurrent it has been proposed that

$$\begin{aligned} K_v &= 5.6 \times 10^{-8} Ri^{-8.2} \\ K_t &= 3.0 \times 10^{-9} Ri^{-9.6} \end{aligned}$$

(Peters et al., 1988) with $Ri_{crit} \sim 0.25$. The above two relationships are unbounded as they allow the turbulent mixing coefficient to approach infinity as the Richardson number approaches zero. For mixing in the surface boundary layer where $Ri < Ri_{crit}$ the relationship

$$K = K_{os}\left(1 - \frac{Ri}{Ri_{crit}}\right)$$

(Soloview et al., 2001) has been proposed for both turbulent diffusivity and turbulent viscosity where $Ri_{crit} = 0.25$. This relationship is only applicable to the surface boundary layer and K_{os} is considered to be a function of distance from the ocean surface and surface stress (Soloview et al., 2001).

Below the ocean boundary layer, for both turbulent diffusivity and turbulent viscosity where $Ri < Ri_{crit}$, it has been proposed

$$K = K_{os}\left[\left(1 - \frac{Ri}{Ri_{critical}}\right)^2\right]^3$$

(Large et al., 1994) where $Ri_{crit} = 0.7$ and $K_{os} = 50 \text{ x}10^{-4}\ \text{m}^2\text{s}^{-1}$.

To achieve a parametrization which can estimate turbulent diffusivity for the full range of Richardson number ($0 < Ri < \infty$), the estimate of diffusivity for any given Ri is considered to be the sum of the estimate of diffusivity from the sub-critical Ri relationship and the estimate of diffusivity from the super-critical Ri relationship, i.e. $K(Ri) = K(Ri)_{subcrit} + K(Ri)_{supercrit}$ for both K_v and K_t (Soloview et al., 2001; Large et al., 1994; Peters et al., 1988). The super-critical relationship for K_v and K_t

can either be of the form of equation 3.4 (Soloview et al., 2001; Peters et al., 1988) or both K_v and K_t are considered to be zero when $Ri > Ri_{crit}$ (Large et al., 1994).

3.2.2 Other sources of mixing

Mixing in the ocean has been identified to potentially arise from several sources, of which stratified shear flow is only one (Large et al., 1994; Peters et al., 1988; Pacanowski and Philander, 1981). Consequently when calibrating a Richardson number based parametrization of turbulent diffusivity to direct observations (Peters et al., 1988) or when using such a parametrization in an ocean model (Large et al., 1994; Pacanowski and Philander, 1981), the observed (or modelled) diffusivity is represented as a sum of diffusion terms. Most commonly a single term representing a constant background diffusivity is added to the Richardson number parametrization for diffusivity (Peters et al., 1988; Pacanowski and Philander, 1981). However, other terms representing convective overturning and double diffusion can also be included (Large et al., 1994; Soloview et al., 2001) The background diffusivity is considered to arise from mixing processes occurring at vertical scales smaller than the vertical scales used to calculate the Richardson number (Large et al., 1994; Peters et al., 1988; Pacanowski and Philander, 1981). Such smaller scale mixing processes include finescale shear instability (Polzin et al., 1997), and time variant processes, such as diurnal cycles (Peters et al., 1988) and inertial motions (D'Asaro, 1985). Hence, ignoring convection and double diffusion, the full expression for turbulent diffusivity is of the form $K_s(Ri) = K_s(Ri)_{subcrit} + K_s(Ri)_{supercrit} + K_{bs}$ where K_{bs} is the constant background diffusivity. Values for the background mixing terms for turbulent diffusivity are typically an order of magnitude lower than those for turbulent viscosity, with all values ranging between 1x10^{-6} to 1x10^{-4} m^{2}s^{-1} (Table 3.2).

The parametrization of Pacanowski and Philander (1981) is a variation on the form of equation 3.4

$$K_t = \frac{K_v}{(1+\alpha Ri)} + K_b$$

$$K_v = \frac{K_{ov}}{(1+\alpha Ri)^n} + V_b$$

where $\alpha = 5$, $n = 2$, $K_{ov} =$ 5x10^{-3} m^2 s^{-1}, $K_b =$ 1x10^{-5} m^2 s^{-1} and $V_b =$ 1x10^{-4} m^2 s^{-1}. K_b and V_b represent constant background turbulent diffusivity and viscosity respectively. In this parametrization, turbulent diffusivity and turbulent viscosity are related by arbitrarily equating turbulent diffusivity under neutral stability to turbulent viscosity. The parametrization of Pacanowski and Philander (1981) has been approximated into the form of equation 3.4 by Yu and Schopf (1997) using parameters given in Table 3.1.

3.3 Fitting a parametrization

Following the approach taken in previous studies (Large et al., 1994; Peters et al., 1988; Pacanowski and Philander, 1981) vertical mixing in this thesis is represented as a sum of mixing attributable to shear flow in a stable stratification (equation 3.4) and a constant background diffusivity term (K_{bs}) hence

$$K_s \;=\; K_{os}(1+\alpha_s Ri)^{-n_s} \;+\; K_{bs} \tag{3.5}$$

Equation 3.5 could potentially be expanded to cover double diffusive and convective mixing, following the approach in Large et al. (1994), by including additional terms for these processes. However the observational data used in the determination of the parametrization (see below) contains no examples of either double diffusive or convective mixing. Hence, we consider only mixing due to shear flow in stable stratification.

Equation 3.5 is considered valid for all values of the Richardson number above 0.25 and K_{os} is considered to be a constant. The value of 0.25 was selected as the smallest valid value for the Richardson number in equation 3.5 as it represents the most commonly used value for Ri_{crit} from previous studies (Thorpe, 2005; Soloview et al., 2001; Peters et al., 1988). As K_{os} is defined as constant the relationship is only appropriate for use below the ocean mixed layer.

3.3.1 Data set description

Three sets of turbulence measurements were used in the calibration of equation 3.5; two from the North Atlantic and one from the Southern Ocean (Figure 3.1). Each turbulence station in each dataset consists of between 5 to 19 profiles, to a maximum depth of 150 to 300 m (Table 3.3, 3.4, and 3.5). Measurements were taken using an MSS90L free-fall microstructure profiler as described in Chapter 2.

3.3.1.1 Porcupine Abyssal Plain (PAP) site dataset

Measurements were taken as part of UK RSS Discovery cruise D306 to the Porcupine Abyssal Plain in June - July 2006. The purpose of this cruise was to investigate carbon cycling in the pelagic zone (Burkill, 2006). Turbulent mixing was measured at fifteen stations taken as part of an eleven day time series on the site of the long term PAP observatory (12 stations) and associated mesoscale survey of the area (3 stations) (Table 3.3, figure 3.2).

While each turbulence station was in progress, horizontal current velocities down to approximately 300 m were measured using a ship-mounted 150 kHz RDI Acoustic Doppler Current Profiler (ADCP) and logged using RD Instruments data acquisition software (DAS version 2.48 with profiler firmware 17.20). The instrument was configured as described for cruise D321 in Chapter 2. Calibration was carried out over the continental shelf on route to the survey site, when values of misalignment angle (0.45^o) and the amplitude factor (1.0023) were derived. ADCP data for the cruise were processed by Roz Pidcock and John Allen (Burkill, 2006).

3.3.1.2 Iceland Basin dataset

Measurements were taken as part of UK RSS Discovery cruise D321 to the Iceland Basin in July to August 2007. The purpose of this cruise was to examine controls on export production in the region (Allen, 2007). On arrival at the survey site it was found that within the survey area was an eddy dipole, consisting of a cyclonic eddy and an anti-cyclonically rotating mode-water eddy. During the three week survey turbulent mixing was measured at fifteen stations in various locations in and around the eddy dipole structure (Table 3.4, figure 3.3).

While each turbulence station was in progress, horizontal current velocities down to approximately 300 m were measured using a ship-mounted 150 kHz RDI ADCP as described in Chapter 2 (Allen, 2007).

3.3.1.3 Southern Ocean dataset

Measurements were taken as part of UK RSS James Cook cruise JC29 to the Kerguelen Plateau in November to December 2008 (Naveira Garabato, 2008). The purpose of the cruise was to investigate the physics of the Antarctic Circumpolar Current (ACC) and the Southern Ocean overturning circulation. Turbulent mixing was measured at nine turbulence stations on the northern edge of the Kerguelen plateau (Table 3.5, Figure 3.4).

While each turbulence station was in progress, horizontal current velocities down to approximately 300 m were measured using a ship-mounted 150 kHz RDI Ocean Surveyor ADCP and logged using RD Instruments data acquisition software (VmDas version 1.42). The instrument was configured to sample over 120 second intervals with 60 bins of 8 m thickness and a blanking distance at the surface of 6 m. Calibration was carried out over the continental shelf when values for the misalignment angle (-0.9^o) and the amplitude factor (1.0083) were derived. ADCP data for the cruise were processed by Angelika Renner and Mirjam Glessmer (Naveira Garabato, 2008).

3.3.2 Calculation of mixed layer depth

Measurements of temperature and salinity from the microstructure profiler were combined, for each station, to calculate the station density profile and the depth of the mixed layer. Density was calculated (with respect to 0 dbar pressure) using the UNESCO equation of state (UNESCO, 1980). Mixed layer depths for each profile were calculated using a density change criteria evaluated using a temperature change of 0.2^o from the temperature at 10 m depth as described in Chapter 2. Of the three datasets used here, the dataset for JC29 shows a much weaker seasonal stratification than the datasets for D321 or D306. The temperature change of 0.2^o selected as best representing the depth of the homogeneous sections for D321 and D306 datasets does not give such robust results when applied to the JC29 dataset and appears to overestimate the depth of the mixed layer for stations 67 and 69 (Figure 3.5). However, for consistency with the D321 and D306, the temperature change of 0.2^o was retained. Overestimating the depth of the mixed layer results in potentially valid data points being excluded from the fitting process, as opposed to underestimating the depth of the mixed layer which would result in potentially non-valid data being included in the fit.

3.3.3 Calculation of turbulent diffusivity and turbulent viscosity

Turbulent diffusivity can be calculated from estimates of the turbulent kinetic energy dissipation rate

$$K_t = \Gamma \frac{\varepsilon}{N^2}$$

where Γ is the mixing efficiency (Peters et al., 1988; Osborn, 1980). The rate of kinetic energy dissipation (ε) can be calculated from the variance of the vertical velocity shear, measured using a microstructure profiler. For a full description of the calculation of kinetic energy dissipation rate see Chapter 2.

Turbulent viscosity can be calculated from measurements of Reynolds stress

$$K_v = -\langle uw \rangle / (S_h)$$

(Thorpe, 2005) where $<uw>$ is the Reynolds stress, the *u, w* fluctuations of the mean flow (Tennekes and Lumley, 1972) and S_h is vertical shear (equation 3.2). The rate of production of turbulent kinetic energy by the mean flow $\rho \langle uw \rangle / (S_h)$ (Thorpe, 2005), under stable conditions, where there are negligible buoyancy fluxes, is equal to the dissipation rate of turbulent kinetic energy. Hence

$$-\varepsilon = \langle uw \rangle / (S_h)$$

(Thorpe, 2005). K_v can then be determined from

$$K_v = \frac{\varepsilon}{{S_h}^2} \tag{3.6}$$

(Thorpe, 2005). Equation 3.6 depends upon the assumption that the rate of turbulent kinetic energy dissipation is equal in magnitude to the rate of production of turbulent kinetic energy by the mean flow. In this thesis the mean flow is considered to be mesoscale. For consistency the vertical shear used in equation 3.6 is calculated in the same manner as the vertical shear used when estimating the Richardson number (Section 3.3.6).

Equation 3.6 is not considered to be applicable when processes of a smaller vertical scale than the scales of the mean flow, for example internal wave shear, contribute significantly to the dissipation rate (Peters et al., 1988). Dissipation caused through internal wave field interactions is generally accepted to scale with N^2, such that $\varepsilon \propto N^2$(Polzin et al., 1995; Gregg and Sanford, 1988). Scatter-plotting all observations of turbulent dissipation against contemporary observations of N^2 shows no such clear relationship for any of the three data sets (Figure 3.6). However the inclusion of a background mixing term in the parametrization for fitting to observation implicitly assumes a contribution to the observed dissipation from smaller scale processes. Hence, the results of using equation 3.6 to calculate K_v from the data should be viewed with caution.

3.3.4 Calculating the vertical shear

The individual ADCP velocity components recorded while each turbulence station was in progress were averaged in time, for each 8 m depth interval, to produce a station mean velocity profile of 8 m resolution. Where the raw ADCP data were recorded with higher vertical resolution than 8 m (cruises D321 and D306) the ADCP data were first averaged into 8 m intervals. The gradient in velocity from the mean profile was calculated, between successive depth levels, from the individual horizontal velocity components by first order differencing. The absolute gradients for the mean profile were then combined by taking the root of the sum of the two components squared to give the absolute vertical shear at the mid point of each depth interval (equation 3.2).

3.3.5 Calculating the buoyancy frequency

Prior to the calculation of the buoyancy frequency, for consistency with the ADCP data, the microstructure measurements of temperature and salinity for each cast were averaged into a profile divided into 8 m intervals from which density was then calculated. The buoyancy frequency was calculated using these measurements of density using equation 3.3. The values for N^2 were averaged across the casts for each station, for each depth interval, to produce a station mean buoyancy profile.

3.3.6 Estimation of Richardson number

The Richardson number was calculated from profiles of vertical shear and buoyancy frequency as described above using equation 3.1.

3.3.6.1 Scale dependency of the Richardson number

The Richardson number is highly scale dependent, with the instantaneous value of the Richardson number (Ri_p) calculated at a point in a stratified shear flow, depending on both the bulk Richardson number of the flow, which is calculated over scales of the same order as the mean flow velocity and flow length scale (Turner, 1973), and the vertical resolution of the measurements of shear and buoyancy used in the calculation (De Silva et al., 1999). At a vertical measurement resolution of smaller scale than the scale of the instability generating the mixing, when Ri_p reduces below the critical value and vertical turbulent mixing is occurring, Ri_p tends towards a constant value independent of the bulk Richardson number (De Silva et al., 1999).

Consequently establishing a relationship between observed diffusivity and bulk Richardson number relies on the measurement scale of the bulk Richardson number being of the same order as the vertical scale of the shear generating the diffusivity. For example, when vertical turbulent mixing is a result of finescale shears (instability on vertical scales of 2 to 3 m, Polzin (1996) the Richardson number calculated at a vertical resolution of 3 m shows a close correlation to observed mixing, while the Richardson number calculated at a vertical resolution of 10 m shows no correlation (Toole and Schmitt, 1987; Polzin, 1996).

At the mesoscale, in strong western boundary currents, mixing has been observed to be associated with vertical shear generated during frontogenesis (Nagai et al., 2009; Van Gastel and Pelegri, 2004). In the meanders of the Gulf Stream current shear generating mixing is observed to occur on vertical scales of greater than 25 m (Van Gastel and Pelegri, 2004). Observations of enhanced turbulent dissipation during frontogenesis in the Kuroshio suggest a vertical scale of $\sim$ 50 m for vertical shear (Nagai et al., 2009). However, it is not clear from the observations whether the mixing in this case is due to current shear or other sub-mesoscale mixing processes (Nagai et al., 2009). This would suggest that vertical length scales of of at least 25 m are appropriate for calculating the Richardson number relevant to the diffusivity arising from mesoscale shear.

3.3.6.2 Smoothing window size

Profiles of vertical shear and buoyancy frequency calculated from ADCP data and microstructure measurements of temperature and salinity show not only large scale velocity and density trends, but also the signatures of smaller scale processes as variability about the mean profile. Such smaller scale processes include finescale shear instability (Polzin et al., 1997) and time variant processes, such as diurnal cycles (Peters et al., 1988) and inertial motions (D'Asaro, 1985).

In order to calculate the bulk Richardson number appropriate to mesoscale flow, the variability due to time variant and smaller scale processes needs to be removed from the measurements. Previous studies have used a combination of temporal averaging of a long (11 day) timeseries of results, combined with vertical smoothing of the shear and buoyancy data through the application of two triangular filters (Peters et al., 1991, 1988). In calculating the shear, the individual velocity components were first smoothed using an 8 m triangular filter. Vertical shear was then calculated from the smoothed velocity components by first order differencing at 4 m depth intervals and a further 16 m triangular filter was then applied to the resultant vertical shear. The effect of the two triangular filters is a vertical smoothing of the shear on a scale of $\sim$ 21 m (Peters et al., 1991).

The vertical scales of overturning due to turbulent mixing can be estimated from the Thorpe length scale. The Thorpe scale is defined as the root mean square of the vertical displacements required to reorder a measured profile of potential density so that it is gravitationally stable (Johnson and Garrett, 2004; Stansfield et al., 2001; Thorpe, 1977). The Thorpe scale (L_T) is related to the Ozmidov Scale (L_O see Chapter 1), $L_O \approx 0.8 L_T$ (Dillon, 1982). In this thesis the Thorpe scale is preferred to the Ozmidov Scale as it gives an estimate of the vertical scale of turbulent overturning which can be measured directly from the CTD measurements taken by the microstructure profiler for each station. For the observations presented in this thesis the Thorpe length scale is less than 8 m in all cases observed below the seasonal thermocline, except JC29 station 7 at $\sim$ 140 m depth (Figure 3.7, 3.8 and 3.9). This would suggest that averaging the buoyancy data into 8 m depth intervals, for consistency with the ADCP data (Section 3.3.1), should be sufficient to remove the variability from overturning due to turbulent mixing from the shear and buoyancy profiles in nearly all cases.

The relatively short duration of each of the observations in this thesis relative to the inertial or diurnal periods at the observation sites (of order 1 h for observations compared to 14 to 16 h inertial period at latitudes of 60^o and 47^o respectively) means temporal averaging of the measurements will not be sufficient to remove all time variant signals from the data. This suggests that any vertical smoothing filter used in estimating the bulk Richardson number appropriate to mesoscale flow will also be required to remove time variant signals from the raw data. The vertical scale of the mixing patches associated with increased dissipation from breaking inertial frequency internal waves has been observed at ~ 10 m (Gregg et al., 1986). This would suggest that the application of a filter to remove signals with a wavelength less than 25 m, as suggested above, would also remove the variability due to internal waves and time variant processes from the profiles.

Considering the vertical length of the profiles in the dataset, the shortest profile in the full dataset is 80 m (10 data points) in length, while the full dataset has a mean profile length of 152 m (19 data points). As the profiles have an 8 m vertical resolution, this would suggest that a smoothing window of 72 m is the maximum size window that could be applied to all the profiles.

3.3.6.3 Smoothing shear and buoyancy

The filter applied to smooth the buoyancy and shear data (calculated as described above) was a running average filter

$$f_o(i) = \frac{1}{N} \sum_{j=\frac{-(N-1)}{2}}^{\frac{N-1}{2}} f_i(i-j)$$

(Van Gastel and Pelegri, 2004) where $f_i(i)$ is the input function, $f_o(i)$ the output function, N is an odd integer defining the physical size of the smoothing window $N\Delta z$, and Δz is the sampling interval (8 m for the results in this thesis). When applied to vertical profiles of shear and buoyancy, this filter has the effect of removing signals with vertical wavelength smaller than the size of the smoothing window (Van Gastel and Pelegri, 2004).

3.3.7 Fitting to data

Equation 3.5 was fitted to observations of the Richardson number and contemporaneous observations of turbulent viscosity and turbulent diffusivity respectively by considering the parameters α_s, n_s, K_{os} and K_{bs} to be free in each case (free fit). K_{os} was constrained to be within the range 1x10^{-5} to 1x10^{-1} m^2 s^{-1}, α_s, and n_s were constrained to be with the range 1 to 100, and K_{bs} was constrained to be within the range 1x10^{-8} to 1x10^{-3} m^2 s^{-1}. These ranges were chosen to encompass the range of previous values used for these parameters (Table 3.1) and to provide flexibility for the optimizer routine without artificially constraining the fit.

The Richardson number was calculated, as described above, using different sized smoothing windows from 24 m to 72 m in size, for all observations of shear and buoyancy below the mixed layer depth. Observations were fitted to equation 3.5 using a least squares fit (Emery and Thomson, 1997). The least squares fit minimises the sum of the square of the differences between the log of the observed turbulent diffusivities, or viscosities, and the log of the turbulent diffusivities, or viscosities, calculated from equation 3.5 using the parameter set under evaluation. The parameter set and smoothing window combination with the lowest residual sum of squares (hereafter termed the residual) was selected as the best fit.

In addition to the least squares residual, the correlation of determination (R^2) was calculated as a measure of the goodness of fit for the parametrization. The correlation of determination for a fit to data is defined as the ratio of the variance of the fit to the total variance of the observations

$$R^2 = \frac{\sum_{N_k}^{n=1} (K_{fit}(n) - \overline{K_{fit}})^2}{\sum_{N_k}^{n=1} (K_{obs}(n) - \overline{K_{obs}})^2}$$

(Emery and Thomson, 1997) where N_k is the number of observations, $K_{fit}(n)$ is the value of the parametrization and $K_{obs}(n)$ the observation at point n. The overbar represents the mean of all the values.

3.4 Results

3.4.1 The effect of smoothing on the Richardson number

The smoothing filter described in Section 3.3.6.3, was applied to the 8 m vertical resolution shear and buoyancy profiles, calculated as described in Section 3.3, using a range of smoothing windows from 24 m to 72 m in size. Qualitatively the filter appears to perform as expected in removing smaller (than window size) variability from the profiles while preserving the larger scale signal (for example D306 station 179004 in Figure 3.10.

The shear data from the full dataset were tested using a Kolmogorov-Smirnov test (Press et al., 1989) and found to be distributed lognormally (Figure 3.11). The mean value of the shear, calculated from the log transformed shear data, is constant at 1.7 x10^{-3} s^{-1} regardless of the size of the smoothing window applied to the individual profiles. As the smoothing window is increased in size the standard deviation, calculated from the log transformed data, reduces from 1.8 x10^{-3} s^{-1} for the unsmoothed data to less than 1.3 x10^{-3} s^{-1} for smoothing window sizes greater than 40 m (Figure 3.11). Expressed as a percentage of the mean the standard deviation reduces from 120 % in the unsmoothed case to 67 % for a smoothing window of 72 m (Table 3.6).

The N^2 data from the full dataset were tested using a Kolmogorov-Smirnov test (Press et al., 1989) and found to be distributed lognormally (Figure 3.12). The mean value of N^2, calculated from the log transformed data, increases from 1.2 x10^{-5} s^{-2} for the unsmoothed data to 1.5 x10^{-5} s^{-2} for smoothing windows above 56 m in size. The standard deviation is 3.1 x10^{-5} s^{-2} for unsmoothed data, increasing to 3.4 x10^{-5} s^{-2} for smoothing windows of 40 and 56 m, and to 3.5 x10^{-5} s^{-2} for a smoothing window of 72 m (Figure 3.12). Expressed as a percentage of the mean, the standard deviation is greater than 200 % in all cases (Table 3.6).

The Richardson number calculated using equation 3.1 from the 8 m vertical resolution shear and buoyancy data smoothed using smoothing windows from 24 to 72 m in size, as described above, was also tested using a Kolmogorov-Smirnov test (Press et al., 1989) and found to be distributed lognormally (Figure 3.13). The cumulative effect of smoothing both shear and buoyancy data on the Richardson number is to reduce the mean of the Richardson number dataset, calculated from the log transformed data, from 6 for the unsmoothed data to 5 for all smoothing windows above 24 m. The standard deviation, calculated from the log transformed data, reduces from 19 for the unsmoothed data to 8 for all smoothing windows above 40 m (Figure 3.13). Expressed as a percentage of the mean, the standard deviation reduces from 300 % for the unsmoothed data to 149 % for a smoothing window of 72 m (Table 3.6).

3.4.2 Turbulent diffusivity

When equation 3.5 is fitted to all the data for turbulent diffusivity from all three datasets simultaneously, the best fit (lowest residual sum of squares = 122.1) is for a smoothing window of 56 m with corresponding parameter values of $\alpha_s = 1$, $n_s =$ 1.49, $K_{os} = 3.62$ x10^{-4} m^2s^{-1} and $K_{bs} = 8.14$ x10^{-6} m^2s^{-1} (Table 3.7). This gives a parametrization for turbulent diffusivity of

$$K_s \;=\; 3.6\times10^{-4}(1+Ri)^{-1.5} \;+\; 8\times10^{-6} \;\; m^2s^{-1}$$

Observations of turbulent diffusivity from the full dataset were tested using a Kolmogorov-Smirnov test (Press et al., 1989) and found to be distributed lognormally. R^2 calculated for the log transformed results of this parametrization and the log transformed observations was 0.4 (Table 3.7).

In order to assess any potential bias in the parametrization, the distribution of the difference between the log of the observed diffusivity and the log of the diffusivity calculated using the parametrization was calculated for the whole dataset (Figure 3.14). The mean of the distribution is zero with a standard deviation of 0.4, which suggests that there is no consistent bias in the parametrization. Comparing the observations of turbulent diffusivity to the values calculated using the parametrization, 60 % of the calculated values are within a factor of two of the observations (Figure 3.15). The parametrization appears to be representative of the observations of diffusivity across the range of Richardson numbers observed (Figure 3.16).

The parametrization was fitted to the individual datasets smoothed using a 56 m smoothing window on shear and buoyancy. The fit to the D306 and JC29 datasets yields R^2 values of 0.26 and 0.28 respectively which are lower than the R^2 value for fitting to the whole dataset. However, the R^2 value when fitting the parametrization to the D321 dataset is 0.53 which is higher than when fitting to the full dataset (Table 3.8).

Previous studies have commonly used a value of $\alpha_s = 5$ (Table 3.1). In order to assess the impact of fixing $\alpha_s = 5$ equation 3.5 was fitted to the full dataset, as described above, with $\alpha_s = 5$ and the remaining parameters, n_s, K_{os} and K_{bs} free. For all smoothing window sizes the best fit residual for a fit with $\alpha_s = 5$ is 122.6 ($R^2 = 0.39$) which is slightly larger than the best fit residual for the all parameters free fit (Table 3.7). For all sizes of smoothing window, the fit with $\alpha_s = 5$ residual is within 2 % of the equivalent free fit residual (Table 3.9). For all smoothing window sizes and Ri between 1 and 100, values of K_t calculated using the parameters from an $\alpha_s = 5$ fit are within 20 % of the values of K_t calculated using the parameters from the equivalent free fit (Figure 3.17).

K_{bs} is considered to be a constant term representing the diffusivity from processes with a vertical scale smaller than the scales for which the Richardson number is calculated (Section 3.2.2). It is not unreasonable to expect that the the diffusivity from such processes may vary from place to place in the ocean. In an attempt to estimate the likely variability in K_{bs} equation 3.5 was fitted to the three individual data sets, (using a 56 m smoothing window on shear and N^2 as described above) with the values of $\alpha_s = 1$, n_s= 1.49, K_{os} = 3.62 x10^{-4} m^{2}s^{-1}, and only K_{bs} free. Fitting equation 3.5 in this manner gave estimates of K_{bs} for the D306 dataset of 7.5 x10^{-6} m^2 s^{-1} with a least squares residual of 65.8 ($R^2 = 0.27$), for the D321 dataset of 8.5 x10^{-6} m^2 s^{-1} with a least squares residual of 23.8 ($R^2 = 0.51$), and for the JC29 dataset of 1.8 x10^{-5} m^2 s^{-1} with a least squares residual of 31.6 ($R^2 = 0.21$). These values of the residual are within 2 % of the residual values for fitting the full parametrization to the individual data sets (Table 3.8).

3.4.3 Turbulent viscosity

When equation 3.5 is fitted to all the data for turbulent viscosity from all three datasets simultaneously, the best fits do not appear to be representative of the observations (Table 3.10, Figure 3.18). The observations of turbulent viscosity were tested using a Kolmogorov-Smirnov test (Press et al., 1989) and found to be distributed lognormally. Approximating K_v to a constant value of 1x10^{-3} m^{2}s^{-1} (Figure 3.19), the mean of the log transformed observations, gives a least squares residual of 145.7 which is lower than all the residuals from fitting equation 3.5 to observed K_v (Table 3.10).

3.5 Discussion

3.5.1 Appropriateness of the datasets to mesoscale mixing

Direct observations of vertical mixing and Richardson number used in a previous study to derive parametrizations of vertical mixing have been taken exclusively from around the Equator and have focused on the Equatorial Undercurrent (Peters et al., 1988). The range of Ri reported by Peters et al. (1988) varied from 0.1 to $\sim$14, with a large proportion of the observations being for Richardson numbers less than one. The observational data used in this thesis comes from three separate ocean regions, with one dataset taken in the presence of strong mesoscale features (D321), one dataset from a relatively inactive region of the ocean (D306) and one in close proximity to a vigorous frontal system (JC29). Considering the three datasets individually, the D306 and D321 datasets cover broadly the same range of Ri, (1 <

$Ri < 50$) while the JC29 dataset covers a narrower ranger of smaller value Ri ($0.28 < Ri < 10$). The range of Richardson numbers covered by the observations in this thesis, ($1 < Ri < 50$, Section 3.4), is of the same order as reported in previous studies of the Gulf Stream ($3 < Ri < 40$, Pelegri and Csanady 1994) and of the Florida current ($2 < Ri < 20$, Winkel et al. 2002). This would suggest that a parametrization for vertical mixing based on the observations used in this thesis ought to be more broadly representative of mesoscale ocean mixing than the one based on observations of the Equatorial Under Current.

3.5.2 The effects of smoothing

Both the N^2 and shear data appear to be relatively insensitive to the size of the applied smoothing window, with the means of the two distributions approximately constant (within 16 % for N^2) for smoothing window sizes above 24 m (Table 3.6). The reduction in standard deviation for the shear data with increasing smoothing window size, would suggest that there is variability in the profiles occurring at all the scales considered here (between 24 to 72 m vertical length). However, the almost constant mean and standard deviation for the N^2 data would suggest that variability in N^2 is at larger scales than considered here.

The distribution of the Richardson number data follows the characteristics of the shear data with decreasing standard deviation as smoothing window size increases which suggests that the variability in Ri is driven primarily by the variability in the shear (Table 3.10). This is consistent with previous studies which also found Ri to be more sensitive to the smoothing applied to the vertical shear than to the smoothing applied to the density fields (Van Gastel and Pelegri, 2004). The reduction in standard deviation for Ri with increasing size of smoothing window would suggest that for the 8 m vertical resolution profiles considered here there is no obvious scale separation between the vertical scales of the processes producing the variability. Consequently there is no clear indication which size of smoothing window should be preferred for estimating mesoscale bulk Ri.

3.5.3 Turbulent diffusivity

Comparing the values of the parameters $\alpha_s = 1$, $n_s = 1.5$, $K_{os} = 3.6$ x10^{-4} m^{2}s^{-1}, estimated by fitting observations from all datasets to equation 3.5, with those from previous studies (Yu and Schopf, 1997; Pelegri and Csanady, 1994; Peters et al.,

1988) summarised in Table 3.1, n_s is within the range of previous estimates and K_{os} is of the same order of magnitude. However, α_s is lower than the commonly used value of 5 and at the lower limit of the range of values used to constrain the term while fitting (Section 3.3.7) .

Fixing the value of $\alpha_s = 5$ and fitting to observation results in a parametrization where the range of parameter values (for n_s, K_{os} and, K_{bs}) producing the best fits are within the range of values used for these parameters in previous studies (Table 3.1 and 3.9). However, fixing the value of $\alpha_s = 5$ and fitting to observations does not produce a better (lower residual or higher R^2) fit than fitting with all parameters free (Table 3.9). If we consider Ri above 1 then the parametrization where $\alpha_s = 5$ produces estimates of K_t that are within 20 % of those estimates produced by the free fit parametrization, which is within the factor of two accuracy for the free fit parametrization when compared to observations (Figure 3.15). This would suggest that there is little to choose between the two parametrizations. However, the free fit parametrization is preferred as it represents the fit to observations with the lowest residual and highest R^2 value.

The free fit parametrization, presented in Section 3.4.2, produces reasonable fits to the individual datasets with R^2 values for the individual fits better than 65 % of the R^2 for the fit to the full dataset. That the fit to the D321 dataset produces a higher R^2 value than the fit to the full dataset may well be down to serendipity, as the observations from the D321 dataset appear to be more tightly clustered around the parametrization values in the range where $1 < Ri < 10$ (Figure 3.16).

K_{bs} represents the background vertical diffusivity which is driven by processes that occur on vertical scales of less than that used to calculate the Richardson number, in this case 56 m (Section 3.2.2). Vertical mixing resulting from wave-wave interactions of the internal wave field which occurs at the finescale (< 10 m) is known to vary with proximity to topography and with latitude (Gregg et al., 2003; Ledwell et al., 2000; Polzin et al., 1997). Mixing from inertial processes is highly spatially and temporally variable (Gregg et al., 1986; D'Asaro, 1985). This would suggest that in the ocean background vertical diffusivity is likely to vary from place to place and from time to time. The value of K_{bs} derived from fitting equation 3.5 to the full dataset, is of approximately the same magnitude as values that have been used in previous parametrizations (Table 3.2) and close to estimates of the open ocean value of vertical mixing from wave-wave interactions of the internal wave field (7 x 10^{-6} m^2 s^{-1} Polzin et al. 1995). Estimating K_{bs} for the individual datasets results in values of K_{bs} from 7.5 x10^{-6} m^2 s^{-1} for the D306 dataset to 1.8x10^{-5} m^2 s^{-1} for the JC29 dataset.

However in all cases the residual for the parametrization with the dataset-specific K_{bs} is within 2 % of the residual for fitting the parametrization with the whole dataset value of K_{bs} = 8x10^{-6} m^{2}s^{-1}. This would suggest that the value of K_{bs} derived from the full dataset is not unreasonable as a value of background vertical mixing and that the full parametrization of turbulent diffusivity is robust and generally applicable.

3.5.4 Turbulent viscosity

The fitting of equation 3.5 to observations of turbulent viscosity has been somewhat less successful, with the observations not appearing to be consistent with the form of the relationship (Figure 3.18). This may be due to dissipation from small scale processes, such as internal wave shear, being present in the observations. An underlying assumption when using equation 3.6 is that the vertical scale of the shear used in the calculation of turbulent viscosity is of the same order as the vertical scale of the shear generating the observed turbulent kinetic energy dissipation (Section 3.3.3).

From the data used in this thesis it is not possible to determine whether internal wave shear is significant in the production of the observed dissipation. Finescale internal wave shear occurs at vertical scales that are smaller than it is possible to resolve using the 8 m depth interval ADCP data in this thesis (Section 3.3.6). However, closer investigation of the D321 dataset suggests that internal wave shear may be a contributor to the observed dissipation in at least some cases (Chapter 2) and the JC29 dataset was taken in an area suspected to have elevated levels of internal wave activity due to close proximity to the Kerguelen Plateau (Park et al., 2008). This would suggest a high degree of uncertainty in the observations of turbulent viscosity which would make fitting a parametrization problematic.

3.5.5 Comparison to previous parametrizations of diffusivity

Comparing the observations used in this thesis to the estimations of vertical turbulent diffusivity from previous parametrizations (Large et al., 1994; Peters et al., 1988; Pacanowski and Philander, 1981) shows that for the range of Richardson numbers covered by the observations, calculated using a smoothing window of 56 m, all of the previous parametrizations underestimate the vertical turbulent diffusivity observed (Figure 3.20).

The quality of the estimations of vertical turbulent diffusivity from previous parametrizations was quantitatively compared to observations by calculating a 'residual' as the sum of the squares of the difference between the log transformed observations and the log transformed estimates of diffusivity from the previous parametrization. This residual is directly comparable to the residual for the fitted parametrization presented in this thesis as described in Section 3.3.7. The residual calculated by comparing the parametrization of Pacanowski and Philander (1981) to the observations (using a 56 m smoothing window for Ri) in this thesis is 234, when comparing the parametrization of Large et al. (1994) the residual is 419, and when comparing the parametrization of Peters et al. (1988) the residual is 1625. Changing the size of the smoothing window changes the residuals when comparing the previous parametrizations, but in no case is the residual from a previous parametrization smaller than the residual for the parametrization presented in this thesis (Table 3.11). Hence the parametrization derived in this thesis provides a better fit to observations than previous parametrizations.

The majority of the observations (73 %) are for Richardson numbers in the range of 1 to 10, with very few (~ 3 %) being for Richardson numbers less than 1 (Figure 3.20). However, the parametrization derived in this thesis is consistent with the parametrizations of Large et al. (1994) and Pacanowski and Philander (1981) for values of Richardson number higher than 20 (Figure 3.20). This would suggest that the parametrization presented here is best suited for use with all values of the Richardson numbers greater than one. Despite using values of Richardson number of greater then 0.25 in deriving the parametrization (Section 3.3) the scarcity of observations in the range $0.25 < Ri < 1$ makes any application of the parametrization to this range of Ri tentative.

3.5.6 Comparison to previous parametrizations of viscosity

Comparing the observations of viscosity used in this thesis to the estimations of vertical turbulent viscosity from previous parametrizations (Large et al., 1994; Peters et al., 1988; Pacanowski and Philander, 1981) shows that for the range of Richardson numbers covered by the observations calculated using a smoothing window of 56 m, none of the previous parametrizations appear to represent the observations (Figure 3.21).

The residual when comparing the parametrization of Pacanowski and Philander (1981) to the observations of turbulent viscosity (using a 56 m smoothing window for

Ri) in this thesis is 575, when comparing the parametrization of Large et al. (1994) the residual is 648, and when comparing the parametrization of Peters et al. (1988) the residual is 2225. Hence none of the previous parametrizations of turbulent viscosity represent the observations better than a constant turbulent viscosity of $1\text{x}10^{-3}$ m^2s^{-1}. Changing the size of the smoothing window changes the residuals when comparing the previous parametrizations, but in no case is the residual from comparing a previous parametrization smaller than the residual for a constant turbulent viscosity (Table 3.12).

3.6 Conclusions

The Richardson number parametrization for turbulent diffusivity developed in this thesis (equation 3.5) was based on observations of turbulent diffusivity from three separate ocean regions (Section 3.3.1). The parametrization is intended to provide an estimation of vertical turbulent diffusivity in stratified shear flow that is more applicable to mesoscale ocean features, such as eddies, fronts and boundary currents, than previous parametrizations (Large et al., 1994; Peters et al., 1988; Pacanowski and Philander, 1981) based on data from the Equatorial Undercurrent. This parametrization is considered to be most applicable to values of the Richardson number greater than one.

The observations of turbulent viscosity reported here are found to be best represented by a constant turbulent viscosity of $1\text{x}10^{-3}$ m^2s^{-1}. This may well be due to the turbulent dissipation from small scale processes, e.g. internal wave shear, representing a significant part of the observed turbulent dissipation for some, if not all, observations. The presence of significant amounts of turbulent dissipation from small scale processes invalidates the calculation of turbulent viscosity (equation 3.6). Unfortunately there is no method of determining to what degree small scale processes contribute to the observed dissipation.

Turbulent viscosity			Turbulent diffusivity			Reference.
α	n	K_{os} (m^2 s^{-1})	α	n	K_{os} (m^2 s^{-1})	
5	1.5	5 x10^{-4}	5	2.5	5 x10^{-4}	Peters et al. (1988)
			10	1.5	2.6 x10^{-3}	Pelegri and Csanady (1994)
5	2	50 x10^{-4}	5	3	50 x10^{-4}	Yu and Schopf (1997)

Table 3.1: Constants used in the turbulent mixing / Richardson number parametrizations of the form of equation 3.4 from the literature.

Turbulent viscosity (m^2 s^{-1})	Turbulent diffusivity (m^2 s^{-1})	Reference
2 x10^{-5}	1 x10^{-6}	Peters et al. (1988)
1 x10^{-4}	1 x10^{-5}	Large et al. (1994)
1 x10^{-4}	1 x10^{-5}	Yu and Schopf (1997)

Table 3.2: Constants used for the background turbulent viscosity and turbulent diffusivity in parametrizations from the literature.

Station number	Date	Position (deg. min.)	Number of Casts	Maximum depth of profile (m)
177004	25/06/06	48º 50N 16º 30W	14	233
177009	26/06/06	48º 50N 16º 30W	6	225
178005	27/06/06	48º 50N 16º 29W	10	209
178006	27/06/06	49º 02N 16º 26W	6	225
179004	28/06/06	49º 02N 16º 09W	7	225
181008	30/06/06	49º 00N 16º 27W	11	241
182004	01/07/06	48º 50N 16º 30W	10	265
182009	01/07/06	48º 52N 16º 30W	19	281
183008	02/07/06	48º 50N 16º 30W	5	289
184006	03/07/06	48º 51N 16º 30W	7	281
185004	04/07/06	48º 50N 16º 31W	7	289
186005	05/07/06	48º 50N 16º 30W	7	289
187005	06/07/06	48º 50N 16º 30W	10	273
187008	06/07/06	48º 50N 16º 30W	7	273
188004	07/07/06	48º 50N 16º 30W	10	265

TABLE 3.3: Summary of turbulence stations for UK RSS Discovery cruise D306 to Porcupine Abyssal Plane Jun. to Jul. 2006.

Station number	Date	Position (deg. min.)	Number of Casts	Maximum depth of profile (m)
16222	02/08/07	58° 50N 19° 51W	10	141
16226	05/08/07	58° 50N 21° 00W	10	152
16232	06/08/07	59° 01N 21° 00W	10	139
16241	09/08/07	59° 52N 19° 37W	10	135
16242	09/08/07	59° 52N 20° 07W	12	130
16247	10/08/07	59° 56N 20° 26W	10	138
16260	12/08/07	59° 10N 19° 08W	10	134
16269	13/08/07	59° 12N 19° 28W	9	133
16283	16/08/07	59° 36N 20° 38W	10	139
16285	18/07/07	59° 41N 18° 42W	11	134
16286	19/08/07	59° 17N 19° 47W	10	129
16288	20/08/07	59° 30N 19° 02W	10	204
16289	20/08/07	59° 26N 19° 16W	10	138
16292	20/08/07	59° 22N 19° 26W	10	133
16295	20/08/07	59° 18N 19° 40W	10	130

Table 3.4: Summary of turbulence stations for UK RSS Discovery cruise D321 to the Iceland Basin July to Aug. 2007.

Station number	Date	Position (deg. min.)	Number of Casts	Maximum depth of profile (m)
7	13/11/08	46º 31S 71º 55E	10	163
11	14/11/08	46º 33S 71º 54E	6	195
22	20/11/08	45º 19S 65º 47E	8	195
29	24/11/08	43º 49S 68º 27E	9	195
43	29/11/08	46º 59S 74º 37E	7	195
48	30/11/08	47º 32S 74º 09E	8	195
55	02/12/08	47º 39S 71º 15E	8	203
67	06/12/08	45º 32S 72º 35E	9	235
69	07/12/08	38º 04S 42º 19E	8	195

Table 3.5: Summary of turbulence stations for UK RSS James Cook cruise JC29 to the Southern Ocean Nov. to Dec. 2009.

Smoothing window (m)	Shear (x10^{-3} s^{-1})		N^2(x10^{-5} s^{-2})		Ri	
	Mean ±S.D.	S.D. (as % of mean)	Mean ±S.D.	S.D. (as % of mean)	Mean ±S.D.	S.D. (as % of mean)
0	1.5 ± 1.8	120	1.25 ± 3.13	250	5.88 ± 19.36	329
24	1.7 ± 1.4	83	1.32 ± 3.25	245	5.1 ± 9.51	188
40	1.7 ± 1.3	75	1.39 ± 3.36	241	5.1 ± 8.41	165
56	1.7 ± 1.2	70	1.46 ± 3.43	235	5.2 ± 8.01	154
72	1.7 ± 1.1	67	1.53 ± 3.47	227	5.3 ± 7.91	149

TABLE 3.6: The effects of different size smoothing windows on the distribution of shear, N^2 and Ri data. Mean and standard deviation are calculated from the log transformed data.

Smoothing (m)	α_s	n_s	K_{os} (m^2 s^{-1})	K_{bs} (m^2 s^{-1})	residual	R^2
0	8	1	6.02 x10^{-4}	15.38 x10^{-6}	147.6	0.27
24	12.18	1	1.46 x10^{-3}	7.51 x10^{-6}	127.68	0.38
40	11.44	1	1.54 x10^{-3}	5.72 x10^{-6}	123.22	0.39
56	1	1.49	3.62 x10^{-4}	8.14 x10^{-6}	122.09	0.4
72	1	1.55	4.02 x10^{-4}	9.02 x10^{-6}	127.01	0.39

TABLE 3.7: Results of fitting equation 3.5 to observations of K_T using different sized windows to vertically smooth observed shear and buoyancy. The residual is calculated from the log transformed data as described in Section 3.3.7. The least squares residuals for fitting extant parametrizations of turbulent diffusivity to the observations in this thesis for a range of smoothing window sizes from 24 m to 72 m are given in table Table 3.11.

Smoothing window 56 m						
Dataset	α_s	n_s	K_{os} (m^2 s^{-1})	K_{bs} (m^2 s^{-1})	residual	R^2
D306	1	1.49	3.62 x10^{-4}	8.14 x10^{-6}	65.87	0.26
D321	1	1.49	3.62 x10^{-4}	8.14 x10^{-6}	23.86	0.53
JC29	1	1.49	3.62 x10^{-4}	8.14 x10^{-6}	32.34	0.28

TABLE 3.8: Results of calculating the residual from comparing equation 3.5, using the best fit parameters for α_s, n_s, K_{os}, and K_{bs}, derived from fitting to the whole dataset, to observations of K_T from the individual datasets. A smoothing window of 56 m was used to vertically smooth observed shear and buoyancy. The residual is calculated from the log transformed data as described in Section 3.3.7.

Smoothing (m)	α_s	n_s	K_{os} (m^2 s^{-1})	K_{bs} (m^2 s^{-1})	residual	R^2
0	5	1	$4x10^{-4}$	$14.8x10^{-6}$	147.1	0.26
24	5	1	$6x10^{-4}$	$6.7x10^{-6}$	126.88	0.38
40	5	1.04	$8x10^{-4}$	$5.88x10^{-6}$	122.6	0.39
56	5	1.06	$9x10^{-4}$	$5.84x10^{-6}$	124.39	0.39
72	5	1.11	$1x10^{-3}$	$6.74x10^{-6}$	129.58	0.37

TABLE 3.9: Results of fitting equation 3.5 to observations of K_T using different sized windows to vertically smooth observed shear and buoyancy. Parameter α_s is fixed at 5 and the remaining parameters allowed to vary as described in Section 3.3.7. The residual is calculated from the log transformed data as described in Section 3.3.7.

Smoothing (m)	α_s	n_s	K_{os} (m^2 s^{-1})	K_{bs} (m^2 s^{-1})	residual	R^2
0	1	1	5.12 x10^{-3}	1 x10^{-5}	751.99	0.68
24	1	1	4.24 x10^{-3}	1.1 x10^{-5}	321.31	0.7
40	1	1	4.11 x10^{-3}	1.2 x10^{-5}	252.26	0.69
56	1	1	4.08 x10^{-3}	1.2x10^{-5}	224.09	0.66
72	1	1	4.05 x10^{-3}	1.2 x10^{-5}	215.82	0.62

TABLE 3.10: Results of fitting equation 3.5 to observations of K_v using different sized windows to vertically smooth observed shear and buoyancy. The residual is calculated from the log transformed data as described in Section 3.3.7.

Smoothing window (m)	Least squares residual for fitting to observations		
	Pacanowski and Philander (1981)	Peters et al. (1988)	Large et al. (1994)
0	215	1485	391
24	218	1522	400
40	225	1576	408
56	234	1625	419
72	246	1675	426

Table 3.11: Least squares residual for fitting the parametrizations of Large et al. (1994), Peters et al. (1988) and Pacanowski and Philander (1981) to the observations of turbulent diffusivity in this thesis for a range of smoothing window sizes from 24 m to 72 m. The residual is calculated from the log transformed data as described in Section 3.5.5.

Smoothing window (m)	Least squares residual for fitting to observations		
	Pacanowski and Philander (1981)	Peters et al. (1988)	Large et al. (1994)
0	877	2700	952
24	622	2267	700
40	586	2226	662
56	575	2225	648
72	575	2242	646

Table 3.12: Least squares residual for fitting the parametrizations of Large et al. (1994), Peters et al. (1988) and Pacanowski and Philander (1981) to the observations of turbulent viscosity in this thesis for a range of smoothing window sizes from 24 m to 72 m. The residual is calculated from the log transformed data as described in Section 3.5.5.

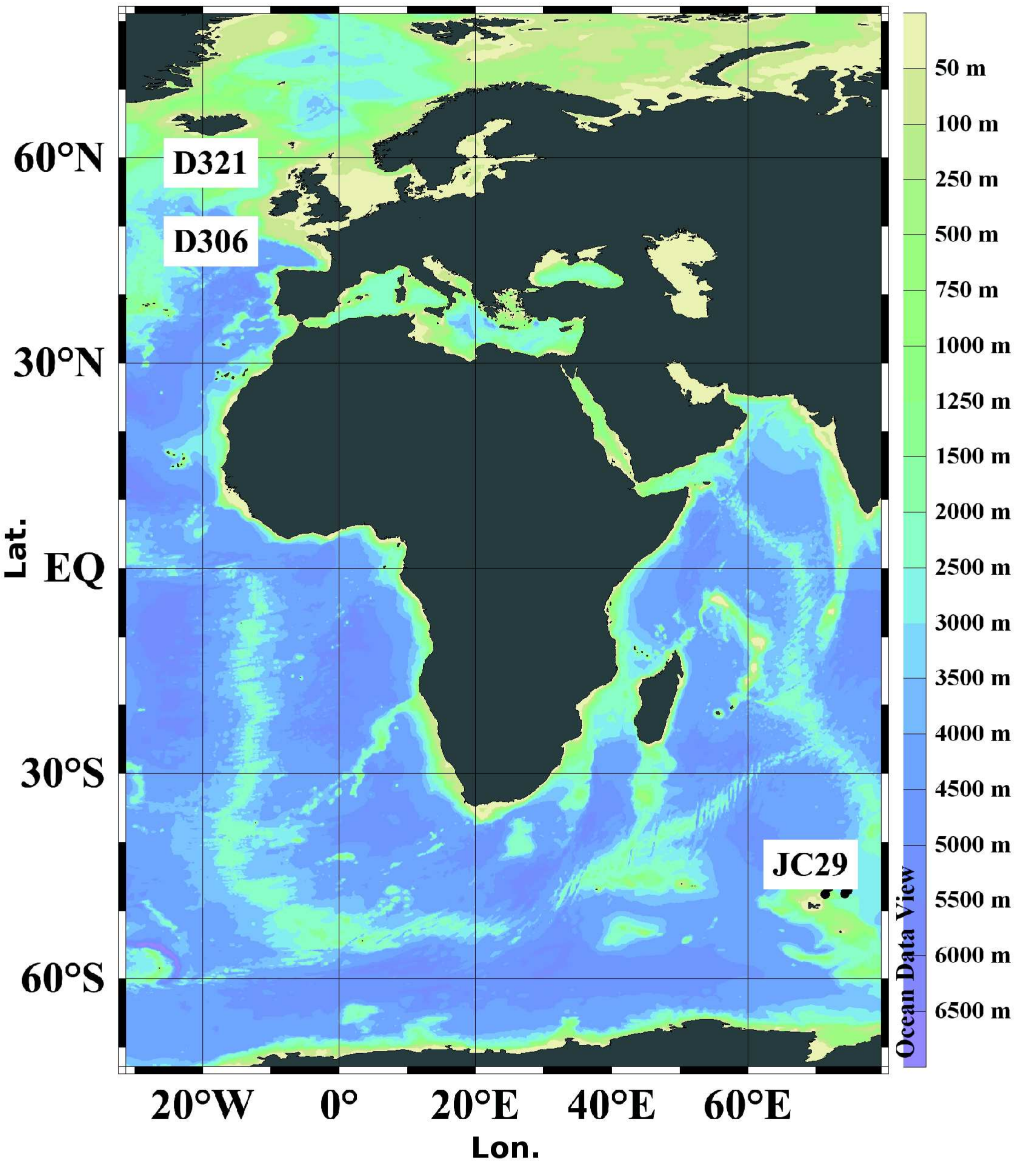

FIGURE 3.1: The locations of the three sets of turbulence measurements used in this thesis. Measurements were made as part of UK RSS Discovery cruise D306 to the Porcupine Abyssal Plane Jun. to Jul. 2006, UK RSS Discovery cruise D321 to the Iceland Basin Jul. to Aug. 2007,and UK RSS James Cook cruise JC29 to the Southern Ocean Nov. to Dec. 2009. Colour indicates water depth.

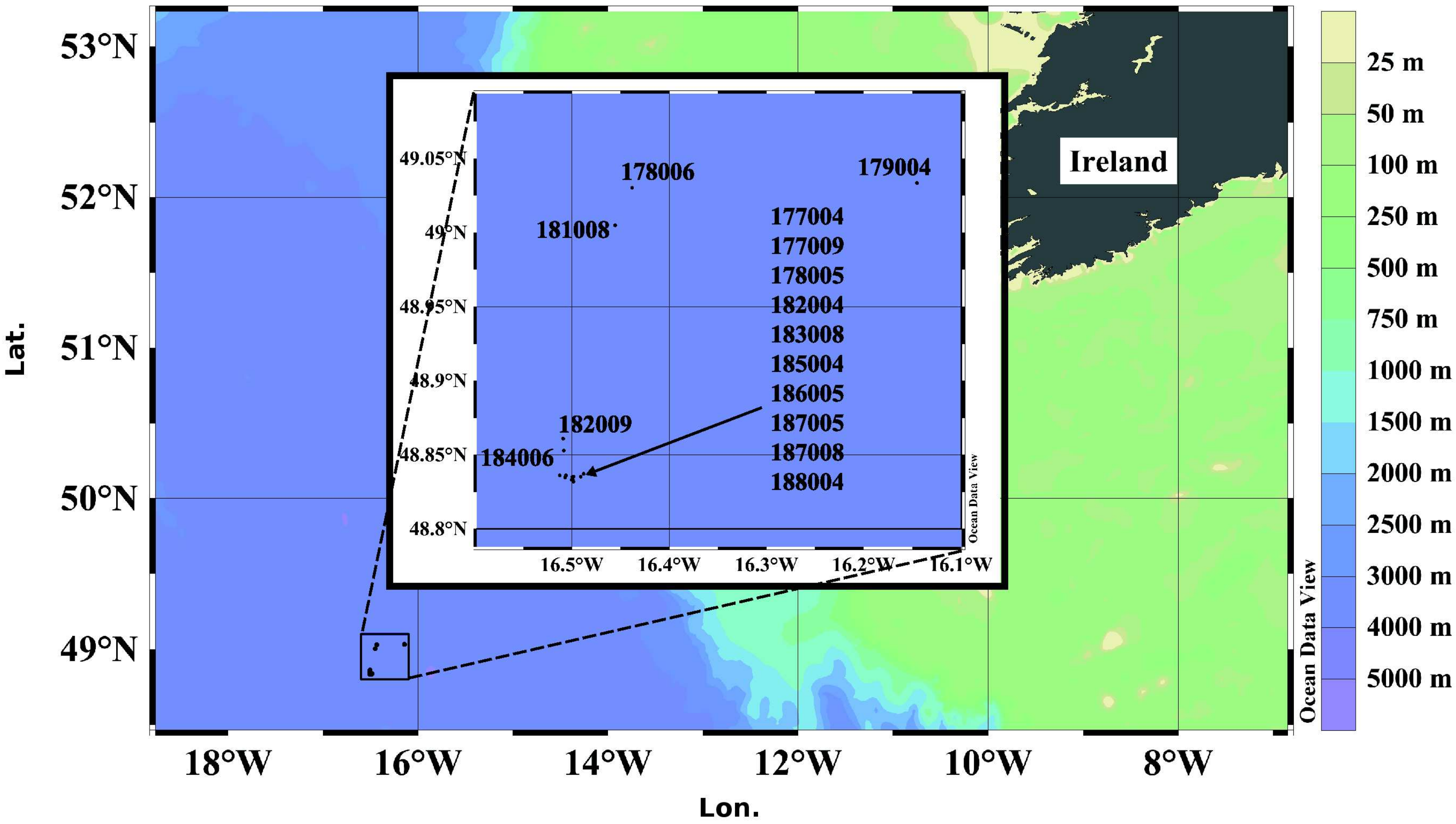

FIGURE 3.2: The position of the stations where turbulence measurements were taken as part of UK RSS Discovery cruise D306 to Porcupine Abyssal Plane Jun. to Jul. 2006. Colour indicates water depth.

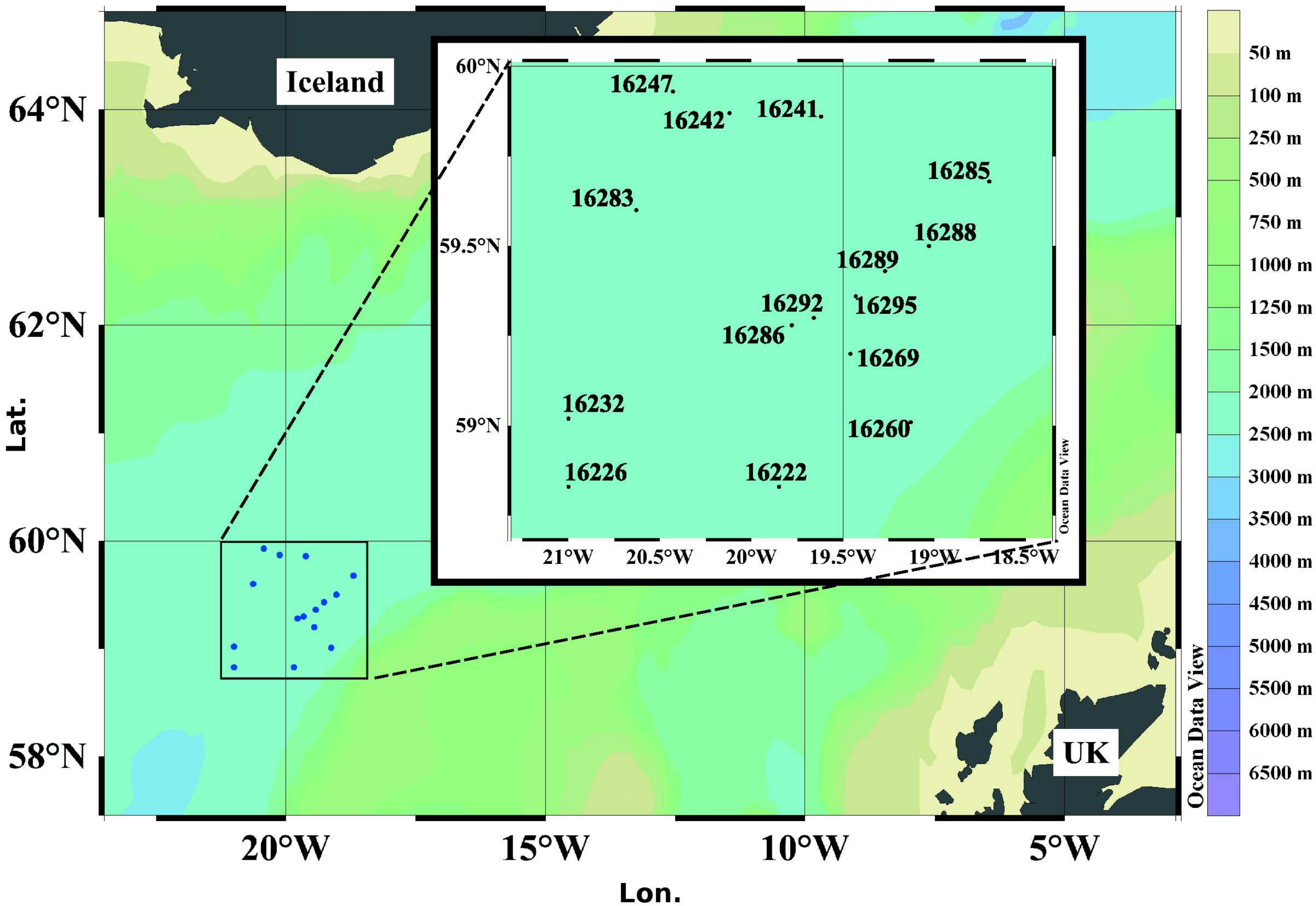

FIGURE 3.3: The position of the stations where turbulence measurements were taken as part of UK RSS Discovery cruise D321 to the Iceland Basin July to Aug. 2007. Colour indicates water depth.

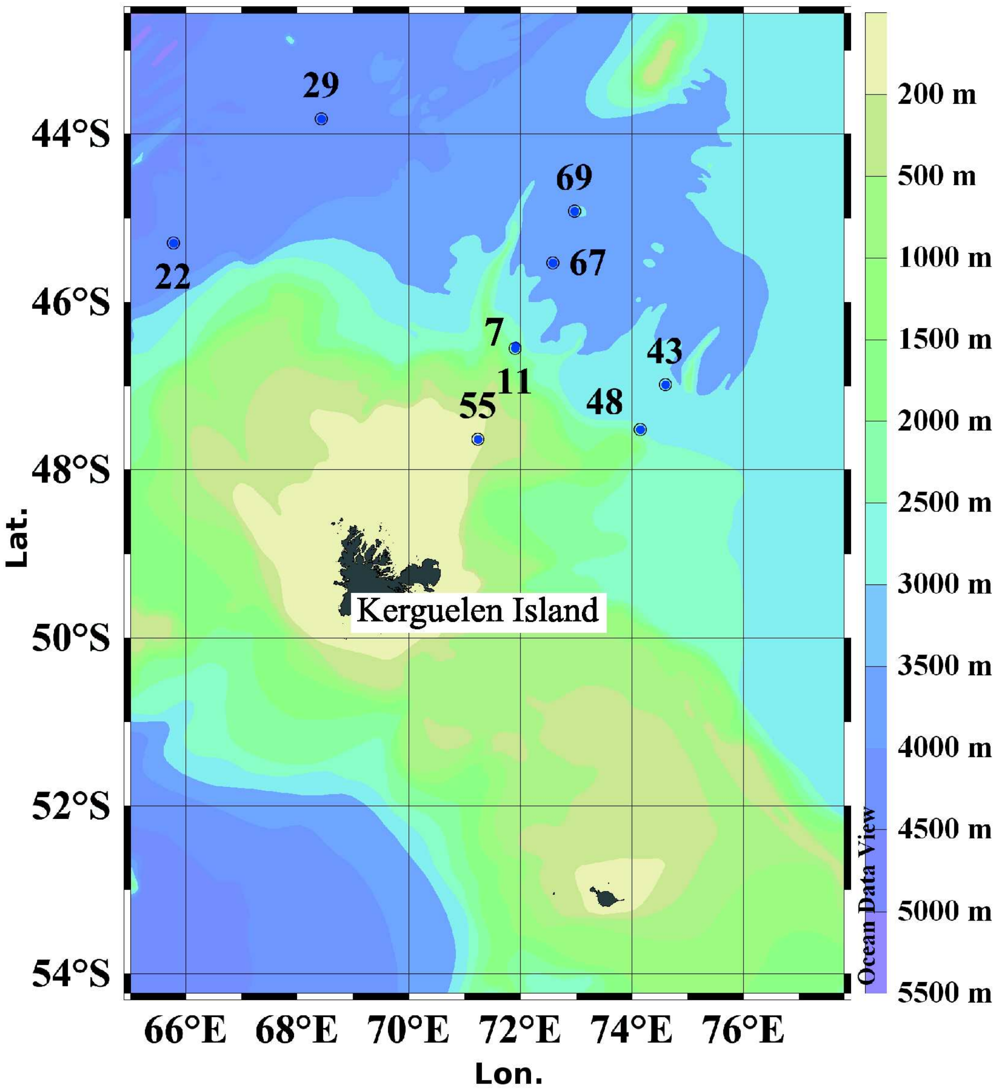

FIGURE 3.4: The position of the stations where turbulence measurements were taken as part of UK RSS James Cook cruise JC29 to the Southern Ocean Nov. to Dec. 2009. Colour indicates water depth.

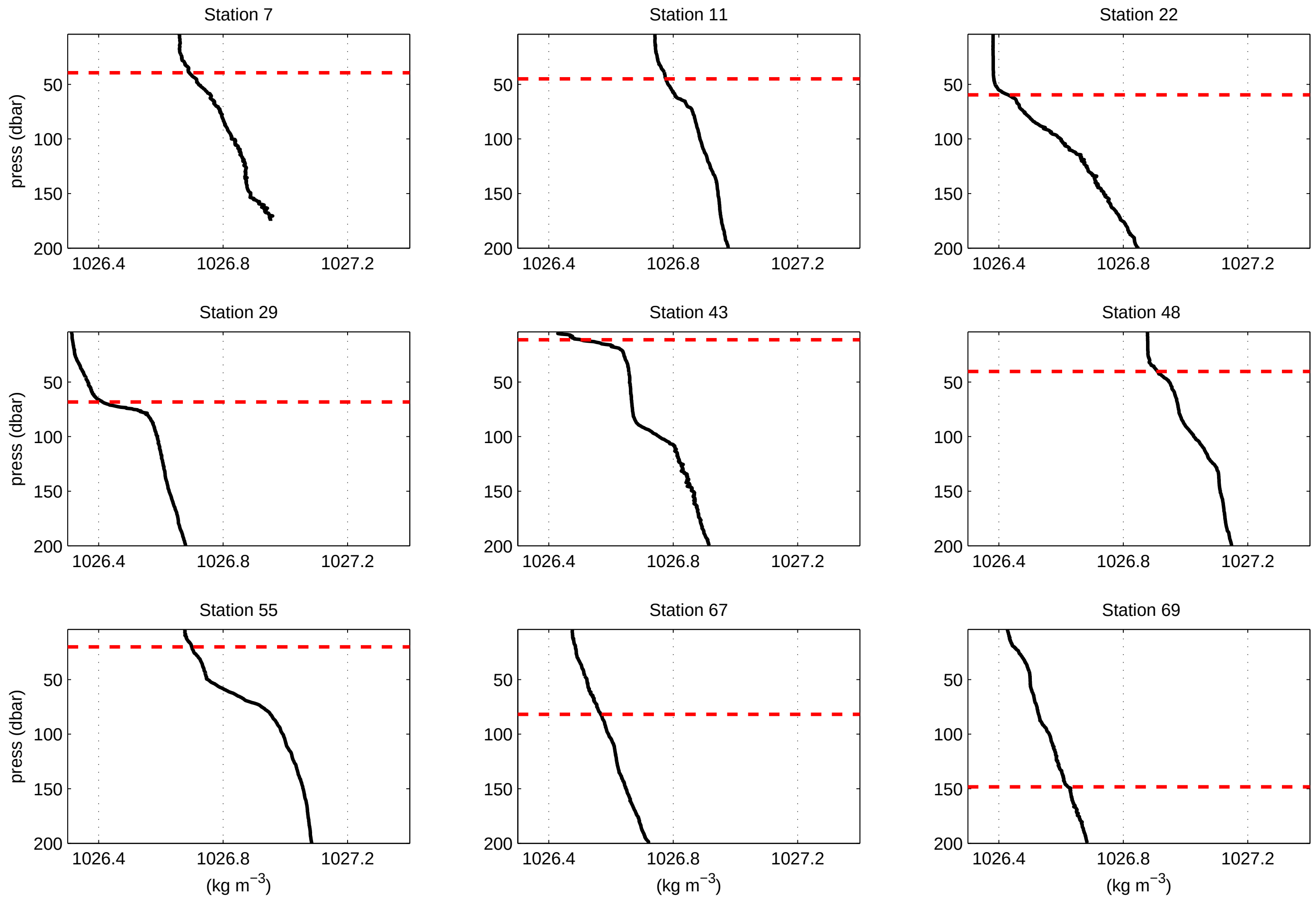

FIGURE 3.5: Profiles of density calculated using CTD measurements from the turbulence profiler for all stations where turbulence measurements were taken as part of UK RSS James Cook cruise JC29 to the Southern Ocean Nov to Dec 2009. The mixed layer depth, calculated as described in Section 3.3.2, is marked in red. For the location of turbulence stations see Figure 3.4.

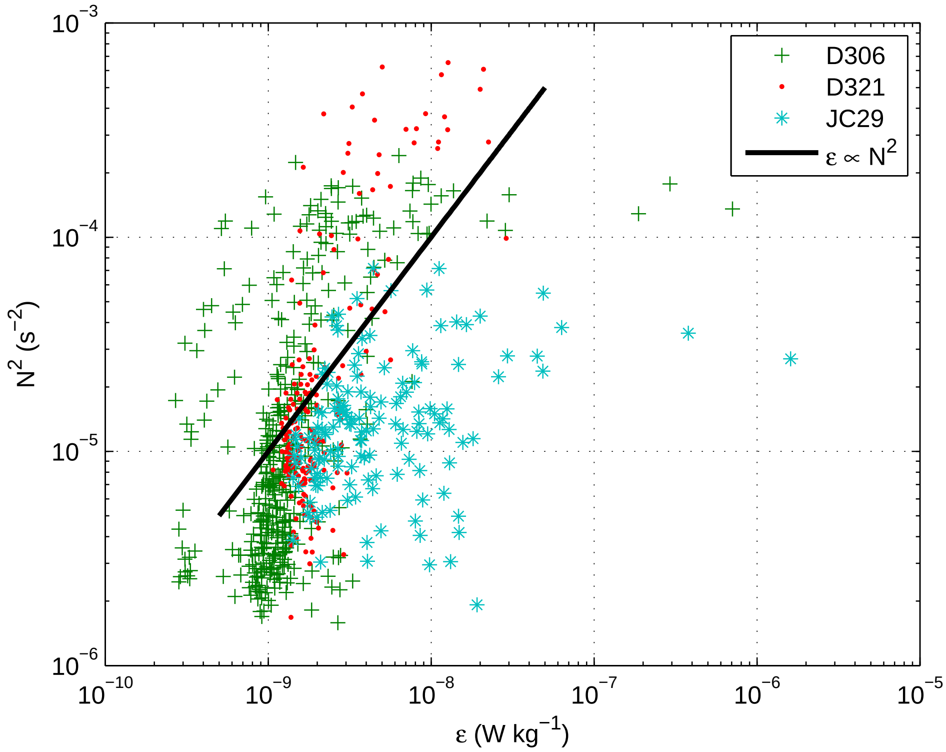

FIGURE 3.6: Scatter plot of N^2 vs turbulent kinetic energy dissipation (ε) for observations from the full dataset. The black line indicates $\varepsilon \propto N^2$.

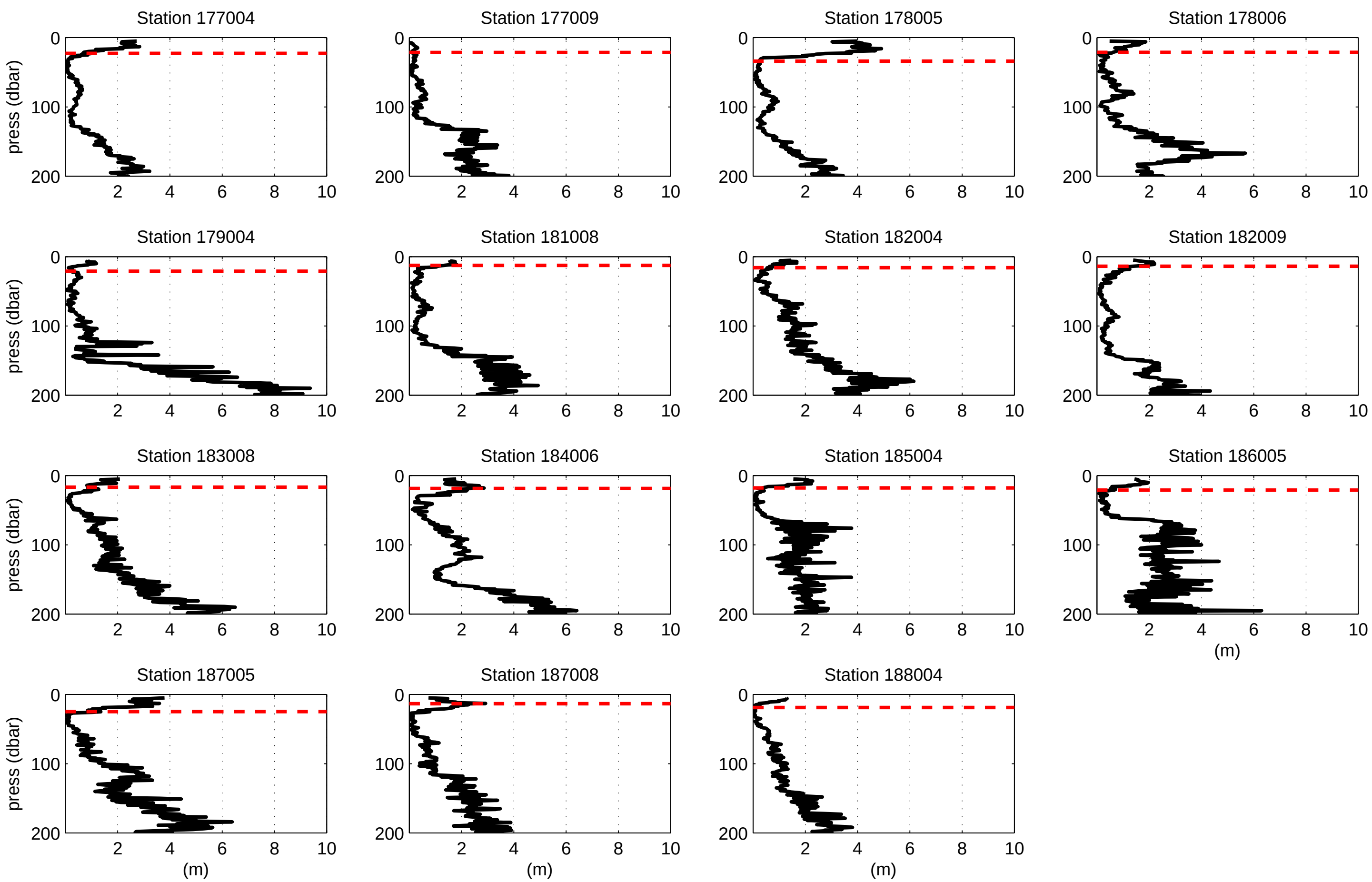

FIGURE 3.7: The Thorpe length scale calculated for turbulence stations of UK RSS Discovery cruise D306. The mixed layer depth for each station, calculated as described in Section 3.3.2, is marked in red. For the location of turbulence stations see Figure 3.2.

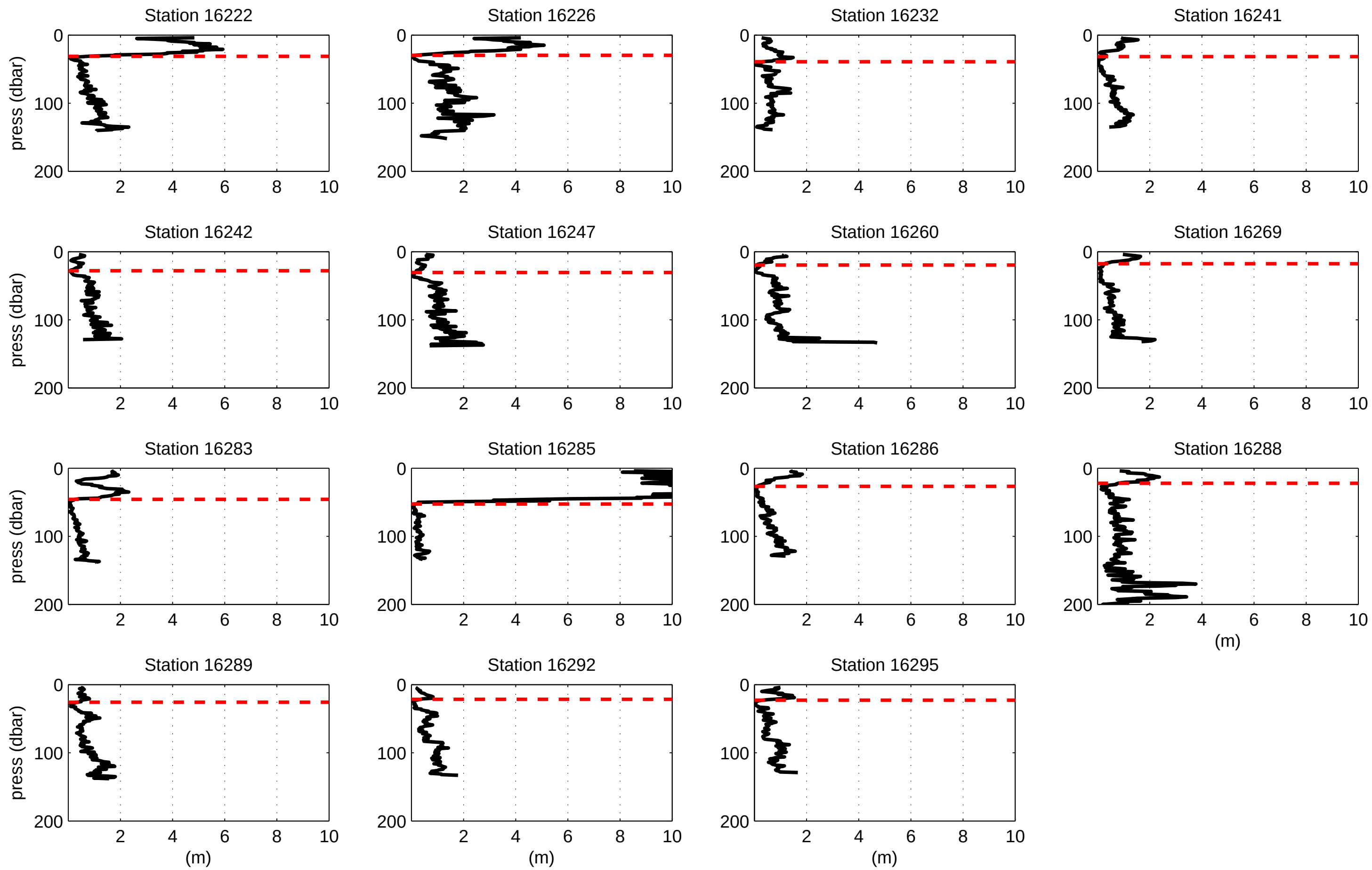

FIGURE 3.8: The Thorpe length scale calculated for turbulence stations of UK RSS Discovery cruise D321. The mixed layer depth for each station, calculated as described in Section 3.3.2, is marked in red. For the location of turbulence stations see Figure 3.3.

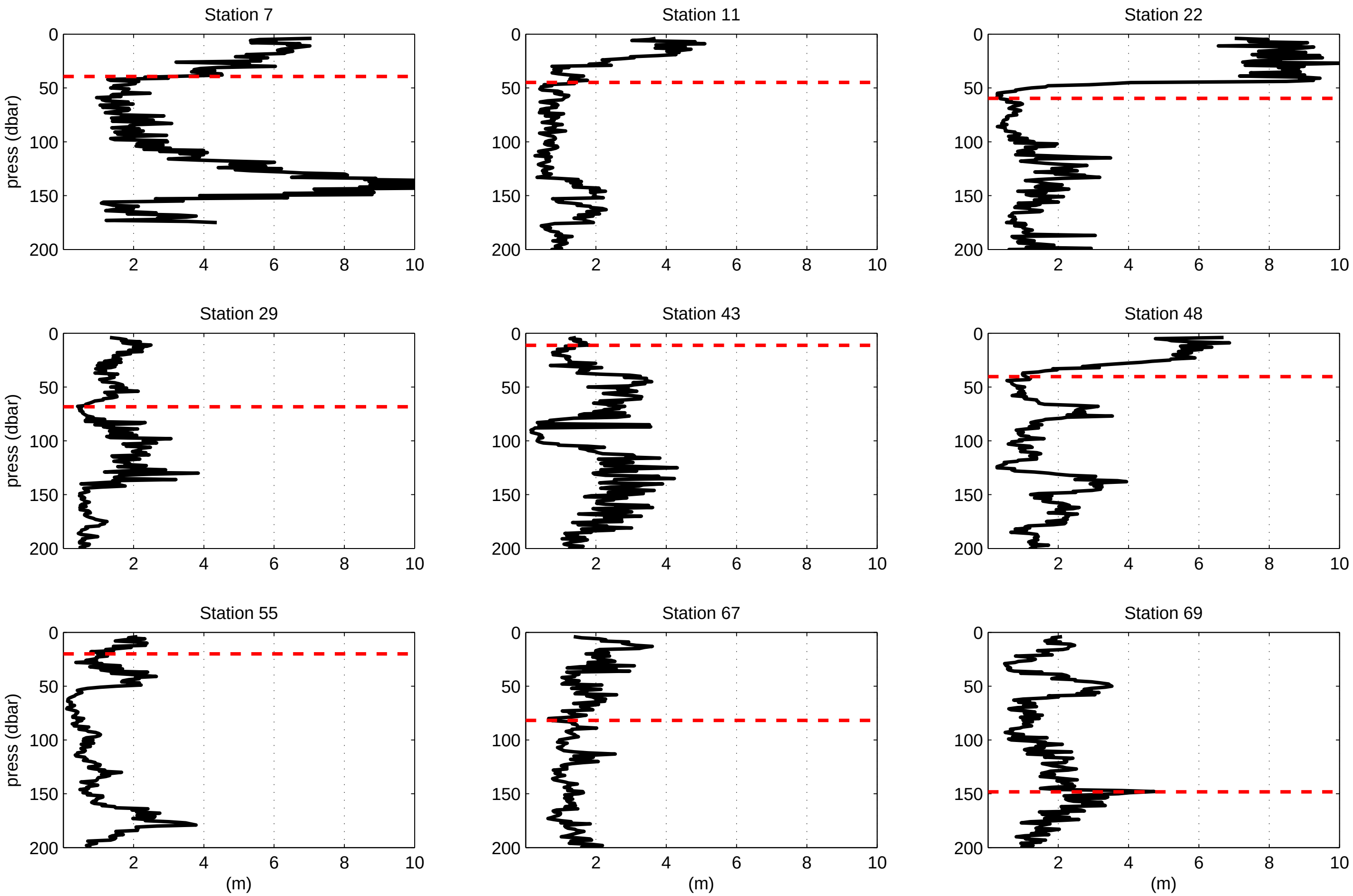

FIGURE 3.9: The Thorpe length scale calculated for turbulence stations of UK RSS James Cook cruise JC29. The mixed layer depth for each station, calculated as described in Section 3.3.2, is marked in red. For the location of turbulence stations see Figure 3.4.

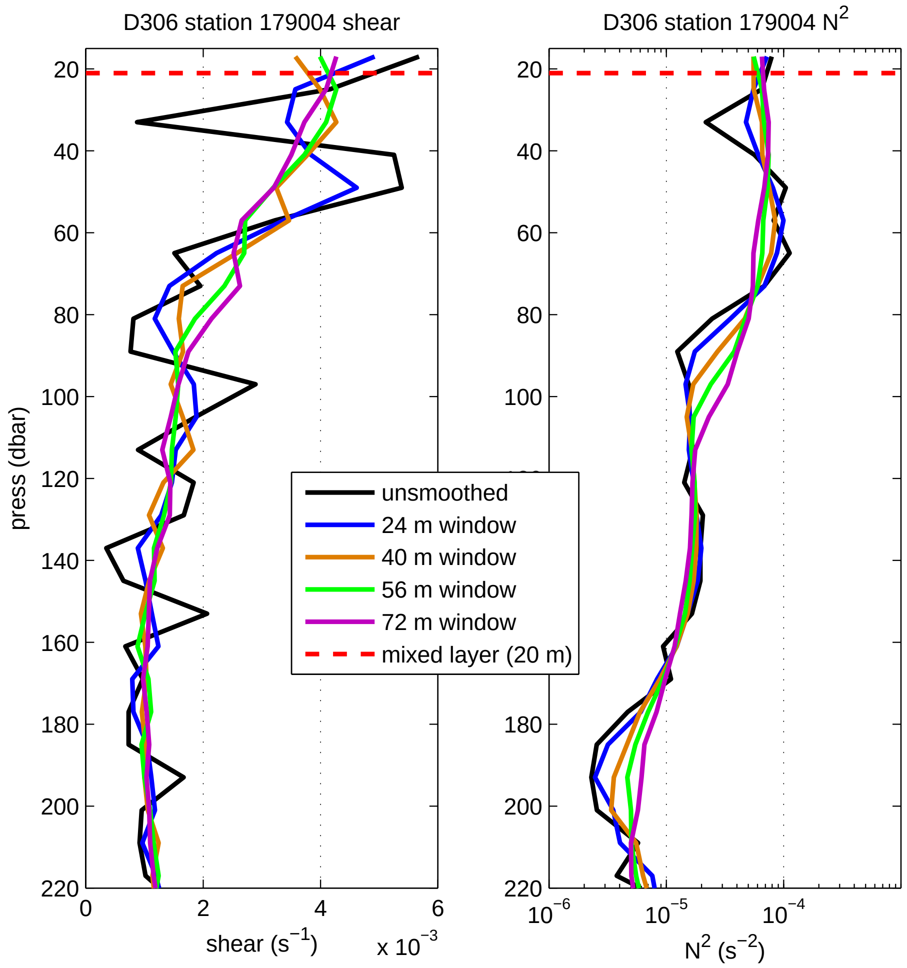

FIGURE 3.10: The effect of applying different sized smoothing windows to the profiles of vertical shear for station 179004 from cruise D306. Unsmoothed shear is shown in solid black, 56 m smoothing window shear is shown in solid green. The mixed layer depth for the station calculated as described in Section 3.3.2 is marked as a dashed red line.

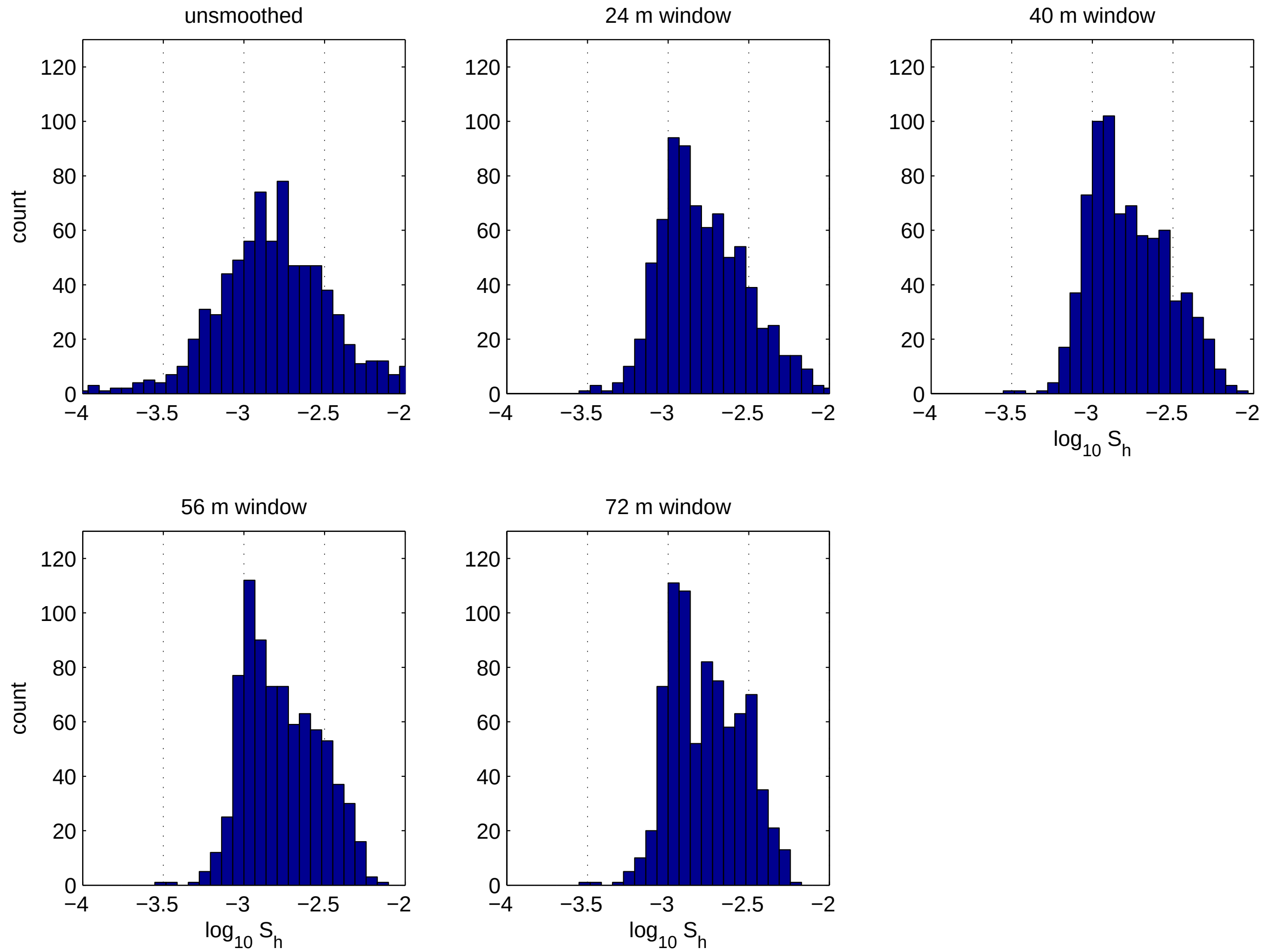

FIGURE 3.11: The distribution of the log transformed shear values. The shear was calculated as described in Section 3.3.4 using different sized smoothing windows from 24 m to 72 m. Values of the log transformed shear were grouped into thirty even sized bins with midpoints from -4 to -2.

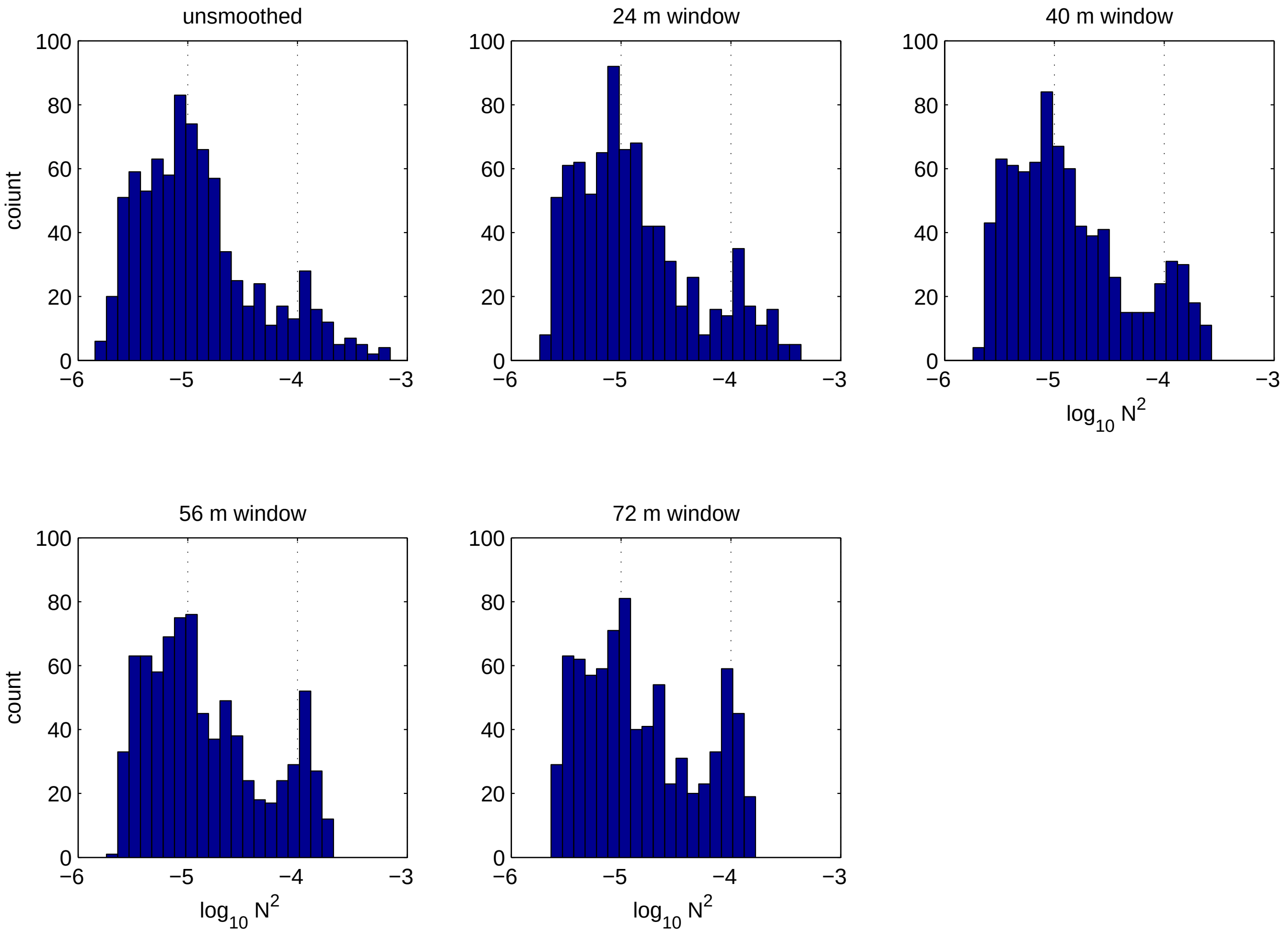

FIGURE 3.12: The distribution of log transformed N^2. $N^2$was calculated as described in Section 3.3.5 using different sized smoothing windows from 24 m to 72 m. Values of log transformed N^2 were grouped into thirty even sized bins with midpoints from -6 to -3.

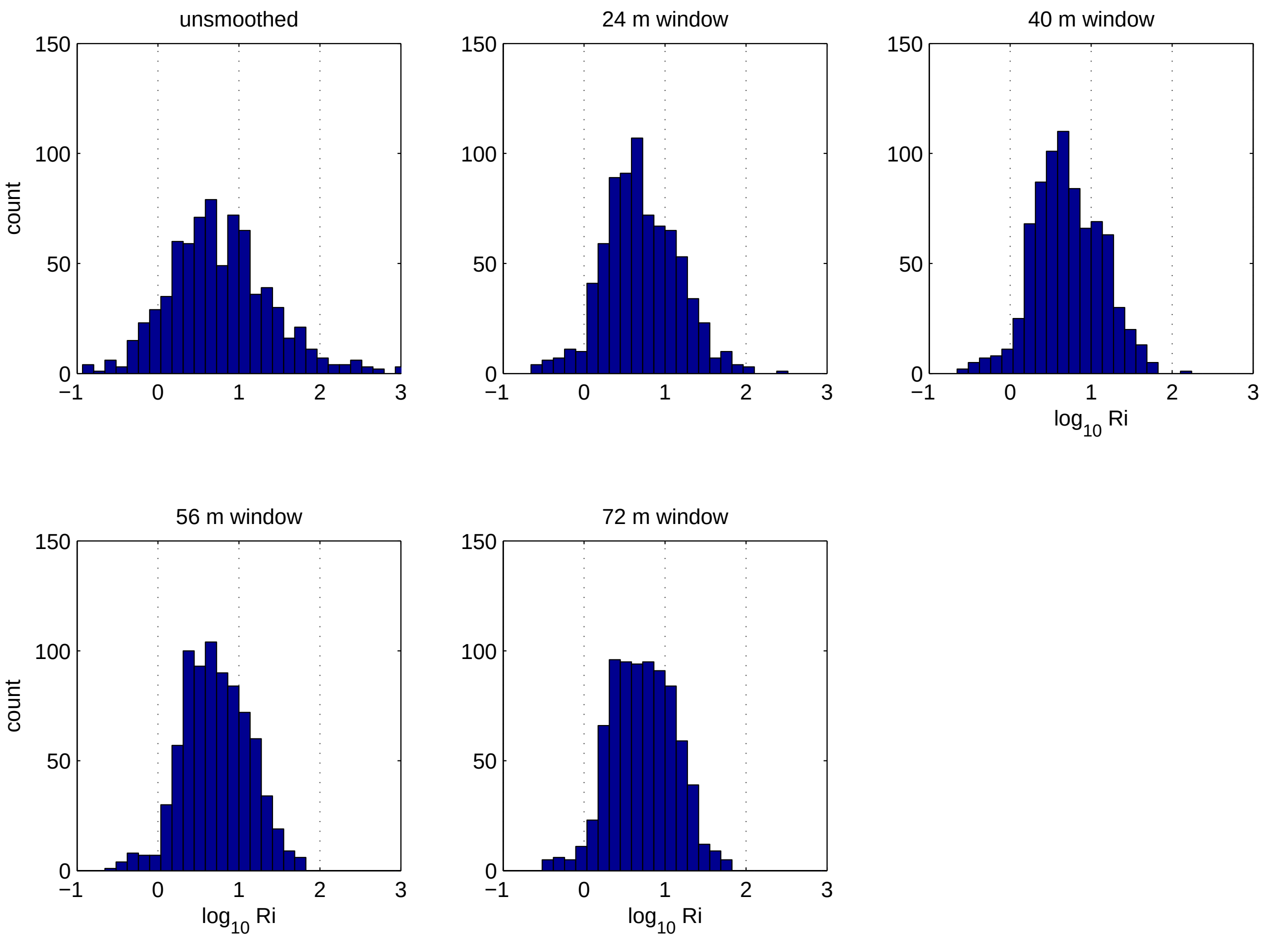

FIGURE 3.13: The distribution of log transformed Ri. Ri was calculated as described in Section 3.3.6 using different sized smoothing windows from 24 m to 72 m on buoyancy and shear profiles. Values of log transformed Ri were grouped into thirty even sized bins with midpoints from -6 to -3.

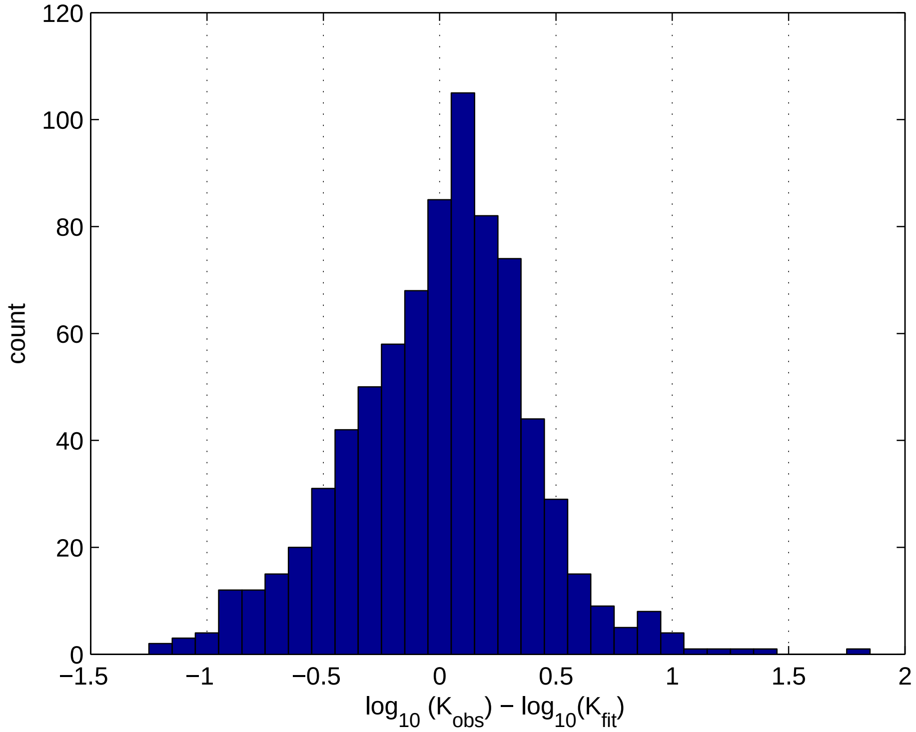

FIGURE 3.14: The distribution of the difference of the log transformed observations of K_t and the log transformed values of K_t calculated using equation 3.5 with the parameters given in Section 3.4.2 . The mean of the distribution is zero.

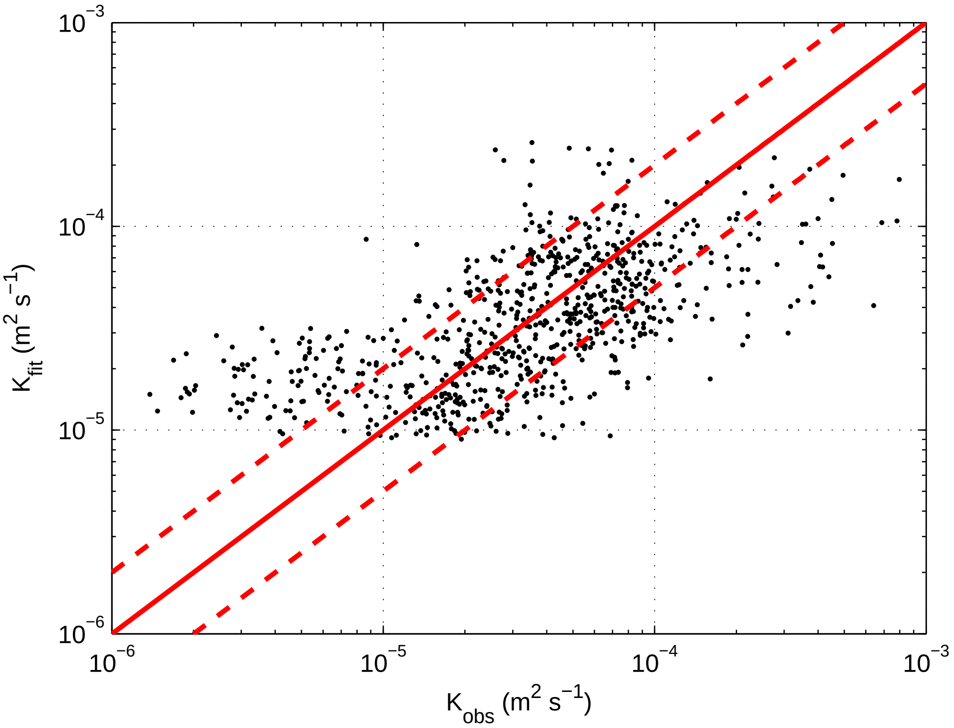

FIGURE 3.15: Scatter plot of turbulent diffusivity (K_{fit}) calculated from equation 3.5 vs observed turbulent diffusivity (K_{obs}) for the same Richardson number. The solid red line plotted is 1:1 and the dashed red lines are 1:0.5 and 1:2 respectively.

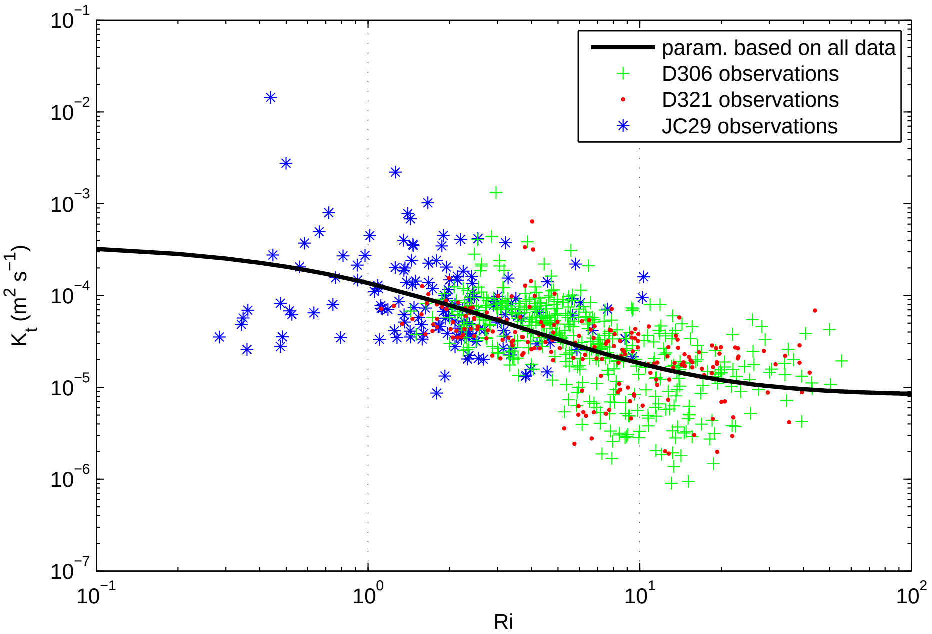

FIGURE 3.16: Turbulent diffusivity (K_t) calculated from equation 3.5 using the best fit parameters given in Section 3.4.2 plotted for Richardson number in the range of 0 to 100. Observations of turbulent diffusivity from the three individual datasets used in the derivation of equation 3.5 are marked.

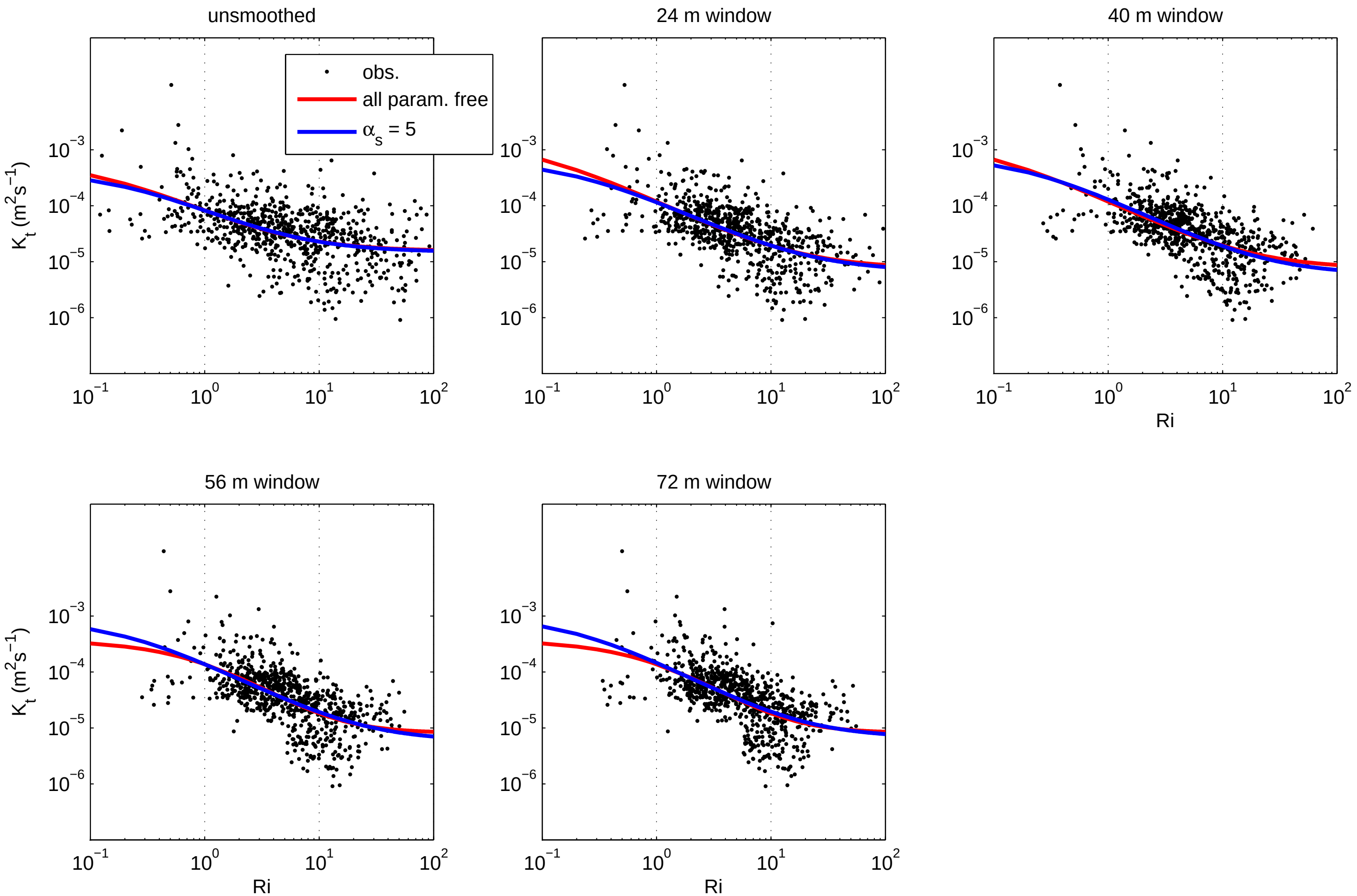

FIGURE 3.17: Comparison of the parametrizations estimated with all parameters free (red line) to those where $\alpha = 5$ (blue line). Ri is calculated as described in Section 3.3.6 using a range of smoothing windows. Observations from the full dataset are marked.

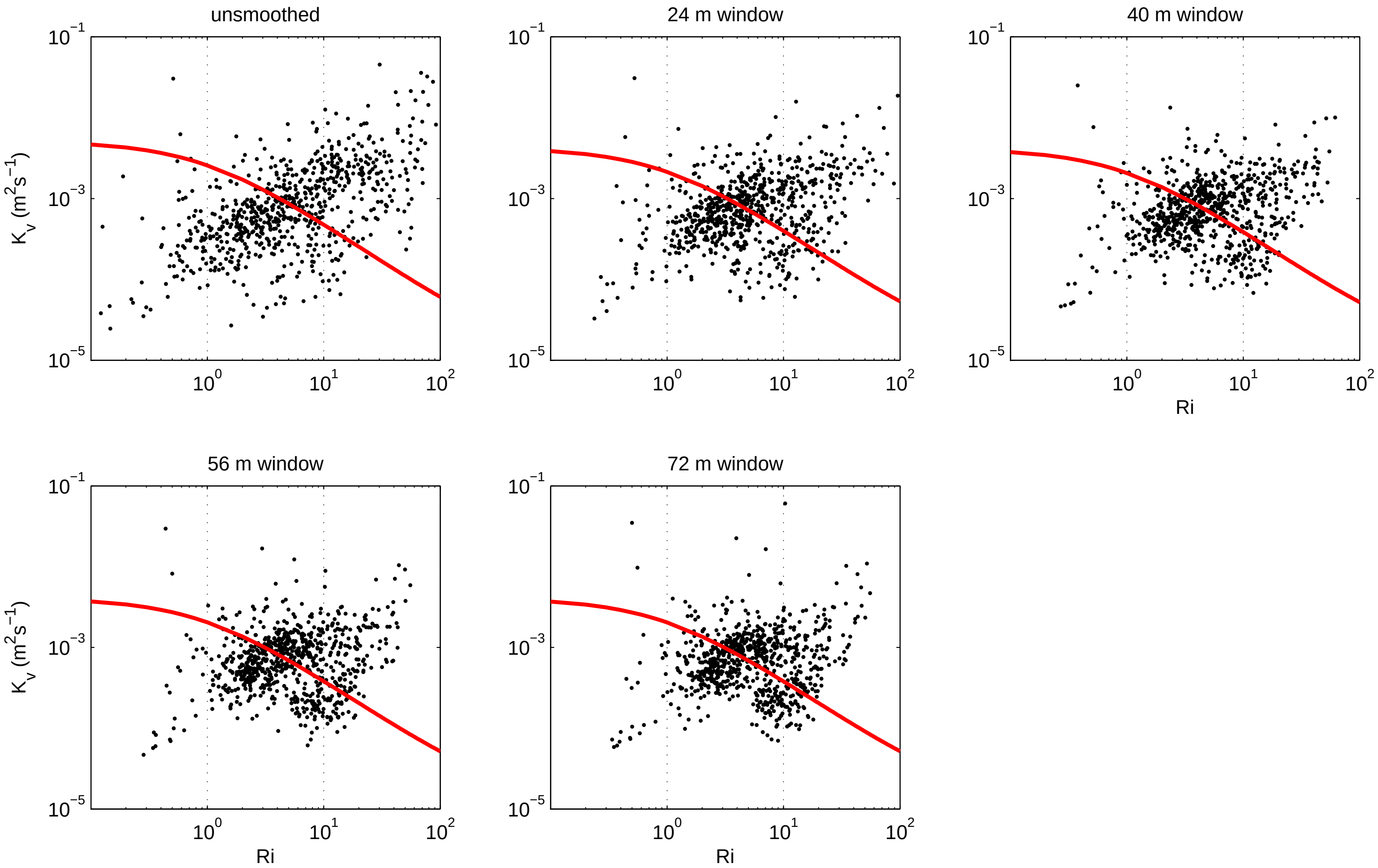

FIGURE 3.18: Best fit parametrizations estimated from all observations of turbulent viscosity (K_v) and Ri calculated using a range of smoothing windows (as described in Section 3.3.6) Observations from the full dataset are marked.

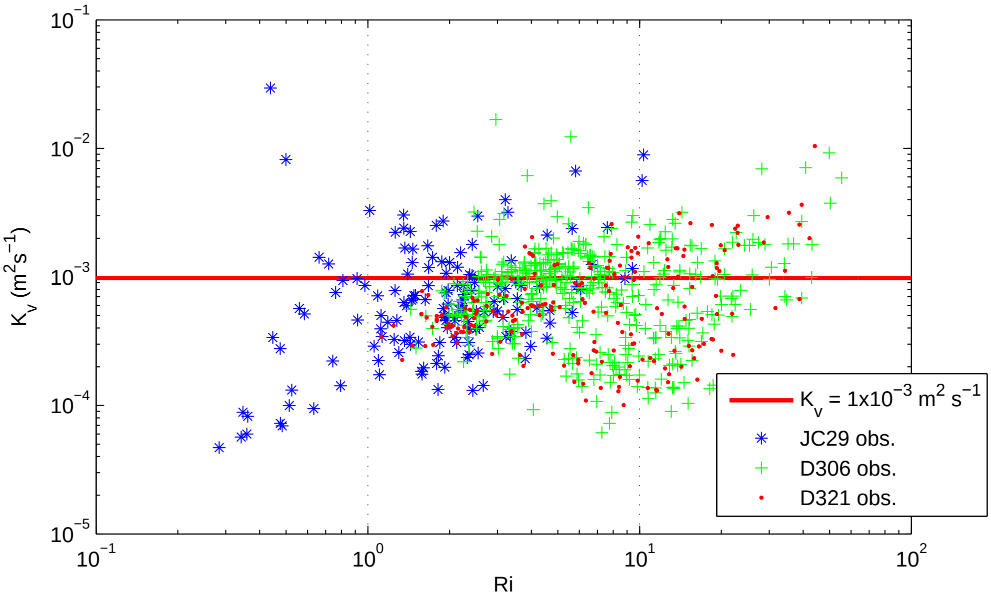

FIGURE 3.19: Observations for turbulent viscosity (K_v) plotted against Richardson number, calculated with a vertical smoothing window of 56 m applied to the buoyancy and shear (Section 3.3.6). The lognormal mean of the observations is shown in red.

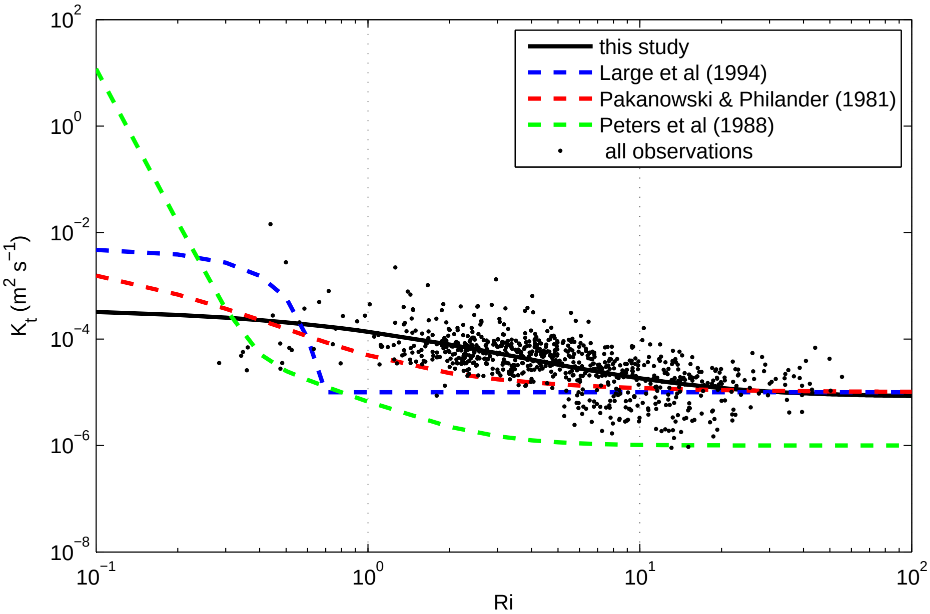

FIGURE 3.20: Turbulent diffusivity (K_t) calculated from equation 3.5 and the parametrizations of Large et al. (1994), Peters et al. (1988) and Pacanowski and Philander (1981) plotted for Richardson number in the range of 0 to 100. Observations of turbulent diffusivity from the three datasets used in the derivation of equation 3.5 are marked.

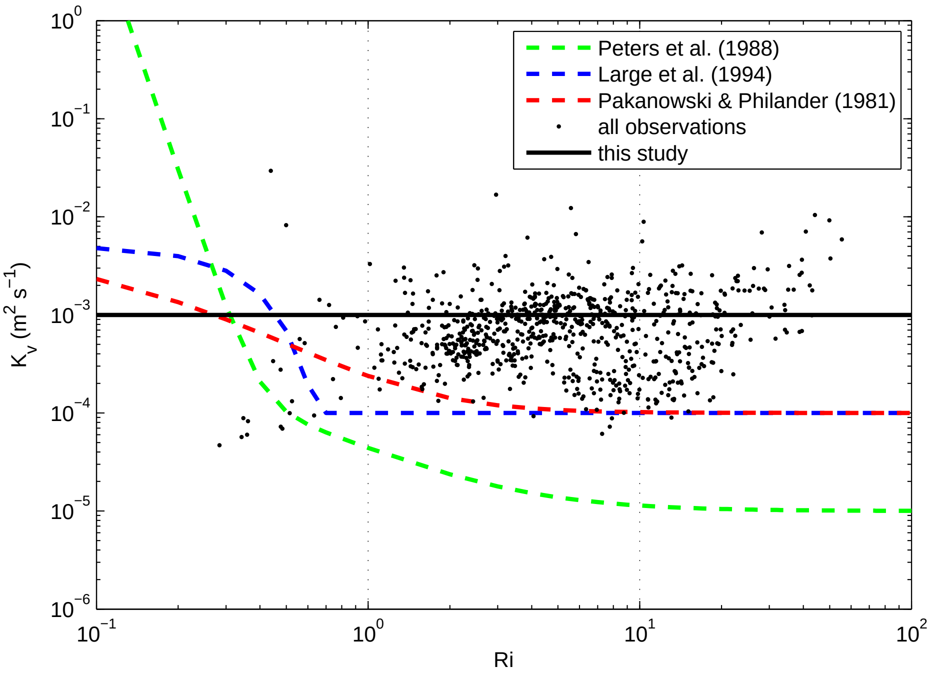

FIGURE 3.21: Turbulent viscosity (K_v), represented as a constant 1x10^{-3} m^2 s^{-1} and calculated from the parametrizations of Large et al. (1994), Peters et al. (1988) and Pacanowski and Philander (1981) plotted for Richardson number in the range of 0 to 100. Observations of turbulent viscosity from the three datasets are marked.

Chapter 4

Modelling a mode-water eddy.

4.1 Introduction

Eddies are potentially of most significance to the vertical supply of nutrient in the oligotrophic sub-tropical gyre where mode-water eddies are often observed to be associated with high production in the Sagrasso Sea (McGillicuddy et al., 2007; Sweeney et al., 2003; McNeil et al., 1999). For consistency with previous studies (Martin and Richards, 2001; Ledwell et al., 2008), and to include potential Ekman-suction effects (Chapter 1) a mode-water eddy is studied in isolation. Focussing on a single isolated eddy will enable a clearer diagnosis of the vertical fluxes, specifically the processes driving any observed vertical flux.

The object of this chapter is to describe the 3D circulation model of an idealised mode-water eddy. The model of the mode-water eddy is used to examine whether there is a shear enhancement to the vertical diffusive flux of nutrients that is driven by the interactions of the eddy and the wind (Chapter 5). The model mode-water eddy is constructed using the Harvard Ocean Prediction System (HOPS) using a Richardson number based parametrization of vertical mixing (Chapter 3).

4.2 Observations

The mode-water eddy model is constructed from observations made in the Iceland Basin of the mode-water component of the eddy dipole (Chapter 2). The observations from the Iceland Basin contain not only measurements of turbulent diffusivity but also high spatial resolution data for hydrography and circulation using both CTD and ADCP. Despite eddies not being of the same potential significance to nutrient supply in the Iceland Basin as in the sub-tropical gyre, the physical characteristics of mode-water eddies in the Iceland Basin appear to be similar to the physical characteristics of mode-water eddies found elsewhere in the North-Atlantic (Chapter 1). The physical characteristics used in the construction of the eddy model include, the vertical density profile within the eddy core, the radius of the eddy, the eddy maximum azimuthal velocity and the vertical velocity profile of the eddy.

4.2.1 An eddy in the Iceland Basin

The observations of a mode-water eddy reported below were taken as part of UK RSS Discovery cruise D321 to the Iceland Basin in August 2007 (See Chapter 2 for a fuller description of the cruise). On arrival at the survey site it was found that within the survey area was an eddy dipole, consisting of a surface cyclonic eddy and an anti-cyclonically rotating mode-water eddy (Chapter 2 Figure 2.2).

During a three week period, the eddy dipole was mapped using conductivity, temperature, depth measurements (CTD) from a combination of towed vehicle (Sea-Soar, maximum depth of $\sim$ 400 m) and conventional full depth ($\sim$ 2900 m) and partial depth ($\sim$ 1000 m) vertical profiles. Horizontal current velocities down to $\sim$ 300 m depth were measured using a ship-mounted 150 kHz RDI acoustic doppler current profiler (ADCP) as described in Chapter 2.

Three surveys of the eddy dipole were carried out; survey one from 5$^{\text{th}}$ August 2007 to 10$^{\text{th}}$ August 2007 using a combination of Sea-Soar with ADCP, survey two from 10$^{\text{th}}$ August 2007 to 15$^{\text{th}}$ August 2007 using conventional CTD with ADCP and survey three from 15$^{\text{th}}$ August 2007 to 22 August 2007 again using ADCP with Sea-Soar (Allen, 2007).

The positions and core diameters of the two eddies were estimated for each survey using the velocities calculated from ADCP data by least squares fitting of the ADCP data, for each depth interval, to a velocity profile of the form

$$V(r) \;=\; V_0\left(\frac{r}{R}\right)\exp\left[\frac{1}{2}\left(1-\frac{r^2}{R^2}\right)\right] \tag{4.1}$$

(Martin and Richards, 2001) where $V(r)$ is the azimuthal velocity at radius r from the eddy centre, V_0 is the maximum azimuthal velocity, and R is the radius of maximum azimuthal velocity (see Chapter 2). The estimated positions and sizes of the eddy cores, calculated as a the mean of all ADCP depth intervals (from 11 to 300 m), for all three surveys, is given in Table 4.1.

In contrast to surveys one and three, survey two was the only survey using CTD to depths potentially able to map the full vertical extent of the mode-water eddy core. Mode-water eddy cores typically extend to depths of $\sim$ 1000 m in the Iceland Basin (Chapter 1). Plotting the ADCP estimated eddy core positions for survey two shows that five CTD stations 16272 to 16277 along 19.8° W transected the mode-water eddy core, with CTD station 16274 (14th August 2007, 59.21° N 19.9° W) in the core itself (Figure 4.1). The section passes through the eddy core but is $\sim$ 15 km from the centre of eddy as estimated from the ADCP velocity (Figure 4.1). The CTD transect from stations 16272 to 16277 was preferred to the transect comprising CTD stations 16265 to 16271 as the transect between CTD stations 16265 to 16271 also passes through the core of the cyclonic eddy (Figure 4.1). The close proximity of the cyclonic eddy core to the mode-water eddy core will distort the isopycnals on one side of the mode-water eddy core. Hence the transect between CTD stations 16265 to 16271 will not give as accurate picture of the mode-water eddy density structure as the transect between CTD stations 16272 to 16277.

The mode-water eddy core is revealed in Figure 4.2 as a 780 m thick pycnostad centred on the 27.36 kg m^{-3} σ_o isopycnal at 550 m depth approximately delimited by the 27.3 and 27.4 kg m^{-3} σ_o isopycnals, where σ_o is defined as the potential density calculated with respect to 0 dbar pressure using the UNESCO equation of state (UNESCO, 1980), minus 1000 kg m^{-3} (Gill, 1982). This large homogeneous lens of water distorts the isopycnals around it bowing those above it upward and bowing those below downward (Figure 4.2). Along the section from station 16257 to station 16251, which is away from the eddy dipole (Figure 4.1) the 27.3 and 27.4 kg m^{-3} σ_o isopycnals, are 279 $\pm$ 28 m apart (mean $\pm$ standard deviation). This would suggest that in the transect of the eddy core (Figure 4.2 and 4.4) the core is approximately delimited by station 16272 (27.3 and 27.4 kg m^{-3} σ_o isopycnals displacement 228 m) and station 16277 (27.3 and 27.4 kg m^{-3} σ_o isopycnals displacement 260 m) giving an upper limit to the horizontal width for the eddy of $\sim$ 90 km.

Fitting to ADCP data and averaging across all three ADCP surveys (Table 4.1) yields peak azimuthal velocity for the mode-water eddy core of 0.29 $\pm$ 0.06 m s^{-1} at a radius of 23 $\pm$ 4 km. This gives an estimated period of rotation for the mode-water eddy $\sim$ 6 days. The results for fitting to each ADCP survey individually are self-consistent. For each survey, the standard deviation of the peak azimuthal velocity estimate for the mode-water eddy is less than 16 % of the mean peak azimuthal velocity for the survey and the standard deviation of the estimate of the mode-water eddy radius of peak azimuthal velocity is less than 8 % of mean radius of peak azimuthal velocity for the survey (Table 4.1, Figure 4.5).

However, there is considerable variation between the surveys with estimates of mode-water eddy peak azimuthal velocity varying between 0.23 and 0.34 m s^{-1} and corresponding radius varying between 18 and 26 km, which gives a variation in rotation period of between 8 and 4 days. The differences in estimated peak azimuthal velocity and corresponding radius for the eddies in the different ADCP surveys may well be attributable to the resolution and the coverage of the surveys. Survey two has 2 transects of each eddy (Figure 4.1), survey one approximately 3 (Figure 4.7), and survey three has 3 transects of the mode-water eddy but insufficient coverage to accurately resolve the position of the cyclone (Figure 4.6). Uncertainty in the position of the cyclone is most likely to be the cause of the much higher variability in the estimates of eddy radius and peak azimuthal velocity for survey three (Figure 4.5). This would suggest that survey one is likely to provide the most accurate estimate of eddy velocity and peak azimuthal velocity from recorded ADCP data.

As eddy radius increases above the radius of peak azimuthal velocity, $(r > R)$ azimuthal velocity will reduce with $V(r) \to 0$ *as* $r \to \infty$ (equation 4.1). Using values of $R = 23$ km and $V_o = 0.29$ m s^{-1} in equation 4.1 the azimuthal velocity is close to zero at 90 km (Figure 4.8). This would suggest that the estimates of eddy radius from hydrography and ADCP data are not inconsistent with each other.

4.2.2 Wind forcing

Wind data from NCEP/NCAR reanalysis (Kalnay et al., 1996), for 2007 were analysed to identify characteristics in the annual distribution of wind speed and direction for the Iceland Basin. NCEP/NCAR reanalysis data are globally gridded at $\sim 2^o$ resolution and are available at 6 hour temporal resolution (Kalnay et al., 1996). Wind data for the NCEP/NCAR reanalysis data grid point that was closest to 59° N 19° W (60° N 20° W) were extracted and analysed for the months January to December 2007.

The maximum and minimum wind speeds, as well as the most frequent wind speeds, were considered. Wind direction was analysed by considering both the most frequent wind direction and also by calculating the 'swing' of the wind, where a swing is defined as a continuous rotation in either a clockwise or anticlockwise direction. A swing starts when the wind direction changes and ends the next time the direction of movement reverses. Hence, for a wind which blows at a bearing of 60°, then rotates to bearing 90^0 and then back to bearing 60°, this would represent two swings; one of +30° followed by one of -30°. The magnitude of the swing is defined as the angle between the wind direction at the start and end of the swing and the swing duration is defined as the length of time taken to complete the movement. The magnitude of swing, the frequency with which different magnitude swings occur and the rate of change of direction during a swing were considered.

From the NCEP/NCAR reanalysis data, wind speeds for the Iceland Basin are between 5 to 13 m s^{-1} for 80 % of observations, with maximum speeds of 30 m s^{-1} and annual mean wind speed of 10 m s^{-1} (Table 4.2, Figure 4.9). The most common wind direction is 40° ±30° (blowing from the SW, Figure 4.9). The magnitude of the wind swing is 60° or less for 87 % of the time (Figure 4.10) with the maximum swing being 322°. On average the wind changes direction by 60° or less 37 times a month and by more than 60° eight times a month (Figure 4.10). The rate of change of wind direction was calculated as the size of the wind swing divided by the time taken for the swing. In the Iceland Basin the mean rate of change in wind direction, averaged over wind swings of 60° or less, is ~ 3° h^{-1}, which is consistent with 37 swings of 60° in 30 days. The mean rate of change in wind direction averaged over wind swings of greater than 60° is ~ 6° h^{-1}. The maximum rate of change in wind direction is 40° h^{-1}.

In order to see if there is any periodic variation in wind speeds, the power spectrum of the wind speeds was calculated using the Welch method (Welch, 1967), using the full 12 month NCEP/NCAR reanalysis data record for 2007. For the Iceland Basin, the power spectrum of NCEP/NCAR reanalysis winds for 2007, shows peaks at ~ 23 days and a cluster of peaks at ~ 2 to 6 days (Figure 4.11). The latter is consistent with wind speeds changing in response to the passage of storms where band pass filtering in the 2 to 6 day period is often used to identify storm tracks (Hoskins and Hodges, 2002). Spectral analysis of NCEP/NCAR reanalysis data at 6 hour temporal resolution, will not be able to resolve any peaks in the wind power spectrum occurring at or near inertial frequency for the Iceland Basin (13.9 hours period at 59°N). However, the D321 meteorological data were recorded at sufficiently high temporal resolution to resolve Iceland Basin inertial frequency.

The D321 meteorological data, recorded at approximately 59° N 19° W between 24th July to 23rd August 2007 were averaged to 30 minute temporal resolution and the wind direction converted to an absolute bearing by combination with ship navigational data before analysis. Power spectrum analysis of the D321 winds dataset for August 2007, as described above, only shows a peak at 3 days with no evidence of peaks in the power spectrum at frequencies higher than or close to inertial (Figure 4.12). The maximum wind speed for the D321 winds is 19 m s^{-1} and the minimum wind speed is 0.1 m s^{-1}. The mean wind speed for the D321 winds is 8.5 m s^{-1} and 28 % of the wind speeds recorded are below 6 m s^{-1} (Figure 4.13).

4.3 The Harvard Ocean Prediction System

The Harvard Ocean Prediction System (HOPS) is a regional-to-basin scale model, which has been designed to be used for simulations of open ocean regions (Robinson, 1966; Spall and Robinson, 1989). The model implements the primitive equations under hydrostatic, Boussinesq and rigid-lid approximations (Section 4.3.1). Subgrid scale horizontal mixing is parametrized by the use of a Shapiro filter (Shapiro, 1975), rather than through the use of Laplacian or biharmonic diffusion terms (Section 4.3.2). Vertical mixing in the upper mixed layer, the depth of which is determined using the model of Niiler and Kraus (1977) is parametrized using constant turbulent viscosity and diffusion coefficients (Section 4.3.4) while below the upper mixed layer vertical mixing is parametrized using either constant turbulent viscosity and diffusion coefficients or a Richardson number based scheme (Section 4.3.5). The model can use a variety of open boundary conditions, including the Orlanski (1976) radiation boundary, as well as closed “no flow” and prescribed flow boundaries (Section 4.3.3). HOPS can be configured to use either a hybrid grid system combining terrain following coordinates below a configurable depth level and uniform vertical resolution above or a uniform vertical resolution grid (Section 4.4.1).

4.3.1 PE model implementation

The zonal (x), meridional (y) and vertical (z) primitive equations, using hydrostatic, Boussinesq, and rigid-lid approximations as implemented in HOPS for a non-terrain following vertical coordinate system are given by

$$\frac{\partial u}{\partial t} + u\frac{\partial u}{\partial x} + v\frac{\partial u}{\partial y} + w\frac{\partial u}{\partial z} + \frac{1\partial p}{\rho\partial x} - 2\Omega v \sin\Phi \;=\; F_m \quad (zonal)$$

$$\frac{\partial v}{\partial t} + u\frac{\partial v}{\partial x} + v\frac{\partial v}{\partial y} + w\frac{\partial v}{\partial z} + \frac{1\partial p}{\rho\partial y} + 2\Omega u \sin\Phi \;=\; F_m \quad (meridional)$$

$$\frac{\partial p}{\partial z} - g \;=\; 0 \quad (vertical)$$

(Spall and Robinson, 1989) where u, v and w are the velocities in the x, y and z directions respectively, Ω is the rotation rate of the earth, Φ the latitude and F_m is a parametrization of the horizontal diffusion in the fluid. The conservation of mass (with incompressible fluid approximation) is represented by

$$\frac{du}{dx} + \frac{dv}{dy} + \frac{dw}{dz} \;=\; 0$$

(Spall and Robinson, 1989) and the conservation of a tracer C (which includes temperature, salinity and biological tracers) is given by

$$\frac{\partial C}{\partial t} + u\frac{\partial C}{\partial x} + v\frac{\partial C}{\partial y} + w\frac{\partial C}{\partial z} \;=\; F_t$$

(Spall and Robinson, 1989) where F_t is a parametrization of the turbulent diffusion of the tracer.

The rigid lid approximation (defining vertical velocity, w, to be zero at the surface) eliminates high speed barotropic gravity waves, such as surface tides, by making their phase speed infinite (Dukowicz and Smith, 1994). Nevertheless, despite the removal of surface tides from the model internal tides can be present (Killworth et al., 1991). The use of the rigid lid approximation also alters long planetary gravity wave dynamics for waves with wavelength greater than the Rossby radius of deformation (Dukowicz and Smith, 1994; Killworth et al., 1991). The dispersion relation for barotropic Rossby waves (planetary waves) on a β-plane is

$$\omega \;=\; \frac{-\beta k}{(k^2 + l^2 + f^2/{c_g}^2)} \tag{4.2}$$

(Dukowicz and Smith, 1994), where k, l are the zonal and meridional wavenumbers, f is the Coriolis parameter and, c_g is the phase speed of barotropic gravity waves. Using the rigid lid approximation c_g is infinite and the third term in the denominator of equation 4.2 is eliminated. The barotropic Rossby radius of deformation ($\mathrm{r_o}$) is given by

$$r_o = \frac{c_g}{f} \tag{4.3}$$

(Gill, 1982). If we consider barotropic Rossby waves with wavelength less than r_o the third term in the denominator of equation 4.2 is small compared to the remaining two terms and the use of the rigid lid approximation will give acceptably accurate wave dynamics. However, if we consider barotropic Rossby waves with wavelengths greater than r_o then the third term in equation 4.2 is no longer small compared to the remaining two terms and the used of the rigid lid approximation will give increasingly inaccurate wave dynamics as the wavelength of the planetary wave increases (Dukowicz and Smith, 1994).

The hydrostatic approximation disregards all vertical acceleration terms in the vertical primitive equation except gravity and is only valid for fluids where the horizontal length scale is much greater than the vertical length scale (Gill, 1982). The hydrostatic approximation is considered sound for modelling flows with horizontal scales >10 km; for example, mesoscale eddies resulting from hydrodynamical instability in larger scale flows. However, there are flows in the ocean which are fundamentally non-hydrostatic and occur on scales of < 1 km which cannot be reproduced using a hydrostatic model; for example, convection and wind/buoyancy-driven upper mixed layer turbulence (Marshall et al., 1997).

The Boussinesq approximation, where density is replaced by its mean value everywhere except when it is multiplied by gravity, is considered to be a good approximation since observations indicate that the density of seawater varies only about 5 % or less globally (Spall and Robinson, 1989). The mean potential density, calculated for the CTD section described above (Section 4.2.1) is 1027.3 ± 0.04 kg m^{-3} and for the two full depth CTD casts used in constructing the eddy model (Section 4.4) is 1027.6 ± 0.23 kg m^{-3}. In both cases the density is varying by less than 0.05 %.

HOPS solves for the horizontal advection of tracers using a "leapfrog" forward time-stepping scheme. Leapfrog is a finite difference method that is formally second order accurate in time and space (truncation error is of order time-step^2 + grid-spacing^2), non-dissipative, and stable (Zhou, 2002; Sod, 1985). For the simple advection equation

$$\frac{\partial C}{\partial t} - c\frac{\partial C}{\partial x} = 0$$

where C*(t,x)* is a function of time, t, and position, x, and c is the phase speed of the motion, the leapfrog scheme can be represented as

$$C_x^{t+1} = C_x^{t-1} + \lambda(C_{x+1}^t - C_{x-1}^t)$$

where $\lambda = c\Delta t \ / \ \Delta x$, C_x^t represents $C(t,x)$ and Δt, Δx are the time-step and grid spacing respectively (Zhou, 2002). The Courant-Fredrichs-Lewy (CFL) condition (Courant et al., 1967) for stability is given by $\lambda \leq 1$ (Zhou, 2002). As the leapfrog method utilises alternate grid points (i.e. calculates C_x^{t+1} from C_x^{t-1} without using C_x^t) it has the potential to develop two independent solutions (Sod, 1985). To reduce this tendency, in HOPS a dissipative Euler forward step is run every ten time-steps. The use of the Euler forward step introduces some numerical dissipation into the scheme as an unwanted side-effect.

4.3.2 Shapiro filtering

Shapiro filtering is used in HOPS in place of horizontal Laplacian viscosity terms to maintain model stability and as a parametrization of small scale mixing (Spall and Robinson, 1989). The Shapiro filter was originally proposed as a parametrization for horizontal diffusion in large scale atmospheric circulation models (Shapiro, 1971). The Shapiro filter is scale selective and the diffusion of the original signal resulting from the application of the filter depends on the wavelength of the signal being filtered, the order of the filter, and the number of filter applications (Shapiro, 1975). In line with previous studies (Popova and Srokosz, 2009; Popova et al., 2002) for the model in this thesis numerical stability was maintained by running a fourth order Shapiro filter every time-step for tracers, momentum, and transport, and a second order Shapiro filter every time-step for vorticity.

The effective diffusivity (K_{shap}) for a signal of given wavelength (L), limited to a fixed whole number of grid cells (m), can be estimated, in HOPS, for a Shapiro filter of order p applied r times every q time-steps by:

$$K_{shap} \ = \ \left[1 - (1 - s^p)^{\frac{q}{2r}}\right] \frac{K_0}{4s}$$

where

$$K_0 = \frac{(\Delta x)^2}{\Delta t}$$

$$s = \sin^2\left(\frac{k\Delta x}{2}\right)$$

$$k = \frac{2\pi}{L}$$

$$L = \frac{2\pi}{m\Delta x}$$

(Lermusiaux, 1997) and k is the wavenumber of the signal. For the configuration used in this thesis a fourth order Shapiro filter is equivalent to a horizontal diffusivity of order 10^3 m^2s^{-1} for features of wavelength 2 km rapidly tailing off to a horizontal diffusivity of order 10^1 m^2s^{-1} for features of wavelength $\geq$ 5km, while a second order Shapiro filter is also equivalent to a horizontal diffusivity of order 10^3 m^2s^{-1} for signals of wavelength 2 km but does not drop to a horizontal diffusivity of order 10^1 m^2s^{-1} until the signal wavelength is $>$ 12 km (Figure 4.14).

4.3.3 Boundary conditions

There are no ideal model boundary conditions for open ocean and adding a boundary to the primitive equations may well cause the problem to become ill-posed without a unique solution (e.g. Temam and Tribbia 2003; Oliger and Sundstrom 1978). Additionally the response of the model interior may well be sensitive to the choice of boundary condition. For example, where a model generates radiating internal waves a boundary condition which is not transparent to waves will cause the internal waves to be reflected back into the model interior altering the solution (Jensen, 1998).

For the eddy model in this thesis the boundary problem is slightly simpler than for a full regional scale model of the ocean which may include exchanges of tracers and momentum in both directions (to and from the model domain) across the model boundary. For the eddy model in this thesis there are only potentially outwards fluxes of momentum and tracer from the model. The boundary of the eddy model in this thesis should also be, as far as possible, transparent to radiating waves and should not interfere with the physics of the isolated eddy. From the available boundary conditions provided by the HOPS the model is run with open, Orlanski radiative (Orlanski, 1976) boundary conditions.

The basis of the Orlanski radiative boundary condition is the Sommerfield radiation condition

$$\frac{\partial C}{\partial t} + c\frac{\partial C}{\partial x_b} = 0$$

(Orlanski, 1976) where t is time, x_b is the direction orthogonal to the boundary and c is the phase speed of the signal in C. The Orlanski radiation condition evaluates c at the first interior boundary point. If c is positive the signal is propagated through the boundary with phase speed c, unless c is larger than that allowed by the CFL criterion when the phase speed is fixed at the maximum allowed (Lermusiaux, 1997).

4.3.4 Mixed-layer sub-model

HOPS implements the Niiler-Kraus model of the upper ocean (Niiler and Kraus, 1977) to determine the depth of the upper mixed layer. The Niiler-Kraus model is a function of momentum and buoyancy fluxes across the sea surface (Niiler and Kraus, 1977). Momentum fluxes depend on the friction velocity which is a function of the wind stress at the surface and the surface density (Niiler and Kraus, 1977). Buoyancy fluxes are a function of temperature and penetrating solar radiation (Niiler and Kraus, 1977). Surface layer values of turbulent viscosity and diffusivity (both 3 x10^{-2} m^2s^{-1}) are applied throughout the diagnosed upper mixed layer.

To allow consistent comparison between model runs, where mixed layer depths may vary due to different wind forcings, the Niiler-Kraus model is disabled and the mixed-layer depth fixed at a maximum depth of 30 m. This depth represents the mean depth of the mixed layer during the D321 cruise (Chapter 2).

4.3.5 Vertical mixing parametrization below the mixed layer

The Richardson number (Ri) based vertical mixing parametrization previously used in HOPS was originally developed to improve modelling of the Equatorial Undercurrent (Pacanowski and Philander, 1981). Neither this parametrization nor any other previous Ri parametrizations (Large et al., 1994; Peters et al., 1988) were considered appropriate for modelling the vertical mixing resulting from the mesoscale flows around a mode-water eddy for reasons given in Chapter 3. Consequently a new Richardson number based parametrization of vertical mixing was developed (Chapter 3).

Vertical mixing of tracers, below the upper mixed layer, is parametrized using the relationship for the turbulent diffusivity, $K = 3.6 \times 10^{-4}(1 + Ri)^{-1.5} + 8 \times 10^{-6}$ m^2s^{-1} derived in Chapter 3. Turbulent viscosity, was parametrized as a constant 1x10^{-3} m^2s^{-1} for reasons discussed in Chapter 3.

In grid cells where the water column is calculated to be gravitationally unstable a large value of the vertical diffusivity and vertical viscosity (3 x 10^{-2} m^2s^{-1} for both) is applied to mix the adjacent cells and restore stability.

4.3.6 Wind stress parametrization

Traditionally, parametrizations for wind stress applied in ocean models (e.g McGillicuddy et al. 2003; Oschlies 2002*a*) neglect the effects of the water speed (Large and Pond, 1981). However, taking water speed into account when considering an anti-cyclonic eddy reveals potential up-welling in the eddy core (Ledwell et al., 2008; McGillicuddy et al., 2007; Martin and Richards, 2001). Taking this into account the wind stress is parametrized using a formulation based on the relative speed of the water and wind

$$\boldsymbol{\tau} = \frac{\rho_a C_d}{(1+\varepsilon)^2} \left|\boldsymbol{u_a} - \boldsymbol{u_o}\right| (\boldsymbol{u_a} - \boldsymbol{u_o}) \tag{4.4}$$

(Bye, 1986) where, ρ_{a} is the density of air (taken as a constant 1.2 kg m^{-3}), ε^2 is the ratio of the densities for atmosphere and ocean ($\varepsilon \approx 0.034$, Martin and Richards 2001), C_d the drag coefficient, and $|\boldsymbol{u_a}|$, $|\boldsymbol{u_o}|$ are the absolute speeds of the air and the water respectively. This results in lower wind stress when wind blows in the same direction as the water current and vice versa (Chapter 1). Both the Bye (1986) wind stress parametrization and the standard wind stress parametrization have been implemented in the model. The latter is obtained by setting $|\boldsymbol{u_o}| = 0$ in equation 4.4.

4.3.7 Drag coefficient parametrization

Previous studies examining the effects of wind forcing on eddy vertical transport (Ledwell et al., 2008; Martin and Richards, 2001) have used the Bye (1986) formula for the wind stress (equation 4.4) combined with a parametrization of the air/sea drag coefficient (C_d)

$$C_d = 1000(0.61 + 0.063u_a)$$

(Smith, 1980) where u_a is the air speed. The Smith (1980) parametrization of the drag coefficient is only valid for wind speeds between 6 to 22 m s^{-1}. A later parametrization for the drag coefficient

$$C_d = 1000(0.5 + 0.071u_a)$$

(Yelland et al., 1998) is of the same form as the Smith (1980) parametrization, and extends the range of wind speeds from 6 to 25 m s^{-1}. Comparisons of the effects of using different drag coefficient parametrizations in the Bye (1986) wind stress formula are shown in Figure 4.15. The Yelland et al. (1998) parametrization of the drag coefficient is comparable to the Smith (1980) parametrization, within the range 6 to 14 m s^{-1}.

To maximize the range of wind speeds for which the wind stress parametrization is valid, the drag coefficient of Yelland et al. (1998) was used in combination with the Bye (1986) wind stress parametrization for wind speeds in the range of between 6 to 25 m s^{-1}. The relationship between winds speeds below 6 m s^{-1} and the drag coefficient appears to be strongly non-linear though there are few measurements of wind speed in this range compared to the range 6 to 25m s^{-1} (166 data points compared to 2298 data points Yelland and Taylor 1996). The only parametrization of drag coefficient for wind speeds below 6 m s^{-1}

$$C_d = 1000\left(0.29 + \frac{3.1}{u_a} + \frac{7.7}{{u_a}^2}\right)$$

(Yelland and Taylor, 1996) becomes infinite for wind speeds of zero m s^{-1}. Consequently wind stress for wind speeds outside the range 6 to 25 m s^{-1} was instead parametrized by linear extrapolation of the Yelland et al. (1998) parametrization.

4.4 Model construction

4.4.1 Model grid

The eddy model was constructed using a 228x189 km horizontal grid, with 1 km resolution, aligned north-south. The west-east dimension was made larger than the north-south to allow for eddy propagation (see below). The model was created with flat bottom topography and constant water depth to eliminate vertical motions caused as a result of interactions between the eddy and bathymetry. Previous studies modelling vertical fluxes in mode-water eddies used the f-plane approximation (Ledwell et al., 2008). However, as the full Coriolis term is important in sub-mesoscale instability processes (Mahadevan and Tandon, 2006) the eddy model in this thesis was run with a full Coriolis implementation. The use of a full Coriolis implementation means that the eddy will not remain stationary within the model grid, but will propagate westwards (Gill, 1982). Hence the horizontal size of the grid was selected to allow for the eddy to remain both within the grid and at least 20 km away from any horizontal boundary over the course of the simuations. The choice of horizontal grid resolution is a balance between resolving, where possible, sub-mesoscale instability processes which can occur on scales of a few kilometres and the validity of the hydrostatic approximation. As the model is intended to investigate fluxes in the upper ocean, the vertical sizes of the grid boxes were selected to best resolve the regions of the upper mixed layer and euphotic zone while not impairing the dynamics induced by the deep core of the mode-water eddy. The grid has 49 depth levels varying in thickness from 5 m at the surface to 289 m at depth (Table 4.3).

4.4.2 Eddy temperature and salinity structure

The temperature and salinity structure for the initialization of the model were created from measurements taken during two full-depth (surface to seabed) CTD casts made during cruise D321. Not all CTD casts made during cruise D321 were full-depth and the transect of the eddy core made during survey 2 (Section 4.2.1) comprises CTD casts to only ∼1000 m. Of the full depth CTD casts, station 16286 (19^{th} August 2007 59.11° N, 20.25° W) was through the mode-water eddy core, and station 162867 (19^{th} August 2007 59.24° N, 20.77° W) was in the waters away from the dipole structure (Figure 4.6). The upper 1000 m of these two profiles compares well to stations 16274 (in the mode-water eddy core) and 16272 (outside the eddy) from the CTD section through the mode-water eddy (Section 4.2.1, Figure 4.1, 4.16). The CTD cast data were averaged in the vertical into the HOPS grid intervals (Figure 4.17). The mode-water eddy core CTD cast was positioned in the centre of the model grid and temperature (T) and salinity (S) values from the mode-water eddy core profile were horizontally extrapolated into the surrounding waters for each depth level (z), according to the formulae

$$T(r,z) = T_o(z) + (T_i(z) - T_o(z)) \exp\left(\frac{-r^2}{2R^2}\right) \tag{4.5}$$

$$S(r,z) = S_o(z) + (S_i(z) - S_o(z)) \exp\left(\frac{-r^2}{2R^2}\right) \tag{4.6}$$

(Ledwell et al., 2008) where r is the distance from the eddy centre, T_o, S_o are the temperature and salinity outside the eddy and, T_i, S_i are the temperature and salinity at the eddy centre. In equations 4.5 and 4.6 R is the radius of peak azimuthal velocity which is difficult to determine accurately from hydrographic observations (Section 4.2.1). Nevertheless, the calculated radius of peak azimuthal velocity for the mode-water eddy model can be equated to the radius of maximum azimuthal velocity for the D321 mode-water eddy estimated by fitting cruise data to equation 4.1 as described in Section 4.2.1.

Assuming the eddy is circular and, as a first approximation, on an f-plane (i.e. $\beta = 0$) in hydrostatic balance the geostrophic azimuthal flow is given by

$$\left(f + \frac{V(r)}{r}\right) V(r) = \frac{1}{\rho_0}\frac{\partial p}{\partial r}$$

where f is the Coriolis parameter, $V(r)$ azimuthal velocity at radius r, ρ_o a reference density, and p pressure. This can be simplified to

$$fV(r) = \frac{1}{\rho_0}\frac{\partial p}{\partial r}$$

as $V(r)/r < f$ for the fitted eddy velocity profile ($0.29/23000 < 1.25 \times 10^{-4}$ s^{-1}, Section 4.2.1). Hence using the hydrostatic balance

$$\frac{\partial p}{\partial z} = -\rho g$$

where g is acceleration due to gravity and ρ *is* density, we have

$$f\frac{\partial V(r)}{\partial z} = \frac{1}{\rho_0}\frac{\partial}{\partial z}\frac{\partial p}{\partial r} = \frac{-g\rho}{\rho_0}\frac{\partial p}{\partial r} \tag{4.7}$$

Consistent with the form used for temperature and salinity we assume

$$p(r,z) = p_o(z) + (p_i(z) - p_o(z))\exp\left(\frac{-r^2}{2R^2}\right)$$

which combined with equation 4.7 becomes

$$f\frac{\partial V(r)}{\partial z} = \frac{-g\rho}{\rho_0}\frac{\partial}{\partial r}\left[p_o(z) + (p_i(z) - p_o(z))\exp\left(\frac{-r^2}{2R^2}\right)\right]$$

which expands to

$$\frac{\partial V(r)}{\partial z} = \frac{g\rho r}{\rho_0 f R^2}(p_i(z) - p_o(z))\exp\left(\frac{-r^2}{2R^2}\right)$$

Differentiating the Martin and Richards (2001) velocity profile (equation 4.1) with respect to z gives

$$\frac{\partial V(r)}{\partial z} = \left(\frac{\partial V_o}{\partial z}\right)\frac{r}{R}\exp\left(\frac{1}{2}\left(1 - \frac{r^2}{R^2}\right)\right)$$

We therefore see that equations 4.5, 4.6, and 4.1 are consistent provided that

$$\frac{\partial V_o}{\partial z} = \frac{g\rho}{\rho_o f R}(p_i(z) - p_o(z))$$

4.4.3 Eddy velocity structure

Data from survey one was used exclusively both to estimate the barotropic velocity fields and to estimate R for equations 4.5 and 4.6. Survey one represented the most consistent and complete of the three surveys (Table 4.1) with three ADCP transects of the mode-water eddy core one of which passes within less than 6 km of the estimated centre of the eddy (Figure 4.7). Survey three has insufficient measurements to resolve the cyclone accurately which results in larger standard deviations, than for the other two surveys, in the estimates of the mode-water eddy core size and position

(Table 4.1 Figure 4.6). Survey two has only two transects of the mode-water eddy core both $\sim$ 15 km from the estimated centre of the eddy (Figure 4.1) The mean value of R estimated from ADCP survey one is 26.1 km.

To estimate the mode-water eddy barotropic velocity component the ADCP data from survey one was averaged in the vertical into the HOPS vertical grid intervals and a velocity profile was fitted to data, for each depth level, as described in Section 4.2.1. Only ADCP data from below 50 m depth was used to exclude mixed layer water velocities.

The values of the mode-water eddy radius and maximum azimuthal velocity calculated from the ADCP data were used in equation 4.1 to create a velocity field on the model grid with origin at the centre of the model eddy for each depth level. Geostrophic velocities corresponding to equations 4.5 and 4.6 were calculated from the model initial temperature and salinity fields for each depth level. The difference between the eddy model geostrophic velocity and the ADCP derived velocity was calculated at each grid point for each depth level. The barotropic component of the model eddy velocity was then estimated by averaging in the vertical the difference at each grid point between the model geostrophic velocity and the ADCP derived velocity field for all depths between 50 to 330 m depth. The resultant barotropic velocity field (Figure 4.18) was added to each depth level of the model geostrophic velocity to give the initial mode-water eddy model velocity field.

As a check of the initial configuration, a velocity profile was fitted to the full model velocity field (sum of geostrophic and barotropic) as described in Section 4.2.1 for each depth level. The values of model eddy radius and peak angular velocity were compared to the observed mode-water eddy radius and peak angular velocity calculated using the D321 ADCP data from survey one, and were found to be acceptable (Figure 4.19 and 4.20).

4.4.4 Forcing

4.4.4.1 Wind

One set of wind forcings was constructed based upon the most commonly occurring wind characteristics from the NCEP/NCAR reanalysis wind data (hereafter “synthetic”). For the synthetic forcings, the effects of a wind of constant speed and direction, a wind varying in speed at a constant direction, a wind at a constant speed varying slowly in direction and a wind at constant speed varying rapidly in direction were considered.

For constant wind speed model forcings the wind speed was set at 10 m s^{-1}, the mean wind speed for the Iceland Basin NCEP/NCAR reanalysis data (Section 4.2.2). For varying wind speed model forcings wind speeds were varied sinusoidally between 6 m s^{-1} and 14 m s^{-1} with a mean of 10 m s^{-1} and a 3 day period. The varying speed model wind forcing is consistent with the most commonly occurring wind speeds and the 3 day peak in the wind speed power spectra (Section 4.2.2). For varying wind direction model forcings wind directions were continuously varied between $+30^o$ and -30^o at a constant rate of 3^o h^{-1}. In another scenario wind direction was also varied by steadily rotating the wind direction through 360^o over a period of nine hours (constant rate $\sim 40^o$ h^{-1}) eight times in 30 days at regular intervals (for a summary of model wind forcings see Table 4.4).

NCEP/NCAR reanalysis data at 6 hour temporal resolution does not show the high frequency variability observed in the 30 minute temporal resolution wind data recorded during the D321 cruise. In order to investigate the effect of high frequency variability in wind forcing a second set of wind forcings were constructed based upon the wind data recorded during the D321 cruise (hereafter “realistic”). For the realistic forcings the effects of a wind with a constant direction varying in only in speed and a wind varying in both speed and direction were considered. For comparative purposes, a forcing of a wind with constant speed and direction was also constructed with the wind speed set to 8.5 m s^{-1} which is the mean wind speed of the D321 cruise wind data.

The D321 cruise wind data cover a period 30 days in duration. In order to provide continuous wind forcing for the model, the cruise data set was looped 'back to back', i.e from start to finish then from finish to start repeatedly, to provide a smooth transition from one 30 day period to the next. For the constant direction wind forcing, a zonal wind with time varying speeds matching the D321 cruise wind data was constructed. For the wind varying in both speed and direction the D321 wind data was used as recorded (for a summary of model wind forcings see Table 4.4).

4.4.4.2 Radiative and evaporative

Radiative forcing and evaporative forcing were represented as constant mean values of the NCEP/NCAR reanalysis data for 2007 (Kalnay et al., 1996). The values used for heat, water, and shortwave radiative fluxes in all runs are given in Table 4.5.

A net positive heat flux into the surface ocean results in a reduction of surface ocean density which causes the surface isopycnals to sink (Section 4.5.3). This sinking of isopycnals results in vertical inert tracer fluxes becoming diapycnal in nature (Ledwell et al., 2008). Radiative and evaporative forcings are included in all model runs, for consistency with previous studies (Ledwell et al., 2008), to ensure that the vertical inert tracer fluxes are diapycnal.

4.4.5 Initial conditions

The initial model eddy core is a $\sim$ 790 m thick pycnostad centred on the 27.35 kg m^{-3} σ_o isopycnal at $\sim$ 560 m depth with the 27.3 and 27.4 kg m^{-3} σ_o isopycnals approximately delimiting the upper and lower boundaries of the eddy core at depths of 100 m and 890 m respectively. Away from the influence of the eddy core, the 27.3 and 27.4 kg m^{-3} σ_o isopycnals, are $\sim$ 344 m apart (Figure 4.21). Defining the width of the eddy core as the length of the section along a transect of the eddy core where the displacement of the 27.3 and 27.4 kg m$^{-3}\sigma_o$ isopycnals is greater than 344 m, the maximum width of the eddy core is $\sim$ 100 km. Over the depth interval from the 100 m to 890 m depth, the eddy core has a mean maximum azimuthal velocity of 23.3 $\pm$ 2 cm s^{-1} at a mean radius of maximum azimuthal velocity 26.6 $\pm$ 0.1 km. From the surface down to 300 m (the depth range of the ADCP data Section 4.2.1) the eddy core has a mean maximum azimuthal velocity of 20.4 $\pm$ 0.7 cm s^{-1} at a mean radius of maximum azimuthal velocity 26.8 $\pm$ 0.1 km. The initial values for the mode-water eddy model compare well to the observed values for the D321 mode-water eddy as described in Section 4.2.1.

4.5 Running the model

To assess how robust the structure of the model mode-water eddy is to external forcing, the model was initialised (see above) and run using both the standard wind stress parametrization and the Bye (1986) wind stress parametrization (Section 4.3.6). At the end of the model run the eddy was compared to the observations described in Section 4.2.1.

The model was forced with a constant zonal wind (speed 10 m s^{-1}) and with constant radiative and evaporative forcing (Section 4.4.4). The model was allowed an arbitrary period of 30 days to 'spin up' and then run for a further 60 days. The spin-up period of 30 days was selected to match the length of the D321 cruise wind data. A previous study using a similar eddy model allowed an 11 day spin up period (Ledwell et al., 2008). A period of 60 days was selected as being twice the length of the D321 wind data record.

On day 90 of the model run temperature, salinity, and velocity (both u and v components) data for all model grid points were output. Using the model results from day 90 of the run, the model eddy velocity data was fitted to equation 4.1 as described in Section 4.2.1. The position of the eddy centre, the radius and, the magnitude of the peak azimuthal velocity were determined at all model depth levels. The mean radius of peak azimuthal velocity and the mean peak azimuthal velocity were calculated for the depth interval of 100 m to 890 m for consistency with the calculations for the initial conditions (model day zero Section 4.4.5) and from the surface to 300 m depth for comparison with observations. A section was taken through the eddy core at the same approximate offset as the observed section ($\sim$ 15 km from the calculated eddy centre see Section 4.2.1). The point closest to the centre of the eddy core and a point 10 km in from both the northern and eastern boundaries of the model were selected as representing the eddy core and an area of the model outside the eddy core respectively. Measurements of temperature and salinity were extracted for all model depths at the two selected points (Figure 4.22).

4.5.1 Standard wind stress parametrization

At the end of the 90 day run the model was still very similar to the initial conditions (model day zero). The eddy core is a $\sim$ 780 m thick pycnostad centred on the 27.35 kg m^{-3} σ_o isopycnal at $\sim$ 560 m depth with the 27.3 and 27.4 kg m^{-3} σ_o isopycnals approximately delimiting the eddy core depths of 110 m and 892 m respectively (Figure 4.23 and 4.24). Away from the influence of the eddy core the 27.3 and 27.4 kg m^{-3} σ_o isopycnals, are $\sim$ 343 m apart (Figure 4.23). Defining the width of the eddy core as the length of the section along the transect where the displacement of the 27.3 and 27.4 kg m^{-3} σ_o isopycnals is greater than 343 m, the maximum width of the eddy core is $\sim$ 100 km (Figure 4.24). Over the depth interval from 100 m to 890 m, the eddy core has a mean maximum azimuthal velocity of 23.25 $\pm$ 2 cm s^{-1} at a mean radius maximum azimuthal velocity of 24.5 $\pm$ 0.2 km. From the surface down to 300 m the eddy core has a mean maximum azimuthal velocity of 20.3 $\pm$ 1.1 cm s^{-1} at a mean radius of maximum azimuthal velocity 24.7 $\pm$ 0.1 km. The eddy moved a distance of 33 km during the 90 day run in an approximately south-westerly direction (Figure 4.25).

4.5.2 Bye (1986) wind stress parametrization

After the 90 day run the model is once again very similar to the initial conditions (model day zero). The eddy core is an $\sim$ 800 m thick pycnostad centred on the 27.35 kg m^{-3} σ_o isopycnal at $\sim$ 508 m depth with the 27.3 and 27.4 kg m^{-3} σ_o isopycnals approximately delimiting the eddy core at depths of 80 m and 885 m respectively (Figure 4.26 and 4.27). Away from the influence of the eddy core the 27.3 and 27.4 kg m^{-3} σ_o isopycnals, are $\sim$ 343 m apart (Figure 4.26). Defining the width of the eddy core as the length of the section along the transect where the displacement of the 27.3 and 27.4 kg m^{-3} σ_o isopycnals is greater than 343 m, the maximum width of the eddy core is $\sim$ 100 km (Figure 4.27). Over the depth interval from the 100 m to 890 m, the eddy core has a mean maximum azimuthal velocity of 21.87 $\pm$ 2 cm s^{-1} at a mean radius of 24.7 $\pm$ 0.2 km. From the surface down to 300 m the eddy core has a mean maximum azimuthal velocity of 17.5 $\pm$ 2.5 cm s^{-1} at a mean radius of maximum azimuthal velocity 25.5 $\pm$ 0.6 km. The eddy moved a distance of 32 km during the 90 day run in an approximately south-westerly direction (Figure 4.25).

In contrast to the run using the standard wind stress parametrization, the depth of the 27.3 kg m^{-3} σ_o isopycnal in the eddy core has shallowed by approximately 20 m with respect to the initial depth of the isopycnal (100 m) over the course of the 90 day model run. Ignoring any heating effects, this is equivalent to a vertical velocity of approximately 0.22 m day^{-1} over the ninety days of the simulation. This would suggest that there is potentially Ekman suction occurring in the eddy core when using the Bye (1986) wind stress parametrization.

4.5.3 Comparison of the eddy model to the Iceland Basin observations

The eddy model, when forced using either the standard or Bye (1986) wind stress parametrizations, appears to reproduce with reasonable agreement the observations of the mode-water eddy part of the D321 dipole (Section 4.2.1). The mean radius of maximum azimuthal velocity is within 2 km of observations (survey 1, radius 26.1 $\pm$ 1 km) for both model runs, and the maximum azimuthal velocity is within 6 cm s^{-1} of observation (survey 1, azimuthal velocity 23 $\pm$ 0.03 cm s^{-1}). The hydrographic characteristics of the eddy core, thickness $\sim$ 800 m and maximum width $\sim$ 100 km, are also close to observation, to within 20 m in core thickness and within $\sim$ 10 km in width (core thickness 780 m, width $\sim$ 90 km, Section 4.2.1). The hydrographic characteristics appear to be robust even after 90 days when compared to the model initial conditions (model day zero Section 4.4.5) and are retained for the duration of both simulations.

The use of the Bye (1986) wind stress parametrization results, as expected, in a raising of the isopycnals within the eddy core, with an estimated vertical velocity of the same order of magnitude as theoretical predictions (e.g. 0.5 m day^{-1} for wind speeds up to 15 m s^{-1} Martin and Richards (2001) and 0.23 m day $^{-1}$ for a constant wind speed of 6.7 m s^{-1}, Ledwell et al. (2008)). This estimate of vertical velocity ignores the effects of surface heating. A net positive heat flux into the surface ocean (Table 4.5) results in a reduction of density in the surface ocean which causes the surface isopycnals to sink (Figure 4.28). Considering the density profile of the waters away from the eddy, the 27.0 kg m^{-3} σ_o isopycnal has sunk by approximately 5 m during the 90 day model run (Figure 4.28). Theoretical predictions of the vertical velocity due to Ekman effects within the eddy core only predict the vertical velocity at the base of the Ekman layer (Ledwell et al., 2008) which in the presence of strong seasonal stratification is approximately the base of the wind mixed layer. Vertical velocities are expected to penetrate below the wind mixed layer with an approximate e-folding length scale for the penetration given by $\frac{fL}{N}$ (Ledwell et al., 2008) where L is the horizontal length scale of the eddy ($\sim$ 25 km, see above) and N is the buoyancy frequency ($\sim$ 4 x10^{-2} s^{-1} across the model mixed layer base of 30 m depth). This would give an e-folding length scale of order 100 m for the penetration of the Ekman driven upwelling into the stratified interior of the eddy model. The vertical Ekman velocity reduces with depth over the penetration length scale which would lead to the apparent vertical velocity in the model at $\sim$ 100 m depth being lower than theoretical predictions (Ledwell et al., 2008). Hence both surface heating and the stratification in the model may contribute to a lower than predicted rise in density surfaces.

4.6 Discussion

The use of the hydrostatic approximation will only allow the model to reproduce ocean processes that are in hydrostatic balance at vertical scales of, at best, down to 1 km (Marshall et al., 1997). However, some ocean processes which can result in large vertical velocities are associated with sub-mesoscale instabilities at horizontal scales of $<$ 1 km and are non-hydrostatic in nature, for example the effects of down-front winds (Thomas and Lee, 2005). For a fuller discussion of sub-mesoscale processes see Chapter 1. Such, potentially sub-grid scale, instability processes will effectively be represented in the model by an increased vertical diffusivity as the model attempts to mix the instability away and restore hydrostatic balance (Section 4.3.5). This use of vertical diffusion as a convective adjustment process may lead to additional erroneous small scale horizontal variability (Molemaker and Dijkstra, 2000). Nevertheless, hydrostatic approximation models have been used successfully to model sub-mesoscale instabilities occurring at scales of order 1km and larger, producing averaged vertical fluxes that are comparable to the equivalent non-hydrostatic simulations (Mahadevan, 2006).

The diffusive flux from the model may consist of both shear driven vertical diffusion arising from the Richardson number parametrization, and vertical diffusion used as a convective adjustment process (Section 4.3.5). Due to the large magnitude of the diffusion coefficients applied in the case of model convective adjustment, sufficiently high temporal resolution model output should allow the separation of the diffusive flux into components that are due to shear and those that are a proxy for convective adjustment (Chapter 5). This would suggest that despite the use of vertical diffusion used as a convective adjustment process in HOPS it will still be possible to use the model to isolate any enhancement to the vertical diffusive flux resulting from shear.

The use of the rigid-lid approximation filters out surface gravity waves and affects the dynamics of long wavelength Rossby waves (Dukowicz and Smith, 1994; Killworth et al., 1991). The wavelength of barotropic Rossby waves in the Iceland Basin ($f \sim 1.25$ x10^{-4} s^{-1} at 59^{o} N) from equation 4.3 is $\sim$ 1400 km where $c_g = \sqrt{g/H}$, $H \sim 3000$ m is the depth of the water column and $g = 9.8$ m s^{-2} is acceleration due to gravity (Gill, 1982). The wavelength of barotropic Rossby waves is significantly larger than the size of the entire model domain ($\sim$ 200 km). This would suggest that long wavelength Rossyby waves will not be generated within the eddy model. The rigid-lid approximation, while excluding surface gravity waves, does not affect baroclinic waves such as the internal tides (Killworth et al., 1991). The primary focus of the work here is to investigate fluxes below the mixed layer and HOPS has been successfully used to reproduce sub-surface fluxes in previous studies (Popova and Srokosz, 2009; Popova et al., 2002). Hence the rigid-lid approximation is not expected to affect the calculations of vertical flux in this model.

The use of a Shapiro filter to maintain model numerical stability (Section 4.3.2), along with the use of the periodic Euler forward time-step (Section 4.3.1) will introduce a degree of numerical horizontal diffusion, though the leapfrog time-stepping scheme is non-dissipative (Sod, 1985). Note that physical effective horizontal diffusion is not explicitly represented. A magnitude for the effective horizontal diffusion due to the Shapiro filter can be estimated for a given tracer by calculation of the effective diffusion imposed by the filter at each output step. As the effective diffusion is dependent on the instantaneous horizontal tracer concentration gradients at each application, the estimate of horizontal diffusion will only be approximate, but may be useful in indicating the potential magnitude of this flux for a given model run (see Appendix A).

The Orlanski radiative boundary condition used in this model should be transparent to internal baroclinic waves generated in the model interior. Orlanski boundaries have been shown to perform well in simple test cases involving a single radiating internal wave (e.g. Jensen 1998) and in more complex coastal scenarios where there is no exchange of properties across the boundary (Chapman, 1985). However, the calculation of the phase speed at the model boundary (see Section 4.3.3) can become problematic since the Sommerfield radiation condition used here is only strictly justified for waves with a constant phase velocity and not for a combination of waves with different phase velocities (Blayo and Debreu, 2005). This would suggest that some of the radiating internal waves that are generated within the model domain may not pass through the boundaries and may potentially be reflected back into the model interior increasing the wave-driven variability in model vertical velocities throughout the model domain. The increased variability in the vertical velocities caused by the reflection of internal waves can be filtered out by considering fluxes averaged over long (e.g. many days) time periods. Additionally the lack of transparency at the boundary to outwards propagating waves may well generate spurious horizontal flows in proximity to the model boundary. The size of the model grid has been determined so that the impact of such boundary issues can be mitigated by considering only model properties in a subset of the model domain which is away from the boundary region In the case of the example model run above (Section 4.5) the eddy is at all times more than 50 km away from the model boundary.

Fixing the maximum depth of the upper mixed layer (Section 4.3.4), allows for easier comparison between different wind forcing scenarios. The Niiler-Kraus mixed layer model is sensitive to maximum wind speeds (Niiler and Kraus, 1977) and so will respond differently to wind forcings with the same temporal mean value but different maxima. For example, wind scenarios Scc and Slc (Table 4.4) have the same mean wind speed (over a 30 day period) but different maximum wind speeds which will result in a deeper Niiler-Kraus mixed layer for scenario Slc than scenario Scc. Fixing the maximum depth of the upper mixed layer will exclude from the model the vertical fluxes resulting from the changing of mixed layer depth and this will allow clearer diagnosis of the vertical fluxes below the mixed layer which is the primary focus here.

Vertical viscosity, parametrized in the model as a constant value of 1x10^{-3} m^2s^{-1} estimated from observation (see Chapter 3), is larger than in other typically used parametrizations, for example the parametrizations of Large et al. (1994) and Pacanowski and Philander (1981) both use a constant background vertical viscosity of 1x10^{-4} m^2 s^{-1}. The use of a large vertical viscosity may potentially have an effect on the model physics, damping the transfer of momentum from the surface layer into the model interior and reducing the magnitude of the vertical fluxes compared to other parametrizations. The effect of the model viscosity on the estimated vertical fluxes will depend, to some extent, on the variability of the forcing applied to the model. The extent to which vertical viscosity influences model flux can be estimated by comparing scenarios run with identical forcing but different vertical viscosities (see Appendix A).

The maximum wind speed recorded during cruise D321 of 19.1 m s^{-1} is within the range of wind speeds for which the drag coefficient parametrization is valid (6 to 25 m s^{-1} Section 4.3.7). Nevertheless, approximately 30 % of the wind speeds in the wind data recorded during the cruise are below 6 m s^{-1} (Section 4.2.2). Calculating the drag coefficient for wind speeds below 6 m s^{-1} by linear extrapolation (Section 4.3.7) will potentially lead to an under estimate of the absolute value of the drag coefficient. However, the drag coefficient is valid for all synthetic wind forcing scenarios and for the majority of the realistic wind forcing data (Table 4.4). The primary focus of the model is in investigating shear enhancement to the vertical diffusive flux which is potentially driven by the interactions of the eddy and the wind. Comparison of vertical fluxes between model runs that use realistic wind forcing data and a consistent calculation of drag coefficient is still considered to give valid results though the estimates of vertical flux will potentially be lower than might be observed.

4.7 Conclusions

A model of a mode-water eddy has been constructed using HOPS and configured to the observations of the mode-water eddy part of the eddy dipole surveyed during cruise D321. After a 90 day model run using both the standard and the Bye (1986) wind stress parametrizations with constant wind speed, evaporative and radiative forcing, the eddy model reproduces the observations of the D321 mode-water eddy with reasonable accuracy.

The approximations used in HOPS and in the calculation of the drag coefficient are not considered to affect the use of the model to examine whether there is a shear enhancement to the vertical diffusive flux of nutrients that is driven by the interactions of the eddy and the wind.

Survey	Cyclone				Mode-Water			
	Lat.(°N)	Lon.(°E)	Radius (km)	Az.Vel. (m s^{-1})	Lat.(°N)	Lon.(°E)	Radius (km)	Az.Vel. (m s^{-1})
1	59.75 ± 0.01	-19.73 ± 0.01	27.5 ±1.5	0.26 ± 0.03	59.4 ± 0	-20.1 ± 0.05	26.1 ± 1	0.23 ± 0.03
2	59.67 ± 0.01	-19.56 ± 0	16.76 ± 0.9	0.31 ± 0.04	59.19 ± 0	-19.76 ± 0	17.83 ± 0.9	0.31 ± 0.05
3	60.39 ± 0.16	-18.82 ± 0.12	19.37 ± 4.3	0.21 ± 1.5	59.32 ± 0.01	-19.66 ± 0.04	25.5 ± 2	0.34 ± 0.04

TABLE 4.1: Position sizes and maximum azimuthal velocities of the eddy cores in the D321 survey area estimated from ADCP data by fitting equation 4.1 as described in Section 4.2.1 Values presented are the mean ± standard deviation of the fit to ADCP data within 11m to 400 m depth. Note the position of the cyclone estimated using ADCP survey 3 data is considered to be unreliable due to insufficient ADCP measurements being taken to constrain the fit.

Iceland Basin wind speed		
Max	Min	Most frequent
30 m s^{-1}	0.2 m s^{-1}	5 to 13 m s^{-1} (80 % of time)

TABLE 4.2: Wind speeds for the Iceland Basin (60°N 20°W) for 2007. Data from 12 months worth of 6 hourly NCEP/NCAR Reanalysis.

Depth (m)	Thickness (m)	Depth (m)	Thickness (m)
2.5	5	333.2	212.3
7.5	5	451.8	25
12.5	5	478.3	27.9
17.5	5	507.8	31.2
22.5	5	540.8	34.9
27.5	5	577.8	39
32.5	5	619	43.6
37.5	5	665.1	48.7
42.5	5	716.7	54.4
47.5	5	774.3	60.8
52.7	5.5	838.6	68
58.4	6	910.6	75.9
65.4	8	991	84.9
74.4	10	1080.9	94.9
85.4	12	1181.3	106
98.9	15	1293.6	118.5
111	9.2	1419.1	132.4
120.7	10.1	1559.3	148
131.2	11	1716.1	165.4
142.6	12	1891.2	184.9
155.2	13.1	2087	206.7
168.8	14.3	2305.8	231
183.8	15.6	2550.4	258.1
200	17	2823.7	288.5
217.8	18.5		

TABLE 4.3: Depth of midpoint and thickness of the grid levels used to construct the model grid as described in Section 4.4.1.

Tag	Description
NW	No wind blowing
Synthetic	
Scc	Constant zonal wind with speed of 10 m s^{-1}, the mean NCEP wind speed for 2007.
Slc	Wind speed varying sinusoidally between 6 m s^{-1} and 14 m s^{-1} (mean speed 10 m s^{-1}) with a 3 day period.
Scl	Wind speeds constant at 10 m s^{-1}. Wind direction varying continually between +30^o and -30^o at a rate of 3^o h^{-1}
Sch	Wind speeds constant at 10 m s^{-1}. Wind direction rotating through 360^o over a period of nine hours (rate $\sim$ 40^o h^{-1}) 8 times in 30 days at regular intervals.
Realistic	
Rcc	Zonal wind with speed constant at mean wind speed of D321 cruise data set (8.55 m s^{-1}).
Rrc	Zonal wind with speed taken from Iceland Basin D321 wind data (30 days duration) in a repeating loop at sampling frequency of every 30 mins.
Rrr	Iceland Basin D321 wind data (30 days duration) in a repeating loop at sampling frequency of every 30 mins.

TABLE 4.4: Description of model wind forcing scenarios (Section 4.4.4.1). Tags are constructed of three fields. Field one is either 'S' or 'R' indicating a 'synthetic' or 'realistic' forcing. Field two indicates the rate of change of wind speed, c = constant, l = low, h = high and r = realistic. Field three indicates the rate of change of wind direction, c = constant, l = low, h = high and r = realistic.

Heat flux (W m^{-2})	Water flux (cm d^{-1})	Shortwave radiation (W m^{-2})
51.6	-0.13	167.7

Table 4.5: Radiative and evaporative forcing, taken from 6 hourly NCEP reanalysis data for August 2007.

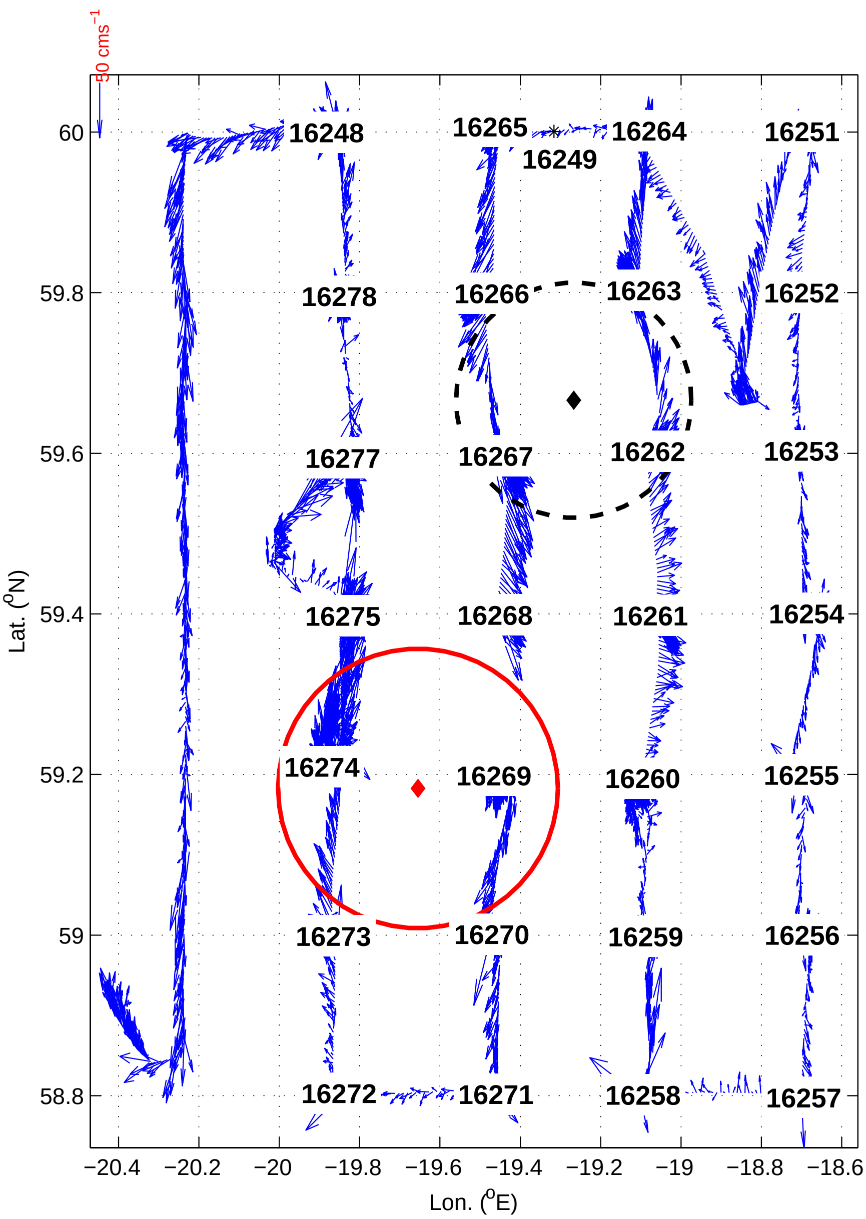

FIGURE 4.1: Current velocities from Acoustic Doppler Current Profiler (ADCP) data for a 4 m depth level centred on 67 m depth and the locations of conductivity-temperature-depth (CTD) stations for survey two (10$^{\text{th}}$ August 2007 to 15$^{\text{th}}$ August 2007). The positions of the dipole eddies, estimated by fitting ADCP data to equation 4.1 as described in Section 4.2.1, are marked. The mode-water eddy is in red, the cyclone in black. The depth of 67 m was selected as being the first ADCP depth level below the observed euphotic depth of 64 m.

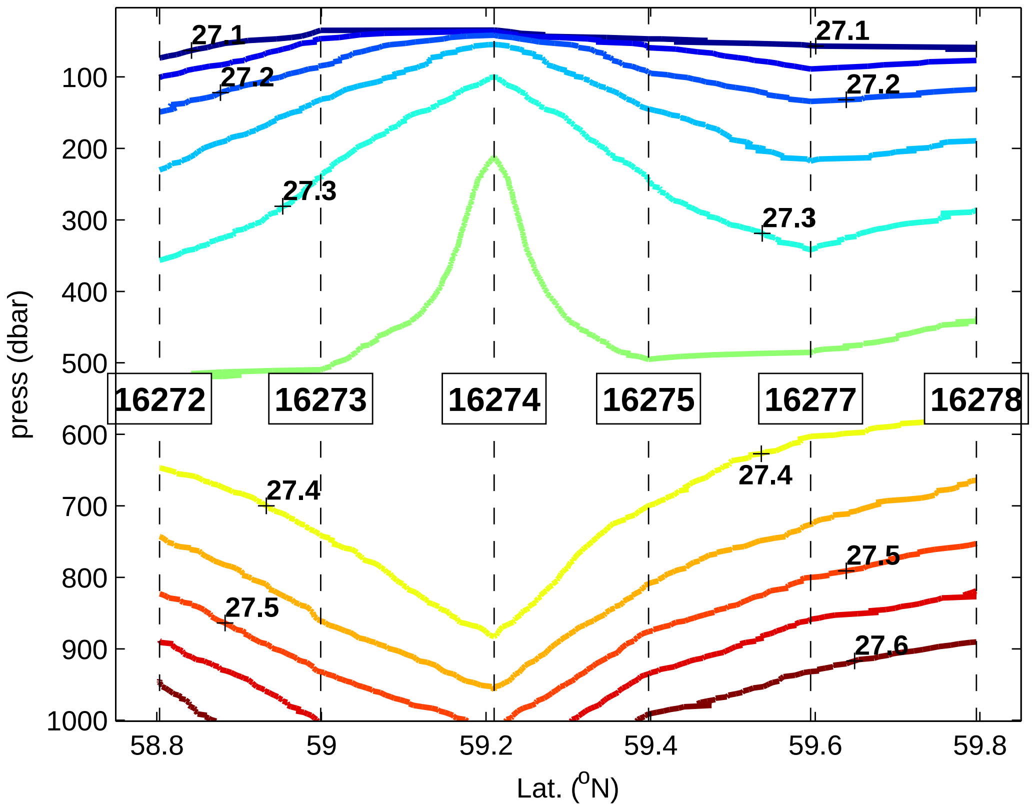

FIGURE 4.2: A contoured cross section of potential density (σ_o contours are shown every 0.05 kg m^{-3}) through the mode-water eddy core from conductivity-temperature-depth (CTD) stations 16272 to 16278 from survey two (see Figure 4.1 for station locations). σ_o is potential density calculated with respect to 0 dbar pressure minus 1000 kg m^{-3}. The position of each CTD station is indicated.

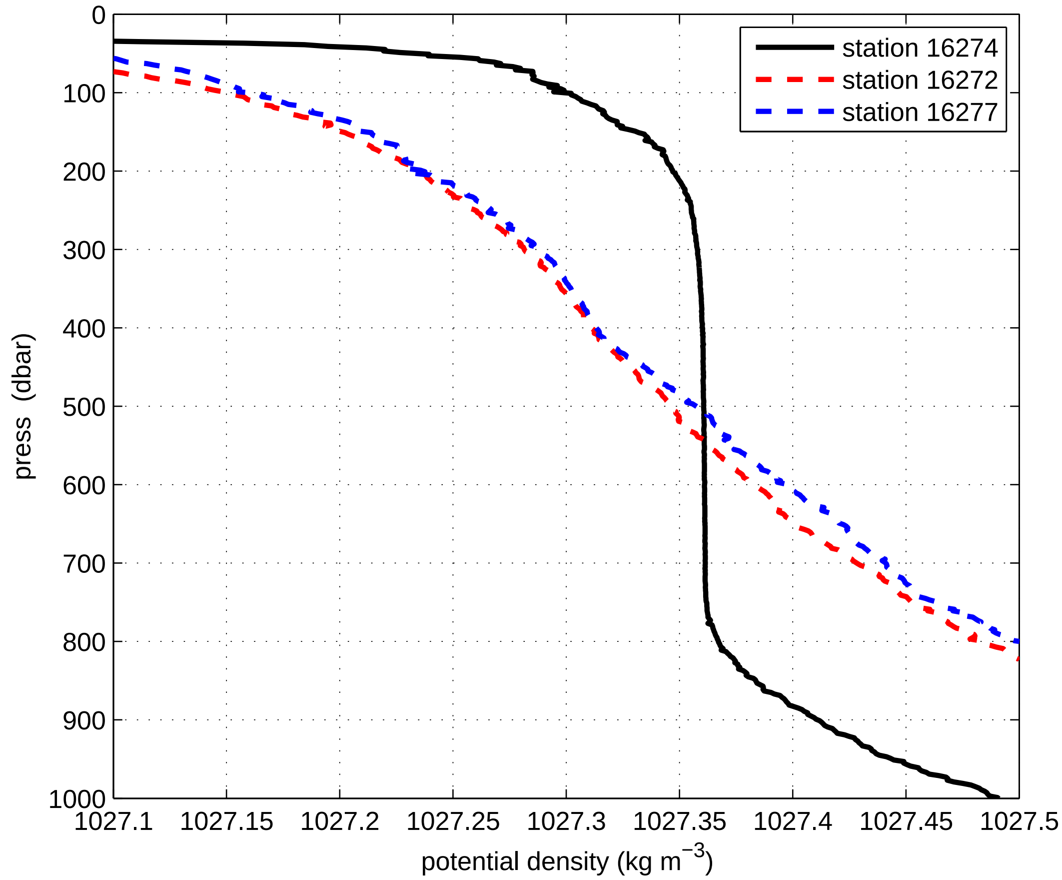

FIGURE 4.3: Potential density from conductivity-temperature-depth (CTD) stations 16272, 16274 and 16277 (see Figure 4.1 for station locations). Station 16274 is in the mode-water eddy core. Stations 16272 and 16277 mark the outer edges of the mode-water eddy core (Section 4.2.1).

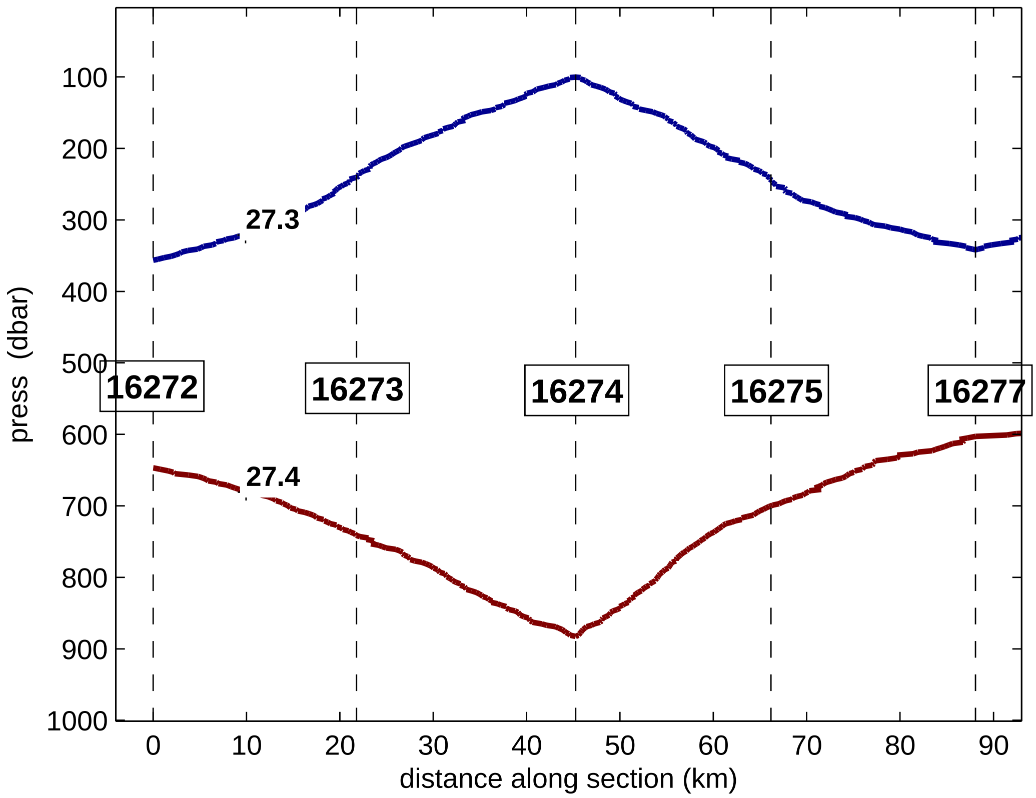

FIGURE 4.4: A cross section of potential density showing σ_o contours 27.3 and 27.4 kg m^{-3} which delimit the mode-water eddy core, through the mode-water eddy core from conductivity-temperature-depth (CTD) stations 16272 to 16277 from survey two (see Figure 4.1 for station locations). σ_o is potential density calculated with respect to 0 dbar pressure minus 1000 kg m^{-3}. The position of each CTD station is indicated. The 27.3 and 27.4 kg m^{-3} σ_o isopycnals are displaced vertically by 228 m at station 16272, 260 m at station 16277 and $\sim$ 780 m at station 16274.

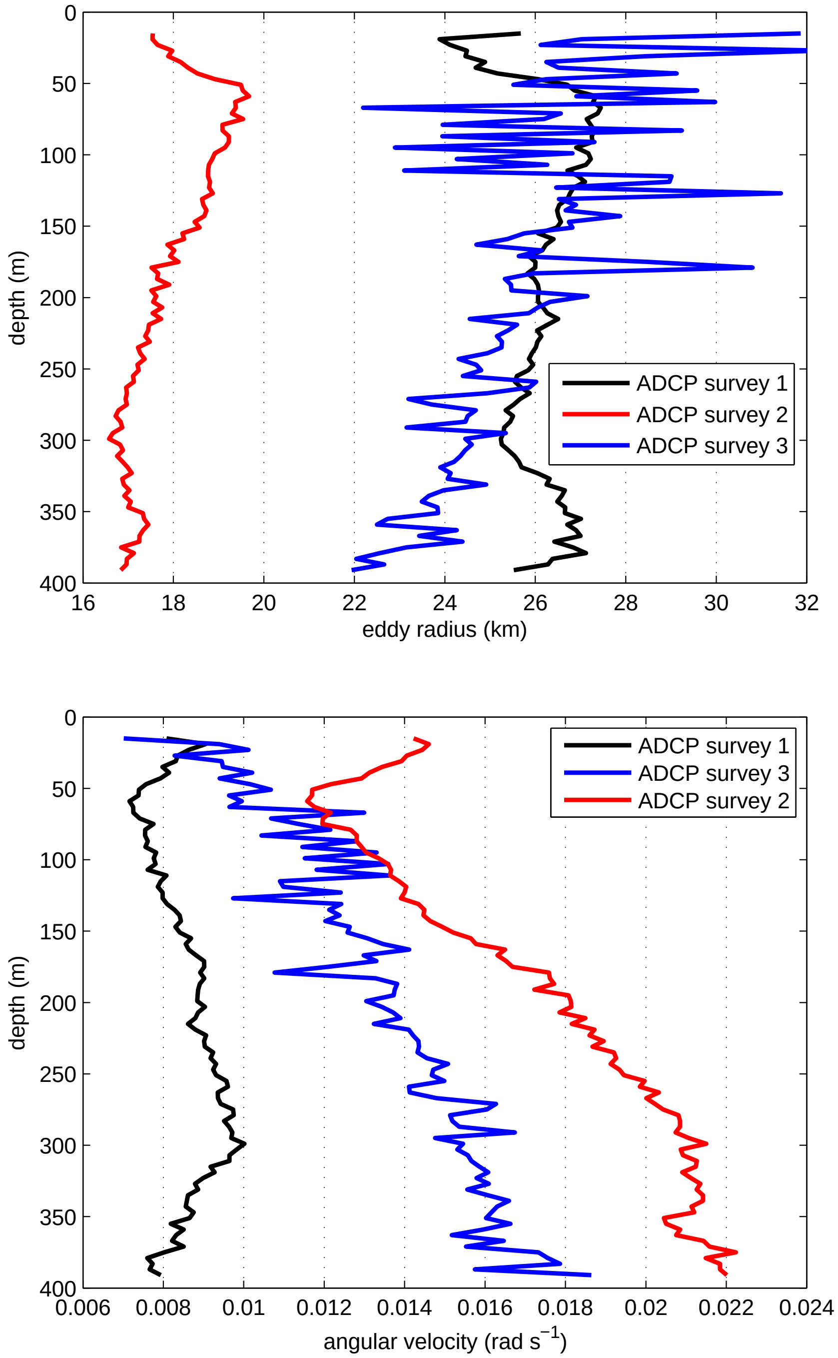

FIGURE 4.5: The radius of the mode-water eddy estimated by fitting Acoustic Doppler Current Profiler (ADCP) data for each depth level to equation 4.1 as described in Section 4.2.1 (upper panel). The peak azimuthal velocity of the mode-water eddy estimated by fitting ADCP data, for each depth level to equation 4.1 as described in Section 4.2.1(lower panel).

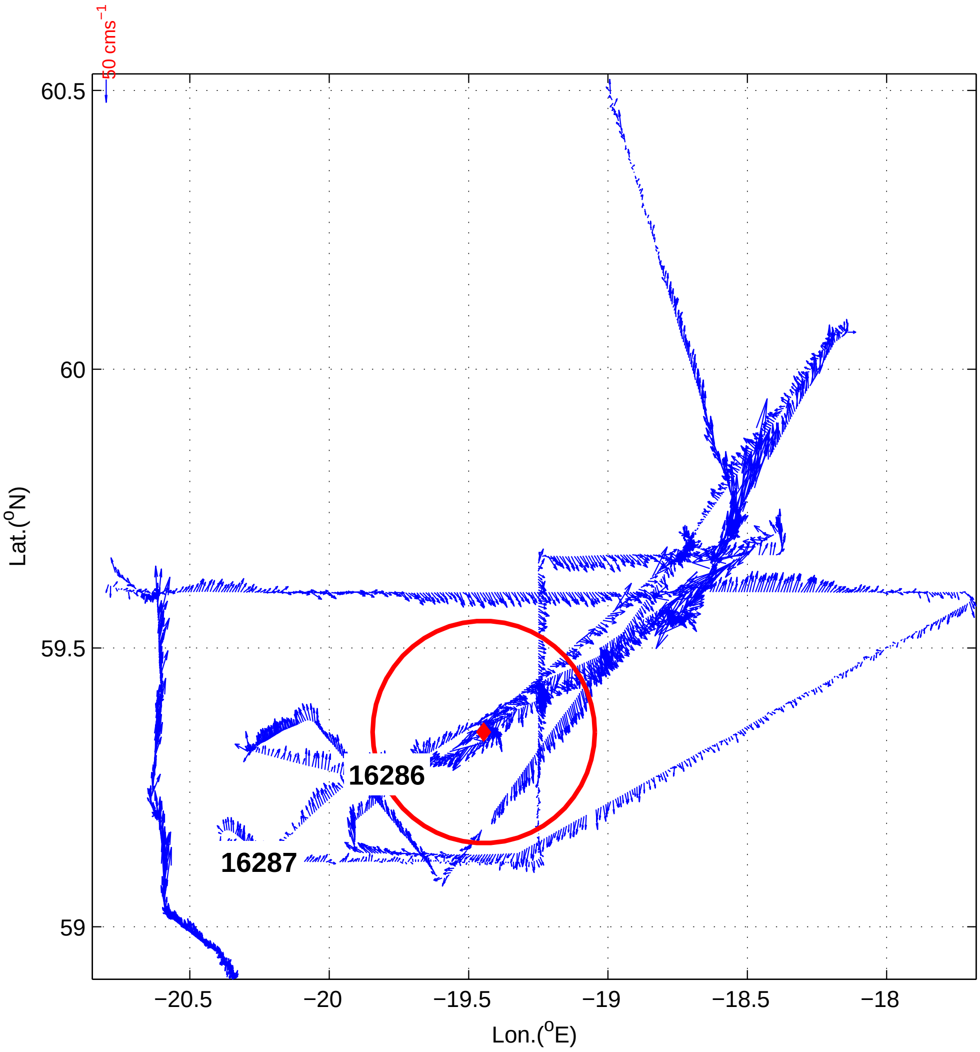

Figure 4.6: Current velocities from Acoustic Doppler Current Profiler (ADCP) data for a 4 m depth level centred on 67 m depth and the locations of conductivity-temperature-depth (CTD) stations for survey three (15th August 2007 to 22nd August 2007). The position of the mode-water eddy estimated by fitting ADCP data to equation 4.1 as described in Section 4.2.1 is marked in red. Note the position of the cyclone estimated using ADCP survey 3 data is not shown as the position is considered to be unreliable due to insufficient ADCP measurements being taken to constrain the fit.

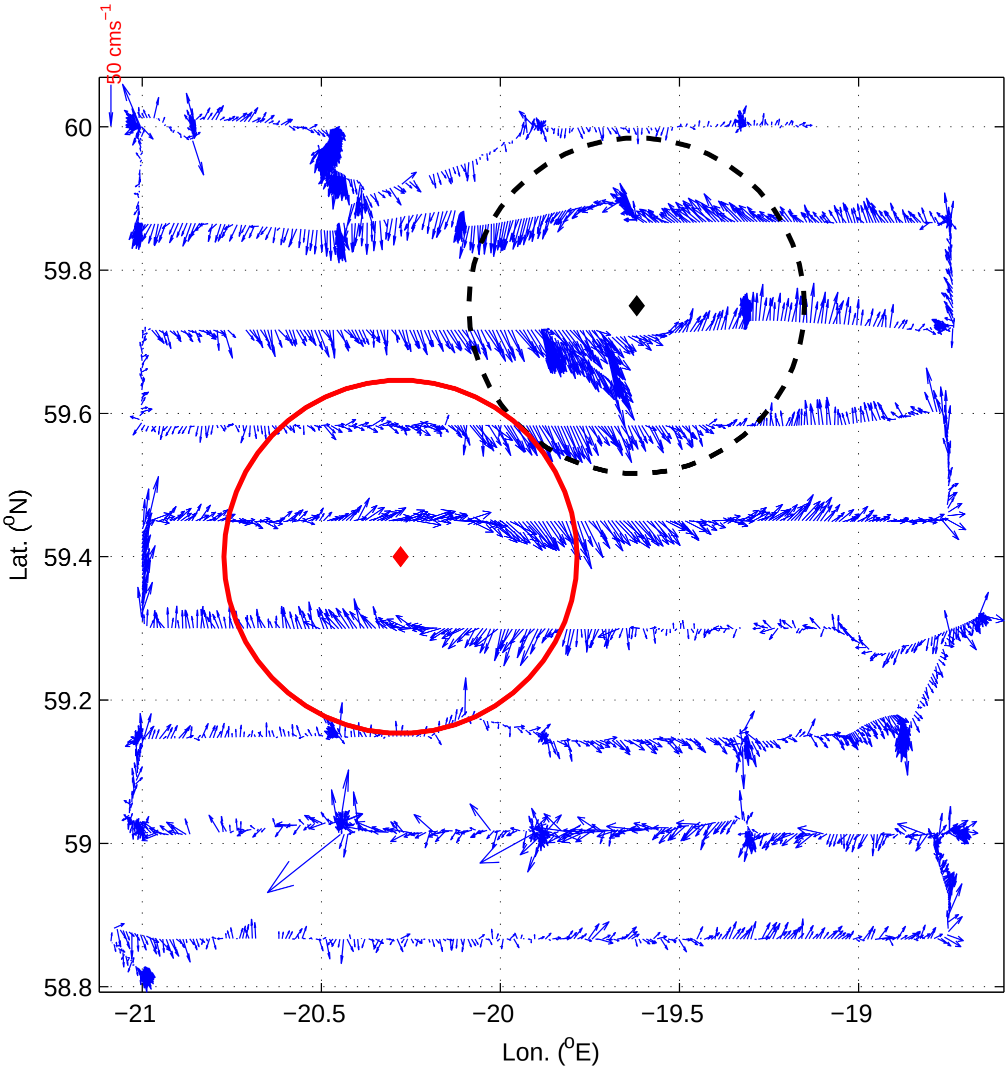

Figure 4.7: Current velocities from Acoustic Doppler Current Profiler (ADCP) data for a 4 m depth level centred on 67 m depth for survey one (5th August 2007 to 10th August 2007). The positions of the dipole eddies estimated by fitting ADCP data to equation 4.1 as described in Section 4.2.1 are marked. The mode-water eddy is in red, the cyclone in black.

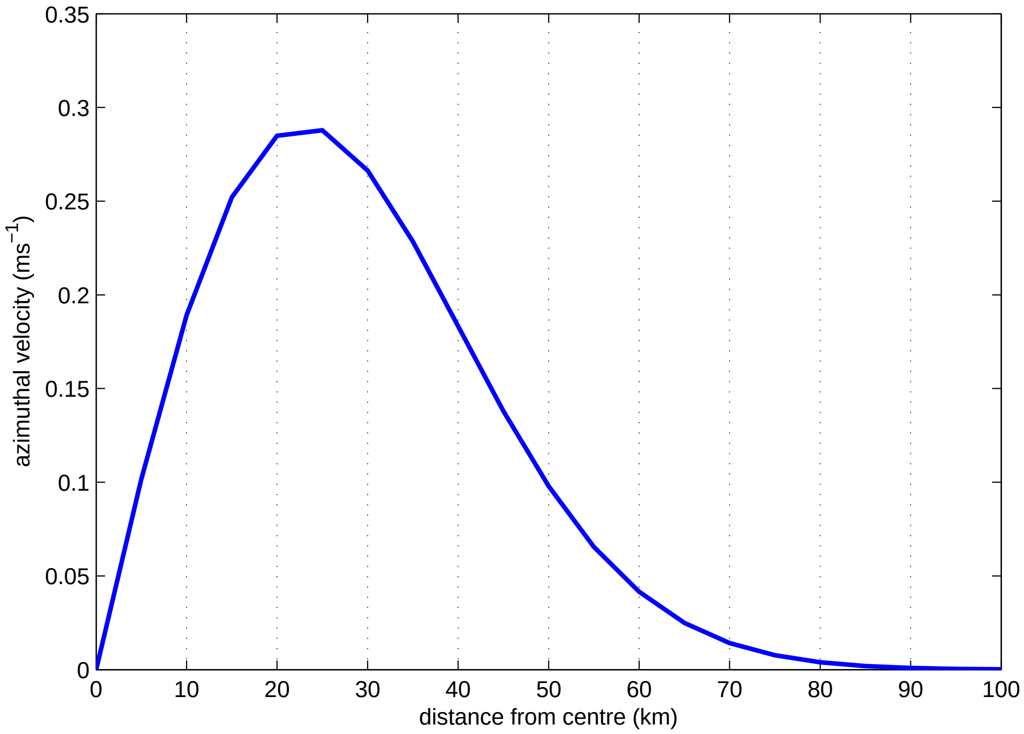

FIGURE 4.8: The azimuthal velocity of the mode-water eddy, calculated using equation 4.1 as described in Section 4.2.1, with R = 23 km and V_o = 0.29 m s^{-1} for distances from the centre up to 100 km.

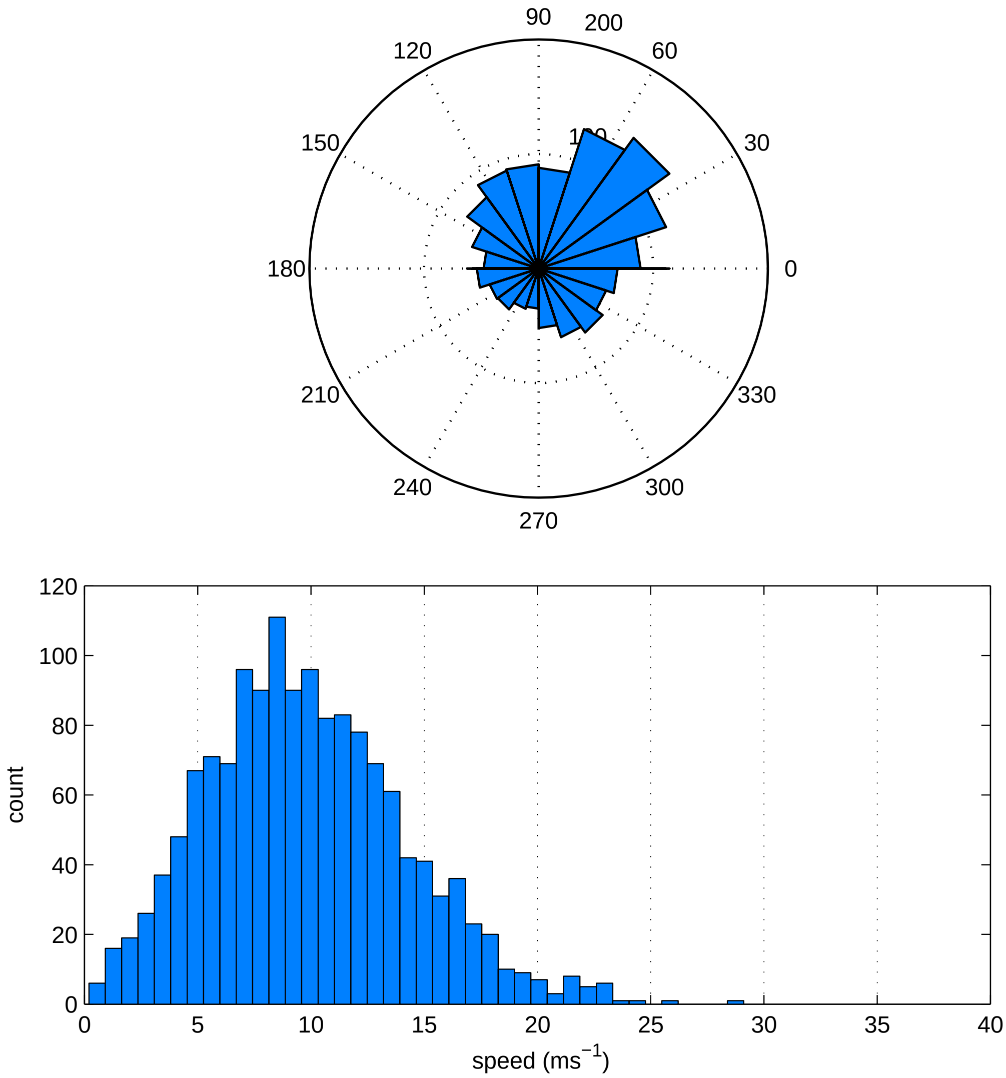

FIGURE 4.9: Distribution of wind direction and speed for the Iceland Basin (60°N 20°W) from 6 hourly NCEP/NCAR reanalysis data for 2007. Circular lines in top plot indicate the number of occurrences.

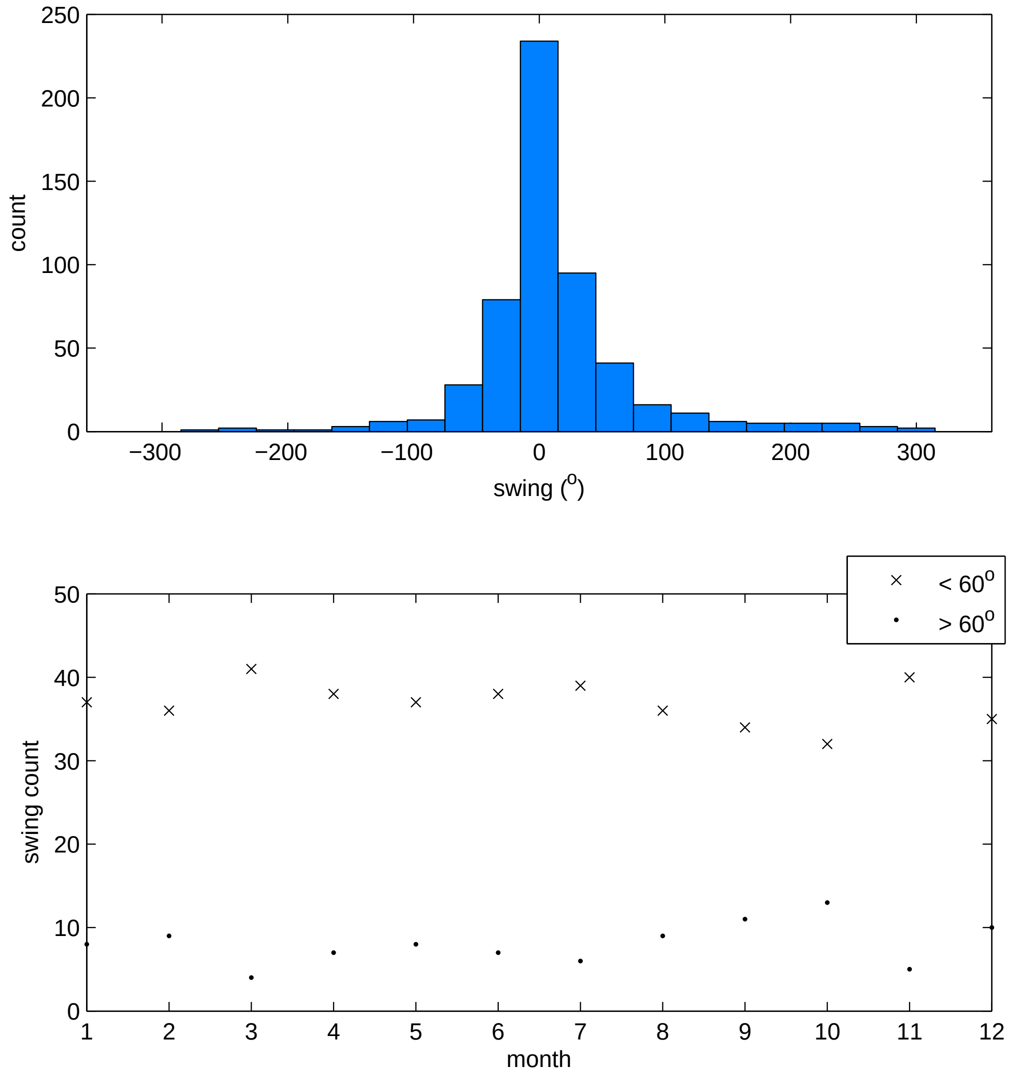

FIGURE 4.10: Distribution of wind swings for the Iceland Basin (60^{o}N 20^{o}W) from 6 hourly NCEP/NCAR reanalysis data for 2007. The top plot includes data for all months.

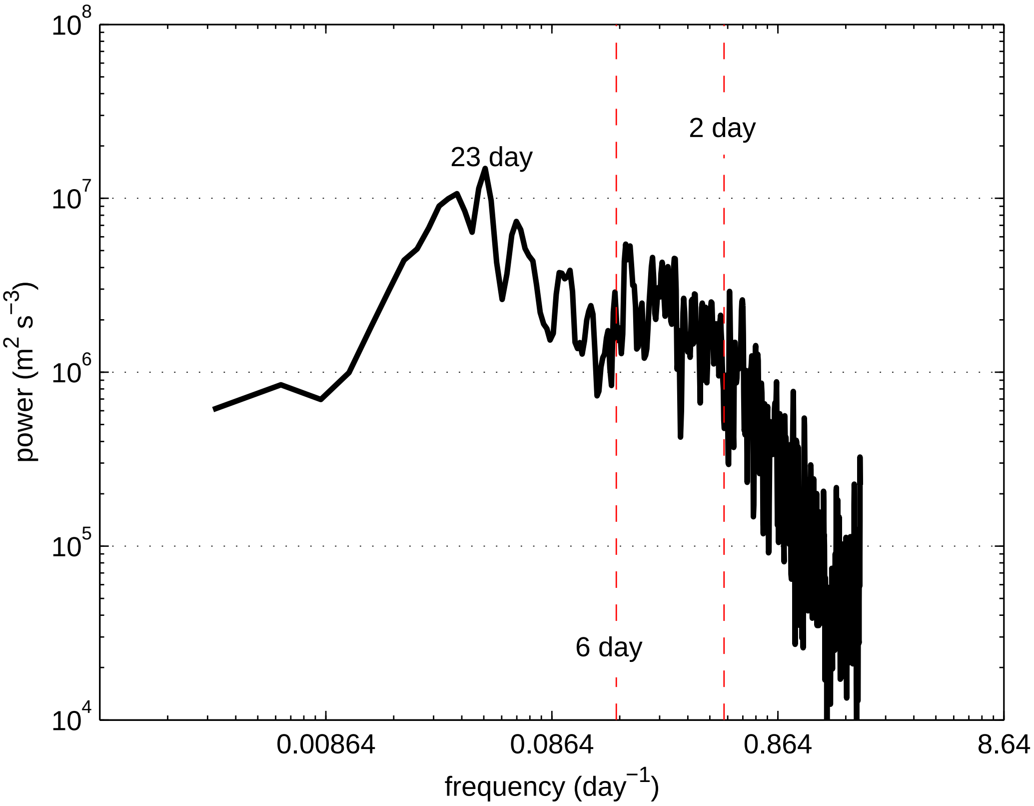

FIGURE 4.11: Power spectrum of wind speeds for the Iceland Basin (60°N 20°W) from 6 hourly NCEP/NCAR reanalysis data for 2007. A peak at 23 days is marked with dashed lines along with the cluster of peaks between 2 to 6 days period.

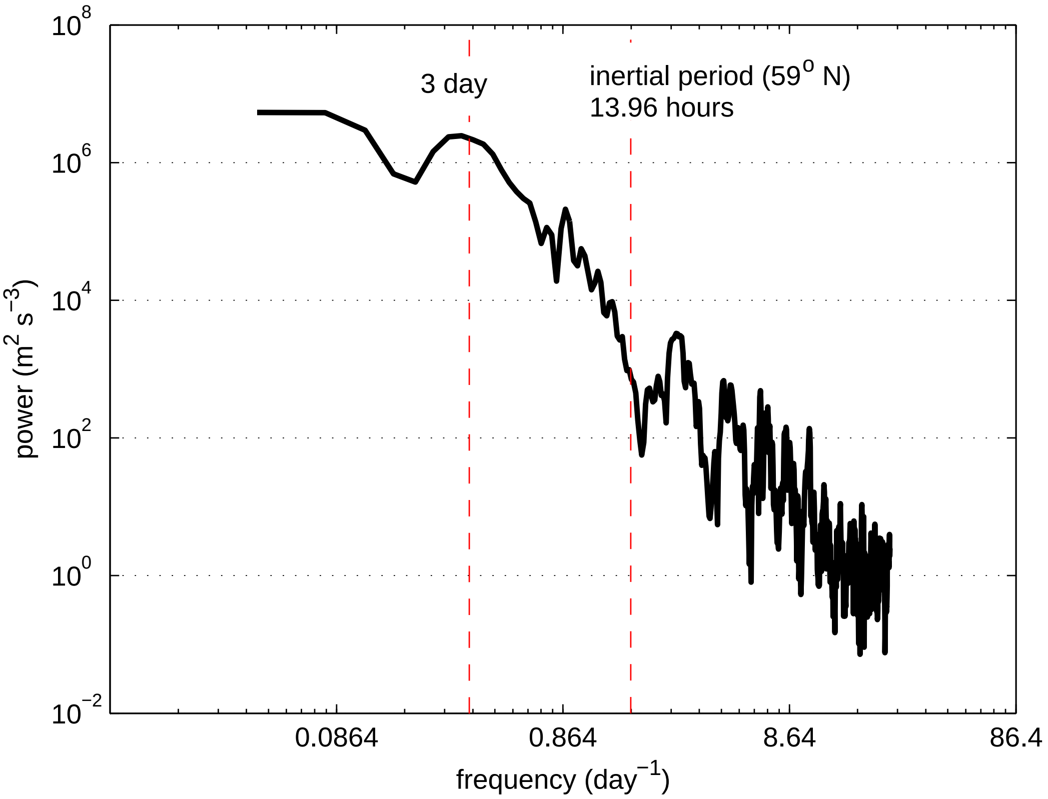

FIGURE 4.12: Power spectrum of wind speeds for the Iceland Basin (59°N 19°W) from D321 cruise data for August 2007. A peak at 3 days is marked as a dashed line. The inertial frequency for 59° N is also marked as dashed line.

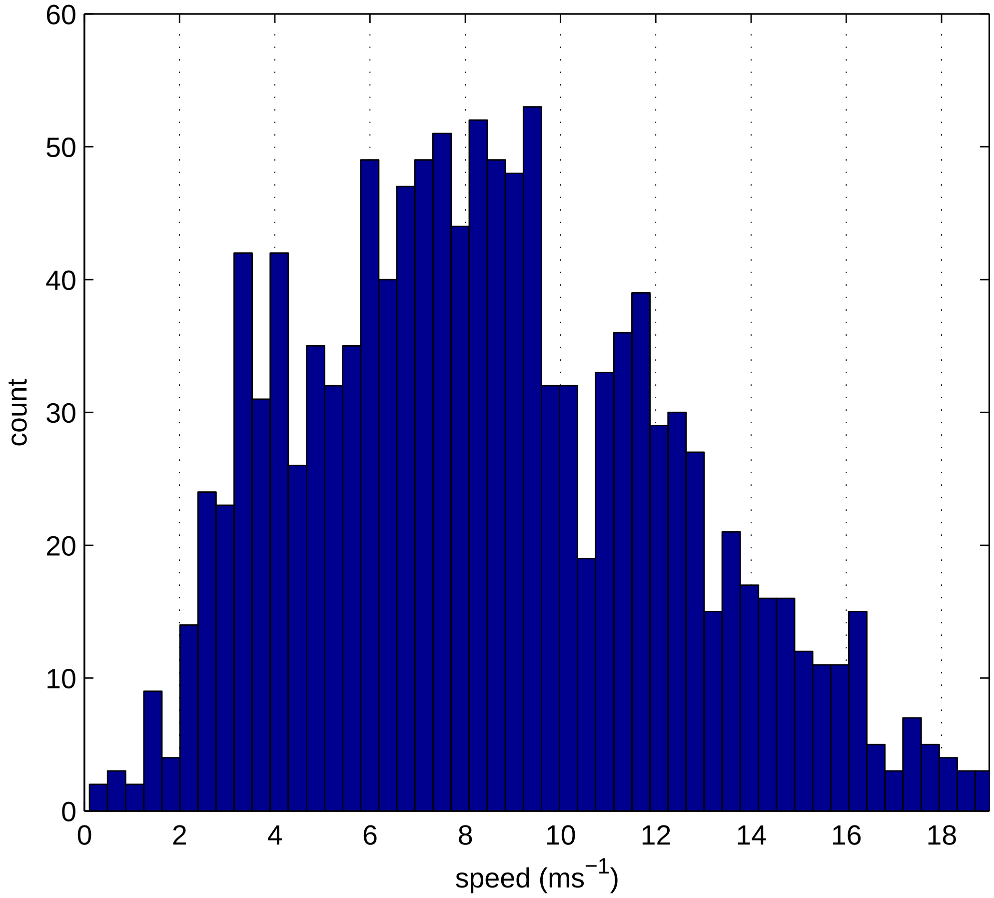

FIGURE 4.13: Distribution of the wind speeds for the Iceland Basin (59°N 19°W) from D321 cruise data for August 2007.

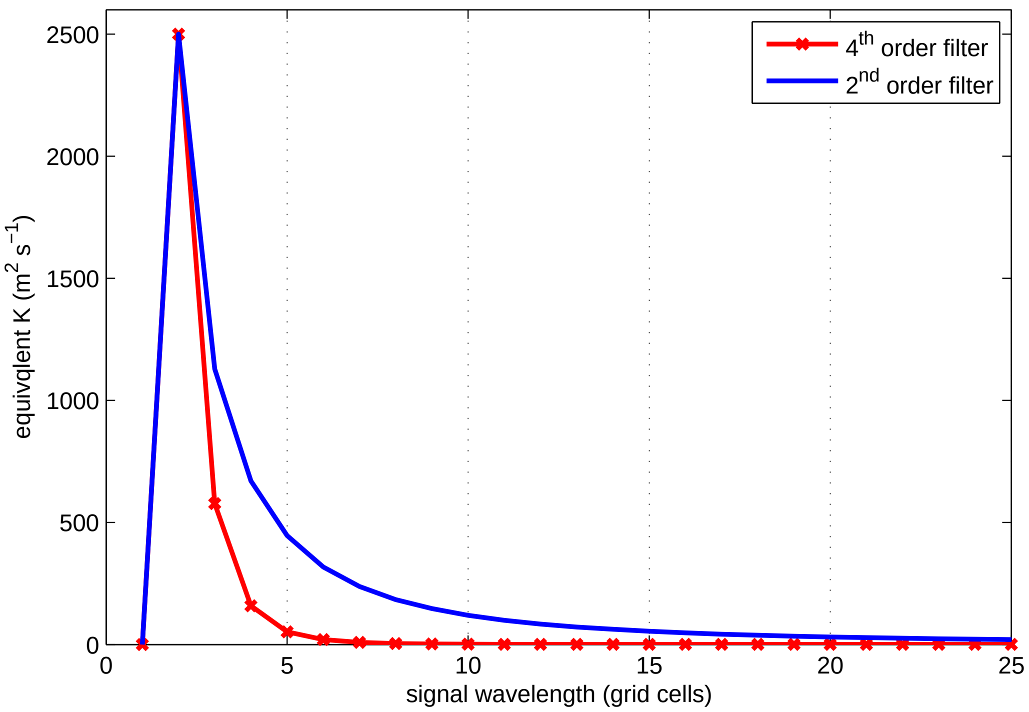

FIGURE 4.14: Equivalent diffusivity from the application of a Shapiro filter of 4^{th} and 2^{nd} order to signal of different wavelengths. Signal wavelengths are in units of grid cells (1 km length for the model in this thesis).

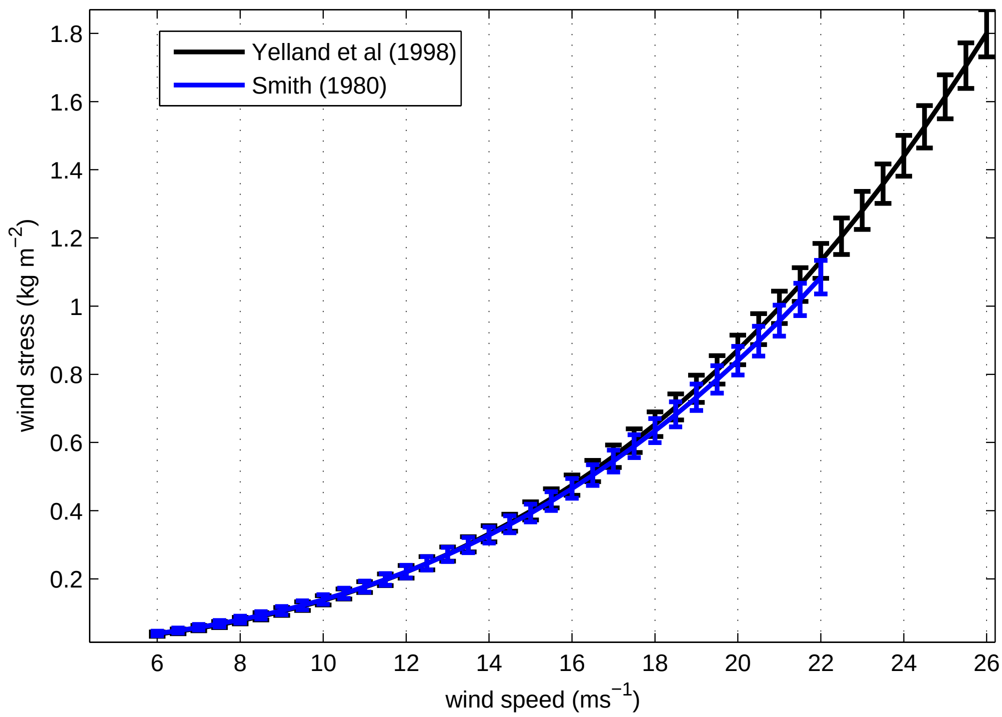

FIGURE 4.15: Comparison of the effect of using the drag coefficient calculated using the Smith (1980) formula and the Yelland et al. (1998) formula in the Bye (1986) parametrization for wind stress. Error bars represent $\pm$ 0.5 m s^{-1} water speeds with respect to the wind direction (+ in line and – opposed to the wind direction).

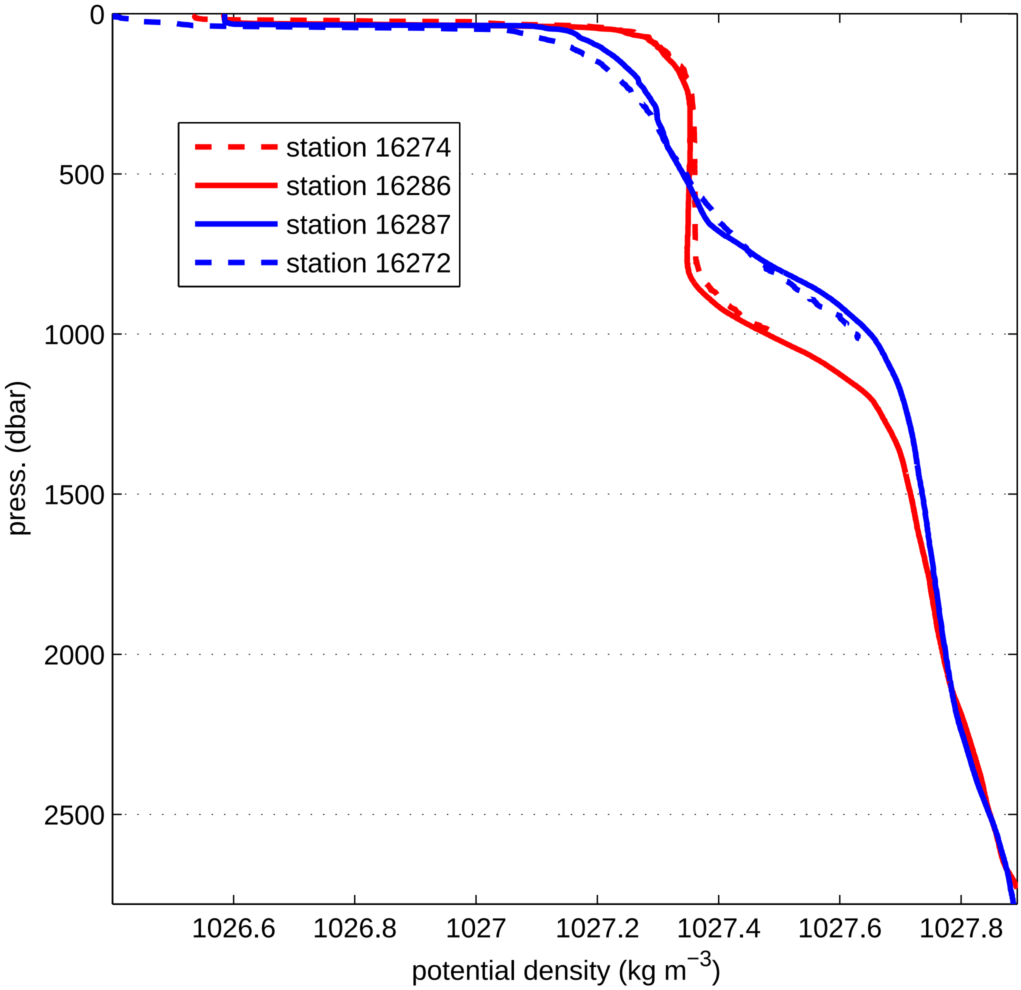

FIGURE 4.16: Potential density from conductivity-temperature-depth (CTD) stations 16272, 16274, 16287 and 16286 (see Figure 4.1 and 4.6 for station locations). Stations 16274 and 16287 are in the mode-water eddy core.

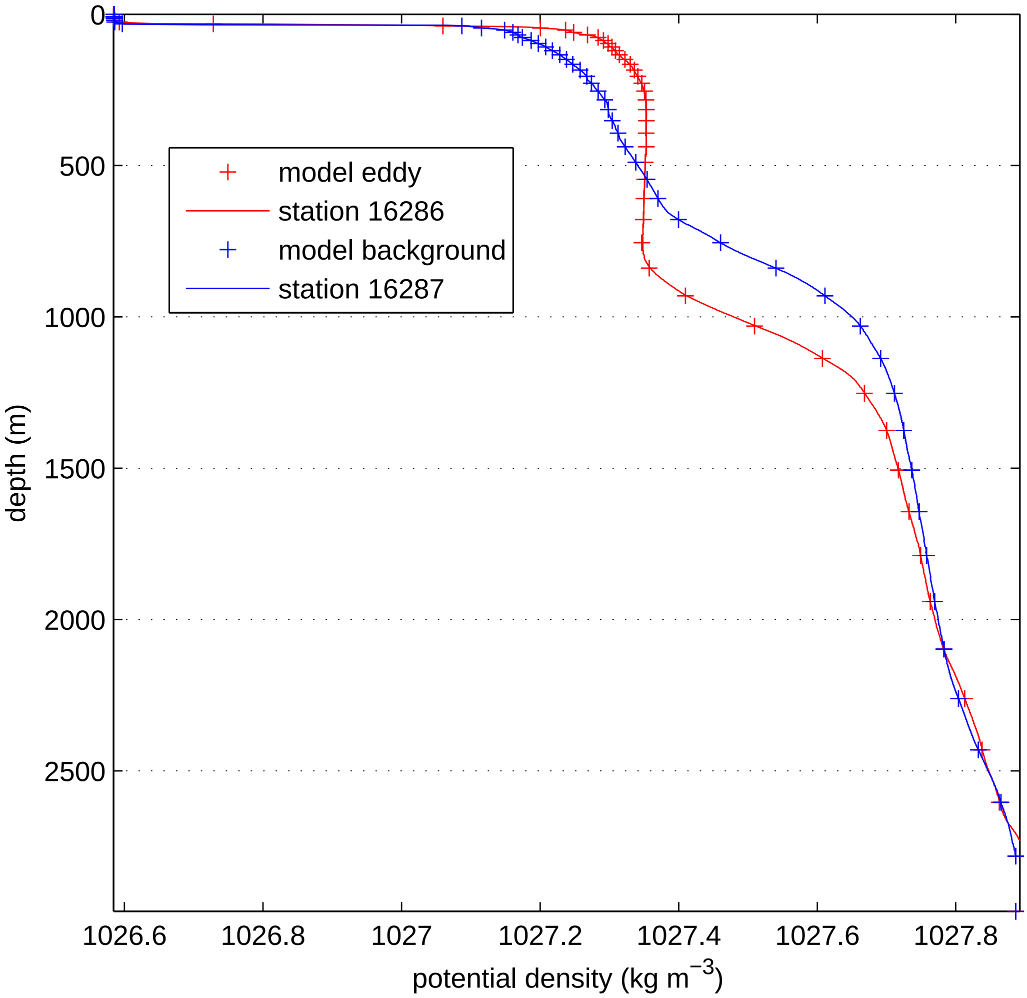

FIGURE 4.17: Potential density from conductivity-temperature-depth (CTD) stations 16287 and 16286 (see Figure 4.6 for station locations). Values used for each depth level of the mode-water eddy model are shown as crosses.

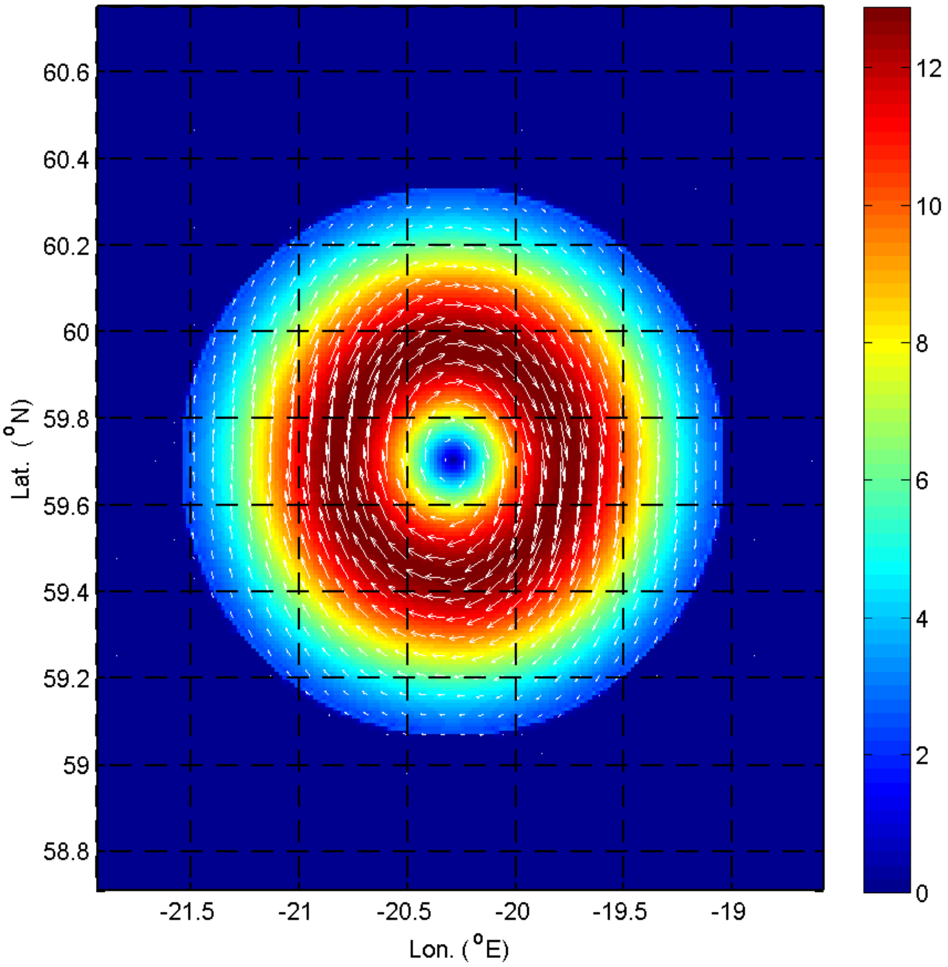

FIGURE 4.18: Barotropic velocity component of the mode-water eddy model (cm s^{-1}). Arrows indicate the direction of the circulation.

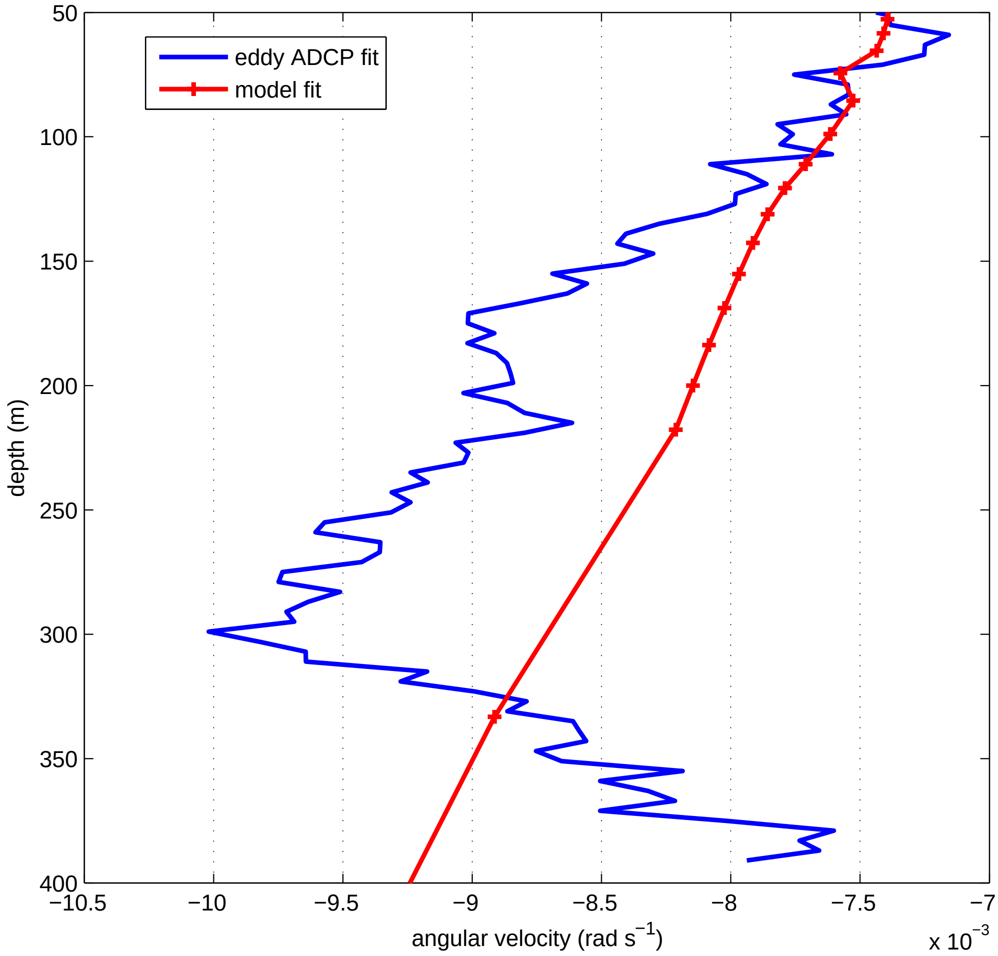

FIGURE 4.19: Comparison of model with observed peak azimuthal velocities. The peak azimuthal velocity of the mode-water eddy estimated by fitting Acoustic Doppler Current Profiler (ADCP) data from survey one to equation 4.1 as described in Section 4.2.1 for each depth level is plotted in blue. The the peak azimuthal velocity of the mode-water eddy model calculated in equivalent fashion is plotted in red. Note x-scale is from -10.5 x10^{-3} radians s^{-1} to -7 x10^{-3} radians s^{-1}.

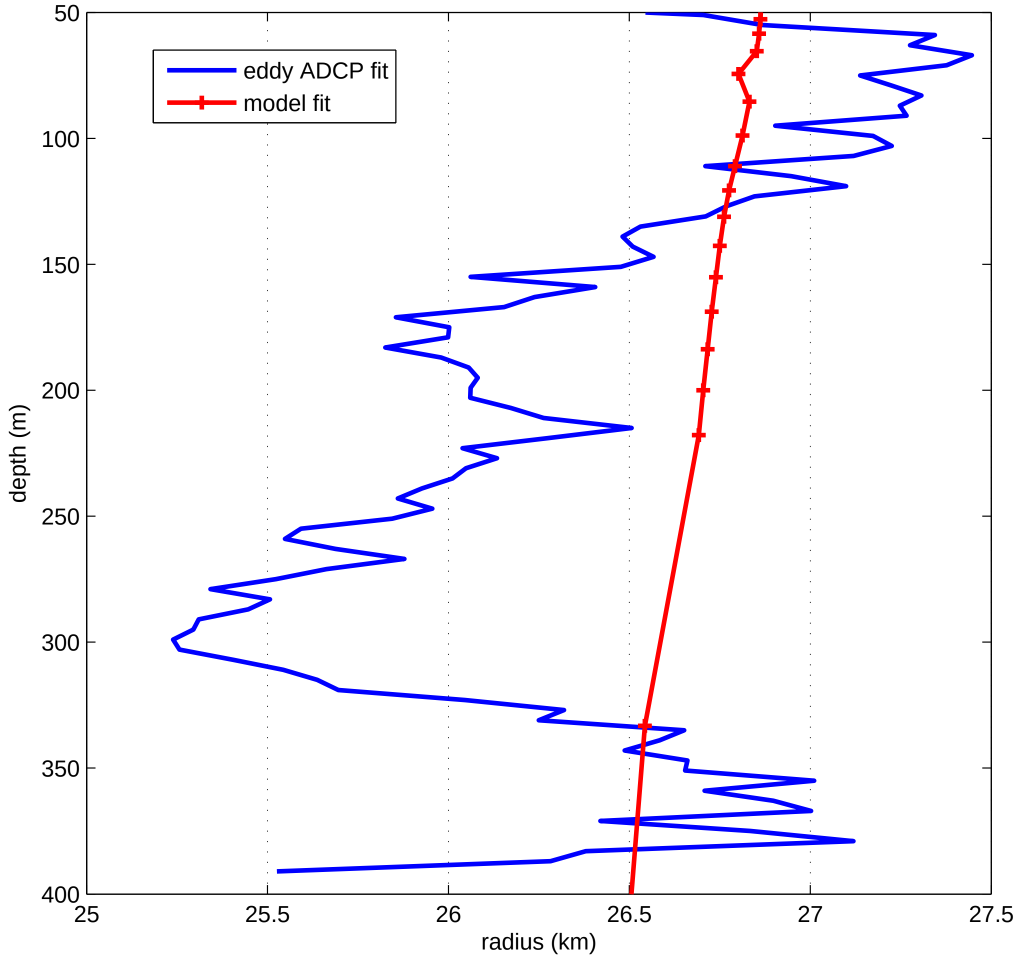

FIGURE 4.20: Comparison of model with observed radius of peak azimuthal velocity. The peak azimuthal velocity radius of the mode-water eddy estimated by fitting Acoustic Doppler Current Profiler (ADCP) to equation 4.1 as described in Section 4.2.1, for each depth level from survey one is plotted in blue. The the radius of the mode-water eddy model calculated in equivalent fashion is plotted in red. Note x-scale is from 25 km to 27.5 km.

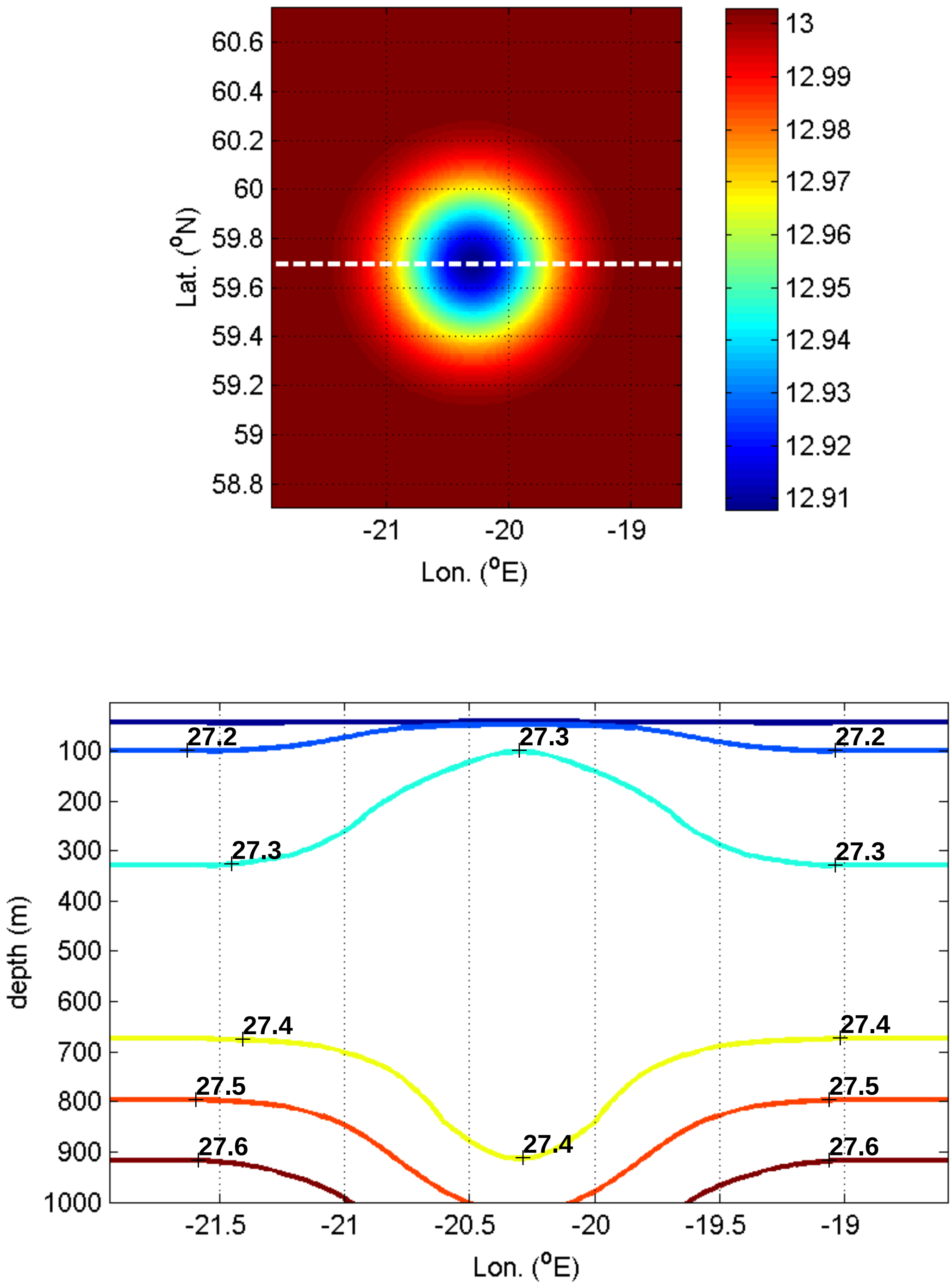

FIGURE 4.21: A contoured cross section of σ_o (contours every 0.05 kg m^{-3}) through the mode-water eddy core taken from the eddy model initial conditions (lower panel). σ_o is potential density calculated with respect to 0 dbar pressure minus 1000 kg m^{-3}. The upper panel shows the surface temperature of the mode-water eddy model and position of the density section.

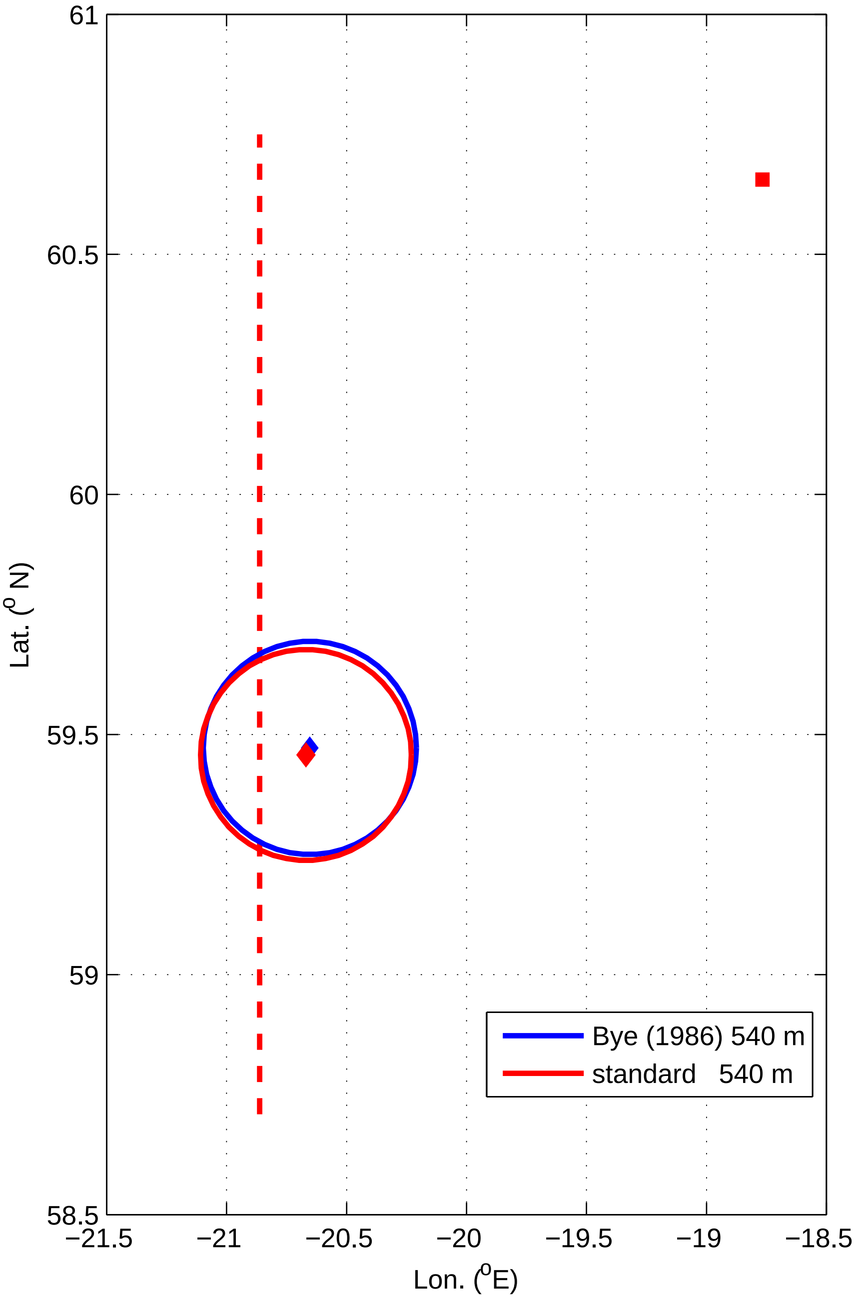

FIGURE 4.22: The position of the eddy core on day 90 of the model run estimated by fitting model velocity data at 540 m depth to equation 4.1 as described in Section 4.2.1. The position of the section through the eddy core (Figure 4.24 and 4.27) is shown as are the positions where the potential density profiles were calculated (Figure 4.23 and 4.26).

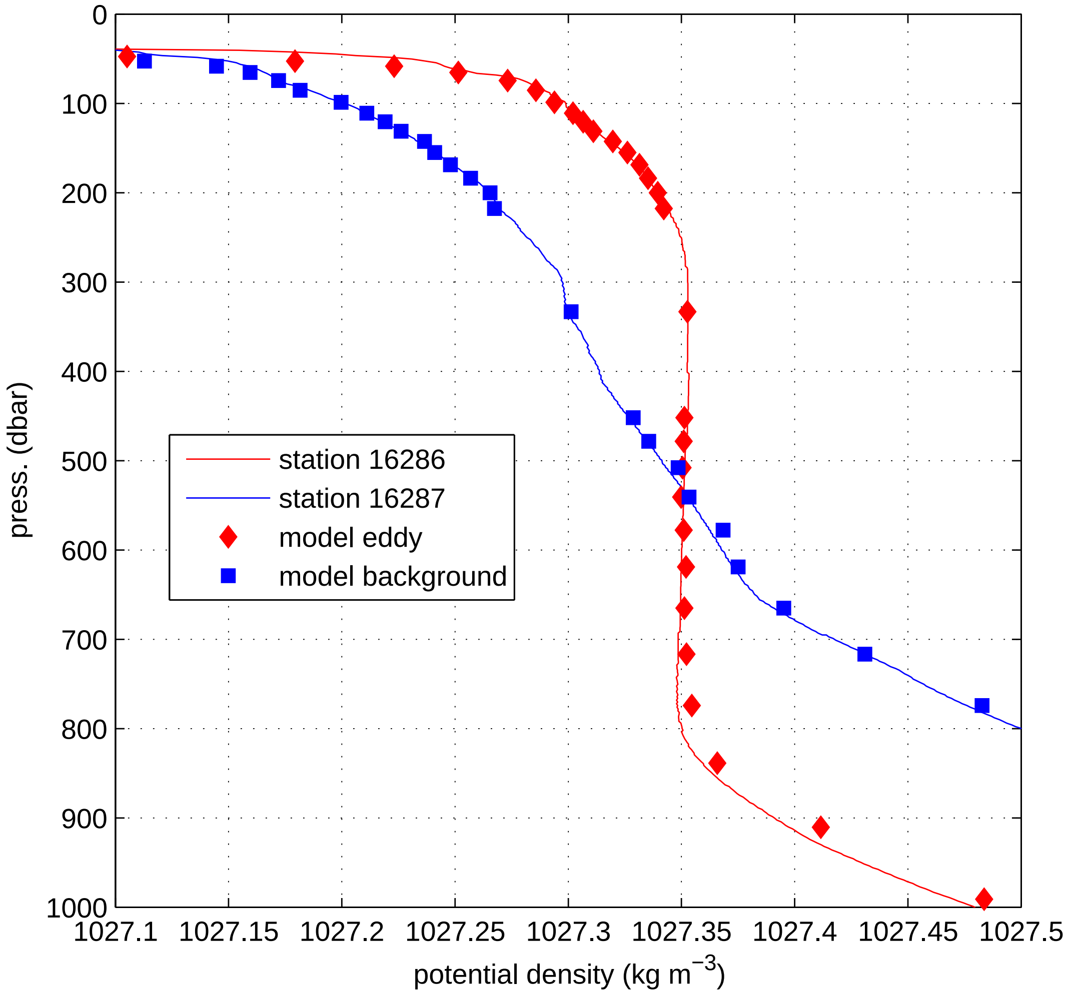

FIGURE 4.23: Potential density from conductivity-temperature-depth (CTD) stations 16287 and 16286 (solid lines, see figure 4.6 for station locations). Values of density for each depth level of the eddy model after 90 days using a constant zonal wind and the standard wind stress parametrization are shown. The positions relative to the eddy where the model density profiles were calculated is shown in Figure 4.22.

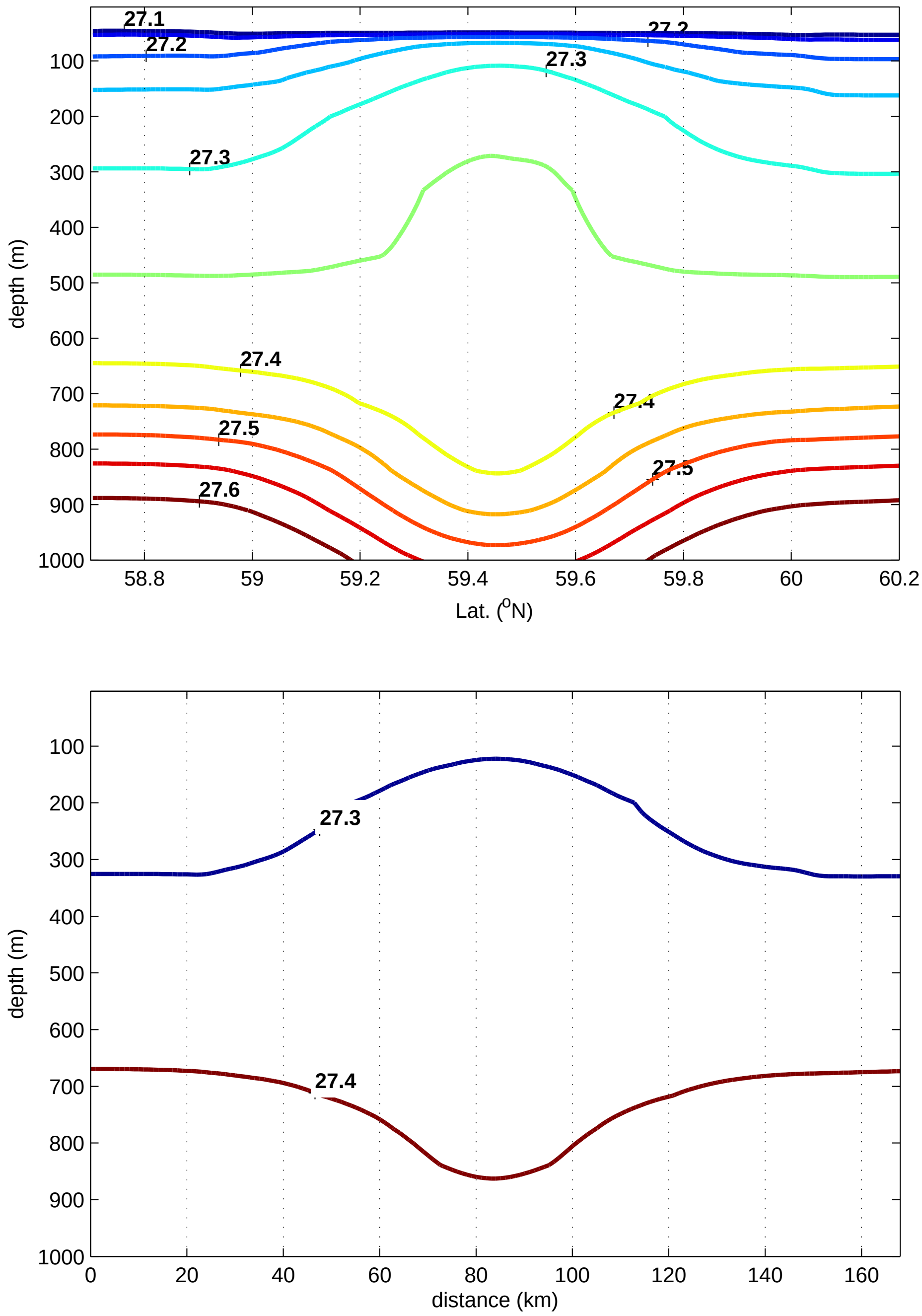

FIGURE 4.24: A contoured cross section of density (σ_o contours every 0.05 kg m^{-3}), offset as in Figure 4.22, after 90 days using a constant zonal wind and the standard wind stress parametrization (upper panel). σ_o is density calculated with respect to 0 dbar pressure minus 1000 kg m^{-3}. A cross section of potential density showing σ_o contours 27.3 and 27.4 kg m^{-3} which delimit the mode-water eddy core, offset as in Figure 4.22 after 90 days using a constant zonal wind and the standard wind stress parametrization (lower panel).

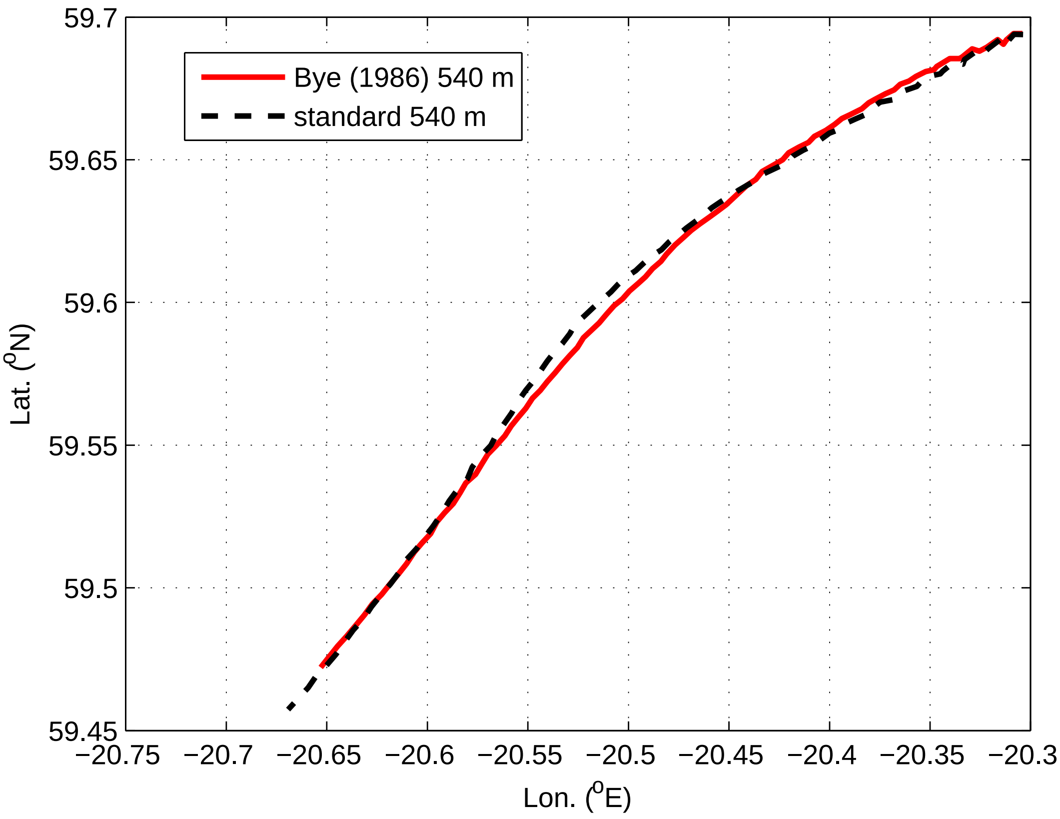

FIGURE 4.25: Position of the model mode-water eddy core at 540 m depth estimated by fitting model velocity data to equation 4.1 as described in Section 4.2.1 for models using both the standard and the Bye (1986) wind stress parametrization.

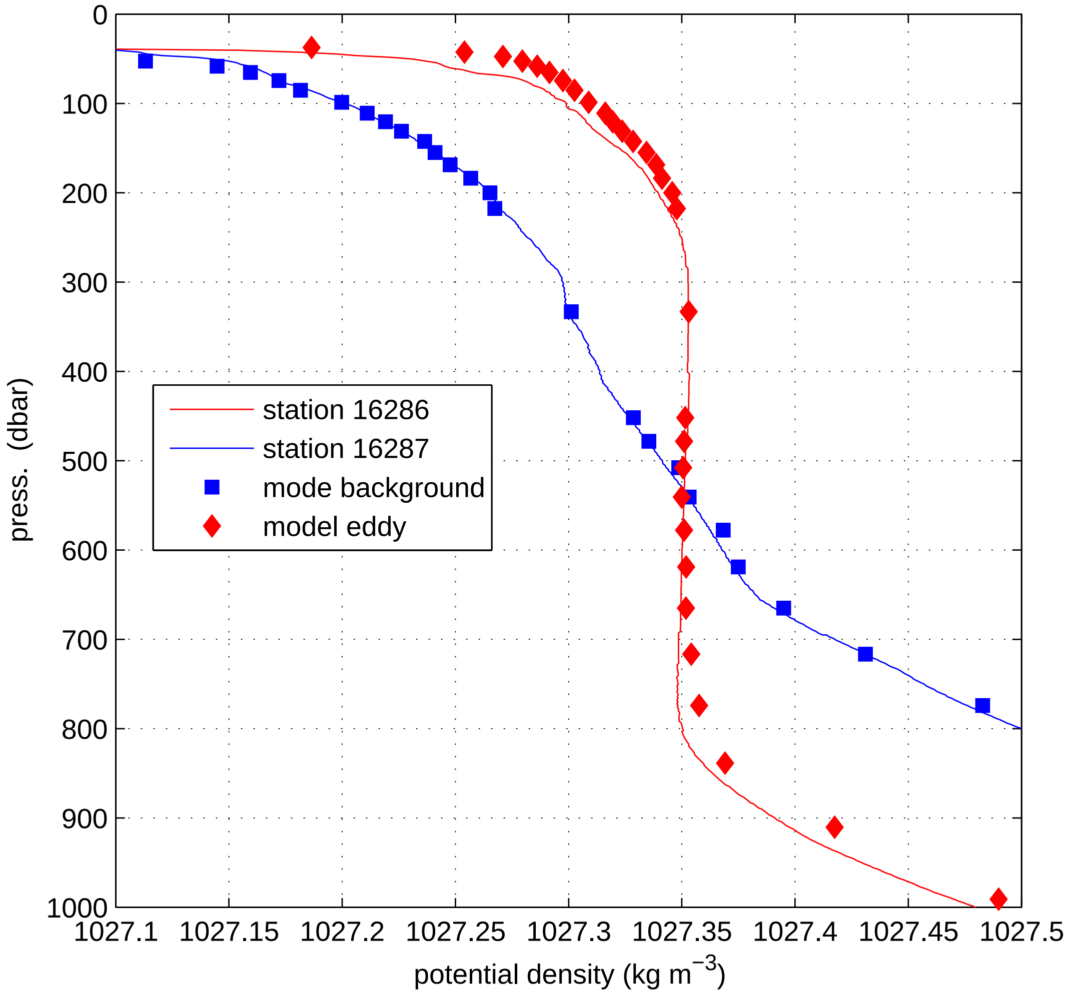

FIGURE 4.26: Potential density from conductivity-temperature-depth (CTD) stations 16287 and 16286 (solid lines, see Figure 4.6 for station locations). Values of density for each depth level of the eddy model after 90 days using a constant zonal wind and the Bye (1986) wind stress parametrization are shown. The positions relative to the eddy where the model density values were calculated is shown in Figure 4.22.

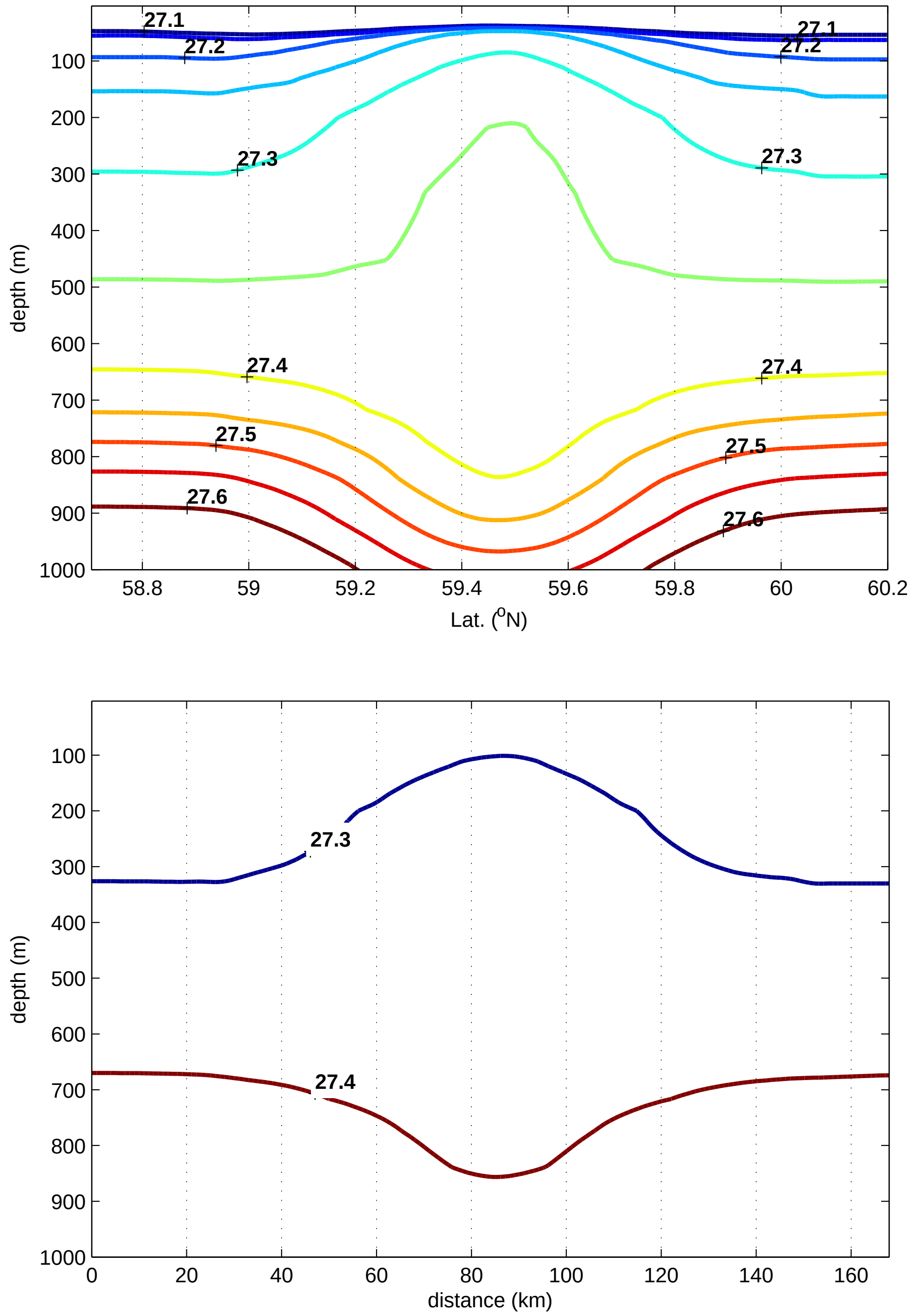

FIGURE 4.27: A contoured cross section of density (σ_o contours every 0.05 kg m^{-3}) offset as in Figure 4.22 after 90 days using a constant zonal wind and the Bye (1986) wind stress parametrization (upper panel). σ_o is density calculated with respect to 0 dbar pressure minus 1000 kg m^{-3}. A cross section of potential density showing σ_o contours 27.3 and 27.4 kg m^{-3} which delimit the mode-water eddy core, offset as in Figure 4.22 after 90 days using a constant zonal wind and the Bye (1986) wind stress parametrization (lower panel).

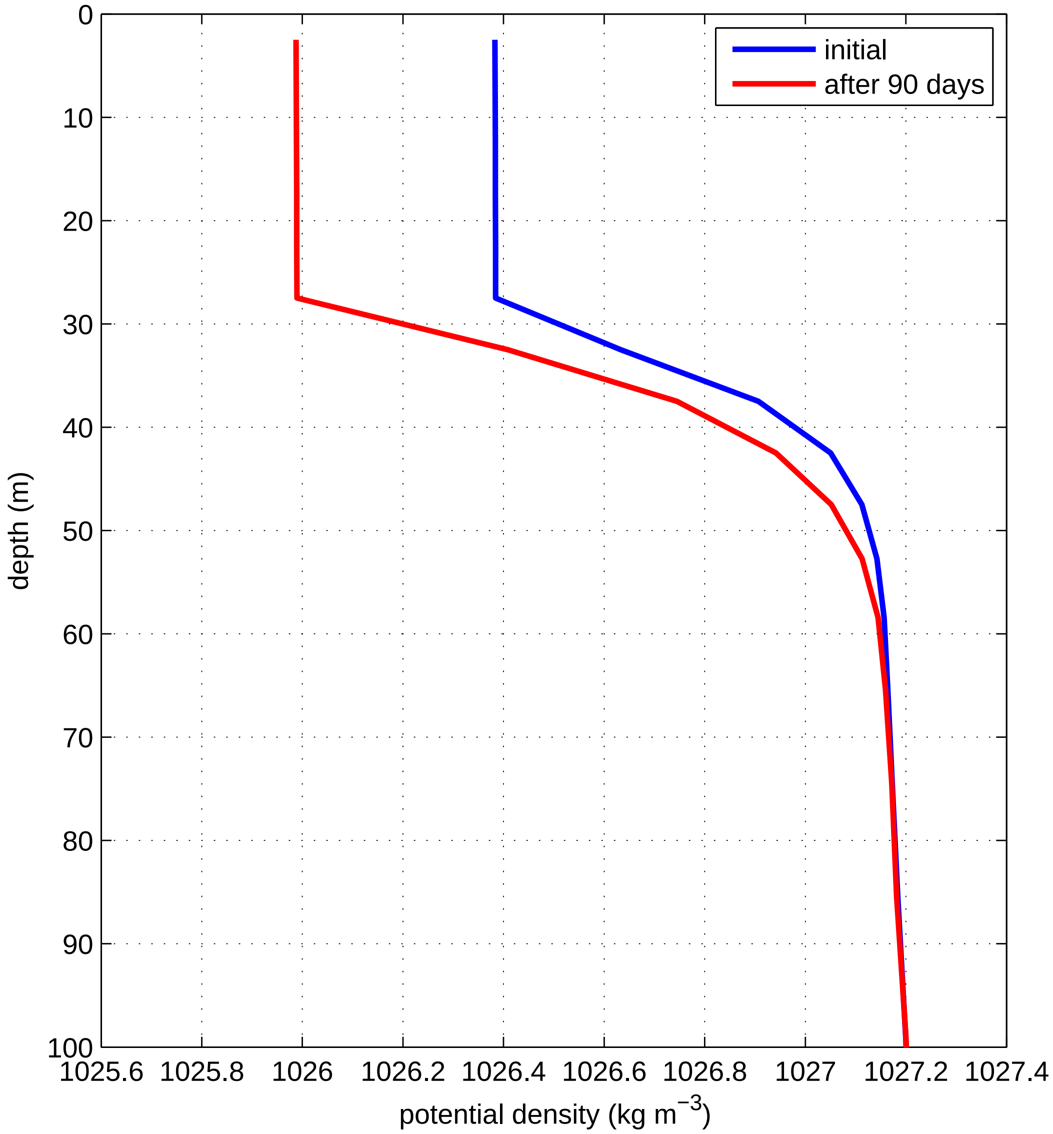

FIGURE 4.28: Values of density for each depth level of the eddy model taken at the position away from the eddy shown in Figure 4.22. The blue line shows the density on day one of the model run, the red line after 90 days forced by a constant zonal wind and the Bye (1986) wind stress parametrization.

Chapter 5

Modelling nutrient supply in a mode-water eddy

5.1 Introduction

The objective of this chapter is to use the eddy model developed in Chapter 4 to examine the effect of interactions between the eddy and the wind on vertical nutrient fluxes. The vertical flux will be quantified and the contribution of vertical effective diffusive flux (hereafter referred to as the diffusive flux) to total vertical flux investigated. The model study will be restricted to Ekman suction, sub-mesoscale physics and enhanced vertical mixing processes. Neither convective formation nor eddy pumping will be considered as the former is beyond the scope of the model and the latter has already been extensively studied (e.g. McGillicuddy and Robinson 1997; Oschlies and Garcon 1998; McGillicuddy et al. 1998, 1999; Oschlies 2001, 2002*a*,*b*; McGillicuddy et al. 2003; Martin and Pondaven 2003).

5.2 Model output and analysis

The eddy model was constructed and initialised as described in Chapter 4. For each wind forcing scenario (described in Chapter 4, summarised in Table 5.1) the model was run for a period of 90 days using both the standard and Bye (1986) wind stress parametrizations (Chapter 4). A period of 30 days, the length of the recorded cruise D321 wind data (Chapter 4), was allowed at the start of each run for the model to 'spin up'. A maximum run duration of 90 days was selected as being the longest duration for which the eddy remains further than 50 km from the model boundary, where 50 km is the approximate radius of the eddy (Chapter 4).

Inert tracer one (T_1) was initialised, on day 30 of each model run, at an arbitrary concentration of 1 unit m^{-3} for grid levels 13 (65 m) and below and at 0 units m^{-3} above. Tracer T_1 is used to estimate directly tracer fluxes into the eupthotic zone. Tracer fluxes into the euphotic zone were calculated by measuring the changes in concentrations of T_1 above an assumed 65 m euphotic depth. A depth of 65 m was selected to correspond with observations of the base of the euphotic zone during cruise D321 (Chapter 2). For each model grid box above the euphotic depth T_1 concentrations were converted into tracer volumes. The total T_1 flux between successive model outputs was then calculated by first order differencing the calculated tracer volumes.

A second inert tracer, (T_2), was initialised at an arbitrary concentration of 1 unit m^{-3} in a horizontal layer one vertical model grid box thick (8m) at model grid level 13 (65 m). Tracer T_2 is used to estimate time integrated up-welling speed for a tracer initially released at the base of the assumed euphotic zone.

5.2.1 Potential issues with model output

Model output was sampled for each grid point of the model once a day (24 hours) for all model runs. Model output included, temperature, salinity, horizontal velocity components, inert tracer concentrations (T_1 and T_2), inert tracer horizontal and vertical advective fluxes (T_1 only), inert tracer vertical diffusive flux (T_1 only), and vertical turbulent diffusion coefficient (K). Temperature, salinity, inert tracer concentrations, and horizontal velocity components were output as the instantaneous snapshot value of the quantity on the output time-step. Inert tracer fluxes and vertical turbulent diffusion coefficient were output as a mean value for the output period, i.e. as a mean of the preceding 24 hours' model time.

Horizontal effective diffusion is not explicitly represented within the model. The Harvard Ocean Prediction System (HOPS) uses a Shapiro filter (Shapiro, 1971) both to maintain model numerical stability and as a proxy for horizontal effective diffusion (Chapter 4). Horizontal effective diffusion of the inert tracer was estimated for scenario Rrr (described in Table 5.1) and found to be at least four orders of magnitude lower than the vertical diffusive flux and two orders of magnitude lower than the horizontal advective flux (Appendix A). Consequently horizontal effective diffusion has not been considered further.

HOPS uses a 'leapfrog' time-stepping scheme, with a periodic (every 10 time-steps) Euler forward time-step (Chapter 4). To best match the changes in the inert tracer concentration over the output period, twice the calculated model fluxes are stored every second time-step. At the end of the output period the mean, over the output period, of the stored fluxes is output with the tracer fields. Consequently, there is no exact correspondence between the output tracer fluxes and the output tracer concentrations at a give time step (Appendix A). Nevertheless, the output fluxes compare to changes in the output tracer concentration accurately enough to be representative of the fluxes occurring between model output intervals (Appendix A).

The diffusive flux in the model will potentially consist of both shear driven vertical diffusion and enhanced vertical diffusion arising from a convective adjustment process (Chapter 4). The Richardson number parametrization of vertical mixing used in the eddy model is considered to be valid for the range of Richardson numbers produced by the eddy model (Appendix A). Convective adjustment is implemented in the model as a large turbulent diffusion coefficient (0.03 m^2 s^{-1} Chapter 4) which is four orders of magnitude above the lowest (background) value of the Richardson number vertical mixing parametrization (8 $x10^{-6}$ m^2 s^{-1} Chapter 3).

In order to diagnose if any of the output vertical diffusion was likely to have resulted from a model convective adjustment, model runs where the output mean turbulent diffusion coefficient was an order of magnitude or more above the background value were re-run with model output of turbulent diffusion coefficient and horizontal velocity components sampled every three hours. A three hour output sample interval means that the model outputs every 108 time steps. If convective adjustment occurs for one time step and the turbulent diffusion coefficient is background at all other times, the value of the turbulent diffusion coefficient output by the model will be 2.85 $x10^{-4}$ m^2 s^{-1}. Values of the turbulent diffusion coefficient in the model output larger than this value indicate that convective adjustment may have occurred at some time since the last output.

5.2.2 Model sub-domains

Inert tracer T_1 fluxes were only considered over a sub-domain of the model to minimise any numerical affects associated with the model boundary conditions (Chapter 4). As the eddy moved within the model domain during the course of a run (Chapter 4) the model sub-domain was defined dynamically relative to the centre of the eddy.

In order to diagnose the spatial distribution of tracer flux around the eddy, the model was divided into three concentric circular zones about the eddy centre at any given instant. Zone 1 was defined as the area within a radius of 25 km, which is approximately the radius of peak azimuthal velocity for the eddy (Chapter 4). Zone 2 was defined as the area within a radius of 50 km, which is the approximate radius of the model eddy as diagnosed by displacement of isopycnals (Chapter 4). Zone 3 was defined as the area within a radius of 70 km The radial distribution of fluxes was further studied by dividing the region between the 25 km core and 70 km from the centre into nine 5 km width concentric annuli concentric with the eddy centre (Figure 5.1).

5.2.3 Determining the centre of the eddy

The position and diameter of the eddy was estimated from the model horizontal velocity field for a chosen depth level, for definition of the eddy sub-domains, by fitting a velocity profile of the form

$$V(r) \;=\; V_0\left(\frac{r}{R}\right)\exp\left[\frac{1}{2}\left(1-\frac{r^2}{R^2}\right)\right] \tag{5.1}$$

(Martin and Richards, 2001) where $V(r)$ is the azimuthal velocity at radius r from the eddy centre, V_o is the maximum azimuthal velocity, and R is the radius of maximum azimuthal velocity. Visual examination of the model horizontal velocity fields indicated that, though the eddy appears to retain a roughly circular shape throughout the model runs, the azimuthal velocity in some cases is not uniform at a given radius. Consequently, to allow more accurate diagnosis of the eddy centre

$$V_0 \;=\; \left(\frac{(V_{max}-V_{min})}{2}\right)\cos(\theta-\theta_0) \;+\; \frac{(V_{max}+V_{min})}{2}$$

is used where V_{max} and V_{min} are maximum and minimum azimuthal velocities, θ_o is the bearing, with respect to due East, of the peak azimuthal velocity V_{max} and θ the bearing of $V(r)$.

For each model output, values of V_{max}, V_{min}, R and, θ_o, for an eddy centred at position x, y were fitted to the model horizontal velocity field output for the chosen depth level by minimising the root mean square difference between the calculated velocity field and the model output horizontal velocity field. Visual comparison of the fitted equation 5.1 to the model horizontal velocity fields provided a basic check on the method, as did comparison of the azimuthal velocities for both the model and the fit to equation 5.1. The positions of the zones used when calculating inert tracer fluxes were determined using the position of the centre of the eddy, calculated as described above, for depth level 13 (65 m).

5.2.4 Estimating mean tracer flux

There are two sources of variability that need to be addressed for an accurate estimation of fluxes. Instantaneous values of inert tracer flux calculated at a fixed depth level can be expected to include potentially significant amounts of ephemeral reversible fluctuations. These fluctuations are due to the vertical oscillations of density surfaces arising from internal wave motions and are spatially and temporally heterogeneous. Internal wave motions can be expected to occur at the model's inertial period (13.9 hours at 59^{o} N) and at periods associated with the wind forcing.

Additionally, tracer flux calculated at a fixed depth level over a fixed sized sub-domain of the model may exhibit fluctuations in tracer flux as the eddy horizontal circulation moves patches of tracer horizontally in or out of the sub-domain. In this thesis the zones for calculating tracer fluxes are circular and positioned relative to the eddy centre (Section 5.2.2) to minimise the effect of such fluctuations. However, inaccuracy in estimating the position of the eddy centre from one model output to the next may also introduce a fluctuation in the tracer flux calculated at a fixed depth level in each zone. Nevertheless, the effect of these positional fluctuations is considered to be small and of the order of 10 % of the calculated flux (Appendix A).

5.2.4.1 Spatial averaging

For each of the three model sub-domains and the nine concentric annuli, described above, the tracer flux, calculated as described in Section 5.2, was first spatially averaged over the area of the sub-domain or annulus for each model output.

5.2.4.2 Temporal averaging

In order to minimise the impact of adiabatic fluctuations in tracer flux on the calculations of mean inert tracer T_1 flux for the model zones, fluxes were not only spatially averaged for the zone, but also temporally averaged over the duration of the model run. In addition to only calculating tracer fluxes within the previously discussed model zones (Section 5.2.2), in order to minimise any inert tracer fluxes into the zones potentially due to boundary effects, estimates of tracer flux for the zones were limited to the period of the model run where the edge of zone 3 is sufficiently far away from the model boundary.

The eddy centre position was analysed (see above) for all runs. The earliest that the eddy centre approaches within 71 km of the model western boundary is on day 76 of the run using the standard wind stress parametrization with realistic winds (run Rrr, Table 5.1). As the model has a horizontal grid resolution of 1 km this means that the edge of Zone 3 is only one grid cell away from the model boundary. Tracer concentrations within a grid cell of the model boundary are subject to modification by the model boundary condition (Chapter 4). Consequently, estimates of tracer fluxes were restricted to a 45 day period between day 30 (inert tracer release) and day 75 for all model runs.

5.2.4.3 Calculating temporal mean tracer flux

Where tracer fluxes within a zone showed a trend with time, the mean tracer flux at the start and end of the period was estimated by fitting a trend line. Examining the inert tracer T_1 fluxes from the model indicated that there was evidence for two types of trend in the model output flux data. Diffusive flux commonly showed evidence of a trend of the form

$$Y = \frac{A}{t} + C \tag{5.2}$$

(Figure 5.2), where A and C are constants. There was also evidence of a linear trend

$$Y = At + C \tag{5.3}$$

in both vertical advective flux and in total euphotic zone inert tracer flux in some model output (Figure 5.2).

Trend lines of the form of equations 5.2 and 5.3 were both fitted to the model inert tracer flux data by minimising least squares residuals (Emery and Thomson, 1997).

The trend line with the lowest least squares residual was selected as the best fit. A standard estimate of error (s_e) for the trend was calculated

$$s_e = \sqrt{\frac{1}{N-2}\sum_{n=1}^{n=N}[Y_d(n) - Y(n)]^2}$$

(Emery and Thomson, 1997) where $[Y_d(n) - Y(n)]^2$ is the square of the difference between the fitted trend and actual data value for point n, and N is the number of data points.

Due to the magnitude of the fluctuations in model output for some inert tracer fluxes, typically the vertical advective and total euphotic zone fluxes, it was often not obvious whether there was a trend to the flux data (Figure 5.2). A tracer flux was considered to be showing a trend only if the fitted trend line had a correlation of determination, R^2 (Chapter 3), greater than 0.1. Diffusive fluxes where there is clearly a trend (for example Figure 5.2, top panel) typically have an R^2 value in the range of 0.2 to 1. The R^2 values for fluxes where there is clearly no trend are typically lower than 0.01 (for example Figure 5.2, bottom panel). R^2 values in the range 0.01 to 0.2 are indeterminate indicating neither a trend nor lack of a trend. The value of $R^2 = 0.1$ was selected as a criteria to only eliminate the least representative of the fitted trends from consideration. Where there was no clear temporal trend to the inert tracer flux the mean value was calculated for the whole period.

5.2.5 Estimating tracer stripe depth

Vertical velocity can be output from the model as a snapshot value on the output time-step for a given depth level. However, in common with the vertical advective fluxes, vertical velocity fluctuates to high degree between model outputs. Consequently, the change in depth of the inert tracer T_2 stripe is used to get a more reliable estimate of net time integrated up-welling speed. The depth of T_2 still fluctuates between successive model outputs, but the degree of fluctuation is orders of magnitude less than for the vertical velocity.

The depth of the inert tracer T_2 (D_{stripe}) was estimated by calculating a weighted mean of the inert tracer T_2 concentration

$$D_{stripe} = \frac{\sum_{i=1}^{i=N_{lev}}[T_2(i)\ d(i)]}{\sum T_2(i)} \tag{5.4}$$

where N_{lev} is the number of depth levels in the model, $T_2(i)$ is the concentration of T_2 in level i and $d(i)$ is the depth of the centre of level i. Calculation using a weighted mean gives a continuous estimation of tracer stripe depth despite the discrete vertical structure of the model grid.

Vertical diffusion can affect the calculated tracer stripe depth in two ways. Asymmetric vertical diffusion on the upper and lower surfaces of the stripe due to vertical variations in turbulent diffusivity can lead to an asymmetric spread of the tracer stripe which will change the calculated stripe depth independent of the effect of any vertical velocity. Symmetric vertical diffusion applied to a tracer strip in a non-regular spaced vertical grid can also result in a change in calculated tracer stripe depth. For example, consider two simple three-box models. Box-model 1 has a regular vertical grid with 4 m vertical thickness. The depths of the level midpoints are 2 m, 6 m, and 10 m respectively and the total depth is 12 m. Box-model 2 has an irregular grid of vertical thickness of 1 m, 4 m, and 7 m respectively. The depths of the level midpoints for box-model 2 are 0.5 m, 3 m, and 8.5 m and the total depth is once again 12 m. Both models are initialised with a tracer in level 2 of concentration 1 unit and none elsewhere. The initial depth of the tracer stripe in box-model 1 is 6 m and in box-model 2 is 3 m. A uniform diffusion is applied to the tracer concentrations in both models until a steady state is reached, at which point the tracer concentration in each layer is 0.333 units. Using equation 5.4 to calculate the tracer stripe depths gives 6 m for box-model 1 and 4 m for box model 2. Consequently, to give a more accurate estimation of the time integrated up-welling speed the effect of vertical diffusion should be accounted for when estimating changes in tracer stripe depth.

The effects of vertical diffusion on the tracer stripe depth were estimated in the following way. A 3D grid was constructed of the same dimensions as the for eddy model (Chapter 4) and a tracer stripe was initialised in a horizontal layer one vertical grid box thick (8m) at grid level 13 (65 m) to duplicate the initial tracer T_2 injection into the eddy model (Section 5.2). Turbulent diffusion coefficients output from the eddy model at each grid point on day 30 were applied to the tracer distribution. The new concentration of tracer in each grid box was calculated and the tracer stripe depth estimated using equation 5.4. The process was repeated using successive model output turbulent diffusivity coefficients for all 45 days of the model run. The resultant tracer stripe depths, calculated at each horizontal grid point in the 3D model, were then subtracted from the initial 3D model tracer stripe depth to give the change in depth of the tracer stripe due to diffusion.

The change in tracer stripe depth due to diffusion, estimated as described above, was subtracted from the depth of the inert tracer T_2 stripe calculated from the eddy model output for this tracer. The result of this correction is that the depth of the inert tracer T_2 stripe from the eddy model then gives an estimate of the vertical movement of the inert tracer stripe due to advection only.

5.2.5.1 Estimating vertical advective flux

In addition to estimating the flux of T_1 into the euphotic zone due to vertical advection from the model output advective fluxes, a second estimate of the flux of T_1 into the euphotic zone due to vertical advection was calculated using the change in depth of the inert tracer T_2 stripe. For each model output the difference between the inert tracer T_2 stripe depth, corrected for the effect of diffusion, and the initial inert tracer T_2 stripe depth was calculated for each grid point. This vertical distance was then converted into a tracer volume by multiplying it by the area of each grid cell (1x1 km) and by the initial tracer concentration of T_1 (1 unit m^{-3}). The T_1 flux into the euphotic zone between successive model outputs was then estimated by first order differencing the calculated tracer volumes and dividing by the intervening time period.

5.3 Results

The results are presented in the following order. The total flux of tracer into the euphotic zone is presented followed by the results for the individual diffusive and advective flux components. The spatial mean of the fluxes for the three eddy sub-domains are considered as well as the radial distribution of flux across the nine concentric annuli. Runs using both wind stress parametrizations are considered in turn for each flux.

5.3.1 Total tracer flux into the euphotic zone

5.3.1.1 Standard wind stress parametrization

The mean fluxes of the inert tracer T_1 into the euphotic zone for all runs, except Sch, Rrc and, Rrr, are equal to the mean fluxes for the NW run and show the same trend of a decreasing mean flux from day 30 to day 75 of the run. T_1 mean fluxes decrease by approximately 60 % from 0.1 to 0.04 units m^{-2} day^{-1} for zones 2 and 3 and by approximately 70 % from 0.1 to 0.03 units m^{-2} day^{-1} for zone 1 (Table 5.2).

Run Sch shows the same trend as run NW of a decreasing mean inert tracer flux for zones 2 and 3. However, the mean T_1 flux for run Sch is initially higher than for run NW (by 30 % for zone 2 and 10 % for zone 3 Table 5.2) reducing to less than that for run NW (by 25 %, Table 5.2) by day 75 of the run. There is no trend to the inert tracer flux for zone 1 during run Sch. The period mean value of the T_1 flux for zone 1 for run Sch is approximately equal to the mean T_1 flux on day 30 for run NW (0.1 units m^{-2} day^{-1}, Table 5.2).

The mean fluxes of T_1 for run Rrc are approximately equal to those for run Sch for zones 1 and 2. In contrast to run Sch, run Rrc shows no trend in the inert tracer flux for zone 3. However, the period mean T_1 flux for zone 3 for run Rrc is approximately equal to the mean of the day 30 and day 75 mean T_1 fluxes for run Sch (Table 5.2) and the total volume of T_1 fluxed into the euphotic zone for zone 3 by day 75 of the run, for both runs, is approximately equal (5 x10^{10} units). Run Rrr shows no trend in T_1 flux. The period means of the T_1 fluxes for run Rrr for zones 2 and 3 are approximately equal to the day 30 mean T_1 fluxes for zones 2 and 3 for run NW (0.1 units m^{-2} day^{-1}, Table 5.2). The period mean value for the T_1 flux for zone 1 for run Rrr is approximately 60 % higher than the day 30 mean flux for run NW (0.16 units m^{-2} day^{-1}, Table 5.2).

The radial distribution of the T_1 flux for all runs, except Sch, Rrc and, Rrr, is approximately uniform and comparable to the flux in NW in magnitude out to a radial distance of 70 km from the centre of the eddy (Figure 5.3). The radial distribution of inert tracer fluxes for runs Sch and Rrc are approximately equal and uniform out to a radial distance of 70 km from the centre of the eddy (Figure 5.3). The period mean fluxes for runs Sch and Rrc are both slightly smaller in magnitude than the mean day 30 flux for run NW (runs Sch and Rrc fluxes $\sim$ 0.07 units m^{-2} day^{-1}, run NW flux at period start $\sim$ 0.08 units m^{-2} day^{-1}, Figure 5.3). The period mean T_1 flux for run Rrr is higher than the day 30 mean flux for the NW run out to a radial distance of $\sim$ 35 km from the centre of the eddy (Figure 5.3).

5.3.1.2 Bye (1986) wind stress parametrization

The mean flux of T_1 into the euphotic zone for the NW run is the same when using either the Bye (1986) or standard wind stress parametrization (Table 5.2 and 5.3).

The mean fluxes of T_1 into the euphotic zone for all runs, except Sch, Rrc and, Rrr, are equal and show the same trend of a decreasing mean flux from day 30 to day 75 of the run. T_1 fluxes decrease by approximately 50 % from 0.1 to 0.05 units m^{-2} day^{-1} for zone 3, by 46 % from 0.13 to 0.07 units m^{-2} day^{-1} for zone 2 and by 30 % from 0.2 to 0.14 units m^{-2} day^{-1} for zone 1 (Table 5.3).

Run Sch shows the same trend as run Scc of a decreasing mean T_1 flux for zones 2 and 3. However, the mean inert t T_1 for run Sch is initially higher than for run Scc (by 15 % for zone 2 and by 10 % for zone 3, Table 5.3) reducing to less than for run Scc (20 % lower, Table 5.3) by day 75 of the run. There is no trend to the T_1 flux for zone 1 during run Sch. The period mean value of the T_1 flux for zone 1 for run Sch is approximately equal to the mean of the day 30 and day 75 mean inert tracer fluxes for run Scc (0.18 units m^{-2} day^{-1}, Table 5.3).

The mean fluxes of T_1 for run Rrc are approximately equal to those for run Sch for zones 1 and 2. In contrast to run Sch, run Rrc shows no trend in the T_1 flux for zone 3. However, the period mean T_1 flux for zone 3 for run Rrc is approximately equal to the mean of the day 30 and day 75 mean T_1 fluxes for run Sch (Table 5.3) and the total volume of T_1 fluxed into the euphotic zone for zone 3 by day 75 of the run, for both runs, is approximately equal (6 x10^{10} units).

Run Rrr shows the same trend as run Scc of a decreasing mean T_1 flux for zones 2 and 3. However, the mean T_1 flux for run Rrr is initially higher than for run Scc (95 % higher for zone 2 and 76 % higher for zone 3 Table 5.3) reducing to approximately 0 units m^{-2} day^{-1} by day 75 of the run (Table 5.3) . There is no trend to the T_1 flux for zone 1 during run Rrr. The period mean value of the T_1 flux for zone 1 for run Rrr is approximately 20 % higher than the mean T_1 flux on day 30 for run Scc (0.22 units m^{-2} day^{-1}, Table 5.3).

Mean T_1 fluxes are higher for zones 1 and 2 for all runs (except run NW) when using the Bye (1986) wind stress parametrization compared to the equivalent run using the standard wind stress parametrization (Table 5.2 and 5.3).

The radial distribution of the T_1 flux for run NW is the same when using either the Bye (1986) or standard wind stress parametrization (figures 5.3 and 5.4). For all runs, except Sch, Rrc and, Rrr, the radial distribution of T_1 flux is approximately uniform and comparable to the run NW flux in magnitude from approximately 40 to 70 km from the centre of the eddy (Figure 5.4). Out to a radial distance of 40 km from the centre of the eddy the radial distribution of T_1 flux for runs Scl, Slc and Rcc is approximately equal to the radial distribution of tracer flux for run Scc

(Figure 5.4). The radial distributions of T_1 fluxes for runs Sch and Rrc are approximately equal out to a radial distance of 70 km from the centre of the eddy (Figure 5.4). The period mean fluxes for runs Sch and Rrc are both approximately equal to the day 30 mean flux for run Scc (Figure 5.3). The period mean T_1 flux for run Rrr is higher than the day 30 mean flux for the run Scc out to a radial distance of $\sim$ 35 km from the centre of the eddy (Figure 5.4).

Out to a radial distance of 40 km from the centre of the eddy the radial distribution of T_1 flux for all runs (except run NW) is higher when using the Bye (1986) wind stress parametrization compared to the equivalent run using the standard wind stress parametrization (figures 5.3 and 5.4). The use of the Bye (1986) wind stress parametrization in the eddy model with any non-zero speed wind forcing results in a greater T_1 flux into the euphotic zone averaged over both zones 1 and 2 than for the equivalent run using the standard wind stress parametrization. The differences in T_1 flux when using the Bye (1986) wind stress parametrization compared to the standard wind stress parametrization are greatest out to a radial distance of $\sim$ 40 km from the eddy centre.

5.3.2 Diffusive fluxes

5.3.2.1 Standard wind stress parametrization

The mean effective diffusive fluxes (hereafter diffusive fluxes) of T_1 into the euphotic zone for all runs, except Sch, Rrc and Rrr are equal to the mean diffusive fluxes for the NW run and show the same trend of a decreasing mean flux from day 30 to day 75 of the run. T_1 fluxes decrease by approximately 60 % from 0.1 to 0.04 units m^{-2} day^{-1} in all zones (Table 5.4).

Runs Sch, Rrc and, Rrr show the same trend as run NW of a decreasing mean T_1 diffusive flux for all zones. However, the mean T_1 diffusive flux for runs Sch, Rrc and Rrr is initially higher than for run NW for all three zones (Table 5.4). The mean T_1 diffusive flux for run Sch is initially higher than run NW by 30 % for zone 3, 40 % for zone 2 and 173 % for zone 1 and for run Rrr is initially higher than run NW by 90 % for zone 3, 80 % for zone 2 and 110 % for zone 1 (Table 5.4). For run Rrc the mean T_1 diffusive flux is initially higher than run NW by 15 % for zone 3, 30 % for zone 2 and 50 % for zone 1, reducing to 50 % less than run NW for zone 1 by day 75 of the run (Table 5.4).

For all runs where there is a trend to the flux of T_1 into the euphotic zone, the mean T_1 diffusive flux is greater than 92 % of the T_1 flux into the euphotic zone in all zones (Table 5.4). Where there is no trend to the flux of T_1, for zone 1 for runs Sch, Rrc and Rrr, the diffusive flux of inert tracer appears to be approximately equal to the mean of the total flux of T_1 into the euphotic zone for the period day 30 to day 75 of the run (Figure 5.6).

The radial distribution of the T_1 diffusive flux for all runs, except Sch, Rrc and, Rrr, is uniform and equal to the run NW flux in magnitude out to a radial distance of 70 km from the eddy centre (Figure 5.5). The radial distribution of the T_1 flux for run Sch on day 30 is higher than the diffusive flux for run NW on day 30 out to a radial distance of 70 km, with the greatest difference in diffusive flux being out to approximately 30 km from the centre of the eddy (Figure 5.5). The radial distribution of T_1 fluxes for runs Rrc and Rrr on day 30 are both higher than the diffusive flux for run NW on day 30 out to a radial distance of 70 km, with both runs showing a minimum in diffusive flux between approximately 40 and 60 km from the eddy centre (Figure 5.5). For all runs, the radial distribution of the day 75 T_1 diffusive flux is uniform out to 70 km from the eddy centre and approximately equal in magnitude to the run NW diffusive flux (Figure 5.5).

5.3.2.2 Bye (1986) wind stress parametrization

For all runs the mean diffusive flux of T_1 into the euphotic zone is approximately equal to the mean diffusive flux of T_1 for the equivalent run using the standard wind stress parametrization (Table 5.4 and 5.5). The maximum difference is for run Rrc on day 75 where the mean diffusive flux for the standard wind stress parametrization run is 0.027 ± 0.021 units m^{-2} day^{-1} and for the Bye (1986) wind stress parametrization run is 0.039 ± 0.018 units m^{-2} day^{-1} (Table 5.5). The radial distribution of the T_1 diffusive flux for all runs using the Bye (1986) wind stress parametrization is also approximately equal to the radial distribution for the equivalent run using the standard wind stress parametrization (figures 5.5 and 5.7).

For all runs where there is a trend to the flux of T_1 into the euphotic zone, except run NW, the mean T_1 diffusive flux for zone 1 accounts for a smaller percentage of the total flux of inert tracer into the euphotic zone than for the other two zones (Table 5.5). The diffusive flux typically represents less than 65 % of the total euphotic zone flux for zone 1 on day 30, dropping to less than 30 % by day 75 (Table 5.5). For zone 2 the diffusive flux typically represents approximately 80 % of the total euphotic zone flux on day 30, dropping to approximately 50 % by day 75, and for zone 3 the diffusive flux typically represents over 90 % of the total euphotic zone flux on day 30, dropping to between 70 to 80 % by day 75 (Table 5.5). Where there is no trend to the flux of T_1, for zone 1 for runs Sch, Rrc and Rrr, the diffusive flux of T_1 is consistently less than the mean of the total flux of T_1 into the euphotic zone for the period day 30 to day 75 of the run (Figure 5.8).

5.3.2.3 Turbulent diffusion coefficient

For all runs (except for runs Sch, Rrc and Rrr), for both wind stress parametrizations the spatially averaged value of the maximum turbulent diffusion coefficient (K) is between 8 and 9x10^{-6} m^{2}s^{-1} across all zones (Table 5.6 and 5.7). The Richardson number parametrization used to calculate the turbulent diffusion coefficient for all model runs has a minimum value of 8x10^{-6} m^{2}s^{-1} (Chapter 3). The three runs, Sch, Rrc and Rrr, all show an elevated K for both wind stress parametrizations that is at least an order of magnitude greater than the Richardson number parametrization minimum (Table 5.6 and 5.7). The spatial mean values of the maximum K for all runs when using the standard wind stress parametrization are approximately equal to the spatial mean values of the maximum K for the equivalent run using the Bye (1986) wind stress parametrization (Table 5.6 and 5.7). This is consistent with the diffusive fluxes of T_1 for all runs using the standard wind stress parametrization being approximately equal to the diffusive fluxes of T_1 in the equivalent run using the Bye (1986) wind stress parametrization, as noted above.

Runs Sch, Rrc and Rrr, where the spatial mean value of the maximum K was above 8x10^{-6} m^{2}s^{-1} (Table 5.6 and 5.7), were re-run with model output sampled every 3 hours (Section 5.2.1). For all three 'high resolution' runs, within a 70 km radius of the eddy centre (zone 3) both wind stress parametrizations show a maximum value of K that is above the background level (8 x 10^{-6} m^2 s^{-1}) but below the minimum value for convective adjustment to have occurred (2.8 x10^{-4} m^2 s^{-1}, Section 5.2.1 Figure 5.9).

5.3.3 Advective fluxes

5.3.3.1 Standard wind stress parametrization

The mean horizontal advective flux of T_1 for zones 2 and 3 for all runs is approximately zero units m^{-2} day^{-1} when using the standard wind stress parametrization. For zone 1 the mean horizontal advective flux is positive indicating lateral flux into zone 1 of between 0.01 and 0.06 units m^{-2} day^{-1} except for run Rrr when the horizontal advective flux of T_1 is negative, indicating a lateral flux out of the zone (Table 5.8).

For all runs except for runs Rrr and Rrc (for zone 2), when using the standard wind stress parametrization for zones 2 and 3 the mean vertical advective flux of T_1 is approximately zero units m^{-2} day^{-1} (Table 5.9). For zone 1, for all runs except Sch, Rrc and Rrr, the mean vertical advective flux is negative and of the same approximate magnitude as the (positive) mean horizontal advective flux for the run (Table 5.8 and 5.9). This would suggest that for all runs, except Sch, Rrc and Rrr, for all three zones the net mean advective flux of T_1 into the euphotic zone is approximately 0 units m^{-2} day^{-1} (Table 5.8 and 5.9). For runs Sch, Rrc and Rrr, there appears to be a net positive mean advective flux for zone 1 (and for zone 2 for runs Rrc and Rrr). However, the standard errors on the estimates of mean T_1 vertical flux for zone 1 (and for zone 2 for runs Rrc and Rrr) for the three named runs when using the standard wind stress parametrization are approximately an order of magnitude larger than the standard errors for all other estimates of mean T_1 vertical advective fluxes (Table 5.9). This would suggest a high degree of uncertainty is associated with estimates of the mean vertical flux for runs Sch, Rrc and Rrr.

5.3.3.2 Bye (1986) wind stress parametrization

For all runs, in all three zones, the mean horizontal advective flux of T_1 when using the Bye (1986) wind stress parametrization is approximately equal to the mean horizontal advective flux of T_1 for the equivalent run when using the standard wind stress parametrization (Table 5.8 and 5.10).

For all runs, except run NW, in all three zones the mean vertical advective flux of T_1 is positive, with the mean vertical advective flux of T_1 reducing from zone 1 to zone 3 (Table 5.11). For all runs, except run NW, the mean vertical advective flux of inert tracer accounts for a larger percentage of the flux of total inert tracer into the euphotic zone for zone 1 than in the other two zones (Table 5.11). For all runs (except NW, Rrc and Rrr) the mean vertical advective flux typically represents between 30 and 40 % of the total euphotic zone flux for zone 1 on day 30 rising to approximately 50 % by day 75 (Table 5.11). For all runs, except NW, Rrc and Rrr, for zone 2 the mean vertical advective flux typically represents 20 and 30 % of the total euphotic zone flux on day 30 rising to 40 to 60 % by day 75, and for zone 3 the mean vertical advective flux typically represents approximately 10 % of the total euphotic zone flux on day 30 rising to between 20 to 30 % by day 75 (Table 5.11). For zones 1 and 2, for runs Rrc and Rrr, the mean vertical advective fluxes of T_1 can represent more than 100 % of the total flux of T_1 into the euphotic zone for the zone. However, the standard error on these estimates of vertical advective flux are an order of magnitude greater than for other estimates of the mean vertical advective flux (Table 5.11). This would again suggest a high degree of uncertainty is associated with estimates of the mean vertical flux for runs Rrc and Rrr.

5.3.3.3 Tracer stripe vertical movement

For all three zones, in all runs, when using the standard wind stress parametrization the spatial mean depth of the T_2 stripe rises by at most by 2 m (run Rrr for zone 1) and typically rises by less than 1 m from day 30 to day 75 of the run (Table 5.12). The radial distribution of the T_2 stripe depth shows the same pattern in all runs, except runs Rrr and NW, from day 30 to day 75 of the run. For all runs (except Rrr and NW) the T_2 stripe depth rises by up to a maximum of 1 m at an approximate radial distance of 40 km from the eddy centre. For run Rrr the stripe rises by approximately 2 m out to a radial distance of 30 km from the eddy centre. For run NW the tracer stripe depth does not change (Figure 5.10).

For all runs, except run NW, when using the Bye (1986) wind stress parametrization, the spatial mean depth of the T_2 stripe rises by less than 1 m for zone 3, by approximately 2 m for zone 2, and by approximately 7 m for zone 1 from day 30 to day 75 of the run (Table 5.13). The radial distribution of the T_2 stripe depth for all runs, except run NW, when using the Bye (1986) wind stress parametrization shows the T_2 stripe rising out to a radial distance of approximately 45 km from the eddy centre by up to a maximum of 7 m, while between 45 km to 70 km from the eddy centre the T_2 stripe sinks by approximately 1 m (Figure 5.11). A maximum rise of 7 m for the T_2 stripe over 45 days suggests a mean vertical velocity for the T_2 stripe of approximately 0.16 m day^{-1} in the eddy centre.

The vertical flux of T_1 into the euphotic zone due to advection was estimated from the T_2 stripe depth as described in Section 5.2.5.1. Using the Bye (1986) wind stress parametrization the mean vertical advective flux of T_1 for zone 1 in all runs (except Sch, Rrc, Rrr and NW) is greater than 70 % of the mean total flux of T_1 for zone 1 on day 30 of the run, rising to approximately 100 % of the mean total flux of T_1 for zone 1 on day 75 (Table 5.14). For runs Sch, Rrc and Rrr, the mean vertical flux of

T_1, estimated as described in Section 5.2.5.1, for zone 1 is is at least 70 % of the mean total flux of T_1 for zone 1 (Table 5.14).

5.3.4 Summary

The key results of the eddy model can be summarised by considering the results of scenarios Rcc (constant zonal wind speed 8.5ms^{-1}) and Rrr (cruise D321 recorded wind with mean speed 8.5ms^{-1}). The eddy model responds with an increased vertical T_1 flux when the wind forcing varies on a sub-inertial frequency (e.g. scenario Rrr) when compared to other wind forcings. There is a greater amount of T_1 in the euphotic zone on day 75 of the model run for scenario Rrr compared to scenario Rcc for both wind stress parametrizations (Figure 5.12 and 5.13). When using the Bye (1986) wind stress parametrization there is an increased amount of T_1 in the euphotic zone on day 75 of the model run within the radius of peak azimuthal velocity for the eddy ($\sim$ 25 km) compared to the standard wind stress parametrization in both scenarios (Figure 5.12 and 5.13). The diffusive flux contribution to the total amount of T_1 in the euphotic zone is approximately equal in each scenario for both wind stress parametrizations. The diffusive flux is elevated when the wind forcing varies on a sub-inertial frequency compared to other wind forcings (Figure 5.14).

5.4 Discussion

5.4.1 Total tracer flux into the euphotic zone

In all runs, except run NW, using both wind stress parametrizations the mean flux of inert tracer T_1 into the euphotic zone is initially approximately equal when averaged over the area within 70 km radius of the eddy centre (zone 3). However, focussing on increasingly smaller areas around the eddy the mean flux of T_1 into the euphotic zone when using the Bye (1986) wind stress parametrization is consistently greater than when using the standard wind stress parametrization, a feature which intensifies as the run progresses. Mean fluxes of T_1 into the euphotic zone averaged over the area within 25 km from the eddy centre (zone 1) are at least 100 % larger when using the Bye (1986) wind stress parametrization compared to the equivalent run when using the standard wind stress parametrization in all runs except run Rrr (and NW). Run Rrr has a large standard error associated with the total T_1 flux into the euphotic zone for zone 1, equal for both parametrizations to the calculated mean value of the total inert tracer flux. This makes any comparison between the two runs uncertain. For run NW, when there is no wind blowing, the fluxes of T_1 into the euphotic zone are approximately equal for both wind stress parametrizations. Any differences between the results using the two different wind stress parametrizations in run NW can be attributed to a small wind stress which is present when using the Bye (1986) wind stress parametrization due to movement of the water relative to the stationary air (Chapter 1).

5.4.2 Relative flux contributions

Vertical turbulent diffusive flux of inert tracer T_1 appears to be a significant contributor to the total flux into the euphotic zone in all runs. When using the standard wind stress parametrization, for all runs, except Sch, Rrc and, Rrr, the mean diffusive flux of T_1 accounts for more than 92 % of the mean total euphotic zone flux. This would suggest that the primary mechanism supplying inert tracer into the euphotic zone for these runs is vertical diffusion. For runs Sch, Rrc and Rrr, the picture is less clear due to uncertainty in the magnitude of the mean total flux of inert tracer into the euphotic zone. The uncertainty in the magnitude of the mean total flux of inert tracer T_1 is caused by variability in the vertical advective flux. However, in all three runs using the standard wind stress parametrization (Sch, Rrc and Rrr) the diffusive flux appears to be of similar magnitude to the mean of the total flux of inert tracer into the euphotic zone. This would suggest that assuming the primary mechanism supplying inert tracer into the euphotic zone is vertical diffusion for all runs using the standard wind stress parametrization is not unreasonable. However, the relative contribution of the diffusive flux in runs Sch, Rrc and Rrr, may be lower than 92 %.

For all runs using the Bye (1986) wind stress parametrization the mean diffusive flux of T_1 is approximately equal to the mean diffusive flux for the corresponding run using the standard wind stress parametrization. However, when using the Bye (1986) wind stress parametrization the mean diffusive flux consistently accounts for a lower percentage of the mean total flux of T_1 into the euphotic zone as the fluxes are averaged over increasingly smaller areas around the eddy centre. For all runs using the Bye (1986) wind stress parametrization, the mean vertical diffusive flux of T_1 accounts for a smaller percentage of the mean total flux of inert tracer for zone 1 (within 25 km of the eddy centre) than for zone 3 (within 70 km of the eddy centre). For zone 1 the mean diffusive flux is as little as 30 % of the mean total euphotic zone inert tracer flux. This would suggest that there is an additional vertical flux mechanism operating in the runs using the Bye (1986) wind stress parametrization which is not present when using the standard wind stress parametrization. This additional flux mechanism appears to be strongest over the area within 25 km of the eddy centre, within the radius of peak azimuthal velocity, and to be an advective process.

5.4.3 Shear enhanced vertical diffusive flux

For all runs, except Sch, Rrc and, Rrr, using both wind stress parametrizations, the mean of the maximum turbulent diffusion coefficient is approximately equal to the minimum (background) value of the model Richardson number vertical mixing parametrization (8 x10^{-6} m^2s^{-1} Chapter 3). This implies that there is no significant shear enhanced mixing generated by the eddy interacting with the wind at the depth of the base of the euphotic zone during these runs.

Estimating the tracer flux at the base of the euphotic zone using a 1D box model which has vertical resolution and initial tracer concentrations the same as the eddy model and a constant turbulent diffusivity of 8 x10^{-6} m^2 s^{-1} gives a flux of 0.1 units m^{-2} day^{-1} on day 30 reducing to 0.04 units m^{-2} day^{-1} by day 75 (Figure 5.15). The 1D box model flux compares very well with the total euphotic zone flux from the eddy model averaged over zone 3 for standard wind stress parametrization and less well so for the Bye (1986) wind stress parametrization. This further supports the suggestion that vertical diffusion is the primary mechanism supplying inert tracer into the euphotic zone when using the standard wind stress parametrization and that there is an additional advective mechanism present when using the Bye (1986) wind stress parametrization.

In runs Sch, Rrc and, Rrr, using both wind stress parametrizations, the diffusive flux of inert tracer is initially enhanced when compared to all other runs. This is consistent with the magnitude of the turbulent diffusion coefficient being larger in runs Sch, Rrc and Rrr, than in the other runs. The mean maximum turbulent diffusion coefficient for runs Sch, Rrc and, Rrr is consistently an order of magnitude greater than the minimum value of the Richardson number parametrization in all three zones. The peak turbulent diffusion coefficient observed during the runs is five times background value (4.3 x10^{-5} m^2 s^{-1}, Table 5.6 and 5.7). Estimating the tracer flux at the base of the euphotic zone, using the same 1D box model and a constant turbulent diffusivity of 1x10^{-5} m^2 s^{-1} gives a flux of 0.12 units m^{-2} day^{-1} on day 30 reducing to 0.04 units m^{-2} day^{-1} day 75 (Figure 5.15) which compares well with the total euphotic zone flux from the model averaged over zone 3 for both wind stress parametrizations.

The diffusive flux from the model will potentially consist of both shear driven vertical diffusion and vertical diffusion used as a convective adjustment process. Convective adjustment is implemented in the model as a large turbulent diffusion coefficient which is four orders of magnitude above the minimum value of the Richardson number parametrization (Chapter 4). High temporal resolution model output for the turbulent diffusion coefficient in runs Sch, Rrc and Rrr using both wind stress parametrizations (Section 5.2.1) shows no evidence of enhanced turbulent diffusion being used as a convective adjustment process (Figure 5.9). This suggests that the observed increase in the turbulent diffusion coefficient in runs Sch, Rrc and Rrr are as a result of vertical shear in the model.

The area mean turbulent diffusivity measured around the eddy dipole on cruise D321 was 2.5 (95 % confidence interval: 1.6 to 4) x10^{-5} m^2 s^{-1} (Chapter 2) which compares well with the mean turbulent diffusivity averaged over zone 3 in run Rrr of between 4.5 and 7.8x10^{-5} m^2 s^{-1} when using the standard wind stress parametrization and between 3.1 and 8.5x10^{-5} m^2 s^{-1} when using the Bye (1986) wind stress parametrization. This suggests that the model is accurately reproducing the observed levels of mixing around the eddy.

5.4.4 Vertical advective flux

The vertical motion of the inert tracer T_2 stripe gives a time integrated measure of the magnitude of the vertical advection of tracer initially at the base of the euphotic zone. This is complementary to the estimates of vertical advective tracer flux for inert tracer T_1. For all runs, using the standard wind stress parametrization, both the vertical advective fluxes and the rise in the inert tracer stripe depth suggests that there is insignificant vertical advection occurring. This is consistent with the observations of the magnitude of the vertical diffusive fluxes accounting for greater than 92 % of the total observed euphotic zone flux. However, there is an apparent rise in the inert tracer stripe depth for zone 1 for run Rrr using the standard wind stress parametrization ($\sim$ 2 m). With the observed variability in turbulent diffusion coefficient, the diffusive correction to the tracer stripe depth can only be approximate (Section 5.2.5). This would suggest that the observed rise in tracer stripe is possibly still attributable to asymmetric diffusive spread in the model. A vertical movement of 2 m over 45 days gives a net vertical velocity for the tracer strip of 0.04 m day^{-1} which confirms that any vertical advective flux is small.

As discussed above, the fluxes of inert tracer T_1 into the euphotic zone when using the Bye (1986) wind stress parametrization are higher for all runs, except NW, relative to the equivalent run using the standard wind stress parametrization. The relative difference in mean inert tracer flux is greatest for zone 1 and least for zone 3. This suggests that the mechanism responsible is occurring most strongly close to the eddy centre. The vertical flux of inert tracer averaged over zone 1 for all runs using the Bye (1986) wind stress parametrization is up to 50 % greater than the vertical flux attributable to turbulent diffusion.

The rise in inert tracer T_2 strip of approximately 7 m over 45 days in all runs, except NW, when using the Bye (1986) wind stress parametrization gives an approximate vertical velocity of 0.16 m day^{-1}. This is of the same order of magnitude as estimated previously from isopycnal rise (0.22 m day^{-1} Chapter 4). In a previous study using a model of a mode-water eddy and the Bye (1986) wind stress parametrization, a patch of inert tracer injected into the model at 86 m depth rose by 6.7 m over a period of 36 days when the model was forced with a constant 6.7 m s^{-1} wind (Ledwell et al., 2008). This gives an estimate of vertical velocity of approximately 0.19 m day^{-1} for the tracer stripe which is not dissimilar from the results in this thesis. The mode-water eddy of Ledwell et al. (2008) is similar to the one used in this thesis with a maximum azimuthal velocity of 30 cm s^{-1} and a radius of peak azimuthal velocity of 59 km.

The vertical velocity due to Ekman suction in a mode-water eddy core has been estimated in two previous studies. For recorded wind data with speeds between 1 and 15 m s^{-1} the average vertical Ekman velocity has been calculated as $\sim$ 0.5 m day^{-1} (Martin and Richards, 2001) and for a constant wind of 6.7 m s^{-1} the vertical Ekman velocity has been calculated as 0.23 m day $^{-1}$ (Ledwell et al., 2008). However, as discussed in Chapter 4, these estimates represent the theoretical maximum vertical velocity which occurs at the base of the wind affected Ekman layer. Vertical velocities in the eddy model due to Ekman suction are expected to penetrate into the stratified interior of the model on an e-folding length scale of $\sim$ 100 m (Chapter 4) and to be much smaller at the depth of the base of the euphotic zone. In line with theoretical predictions of Ekman vertical velocities, the rise in inert tracer stripe T_2 depth is most pronounced within a radius of 25 km from the eddy centre. This suggests that the rise in inert tracer T_2 strip depth is consistent with an Ekman suction process.

The vertical flux of inert tracer T_1 into the euphotic zone calculated from the vertical Ekman velocity estimated from the rise in inert tracer T_2 strip (Section 5.2.5) accounts for at least 70 % of the total flux of inert tracer T_1 into the euphotic zone for all runs, except NW, using the Bye (1986) wind stress parametrization. The horizontal distribution of the calculated vertical Ekman flux of inert tracer T_1 into the euphotic zone shows a decrease with distance from the eddy centre. The flux is greatest averaged over zone 1 and least when averaged over zone 3.

The combined values of the vertical diffusive flux and the calculated Ekman flux of inert tracer T_1 for all runs using the Bye (1986) wind stress parametrization is of sufficient magnitude to account for the entire observed flux of inert tracer T_1 into the euphotic zone. This would suggest that the additional vertical flux process which is observed in all runs, except NW, when using the Bye (1986) wind stress parametrization, as discussed above, is likely to be dominated by Ekman suction.

5.4.5 Horizontal advective flux

For all runs, using both wind stress parametrizations, the mean horizontal advective flux of inert tracer T_1 averaged over zone 3 is approximately zero. This suggests that the observed fluxes of inert tracer for the three zones result from the wind forcing interacting with the eddy circulation and that there is no flux of inert tracer from elsewhere in the model "contaminating" the results.

The horizontal flux averaged over zone 2 is also zero in all runs using both wind stress parametrizations. However, there is a small positive flux of inert tracer into zone 1 in all scenarios, except Rrr, using both wind stress parametrizations. The mean horizontal flux averaged over zone 1 in run Rrr for both wind stress parametrizations is negative, indicating an outward flux, and of the same approximate magnitude as the mean horizontal fluxes in all other runs. As the mean flux averaged over zone 2 is approximately zero, this suggests that the non-zero horizontal flux of inert tracer averaged over zone 1 represents a re-distribution of inert tracer within zone 2.

5.4.6 Sub-mesoscale processes

Though the variability in the vertical advectve fluxes makes any diagnosis of a net vertical flux into the euphotic zone uncertain, the horizontal fluxes are much more consistent. For the standard wind stress parametrization, where there is no Ekman suction effect, the positive horizontal flux into zone 1, in all runs except Rrr, is balanced by a net downwards flux. The pattern of this circulation is suggestive of an ageostrophic secondary circulation where the down-welling in zone 1 should be matched by an up-welling outside the boundary of zone 1. The radial distribution of T_2 stripe depths indicates that such an up-welling may be occurring at a radial distance of approximately 40 km from the eddy centre (within zone 2). The radius of peak azimuthal velocity occurs approximately at the boundary of zone 1, radial distance 25 km from the eddy centre, which would suggest that this ageostrophic circulation is flowing across the eddy 'jet' in a reverse direction to that which would be expected if frontogenesis was occurring (Chapter 1). This could indicate a down-front wind-generated ageostrophic circulation produced by cross-front advection of dense water over light (Thomas and Lee, 2005). However, the lack of any detectable convective adjustment through increased turbulent diffusivity makes this unlikely (Chapter 1). Ageostrophic circulation as described above, for all runs except Rrr, would act to flatten sloped density surfaces. This would suggest that the circulation could simply be the product of the eddy isopycnals 'slumping' under gravity.

For run Rrr, using the standard wind stress parametrization, the sense of the potential ageostrophic circulation around the border of zone 1 is consistent with frontogenesis. There is a horizontal flow out of zone 1 and a rise in T_2 stripe depth in zone 1 which indicates an up-welling on the anticyclonic side of the eddy 'jet'. The difference between maximum and minimum azimuthal velocities observed for all runs with high variability wind forcing (runs Sch, Rrc and Rrr) using both wind stress parametrizations indicates potential along-flow accelerations in the azimuthal velocity. The difference between minimum and maximum azimuthal velocity is greatest in run Rrr and may indicate azimuthal acceleration of a sufficient strength to induce frontogenesis with a resultant ageostrophic circulation. Frontogenesis may also be occurring in runs Sch and Rrc, but with insufficient strength to overcome the circulation generated by the eddy isopycnal slump.

Potentially both these up-welling processes also occur when using the Bye (1986) wind stress parametrization. The horizontal fluxes of T_1 show the same patterns when using the Bye (1986) wind stress parametrization as the equivalent run using the standard wind stress parametrization. However, the impact of the corresponding up-welling is masked by the magnitude of the Ekman suction driven up-welling.

In all cases the tracer flux resulting from such vertical up-welling, either frontogenesis within zone 1 or isopycnal slump outside zone 1, is small in magnitude when compared to the flux from either Ekman suction or vertical diffusion.

Most sub-mesoscale instability processes such as mixed layer instability (Boccaletti et al., 2007), loss of geostrophic balance (Molemaker et al., 2005), and wind-frontal interactions (Thomas and Lee, 2005) are surface intensified, being strongest where horizontal gradients in density are sharpest (Chapter 1). This suggests that the influence of such sub-mesoscale physics is often most strongly felt in and just below the surface mixed layer. The influence of the large vertical velocities that such sub-mesoscale processes produce in the near surface waters should potentially extend a distance into the waters below. However, it may be the case that the euphotic depth in this eddy model is below the depth to which these velocities penetrate.

Though consistent with observations (see Chapter 3), the vertical viscosity used in the eddy model (1 x10^{-3} m^2 s^{-1}) is high compared to that which is used in other mixing parametrizations. The Richardson number based vertical mixing parametrizations of Large et al. (1994) and Pacanowski and Philander (1981) both use a constant background vertical viscosity of 1x10^{-4} m^2 s^{-1}. Reduced vertical viscosity would be expected to lead to greater downwards diffusion of momentum from the wind-driven mixed layer and potentially to higher shear with associated higher mixing.

If we consider the case where the vertical viscosity is reduced by an order of magnitude to 10^{-4} m^2s^{-1}, consistent with previous parametrizations (Large et al., 1994; Pacanowski and Philander, 1981), the vertical diffusive flux is increased when using both wind stress parametrizations through a combination of convective adjustment and greater shear while the vertical advective flux is little changed (Appendix A). The convective adjustment contribution to the vertical diffusive flux may be suggestive of a hydrostatic sub-mesoscale process (Chapter 4). This suggests that the lack of attributable contribution to vertical inert tracer fluxes from sub-mesoscale processes in the eddy model may be due in part to the damping effect of the vertical viscosity used.

5.5 Conclusions

For this model study there are two dominant mechanisms responsible for fluxing tracer into the euphotic zone; shear enhanced diffusive mixing and Ekman suction when relative speeds of air and sea are accounted for. Within the radius of peak azimuthal velocity for the eddy the vertical fluxes due to Ekman suction appear to dominate over vertical diffusive fluxes. However, when using high frequency (super-inertial) forcing the magnitudes of the diffusive fluxes and fluxes due to Ekman suction appear to be approximately equal. Outside the radius of peak azimuthal velocity for the eddy, vertical diffusion is the dominant mechanism. The effects of sub-mesoscale processes are found to be much less important than enhanced mixing or Ekman suction processes at the base of the euphotic zone and, in this model, are not readily detectable.

Tag	Description
NW	No wind blowing
	Synthetic
Scc	Constant zonal wind with speed of 10 m s^{-1}, the mean NCEP wind speed for 2007.
Slc	Wind speed varying sinusoidally between 6 m s^{-1} and 14 m s^{-1} (mean speed 10 m s^{-1}) with a 3 day period.
Scl	Wind speeds constant at 10 m s^{-1}. Wind direction varying continually between +30^{o} and -30^{o} at a rate of 3^{o} h^{-1}
Sch	Wind speeds constant at 10 m s^{-1}. Wind direction rotating through 360^{o} over a period of nine hours (rate $\sim$ 40^{o} h^{-1}) 8 times in 30 days at regular intervals.
	Realistic
Rcc	Zonal wind with speed constant at mean wind speed of D321 cruise data set (8.55 m s^{-1}).
Rrc	Zonal wind with speed taken from Iceland Basin D321 wind data (30 days duration) in a repeating loop at sampling frequency of every 30 mins.
Rrr	Iceland Basin D321 wind data (30 days duration) in a repeating loop at sampling frequency of every 30 mins.

TABLE 5.1: Description of model wind forcing scenarios (Chapter 4).

Scenario	Zone 3	Zone 2	Zone 1
NW	0.101 : 0.040 ± 0.003 (n)	0.099 : 0.039 ± 0.006 (n)	0.091 : 0.027 ± 0.051 (l)
Scc	0.103 : 0.043 ± 0.008 (n)	0.106 : 0.046 ± 0.008 (n)	0.091 : 0.034 ± 0.046 (l)
Slc	0.104 : 0.043 ± 0.008 (n)	0.109 : 0.045 ± 0.011 (n)	0.095 : 0.030 ± 0.043 (l)
Scl	0.105 : 0.041 ± 0.010 (n)	0.110 : 0.042 ± 0.015 (n)	0.093 : 0.031 ± 0.051 (l)
Sch	0.113 : 0.031 ± 0.066 (l)	0.127 : 0.026 ± 0.044 (l)	0.087 ± 0.027
Rcc	0.106 : 0.040 ± 0.007 (n)	0.105 : 0.043 ± 0.006 (n)	0.089 : 0.032 ± 0.041 (l)
Rrc	0.076 ± 0.014	0.130 : 0.027 ± 0.063 (l)	0.080 ± 0.045
Rrr	0.103 ± 0.030	0.105 ± 0.035	0.163 ± 0.160

TABLE 5.2: Fluxes of inert tracer T_1 into the euphotic zone (units m^{-2} day^{-1}) for all runs using the standard wind stress parametrization. Where the mean flux was estimated by fitting a trend the values are reported as day 30 value : day 75 value ± standard error (s_e) calculated as described in Section 5.2.4.3. The trend fitted is indicated, where (n) is a fit to 1/t and (l) is a fit to t. Where there was no trend values are reported mean ± standard error for the whole period.

Scenario	Zone 3	Zone 2	Zone 1
NW	0.101 : 0.040 ± 0.002 (n)	0.100 : 0.039 ± 0.006 (n)	0.092 : 0.026 ± 0.050 (l)
Scc	0.108 : 0.051 ± 0.004 (n)	0.128 : 0.072 ± 0.006 (n)	0.191 : 0.144 ± 0.043 (l)
Slc	0.107 : 0.054 ± 0.010 (n)	0.130 : 0.072 ± 0.019 (n)	0.203 : 0.142 ± 0.052 (l)
Scl	0.105 : 0.052 ± 0.008 (n)	0.125 : 0.073 ± 0.009 (n)	0.193 : 0.138 ± 0.048 (l)
Sch	0.115 : 0.044 ± 0.035 (l)	0.149 : 0.057 ± 0.036 (l)	0.184 ± 0.030
Rcc	0.104 : 0.047 ± 0.005 (n)	0.118 : 0.063 ± 0.006 (n)	0.167 : 0.114 ± 0.041 (l)
Rrc	0.122 : 0.039 ± 0.061 (l)	0.146 : 0.055 ± 0.063 (l)	0.169 ± 0.045
Rrr	0.176 : 0.015 ± 0.126 (l)	0.225 : 0.007 ± 0.157 (l)	0.220 ± 0.118

TABLE 5.3: Fluxes of inert tracer T_1 into the euphotic zone (units m^{-2} day^{-1}) for all runs using the Bye (1986) wind stress parametrization. Where the mean flux was estimated by fitting a trend the values are reported as day 30 value : day 75 value ± standard error (s_e) calculated as described in Section 5.2.4.3. The trend fitted is indicated, where (n) is a fit to 1/t and (l) is a fit to t. Where there was no trend values are reported mean ± standard error for the whole period.

Scenario	Zone 3	Zone 2	Zone 1
NW	0.100 : 0.040 ± 0.000 (n)	0.100 : 0.040 ± 0.000 (n)	0.100 : 0.040 ± 0.000 (n)
Scc	0.100 : 0.039 ± 0.001 (n)	0.100 : 0.039 ± 0.001 (n)	0.100 : 0.039 ± 0.000 (n)
Slc	0.100 : 0.039 ± 0.001 (n)	0.100 : 0.039 ± 0.001 (n)	0.099 : 0.039 ± 0.000 (n)
Scl	0.101 : 0.039 ± 0.000 (n)	0.101 : 0.039 ± 0.000 (n)	0.100 : 0.039 ± 0.000 (n)
Sch	0.132 : 0.038 ± 0.005 (n)	0.144 : 0.037 ± 0.004 (n)	0.273 : 0.034 ± 0.008 (n)
Rcc	0.100 : 0.039 ± 0.000 (n)	0.100 : 0.039 ± 0.000 (n)	0.100 : 0.040 ± 0.000 (n)
Rrc	0.115 : 0.027 ± 0.021 (l)	0.130 : 0.039 ± 0.016 (n)	0.150 : 0.020 ± 0.041 (l)
Rrr	0.189 : 0.039 ± 0.037 (n)	0.179 : 0.039 ± 0.044 (n)	0.214 : 0.042 ± 0.077 (n)

TABLE 5.4: Diffusive fluxes of inert tracer T_1 into the euphotic zone (units m^{-2} day^{-1}) for all runs using the standard wind stress parametrization. Where the mean flux was estimated by fitting a trend the values are reported as day 30 value : day 75 value ± standard error (s_e) calculated as described in Section 5.2.4.3. The trend fitted is indicated, where (n) is a fit to 1/t and (l) is a fit to t. Where there was no trend values are reported mean ± standard error for the whole period.

Scenario	Zone 3	Zone 2	Zone 1
NW	0.100 : 0.040 ± 0.000 (n)	0.100 : 0.040 ± 0.000 (n)	0.100 : 0.040 ± 0.000 (n)
Scc	0.101 : 0.038 ± 0.001 (n)	0.103 : 0.036 ± 0.001 (n)	0.088 : 0.021 ± 0.005 (l)
Slc	0.102 : 0.038 ± 0.001 (n)	0.103 : 0.036 ± 0.001 (n)	0.087 : 0.020 ± 0.005 (l)
Scl	0.103 : 0.038 ± 0.001 (n)	0.104 : 0.037 ± 0.001 (n)	0.088 : 0.021 ± 0.005 (l)
Sch	0.128 : 0.039 ± 0.004 (n)	0.141 : 0.039 ± 0.004 (n)	0.240 : 0.039 ± 0.004 (n)
Rcc	0.101 : 0.039 ± 0.001 (n)	0.102 : 0.037 ± 0.001 (n)	0.110 : 0.033 ± 0.003 (n)
Rrc	0.126 : 0.039 ± 0.018 (n)	0.127 : 0.040 ± 0.017 (n)	0.154 : 0.024 ± 0.046 (l)
Rrr	0.162 : 0.038 ± 0.032 (n)	0.159 : 0.038 ± 0.040 (n)	0.198 : 0.038 ± 0.078 (n)

TABLE 5.5: Diffusive fluxes of inert tracer T_1 into the euphotic zone (units m^{-2} day^{-1}) for all runs using the Bye (1986) wind stress parametrization. Where the mean flux was estimated by fitting a trend the values are reported as day 30 value : day 75 value ± standard error (s_e) calculated as described in Section 5.2.4.3. The trend fitted is indicated, where (n) is a fit to 1/t and (l) is a fit to t. Where there was no trend values are reported mean ± standard error for the whole period.

Scenario	Zone 3	Zone 2	Zone 1
NW	0.008 ± 0.000	0.008 ± 0.000	0.008 ± 0.000
Scc	0.008 ± 0.000	0.008 ± 0.000	0.008 ± 0.000
Slc	0.008 ± 0.000	0.008 ± 0.000	0.008 ± 0.000
Scl	0.009 : 0.008 ± 0.000 (n)	0.008 ± 0.000	0.008 ± 0.000
Sch	0.040 : 0.015 ± 0.003 (n)	0.040 : 0.015 ± 0.003 (n)	0.040 : 0.015 ± 0.003 (n)
Rcc	0.008 ± 0.000	0.008 ± 0.000	0.008 ± 0.000
Rrc	0.034 : 0.017 ± 0.010 (l)	0.034 : 0.017 ± 0.011 (l)	0.033 : 0.016 ± 0.011 (l)
Rrr	0.078 : 0.045 ± 0.015 (l)	0.078 : 0.045 ± 0.015 (l)	0.077 : 0.045 ± 0.015 (l)

Table 5.6: Average values of the maximum turbulent eddy diffusivity coefficient (x10^{-3} m^{2}s^{-1}) recorded in each zone for all runs using the standard wind stress parametrization. Where the mean value was estimated by fitting a trend the values are reported as day 30 value : day 75 value ± standard error (s_e) calculated as described in Section 5.2.4.3. The trend fitted is indicated, where (n) is a fit to 1/t and (l) is a fit to t. Where there was no trend values are reported mean ± standard error for the whole period.

Scenario	Zone 3	Zone 2	Zone 1
NW	0.008 ± 0.000	0.008 ± 0.000	0.008 ± 0.000
Scc	0.008 ± 0.000	0.008 ± 0.000	0.008 ± 0.000
Slc	0.008 ± 0.000	0.008 ± 0.000	0.008 ± 0.000
Scl	0.009 ± 0.000	0.009 ± 0.000	0.009 ± 0.000
Sch	0.043 : 0.024 ± 0.005 (n)	0.043 : 0.024 ± 0.005 (n)	0.043 : 0.024 ± 0.005 (n)
Rcc	0.008 ± 0.000	0.008 ± 0.000	0.008 ± 0.000
Rrc	0.033 ± 0.002	0.033 ± 0.002	0.033 ± 0.002
Rrr	0.085 : 0.031 ± 0.021 (l)	0.085 : 0.031 ± 0.021 (l)	0.085 : 0.031 ± 0.021 (l)

Table 5.7: Average values of the maximum turbulent eddy diffusivity coefficient (x10^{-3} m^{2}s^{-1}) recorded in each zone for all runs using the Bye (1986) wind stress parametrization. Where the mean flux was estimated by fitting a trend the values are reported as day 30 value : day 75 value ± standard error (s_e) calculated as described in Section 5.2.4.3. The trend fitted is indicated, where (n) is a fit to 1/t and (l) is a fit to t. Where there was no trend values are reported mean ± standard error for the whole period.

Scenario	Zone 3	Zone 2	Zone 1
NW	0.000 : -0.003 ± 0.000 (l)	0.001 : -0.001 ± 0.000 (l)	0.001 ± 0.001
Scc	0.000 : -0.011 ± 0.000 (l)	0.004 : -0.005 ± 0.003 (l)	0.051 ± 0.003
Slc	0.000 : -0.010 ± 0.001 (l)	0.004 : -0.005 ± 0.003 (l)	0.061 ± 0.004
Scl	0.000 : -0.011 ± 0.001 (l)	0.004 : -0.005 ± 0.003 (l)	0.049 ± 0.004
Sch	0.001 : -0.011 ± 0.001 (l)	0.004 : -0.006 ± 0.003 (l)	0.007 ± 0.006
Rcc	0.000 : -0.011 ± 0.000 (l)	0.003 : -0.002 ± 0.002 (l)	0.033 ± 0.002
Rrc	0.003 : -0.009 ± 0.005 (l)	0.003 : -0.004 ± 0.005 (l)	0.030 ± 0.011
Rrr	0.006 ± 0.002	-0.003 ± 0.002	-0.029 ± 0.041

TABLE 5.8: Horizontal advective fluxes of inert tracer T_1 into the euphotic zone (units m^{-2} day^{-1}) for all runs using the standard wind stress parametrization. Where the mean flux was estimated by fitting a trend the values are reported as day 30 value : day 75 value ± standard error (s_e) calculated as described in Section 5.2.4.3. The trend fitted is indicated, where (n) is a fit to 1/t and (l) is a fit to t. Where there was no trend values are reported mean ± standard error for the whole period.

Scenario	Zone 3	Zone 2	Zone 1
NW	0.002 ± 0.000	-0.001± 0.001	-0.004 ± 0.008
Scc	0.005 ± 0.001	0.008 ± 0.001	-0.045 ± 0.006
Slc	0.005 ± 0.001	0.009 ± 0.002	-0.054 ± 0.006
Scl	0.005 ± 0.001	0.008 ± 0.002	-0.043 ± 0.007
Sch	0.007 ± 0.004	0.009 ± 0.005	0.003 ± 0.024
Rcc	0.006 : 0.003 ± 0.003 (l)	0.004 ± 0.001	-0.032 ± 0.006
Rrc	0.005 ± 0.011	0.019 ± 0.008	0.093 ± 0.045
Rrr	0.002 ± 0.028	0.063 ± 0.031	0.574 ± 0.125

TABLE 5.9: Vertical advective fluxes of inert tracer T_1 into the euphotic zone (units m^{-2} day^{-1}) for all runs using the standard wind stress parametrization. Where the mean flux was estimated by fitting a trend the values are reported as day 30 value : day 75 value ± standard error (s_e) calculated as described in Section 5.2.4.3. The trend fitted is indicated, where (n) is a fit to 1/t and (l) is a fit to t. Where there was no trend values are reported mean ± standard error for the whole period.

Scenario	Zone 3	Zone 2	Zone 1
NW	-0.001 ± 0.000	0.001 : -0.001 ± 0.001 (l)	0.001 ± 0.001
Scc	0.000 : -0.006 ± 0.000 (l)	0.004 : -0.002 ± 0.002 (l)	0.038 : 0.069 ± 0.020 (l)
Slc	-0.001 : -0.007 ± 0.000 (l)	0.003 : -0.002 ± 0.002 (l)	0.062 ± 0.004
Scl	0.000 : -0.007 ± 0.000 (l)	0.003 : -0.001 ± 0.002 (l)	0.037 : 0.064 ± 0.024 (l)
Sch	0.000 : -0.007 ± 0.001 (l)	0.003 : -0.002 ± 0.002 (l)	0.013 ± 0.005
Rcc	0.000 : -0.008 ± 0.000 (l)	0.003 : -0.001 ± 0.002 (l)	0.027 : 0.049 ± 0.015 (l)
Rrc	0.001 : -0.006 ± 0.003 (l)	0.003 : -0.003 ± 0.004 (l)	0.026 ± 0.011
Rrr	0.002 ± 0.001	0.002 : -0.005 ± 0.005 (l)	-0.016 ± 0.029

TABLE 5.10: Horizontal advective fluxes of inert tracer T_1 into the euphotic zone (units m^{-2} day^{-1}) for all runs using the Bye (1986) wind stress parametrization. Where the mean flux was estimated by fitting a trend the values are reported as day 30 value : day 75 value ± standard error (s_e) calculated as described in Section 5.2.4.3. The trend fitted is indicated, where (n) is a fit to 1/t and (l) is a fit to t. Where there was no trend values are reported mean ± standard error for the whole period.

Scenario	Zone 3	Zone 2	Zone 1
NW	0.002 ± 0.000	-0.001 : -0.001 ± 0.001	-0.004 : -0.004 ± 0.008
Scc	0.012 : 0.016 ± 0.003 (l)	0.032 : 0.039 ± 0.006 (l)	0.071 ± 0.006
Slc	0.016 ± 0.001	0.040 ± 0.003	0.069 ± 0.008
Scl	0.014 ± 0.001	0.030 ± 0.008 (l)	0.073 ± 0.006
Sch	0.013 ± 0.003	0.033 ± 0.004	0.094 ± 0.021
Rcc	0.008 : 0.011 ± 0.002 (l)	0.022 : 0.028 ± 0.005 (l)	0.056 ± 0.006
Rrc	0.010 ± 0.009	0.035 ± 0.008	0.157 ± 0.039
Rrr	0.008 ± 0.018	0.055 ± 0.021	0.414 ± 0.090

TABLE 5.11: Vertical advective fluxes of inert tracer T_1 into the euphotic zone (units m^{-2} day^{-1}) for all runs using the Bye (1986) wind stress parametrization. Where the mean flux was estimated by fitting a trend the values are reported as day 30 value : day 75 value ± standard error (s_e) calculated as described in Section 5.2.4.3. The trend fitted is indicated, where (n) is a fit to 1/t and (l) is a fit to t. Where there was no trend values are reported mean ± standard error for the whole period.

Scenario	Zone 3	Zone 2	Zone 1
NW	65.39 : 65.33 ± 0.01 (n)	65.41 ± 0.00 (2)	65.28 : 65.62 ± 0.07 (l)
Scc	65.43 : 65.12 ± 0.02 (l)	65.46 : 64.71 ± 0.02 (l)	65.38 ± 0.01 (2)
Slc	65.40 : 65.09 ± 0.01 (l)	65.40 : 64.66 ± 0.03 (n)	65.32 ± 0.01 (2)
Scl	65.37 : 65.12 ± 0.02 (n)	65.42 : 64.79 ± 0.03 (n)	65.38 ± 0.01 (2)
Sch	65.38 : 65.05 ± 0.07 (n)	65.36 : 64.74 ± 0.05 (n)	65.15 ± 0.03 (2)
Rcc	65.37 : 65.18 ± 0.02 (n)	65.41 : 65.00 ± 0.01 (n)	65.38 : 65.50 ± 0.07 (n)
Rrc	65.37 ± 0.02 (2)	65.49 : 65.03 ± 0.07 (l)	65.55 ± 0.06 (2)
Rrr	65.30 ± 0.03 (2)	65.24 : 64.74 ± 0.14 (n)	64.28 : 62.04 ± 0.90 (l)

TABLE 5.12: Mean depth of inert tracer stripe T_2 for all runs using the standard wind stress parametrization. Where the mean depth was estimated by fitting a trend the values are reported as day 30 value : day 75 value ± standard error (s_e) calculated as described in Section 5.2.4.3. The trend fitted is indicated, where (n) is a fit to 1/t and (l) is a fit to t. Where there was no trend values are reported mean ± standard error for the whole period.

Scenario	Zone 3	Zone 2	Zone 1
NW	65.41 : 65.34 ± 0.01 (l)	65.42 : 65.41 ± 0.01 (l)	65.27 : 65.55 ± 0.07 (l)
Scc	65.39 : 64.77 ± 0.01 (n)	65.37 : 63.06 ± 0.04 (n)	65.25 : 58.55 ± 0.08 (n)
Slc	65.40 : 64.62 ± 0.02 (l)	65.35 : 62.81 ± 0.03 (n)	65.18 : 58.21 ± 0.10 (n)
Scl	65.39 : 64.77 ± 0.01 (n)	65.41 : 63.08 ± 0.02 (n)	65.26 : 58.62 ± 0.09 (n)
Sch	65.38 : 64.66 ± 0.04 (l)	65.30 : 62.94 ± 0.04 (n)	64.97 : 58.24 ± 0.19 (n)
Rcc	65.40 : 64.99 ± 0.01 (n)	65.40 : 63.66 ± 0.02 (n)	65.26 : 59.93 ± 0.07 (n)
Rrc	65.42 : 64.99 ± 0.09 (l)	65.47 : 63.46 ± 0.09 (n)	65.56 : 59.30 ± 0.34 (n)
Rrr	65.28 : 65.04 ± 0.16 (n)	65.11 : 63.18 ± 0.13 (n)	63.94 : 56.80 ± 0.64 (n)

TABLE 5.13: Mean depth of inert tracer stripe T_2 for all runs using the Bye (1986) wind stress parametrization. Where the mean flux was estimated by fitting a trend the values are reported as day 30 value : day 75 value ± standard error (s_e) calculated as described in Section 5.2.4.3. The trend fitted is indicated, where (n) is a fit to 1/t and (l) is a fit to t. Where there was no trend values are reported mean ± standard error for the whole period.

Scenario	Zone 3	Zone 2	Zone 1
NW	0.002 ± 0.001	0.000 ± 0.002	-0.003 ± 0.016
Scc	0.014 ± 0.001	0.058 : 0.042 ± 0.013 (l)	0.148 ± 0.011
Slc	0.018 ± 0.002	0.055 ± 0.004	0.154 ± 0.013
Scl	0.015 ± 0.002	0.050 ± 0.002	0.145 ± 0.012
Sch	0.018 ± 0.010	0.052 ± 0.007	0.154 ± 0.044
Rcc	0.010 ± 0.002	0.037 ± 0.001	0.118 ± 0.011
Rrc	0.010 ± 0.019	0.040 ± 0.014	0.122 ± 0.053
Rrr	0.009 ± 0.033	0.046 ± 0.019	0.172 ± 0.126

Table 5.14: The flux of inert tracer T_1 due to Ekman suction, estimated from the rise in inert tracer T_2 stripe depth when using the Bye (1986) wind stress parametrization. Where the mean flux was estimated by fitting a trend the values are reported as day 30 value : day 75 value ± standard error (s_e) calculated as described in Section 5.2.4.3. The trend fitted is indicated, where (n) is a fit to 1/t and (l) is a fit to t. Where there was no trend values are reported mean ± standard error for the whole period.

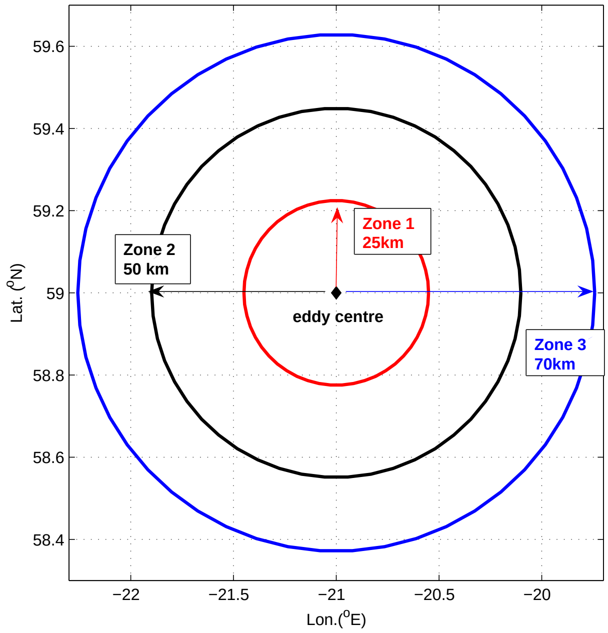

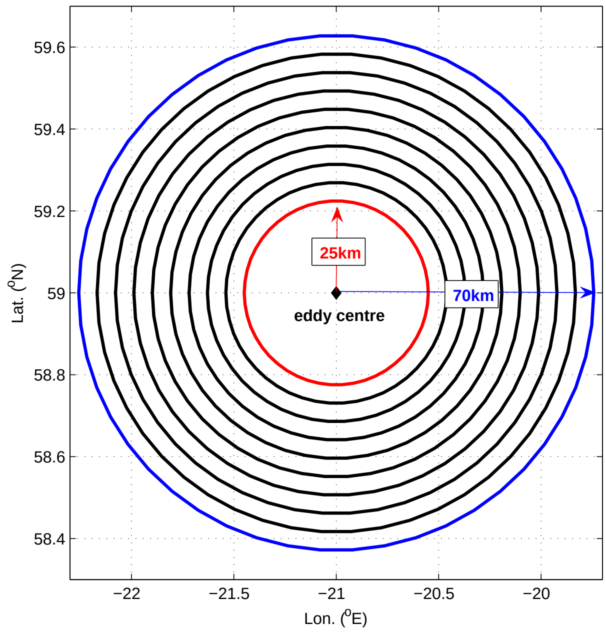

FIGURE 5.1: Cartoons showing the size and positions relative to the eddy centre of regions used in calculating the mean inert tracer fluxes as described in Section 5.2.2. The upper panel shows the three concentric zones used when calculating mean inert tracer fluxes. The lower panel shows the size and relative positions of the concentric radial stripes used when estimating the radial distribution of inert tracer fluxes. Each of the concentric annuli are 5 km in width.

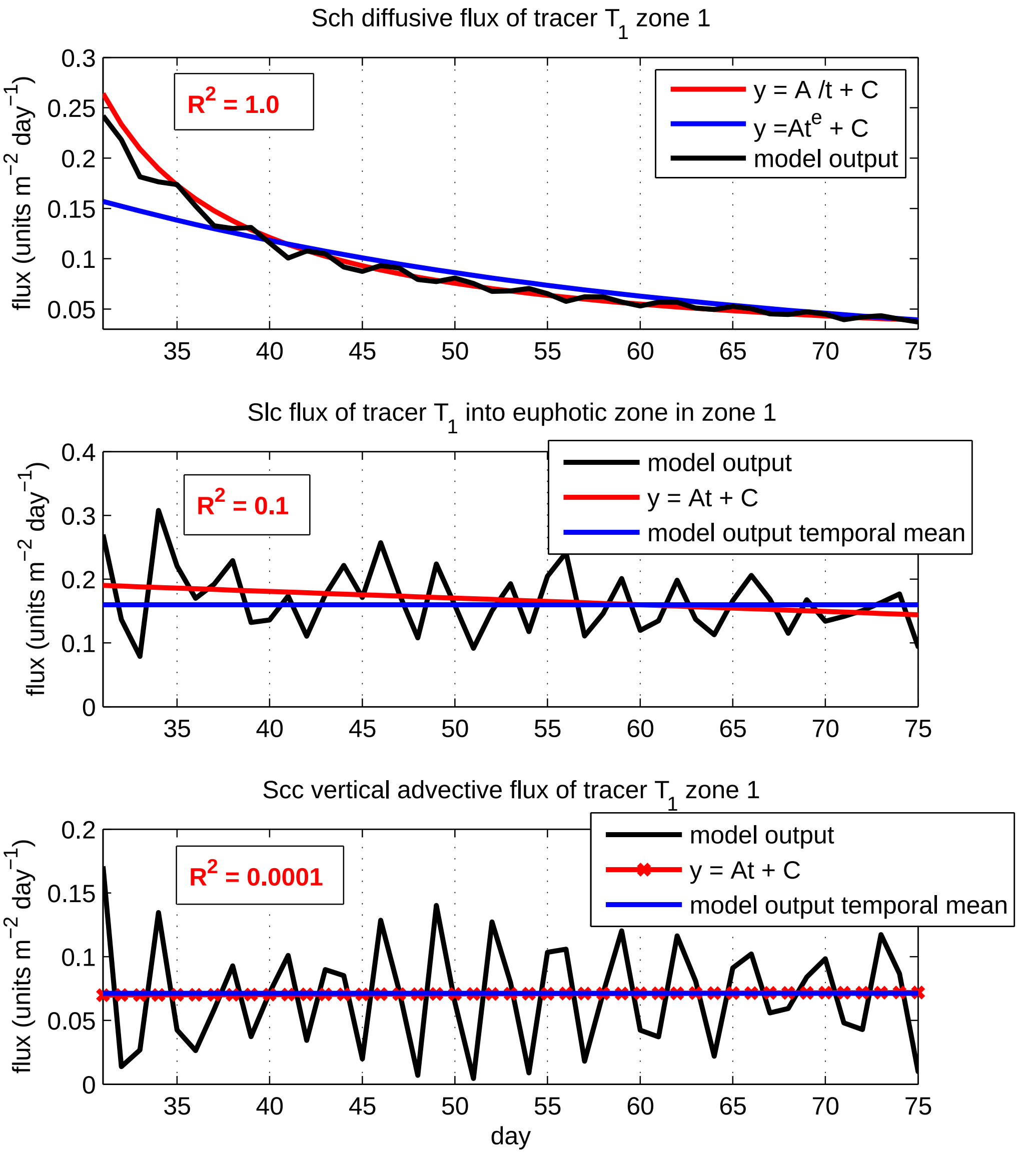

FIGURE 5.2: Examples of fitting trend lines to tracer T_1 fluxes. Top panel shows trends for the diffusive flux for zone 1 from run Sch using the Bye (1986) wind stress parametrization. The best fit is for a trend of y = A/t + c (see Section 5.2.4.2). Middle panel shows fitting trends to the vertical advective flux for zone 1 from run Rrr using the Bye (1986) wind stress parametrization. The best fit is for a trend of y = At + c (see Section 5.2.4.2). Bottom panel shows fitting trends to the vertical advective flux for zone 1 from run Sch using the Bye (1986) wind stress parametrization. There is no obvious trend to the data (see Section 5.2.4.2). The R^2 value for the best fit in each case is shown in red.

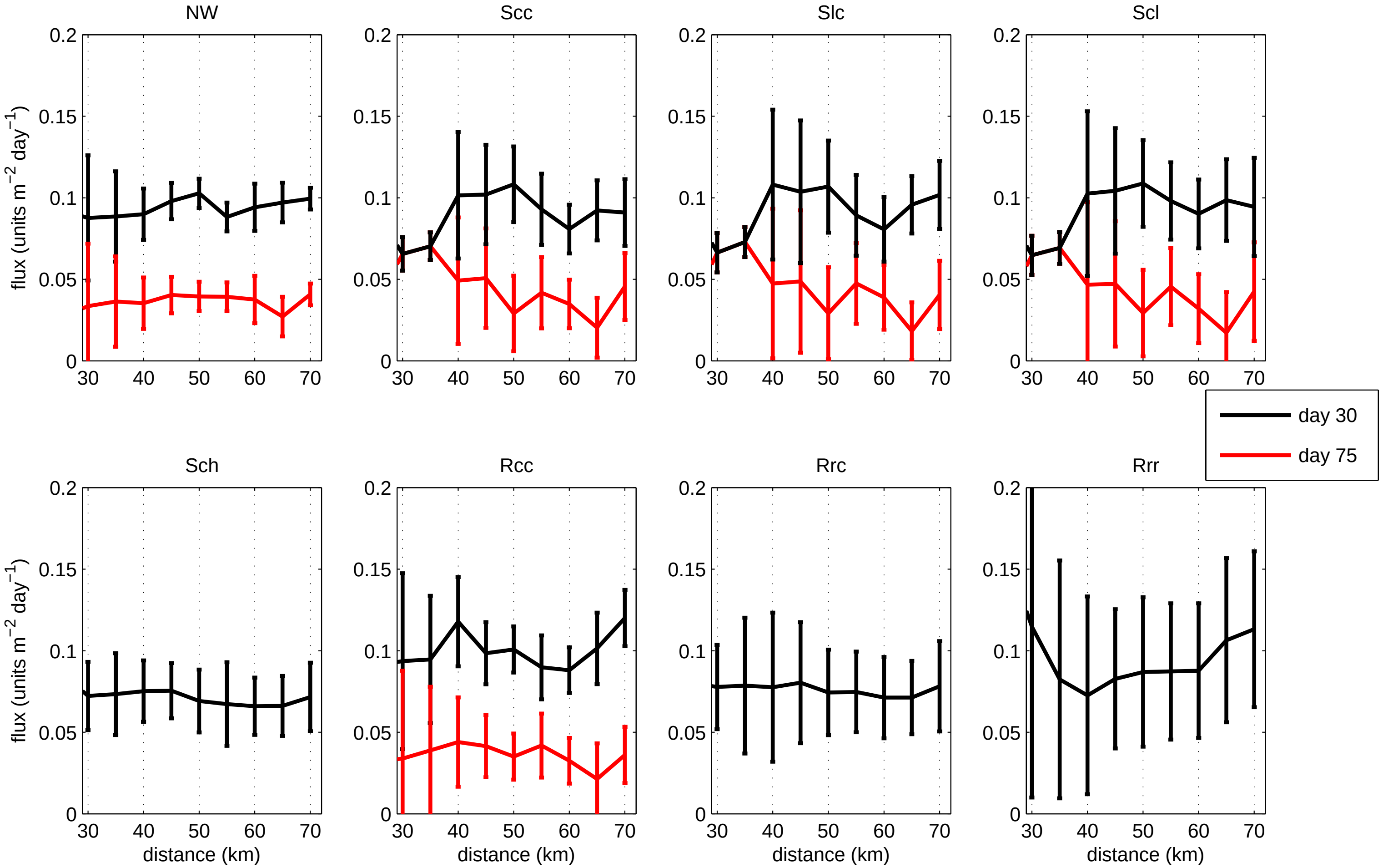

FIGURE 5.3: Radial distribution of fluxes of inert tracer T_1 into the euphotic zone (units m^{-2} day^{-1}) for all runs using the standard wind stress parametrization. Where the spatial mean flux was estimated by fitting a trend (Section 5.2.4.2) the day 30 mean is in black and the day 75 mean is in red. Where there was no trend the temporal mean for the whole period is in black. Error bars show $\pm$ standard error to the mean.

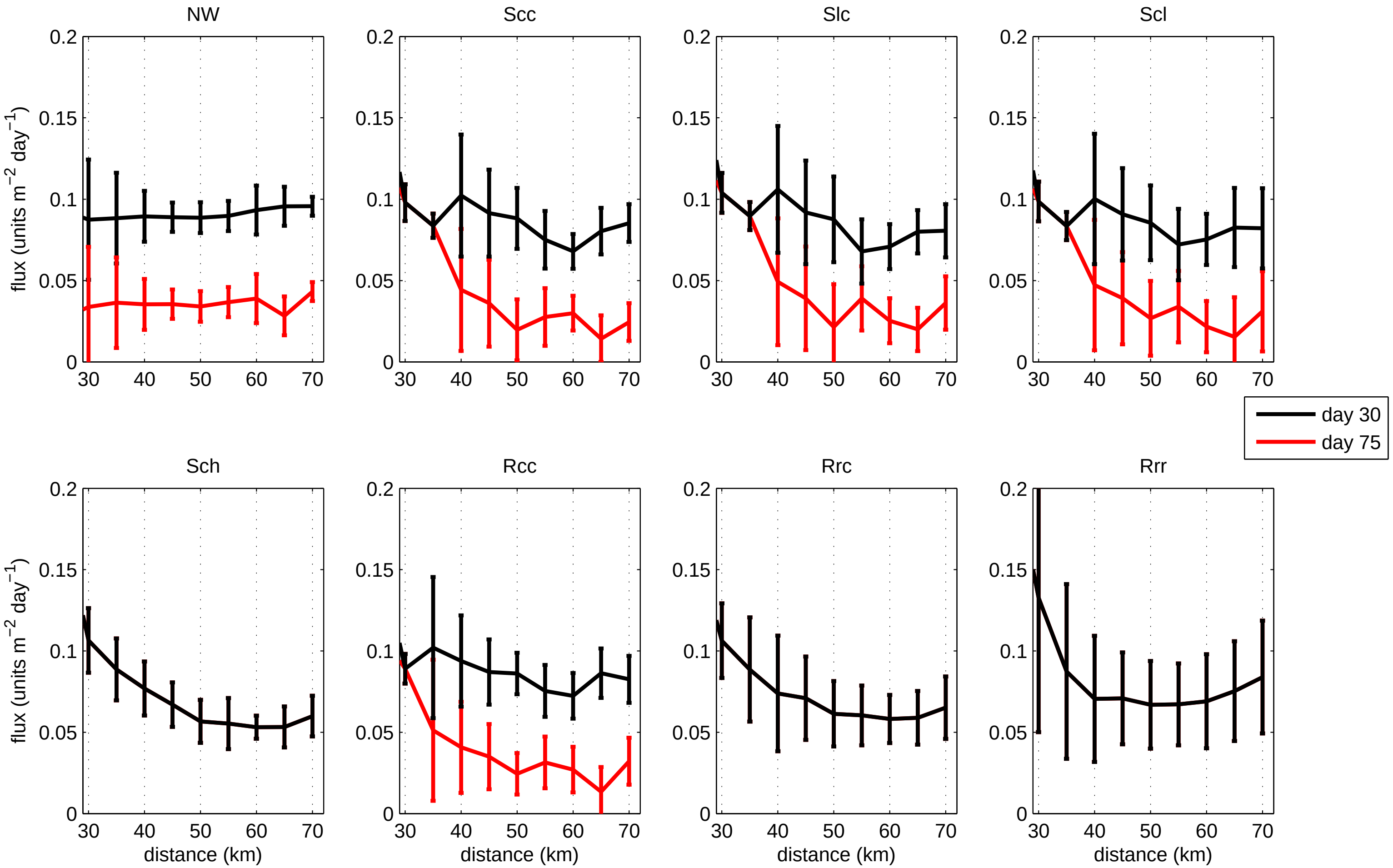

FIGURE 5.4: Radial distribution of fluxes of inert tracer T_1 into the euphotic zone (units m^{-2} day^{-1}) for all runs using the Bye (1986) wind stress parametrization. Where the spatial mean flux was estimated by fitting a trend (Section 5.2.4.2) the day 30 mean is in black and the day 75 mean is in red. Where there was no trend the temporal mean for the whole period is in black. Error bars show ± standard error to the mean.

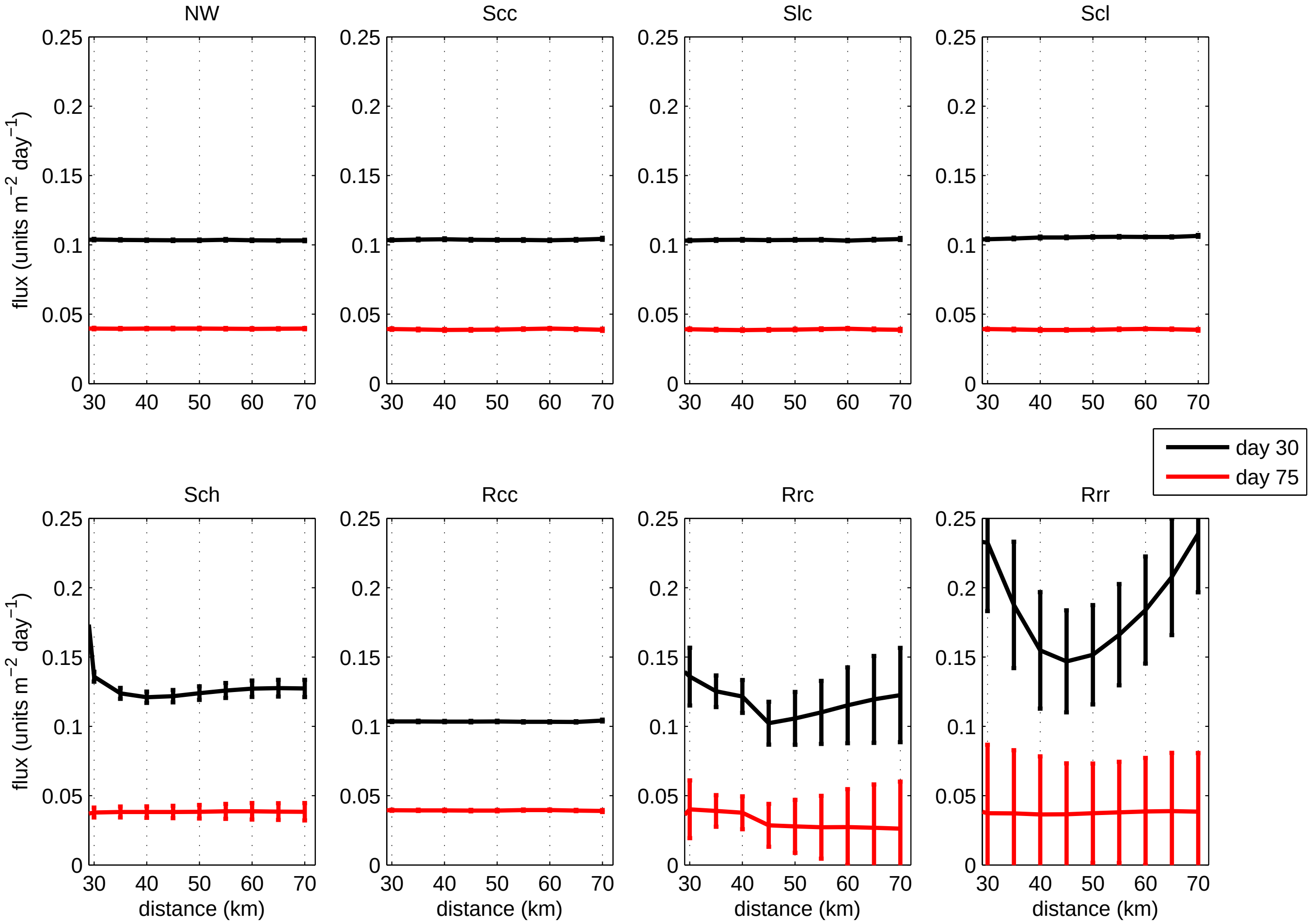

FIGURE 5.5: Radial distribution of diffusive fluxes of inert tracer T_1 into the euphotic zone (units m^{-2} day^{-1}) for all runs using the standard wind stress parametrization. The spatial mean flux was estimated by fitting a trend (Section 5.2.4.2). The day 30 mean is in black and the day 75 mean is in red. Error bars show ± standard error to the mean.

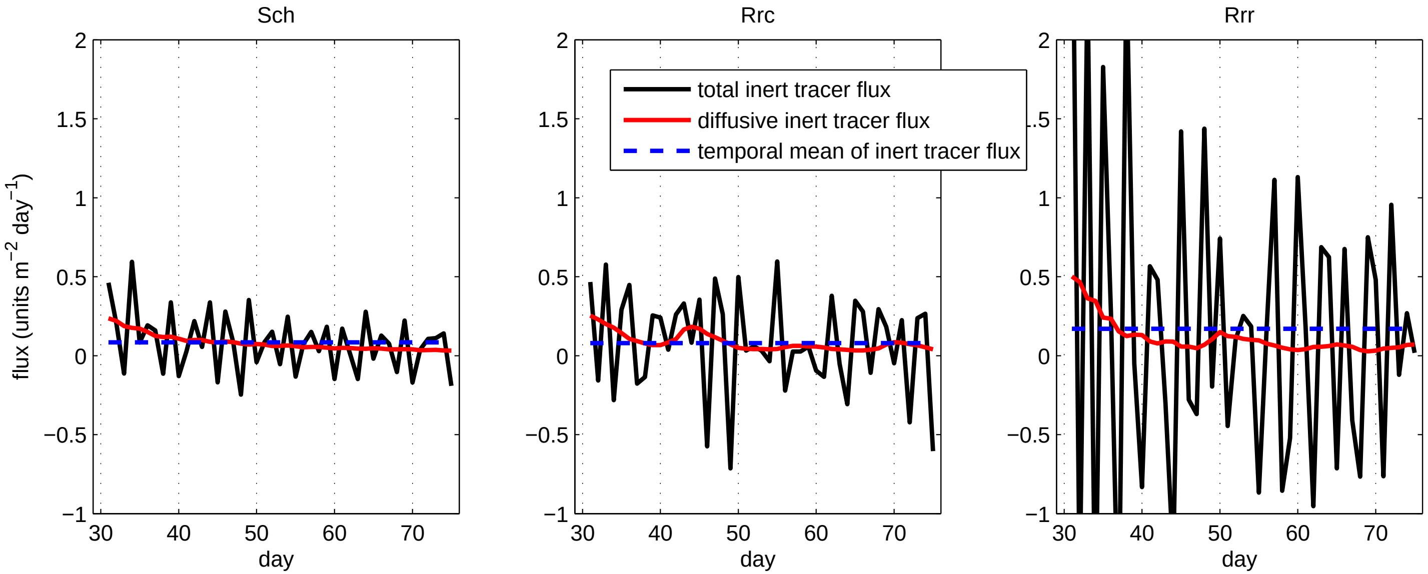

FIGURE 5.6: Total flux of inert tracer T_1 into the euphotic zone and the diffusive flux of inert tracer into the euphotic zone for zone 1 runs Sch, Rrc and, Rrr (see Table 5.1) using the standard wind stress parametrization.

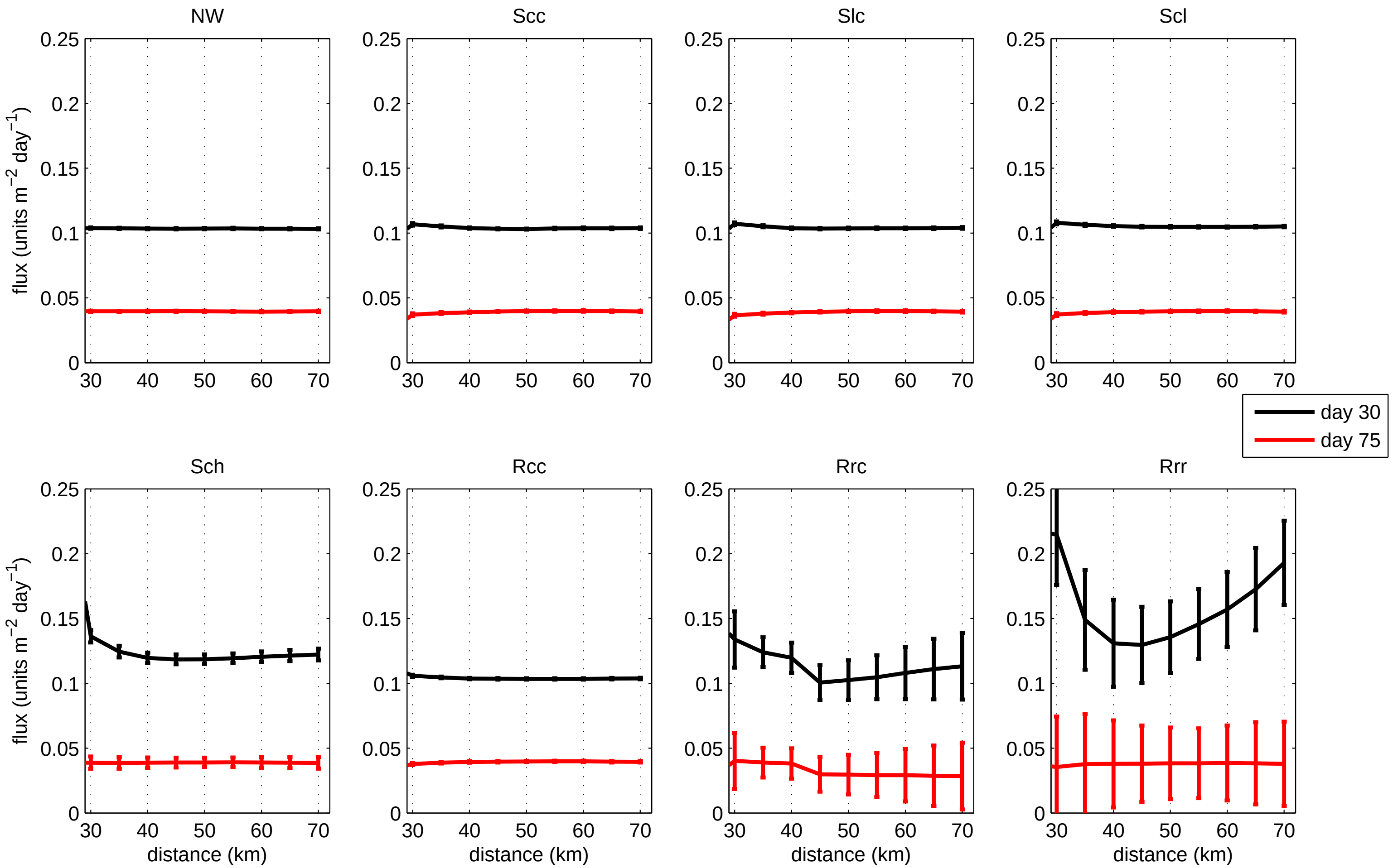

FIGURE 5.7: Radial distribution of diffusive fluxes of inert tracer T_1 into the euphotic zone (units m^{-2} day^{-1}) for all runs using the Bye (1986) wind stress parametrization. The spatial mean flux was estimated by fitting a trend (Section 5.2.4.2. The day 30 mean is in black and the day 75 mean is in red. Error bars show ± standard error to the mean.

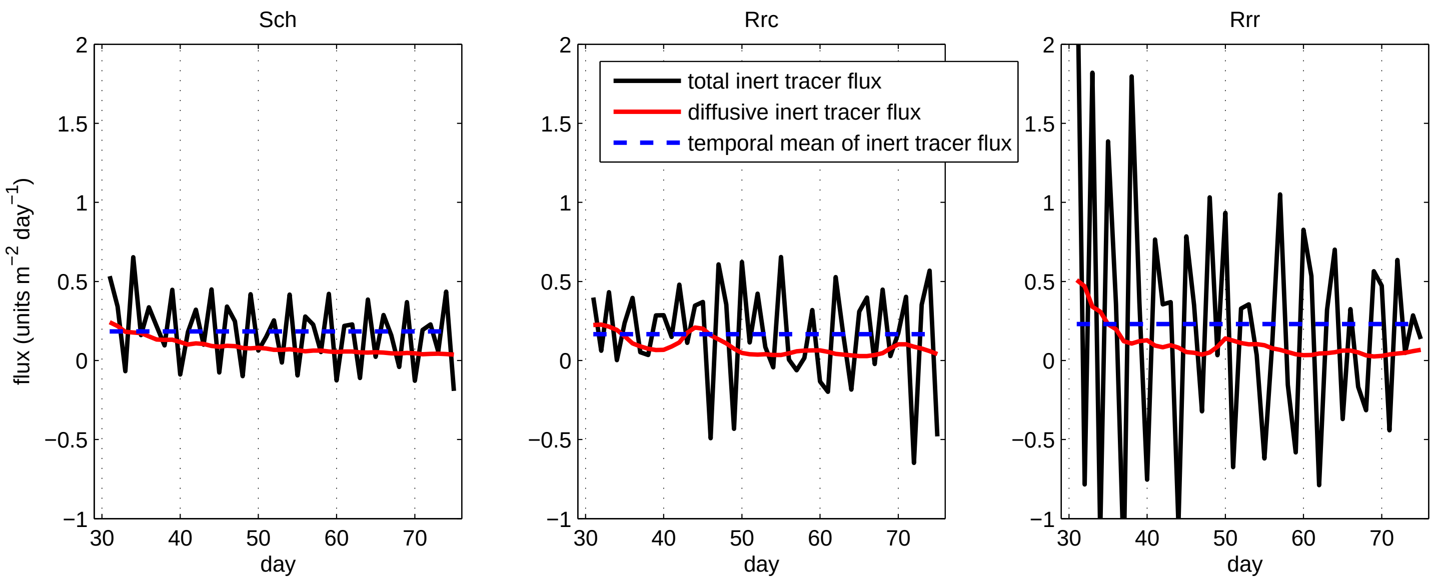

FIGURE 5.8: Total flux of inert tracer T_1 into the euphotic zone and the diffusive flux of inert tracer into the euphotic zone for zone 1 runs Sch, Rrc and, Rrr (see Table 5.1) using the Bye (1986) wind stress parametrization.

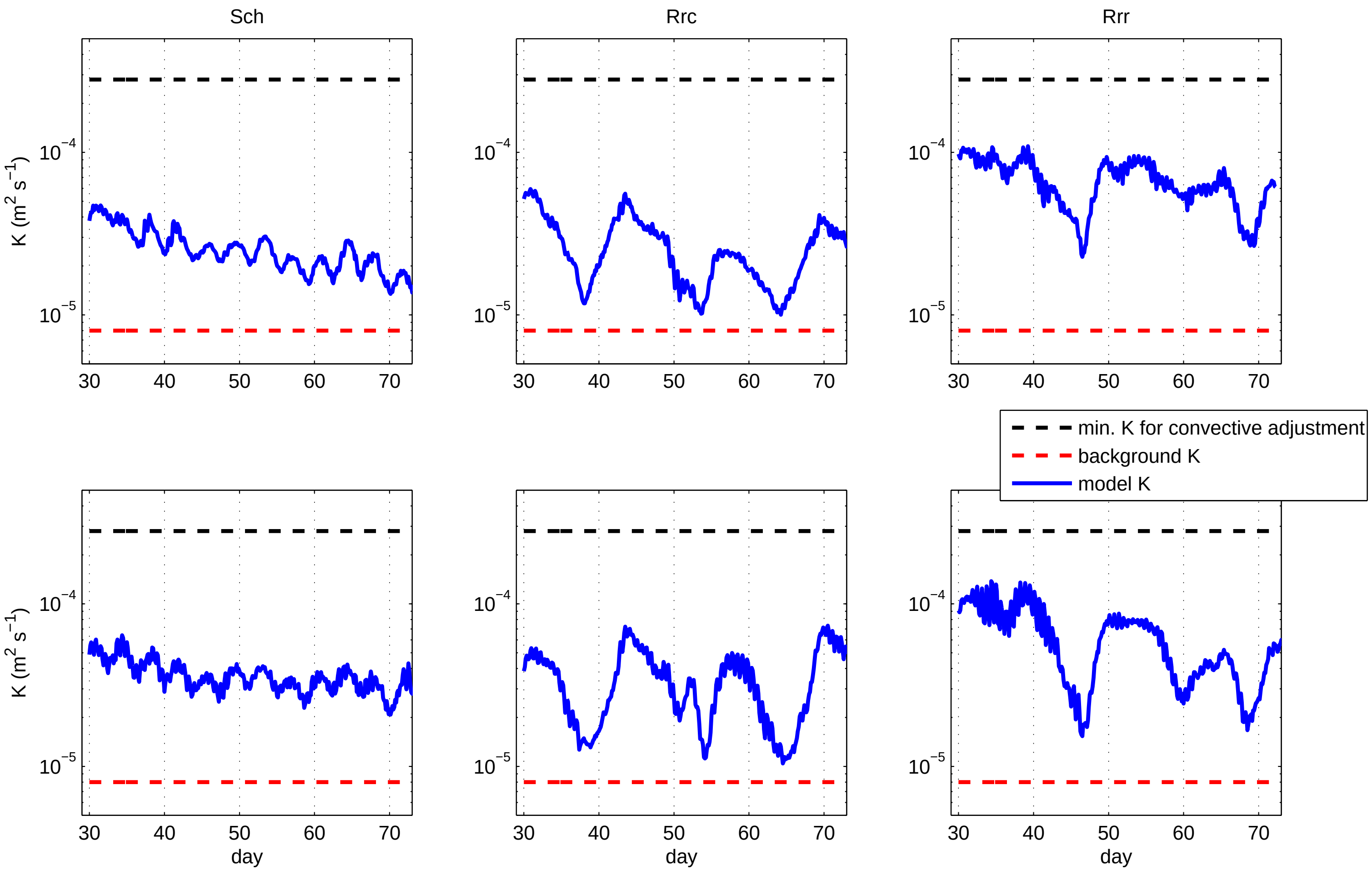

FIGURE 5.9: The maximum values of the turbulent diffusion coefficient (K) recorded during the high resolution (3 hour output) for the Sch, Rrc and Rrr model runs (Table 5.1). The model value of K is plotted in blue. The Richardson number parametrization minimum value of K (Chapter 3) is marked as a red dashed line. The minimum period mean value of K for convective adjustment to have occurred is marked as a black dashed line. The upper three panels are runs using the standard wind stress parametrization, the lower three panels are runs using the Bye (1986) wind stress parametrization.

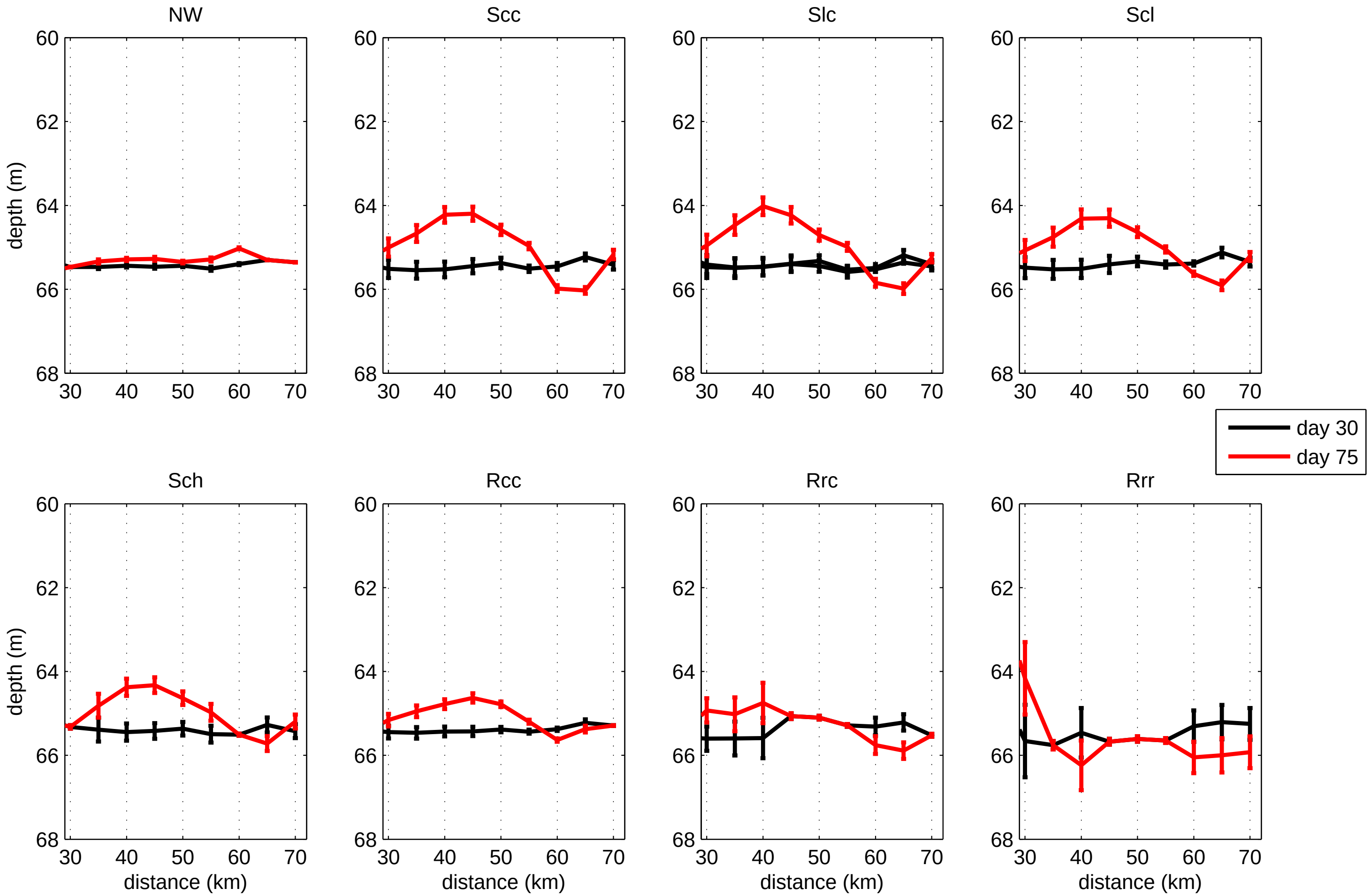

FIGURE 5.10: Radial distribution of the depth of inert tracer T_2 stripe (m) for all runs using the standard wind stress parametrization. The spatial mean flux was estimated by fitting a trend (Section 5.2.4.2). The day 30 mean is in black and the day 75 mean is in red. Error bars show ± standard error to the mean.

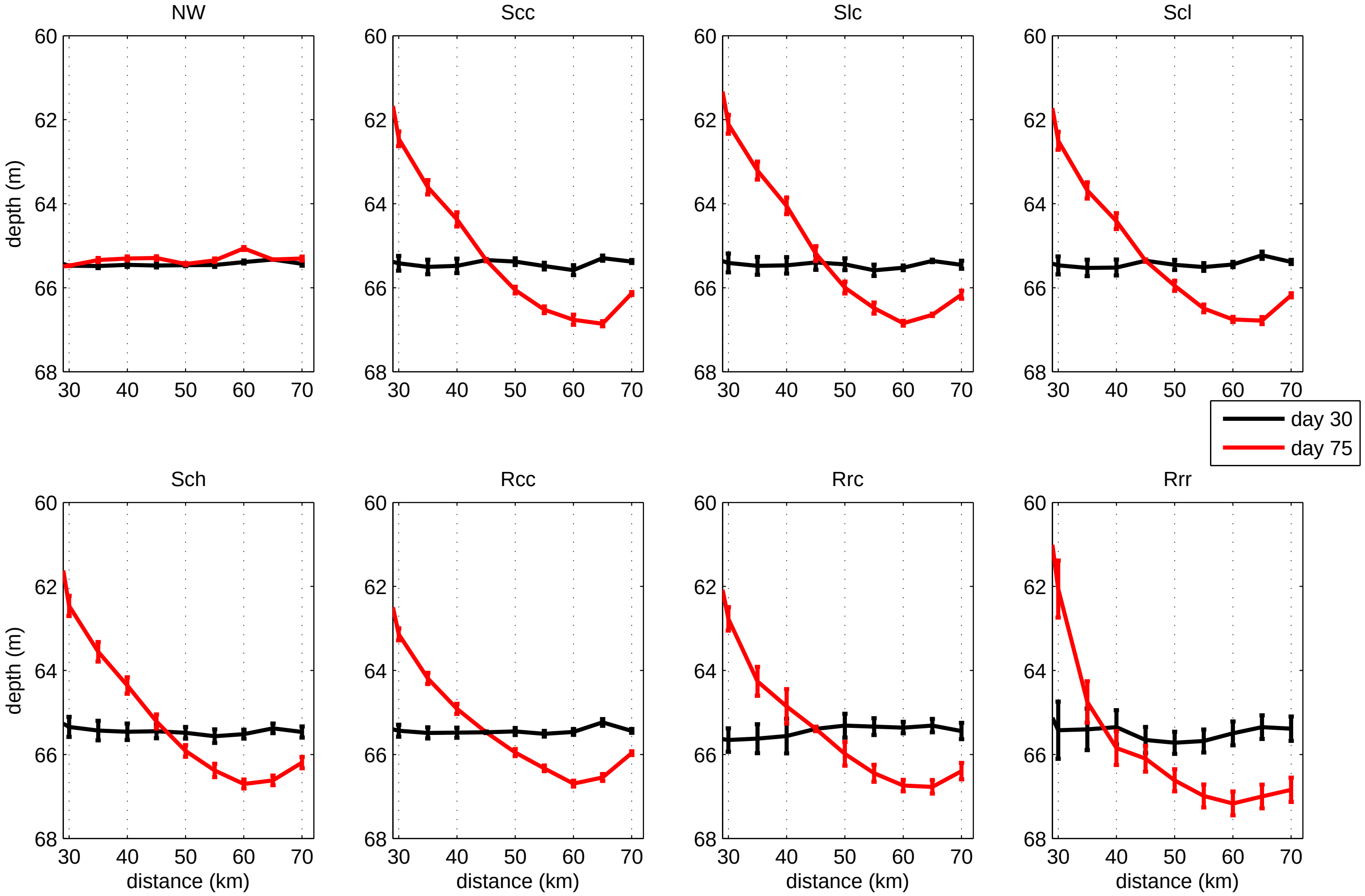

FIGURE 5.11: Radial distribution of the depth of inert tracer T_2 stripe (m) for all runs using the Bye (1986) wind stress parametrization. The spatial mean flux was estimated by fitting a trend (Section 5.2.4.2). The day 30 mean is in black and the day 75 mean is in red. Error bars show ± standard error to the mean.

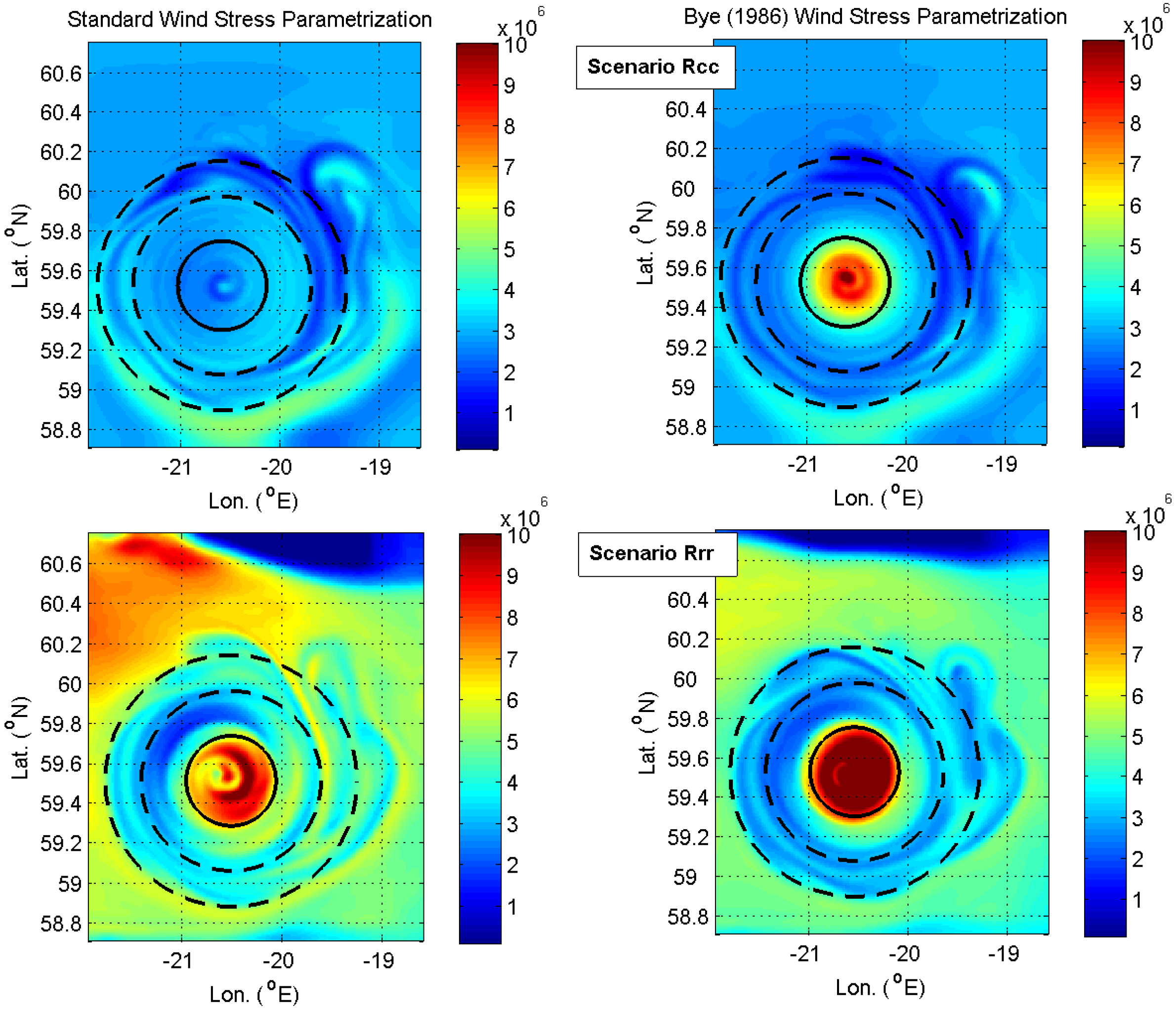

FIGURE 5.12: The amount of inert tracer T_1 (units) in the euphotic zone on day 75 of the model run for scenarios Rcc (upper panels) and Rrr (lower panels) using the Bye (1986) and standard wind stress parametrizations. The boundary of zone 1 (radius 25 km Figure 5.1) is marked as a solid black line. The boundaries of zones 2 (radius 50 km) and 3 (radius 70 km) are marked as dashed black lines.

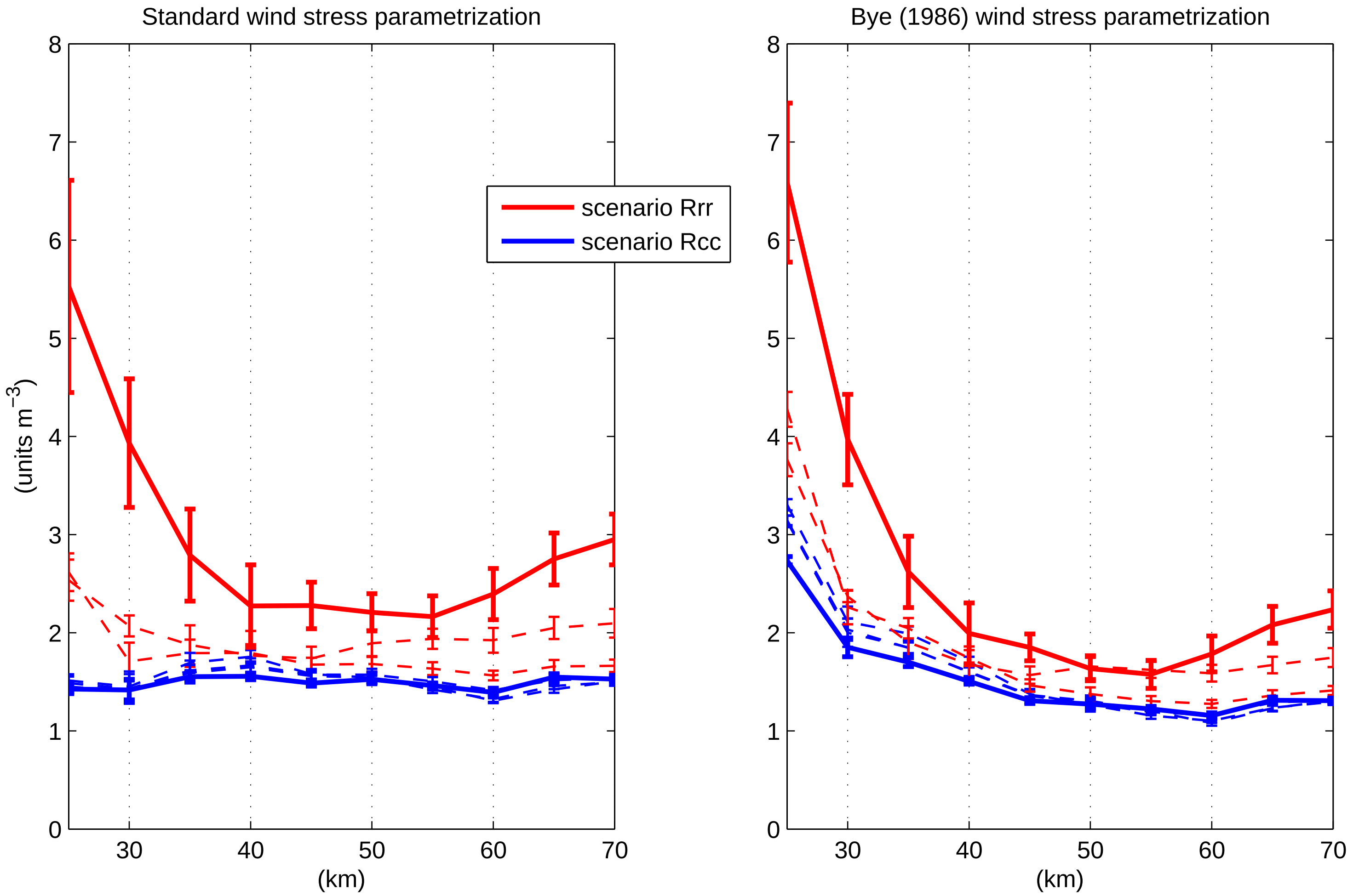

FIGURE 5.13: The radial distribution of the mean concentration of inert tracer T_1 (units m^{-3}) in the euphotic zone on day 75 of the model run using the Bye (1986) and standard wind stress parametrizations. The temporal mean concentration for each of the radial annuli (Figure 5.1) was estimated by fitting a trend (Section 5.2.4.2). Error bars show ± standard error to the mean. Scenario Rrr is marked as a solid red line. Other scenarios with sub-inertial wind forcing frequency (Rrc and Sch) are marked as dashed red lines. Scenario Rcc is marked as a solid blue line. The remaining scenarios are marked as dashed blue lines.

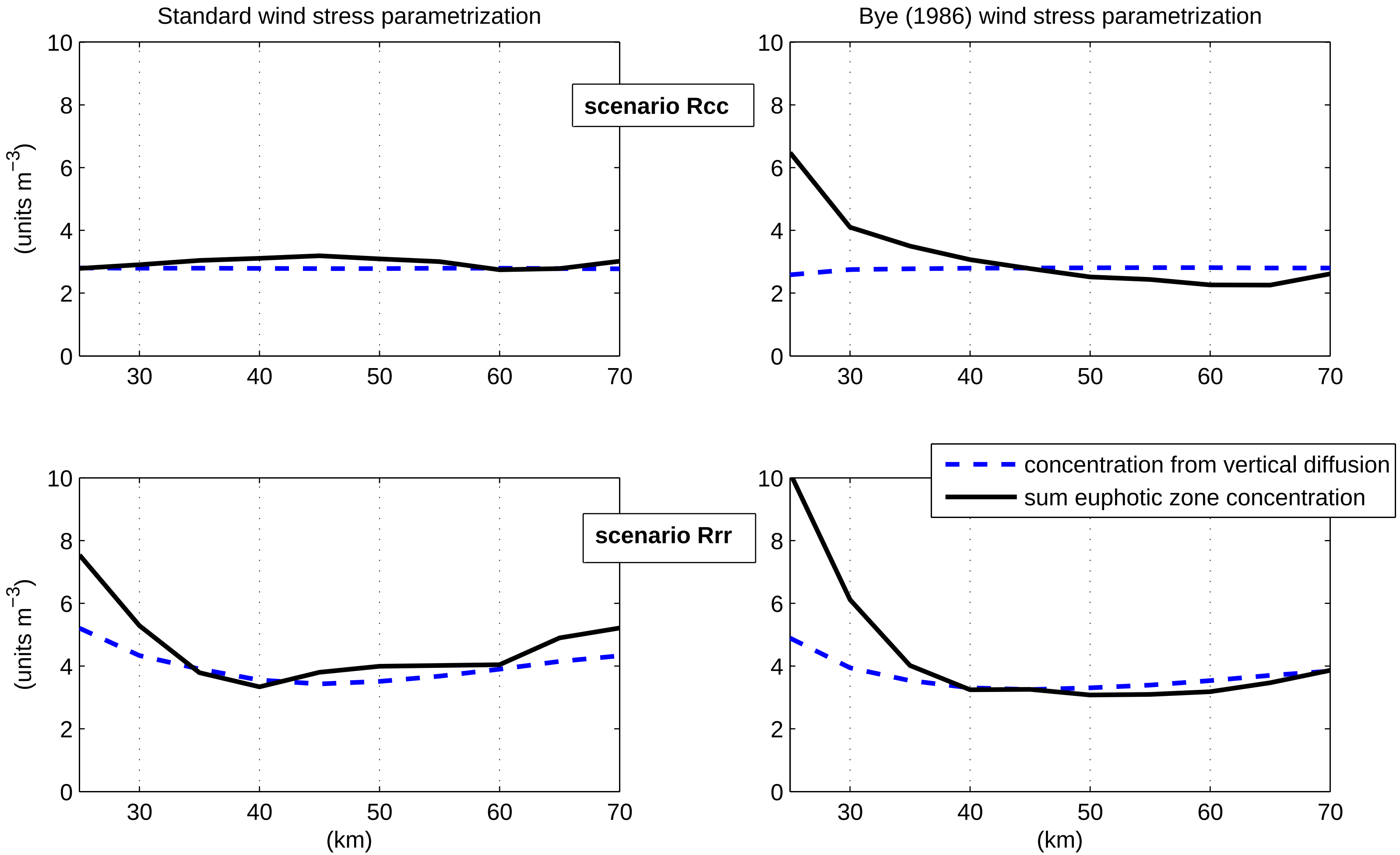

FIGURE 5.14: The mean concentration of inert tracer T_1 (units m^{-3}) in the euphotic zone on day 75 of the model run for scenarios Rcc (upper panels) and Rrr (lower panels) using the Bye (1986) and standard wind stress parametrizations. The concentration of T_1 is spatially averaged over nine radial annuli (Figure 5.1). The net day 75 concentration of T_1 is shown in black. The concentration attributable to the vertical diffusive flux of T_1 from day 30 (tracer release day) to 75 is shown as a blue dashed line.

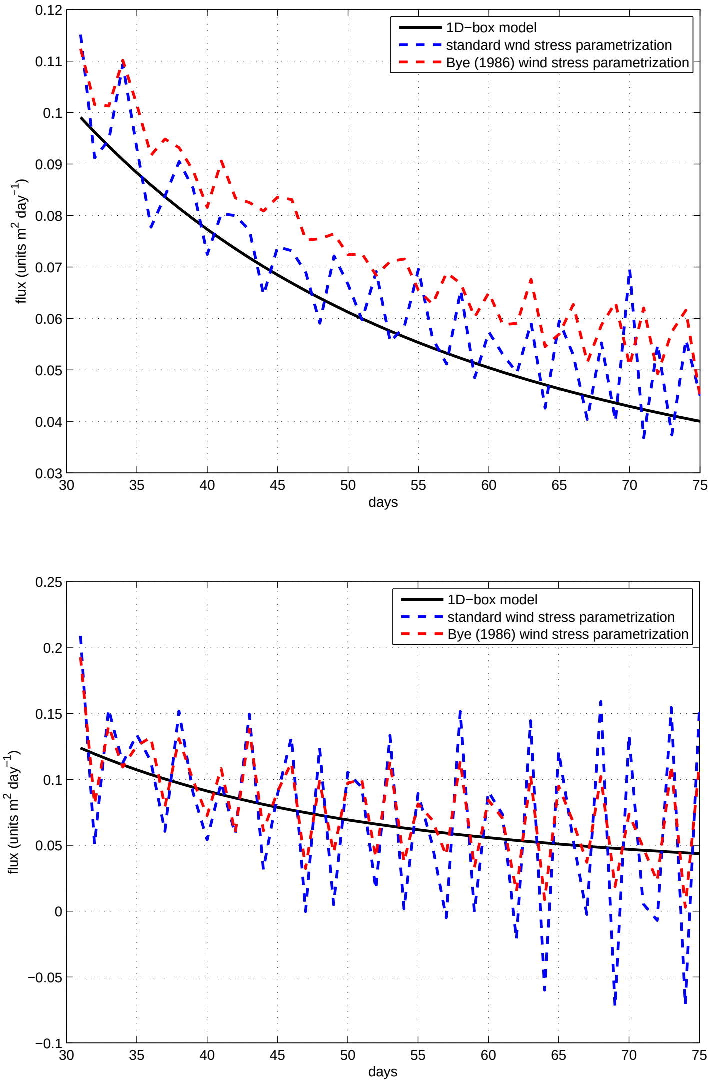

FIGURE 5.15: Comparison of the diffusive flux calculated for a 1D model that was initialised to match model inert tracer distribution with diffusive flux from the full 3D eddy model. The upper panel shows the flux calculated from the 1D model at the base of the euphotic zone using a constant turbulent diffusion coefficient of 8x10^{-6} m^{2}s^{-1} and the total flux of inert tracer into the euphotic zone for run Scc using both wind stress parametrizations. The lower panel shows the flux calculated from the 1D model at the base of the euphotic zone using a constant turbulent diffusion coefficient of 1x10^{-5} m^{2}s^{-1} and the total flux of inert tracer into the euphotic zone for run Sch using both wind stress parametrizations.

Chapter 6

Conclusions

In this thesis the effect that vertical turbulent mixing enhanced by shear from mesoscale circulation has on nutrient supply has been investigated. This investigation has been carried out using a combination of observations and high resolution computer modelling.

6.1 Shear enhanced nutrient supply

6.1.1 Observations and parametrization

The turbulent nutrient fluxes in the Iceland Basin were measured around an eddy dipole, a strong mesoscale feature, consisting of a cyclonic eddy and an anti-cyclonically rotating mode-water eddy, as part of UK RSS Discovery cruise D321. Despite the strong horizontal gradients in water velocity and density observed associated with this mesoscale feature, the vertical turbulent mixing shows an almost uniform horizontal distribution around the dipole (Chapter 2). Nevertheless, with the possible exception of the region within the cyclonic eddy core, vertical variation in the observed turbulent mixing and Richardson number suggested that mesoscale vertical shear from the dipole was contributing towards the observed turbulent mixing. The value of the area mean turbulent diffusivity, the magnitude of the turbulent mixing, reported in this thesis for the base of the euphotic zone is 1.4 (95 % confidence interval: 1 to 2) x10^{-5} m^2 s^{-1}. While this value is lower than recorded in previous studies from the Iceland Basin of 0.97 ± 0.3 x 10^{-4} m^2 s^{-2} (Jickells et al., 2008) and 1.51 ± 0.29 x 10^{-4} m^2 s^{-2} (Law et al., 2001) it is comparable to the value reported within a mode-water eddy core in the Sargasso Sea of 0.35 ± 0.05 x10^{-4} m^2 s^{-1} (Ledwell et al., 2008).

To explore the apparent relationship observed between turbulent diffusivity and Richardson number further, a Richardson number based parametrization of vertical mixing was developed from measurements of turbulent diffusivity from three separate ocean regions including the Iceland Basin (Chapter 3). Values of the vertical turbulent diffusivity calculated from the parametrization proposed in this thesis suggest that extant parametrizations (Large et al., 1994; Peters et al., 1988; Pacanowski and Philander, 1981) may underestimate the vertical turbulent diffusivity in high (> 1) Richardson number shear flow associated with mesoscale ocean features (Chapter 3).

6.1.2 High resolution computer modelling

The Richardson number parametrization developed in this thesis was subsequently applied in a model of a mode-water eddy to examine whether interactions of the eddy and the wind cause an enhancement to the vertical nutrient flux and to determine which vertical flux mechanisms were driving any enhancement. The mode-water eddy model was constructed from observations made in the Iceland Basin and forced using wind data appropriate to the Iceland Basin (Chapter 4). Results from the model suggested that vertical shear-enhanced diffusive mixing is one of two dominant mechanisms responsible for fluxing nutrients into the euphotic zone. The other dominant mechanism is Ekman suction, generated by the interaction of the mesoscale circulation and the wind (Chapter 5).

Using the wind data recorded in the Iceland Basin, turbulent diffusivity around the mode-water eddy was estimated from the model for the base of the euphotic zone at between 3 and 9 x10^{-5} m^{2}s^{-1} (Chapter 2). This value is significantly higher than the minimum (background) value of Richardson number parametrization (8 x10^{-6} m^{2}s^{-1}) and arises as a result of shear enhancement. The model turbulent diffusivity compares very well with observations of turbulent diffusivity both in the uniformity of horizontal distribution and in the magnitude. Analysis of the eddy model suggested that vertical turbulent diffusivity only shows significant shear enhancement of tracer flux when using high frequency (super-inertial) wind forcing.

6.1.2.1 Sub-mesoscale physical processes and turbulent viscosity

The model study in this thesis suggests that the effects of sub-mesoscale processes may be less important than enhanced turbulent mixing or Ekman suction processes at the base of the euphotic zone for an isolated eddy (Chapter 5). Reducing the vertical viscosity in the eddy model results in enhanced diffusive fluxes, some of which are indicative of the model attempting to resolve hydrostatic sub-mesoscale processes. However, direct observations do not support a lower value for vertical viscosity or the use of an extant parametrization that effectively uses a lower value. The use of a non-hydrostatic eddy model could result in the effects of sub-mesoscale processes becoming more apparent.

The observations of turbulent viscosity reported here are found to be best represented by a constant turbulent viscosity of 1×10^{-3} $m^2 s^{-1}$. That there was no robust relationship between observed Richardson number and turbulent viscosity is in some ways surprising given the strength of the relationship between Richardson number and turbulent diffusivity. In this thesis the emphasis has been on investigating vertical mixing at the mesoscale. The lack of any obvious relationship between Richardson number and turbulent viscosity may indicate that turbulent viscosity is driven by processes occurring at vertical scales other than the mesoscale. Changing the vertical viscosity in the mode-water eddy model, in this study, had a significant influence on the vertical diffusive fluxes in the model. This would suggest that further work is required to improve observations of vertical turbulent viscosity and to allow to a better parametrization to be derived.

6.1.3 Nutrient fluxes

Combining the background value of the Richardson number parametrization used in the eddy model (Chapter 3) with the observed area mean nitrate gradient at the base of the euphotic zone for the Iceland Basin (Chapter 2) gives an estimated minimum turbulent nitrate flux of approximately 0.05 mmol m^2 day^{-1}. Using the turbulent diffusivity estimated from the model for the base of the euphotic zone around the mode-water eddy gives a potential maximum turbulent nitrate flux of between 0.18 to 0.54 mmol m^2 day^{-1}. Comparing the estimated minimum turbulent nitrate flux derived from the model with the observed area mean turbulent nitrate flux of 0.13 mmol m^2 day^{-1} for the base of the euphotic zone (Chapter 2) suggests that shear enhanced turbulent diffusivity arising from the presence of the observed strong mesoscale feature is potentially responsible for up to a 160 % increase in turbulent nitrate flux. Comparisons with the model estimated maximum nitrate flux suggest a shear enhancement to the turbulent nitrate flux of up to an order of magnitude. However, the results from the model suggest that this significant increase in turbulent nitrate flux is limited spatially to within the area around the solid body radius (up to 25 km) of the mesoscale feature. The potential basin scale impact of any such mesoscale shear enhancement to nutrient flux remains to be quantified.

The observations of turbulent nutrient flux reported in this thesis support the view that for sub-polar regions such as the Iceland Basin vertical turbulent flux is a minor pathway for nutrient into the surface waters when compared to the convective supply from deep winter mixing (Williams and Follows, 2003; Williams et al., 2000). The magnitude of turbulent macro-nutrient flux is estimated to be at most 13 % of the estimated supply of macro-nutrient by deep winter mixing in the region (Chapter 2). Observations of the vertical turbulent flux of iron into the surface waters of the Iceland Basin are, at best, inconclusive. Profiles of dissolved iron are highly variable leading to an order of magnitude 95 % confidence limits on dissolved iron fluxes. Nevertheless, the magnitude of the observed dissolved iron flux is consistent with the size of the discrepancy between estimated new production requirements for dissolved iron and the supply of dissolved iron by deep winter mixing and aeolean deposition (Chapter 2).

Interestingly the values of turbulent mixing and nitrate flux observed in the Iceland Basin are almost equal to those reported in the oligotrophic sub-tropical gyre between 25° to 28° N (Ledwell et al., 1998; Lewis et al., 1986). Area mean nitrate flux observed in the Iceland Basin of 0.13 (95 % confidence interval: 0.08 to 0.22) mmol m^{-2} day^{-1} matches the nitrate flux observed at 28° N of 0.14 (95 % confidence interval 0.002 to 0.89) mmol m^{-2} day^{-1} (Lewis et al., 1986). Area mean turbulent kinetic energy dissipation observed in the Iceland Basin of 2.0 (95 % confidence interval: 1.79 to 2.4) $x10^{-9}$ W kg^{-1} is also similar to the ensemble mean turbulent kinetic dissipation observed at 28°N of 1.7 ± 0.57 $x10^{-9}$ W kg^{-1} (Lewis et al., 1986). The area mean turbulent diffusivity recorded around the strong mesoscale feature in the Iceland Basin, considered to be in part a product of some degree shear enhancement, of 0.21 (95 % confidence interval: 0.17 to 0.26) $x10^{-4}$ m^2 s^{-1} is again remarkably close to the value reported at 28° N of between 0.12 ± 0.02 $x10^{-4}$ m^2 s^{-1} and 0.17 ± 0.02 $x10^{-4}$ m^2 s^{-1} (Ledwell et al., 1998).

It is not possible to determine whether the open ocean measurements of Lewis et al. (1986) and Ledwell et al. (1998) were subject to any mesoscale activity which may have contributed to the observed turbulent mixing. However, both previous observations of turbulent mixing were carried out at latitudes below 28.9^{o}N and it is possible that parametric subharmonic instability (PSI) of the internal tide may be enhancing these open ocean measurements of turbulent mixing (Hibiya and Nagasawa, 2004; MacKinnon and Winters, 2005; Hibiya et al., 2007). Periodic modulation of the local buoyancy frequency (N) by internal waves results in instabilities which can cause the growth of internal waves with frequencies which are half the frequency (the first sub-harmonic) of the primary wave. If the frequency of the primary wave is between f (inertial frequency) and $2f$ sub-harmonic instability will not occur as the frequency of the sub-harmonic does not correspond to an internal wave. Internal waves have frequencies in the range f to N. At latitude 28.9^o N the frequency $2f$ is equal to the diurnal M_2 tidal frequency (1.4 x10^{-4} s^{-1}) and so internal M_2 tides closer to the equator may be subject to PSI (Thorpe, 2005). PSI has been predicted and observed to enhance turbulent mixing by up to an order of magnitude ($\sim$ 1x10^{-4} m^{2}s^{-1}) between 20^o to 30^o N in the Pacific (Hibiya and Nagasawa, 2004; MacKinnon and Winters, 2005; Hibiya et al., 2007). This suggests that though the magnitude of the turbulent mixing observed by Lewis et al. (1986) and Ledwell et al. (1998) is approximately equal to that reported here the processes responsible for the mixing may still be different.

Lewis et al. (1986) observed vertical nitrate gradients of $\sim$ 40 μmol m^{-4} and observed turbulent diffusivity of between 2 and 8 x10^{-5} m^{2}s^{-1} (estimated from Lewis et al. (1986) fig. 1). These are of the same order as reported here for the Iceland Basin (Iceland Basin nitrate gradient 70 μmol m^{-4} Chapter 2). This suggests that the surprising similarity in observed vertical nitrate fluxes may be due to a serendipitous combination of turbulent diffusivity and vertical nitrate gradient.

6.2 The wider significance of shear enhanced nutrient supply

Vertical turbulent nutrient flux in the Iceland Basin, even when enhanced by the presence of a strong mesoscale feature, appears to have little impact on overall primary production. However, in the oligotrophic post-winter bloom sub-tropical gyre such an enhancement to turbulent nutrient supply is potentially of much greater importance. The mode-water eddy modelled in this thesis has comparable physical properties such as size, rotation speed and period to mode-water eddies encountered in the Sargasso Sea (Ledwell et al., 2008; McGillicuddy et al., 1999) and eddies formed by convection in the Bay of Biscay (Reverdin et al., 2009).

It is not unreasonable to assume that for mode-water eddies, with comparable physical properties to the one modelled in this thesis, forcing by wind with high frequency variability would result in an enhancement to the vertical diffusive flux similar to that found here. Hence, mode-water eddies passing through regions where nutrient concentrations in the surface ocean are limiting may represent a source of additional nutrients through shear enhanced turbulent diffusivity and subsequently generate enhanced production.

Mode-water eddies eddies have been observed to be sites of anomalously high productivity in the Sargasso Sea (Ledwell et al., 2008; McGillicuddy et al., 2007; Sweeney et al., 2003), though there is considerable debate as to the nutrient flux mechanisms responsible for this observed high productivity (Mahadevan et al., 2008; McGillicuddy et al., 2008, 2007). The results from this thesis suggest that shear enhanced turbulent diffusive flux could potentially be a significant contributor.

6.2.1 Basin scale impacts of shear enhanced nutrient supply

Estimation of the basin scale impact that the shear-enhanced diffusivity associated with mesoscale eddies might have is only really possible through numerical modelling. The results from this thesis suggest that the Richardson number parametrizations of vertical mixing (e.g. Large et al. 1994; Pacanowski and Philander 1981) used in some typical eddy permitting ocean general circulation models (OGCM e.g. Popova et al. 2006; McGillicuddy et al. 2003) underestimate the turbulent diffusivity which is generated from the shear typical of mesoscale features at high Richardson number (Chapter 3). Additionally, the use of low temporal resolution (6 hour) wind forcing, which is unable to resolve the local inertial period, may not result in the generation of representative mesoscale shear within the model. The use of higher frequency wind data has already been shown stimulate higher primary production in idealized models where there is intense sub-mesoscale turbulence (Lévy et al., 2009). At best, by using a parametrization with a background diffusivity of order 10^{-5} m^2s^{-1}, some of the current eddy permitting OGCMs may be incorrectly representing the distribution of turbulent nutrient fluxes by underestimating mixing in regions of high mesoscale activity and overestimating mixing in regions of low mesoscale activity. Further work modelling productivity in a basin scale high-resolution OGCM which incorporates the vertical mixing parametrization proposed in this thesis together with high resolution wind forcing would need to be done to quantify the likely basin scale impact.

The use of the Bye (1986) wind stress parametrization in the mode-water eddy model introduces another vertical nutrient flux which is potentially at least as great in magnitude as the shear enhanced vertical diffusive flux (Chapter 5). This flux mechanism is unique to mode-water eddies and observations have suggested that this flux may contribute significantly to observed increased primary production associated with mode-water eddies (Ledwell et al., 2008). However, at a basin scale it has been suggested that the use of the Bye (1986) wind stress parametrization may have at best a neutral effect on vertical nutrient flux compared to using the standard wind stress parametrization (Eden and Dietze, 2009). Mode-water eddies are formed by deep winter convection, which is a non-hydrostatic process. It is not clear that a hydrostatic model such as used by Eden and Dietze (2009) accurately reproduces the formation and dynamics of mode-water eddies. An initial analysis of the similar resolution OCCAM (Webb et al., 1997) model output for the North Atlantic in year 2007 found evidence of 'meddies' but not of mode-water eddies. This analysis is by no means conclusive, but does suggest that further numerical modelling may be required before the basin scale impact of using the Bye (1986) wind stress parametrization can be accurately estimated.

6.3 In conclusion

The shear enhancement to nutrient supply by mesoscale circulation has been investigated and found to be potentially of much greater significance than has previously been considered. High resolution computer modelling suggests that when forced by high variability winds, mode-water eddies appear to be capable of locally enhancing nutrient flux by up to an order of magnitude. However, these modelling results have yet to be confirmed through observation and the long term, basin scale, impact has still to be quantified. The work in this thesis suggests that the vertical turbulent flux in the biologically important upper ocean is a complex, spatially and temporally heterogeneous phenomenon whose role as a stimulus to new production may well be underestimated.

Appendix A

Modelling appendix

There are four main assumptions made when analysing the results from running the eddy model (Chapter 5). These assumptions are, that the horizontal diffusive flux is small and can be neglected, that the inert tracer fluxes output from the model are representative of the changes in inert tracer concentrations, that the vertical mixing parametrization is valid for the range of Richardson numbers produced in the model and, that the position of the centre of the eddy can be consistently and accurately calculated for each model output.

Observations of vertical viscosity (Chapter 3) are most consistent with a constant vertical viscosity of 1 x10^{-3} m^2 s^{-1} as used in the eddy model (Chapter 4). However this value is high compared to what is used in other mixing parametrizations. The Richardson number based vertical mixing parametrizations of Large et al. (1994) and Pacanowski and Philander (1981) both use a constant background vertical viscosity of 1x10^{-4} m^2 s^{-1}.

In this appendix we consider each of the four main assumptions made when analysing the model results in turn and the likely impact that a reduced vertical viscosity would have on the model results.

A.1 Estimating horizontal diffusion

The use of a Shapiro filter and the periodic Euler forward time-step to maintain model numerical stability and solution consistency will introduce a degree of horizontal diffusion into the model even though the leapfrog time-stepping scheme is non-dissipative and physical horizontal diffusion is not explicitly represented (Chapter 4). The Shapiro filter is only applied to the horizontal tracer and velocity fields. Vertical diffusion is parametrized using a Richardson number based parametrization (Chapter 3).

The Shapiro filter is scale selective and the diffusion of the original signal resulting from the application of the filter depends on the wavelength of the signal being filtered, the order of the filter and the number of filter applications (Shapiro, 1975). In line with previous studies (Popova and Srokosz, 2009; Popova et al., 2002), for the model in this thesis numerical stability was maintained by running a fourth order Shapiro filter every time-step for tracers, momentum, and transport, and a second order Shapiro filter every time-step for vorticity. The Euler forward step is run every ten time-steps (Chapter 4).

Here we estimate the likely magnitude of the horizontal diffusion for inert tracer T_1 in the eddy model and compare the magnitude of the horizontal diffusion to the magnitude of the other fluxes.

A.1.1 Method

The magnitude of the horizontal diffusion produced during a single time-step was estimated by applying a fourth order Shapiro filter to a snapshot of the inert tracer T_1 field of the model output. The original model output T_1 field was then subtracted from the filtered T_1 field to produce an estimate of the horizontal diffusion flux for that time-step. This was done within the euphotic zone for each of the three zones described in Chapter 5. The longer term magnitude of the horizontal diffusion in the euphotic zone for each zone was then estimated by taking a mean of the calculated single time-step horizontal diffusion fluxes between day 30 and day 75 for each model run.

A.1.2 Results

The magnitude of the mean horizontal diffusive flux is less than 2 $\times 10^{-6}$ units m^{-2} day^{-1} in all runs (Table A.1 and A.2). The largest horizontal diffusive flux calculated was -1.7 $\times 10^{-6}$ units m^{-2} day^{-1} for scenario Rrr in zone 1 using the standard wind stress parametrization (a negative value indicates a flux out of the zone).

A.1.3 Discussion

The estimated magnitude of the horizontal diffusive flux is consistently four orders of magnitude lower than the lowest observed mean vertical diffusive flux (0.02 units m^{-2} day^{-1} Chapter 5). Compared to the horizontal advective fluxes the estimated horizontal diffusive flux is consistently two orders of magnitude lower than lowest observed mean horizontal advective flux ($\sim$ 1 x10^{-4} units m^{-2} day^{-1} Chapter 5). This would suggest that the magnitude of the horizontal diffusive flux is sufficiently small to justify not considering this flux significant.

The magnitude of the T_1 horizontal diffusive flux depends to a large extent on the tracer gradients. In the eddy model horizontal T_1 gradients in the euphotic zone can be generated both by reversible and non-reversible tracer flux processes such as the vertical movement of density surfaces by internal waves, vertical diffusion and horizontal processes such as stirring. The effects of internal waves on model density surfaces are present in all runs but are most marked for the runs with high frequency realistic wind forcing (Rrc and Rrr Chapter 4). Hence, estimating the magnitude of the horizontal diffusion through averaging a once a day snapshot of horizontal diffusion would be expected to produce an underestimate of the horizontal diffusion flux magnitude especially for the high frequency realistic wind forcing runs. In addition there is no method of estimating the numerical diffusion of T_1 in the model which occurs as a result of the Euler forward time-steps. This would suggest that there is a high degree of uncertainty associated with any estimates of the horizontal diffusive flux. However, this flux is still unlikely to be significant.

A.2 Quantifying inert tracer flux

The Harvard Ocean Prediction System (HOPS) horizontally advects tracers using a "leapfrog" forward time-stepping scheme. Using a leapfrog scheme, the tracer concentrations at time $Ts + 1$ are calculated by adding twice the tracer flux estimated at Ts to the tracer concentrations at time Ts - 1. For example in Figure A.1, at time-step *Ts2* the concentration of tracer at *Ts3* is estimated by adding twice the tracer flux calculated at time-step *Ts2* to the concentration of tracer at *Ts1*. Consequently to best match the changes in the inert tracer concentration over the output period, twice the calculated model fluxes are stored every second time-step. At the end of the output period the mean, over the output period, of the stored fluxes is output with the tracer fields.

Additionally, for numerical consistency (Chapter 4), HOPS runs a forward Euler time-step every ten time-steps where the tracer concentration at *Ts + 1* is calculated by adding the inert tracer flux at time *Ts* to the tracer concentration at time *Ts*. For example in Figure A.1, the concentration of tracer at *Ts5* is calculated at *Ts4* by adding the tracer flux calculated at *Ts4* to the concentration of tracer at *Ts4*. This periodic Euler time-step is not accounted for when the model flux components are stored for later output i.e., in Figure A.1 the output tracer concentration at *Ts5* will not equal the output tracer concentration at *Ts1* plus the sum of two time-steps worth of flux at *Ts2* and two time-steps worth of flux at *Ts4*. This would suggest that there is a potential disparity between the output fields and the output flux components. This disparity only arises due to the way in which the flux components are stored for later output and does not reflect any inherent inaccuracy in the calculation of the output fields.

The model is run with open Orlanski radiative boundaries which allow tracer to flux out of the model domain (Chapter 4). Hence the total volume of inert tracer T_1 within the model domain is not conserved. However, for a fixed sized sub-volume of the model domain the changes in inert tracer T_1 concentration calculated by first order differencing the output T_1 concentrations should equal the sum of the individual T_1 flux terms, horizontal and vertical advective flux and vertical diffusive flux. Any difference will be due to uncertainty in the flux component terms arising from the scheme described above.

Here we estimate the magnitude of the disparity between the the sum of the output T_1 flux components and the changes in output T_1 concentrations.

A.2.1 Method

The sum of the output flux components for inert tracer T_1 into the euphotic zone over a fixed model sub-volume, a box 40 km in from each model boundary (Figure A.2), was compared to the changes in output inert tracer T_1 concentrations in the euphotic zone of the model sub-volume. The size of the sub-volume was chosen to be smaller than the whole model domain to minimise the influence of model boundaries yet be large enough to encompass the model eddy for the majority of the 75 day run period.

A.2.2 Results

In all cases, for all scenarios, the calculated sum of the flux components is consistent with the change in euphotic zone inert tracer T_1 calculated by first order differencing (Figure A.3 and A.4). Expressing the difference between the sum of the flux components and the change in euphotic zone inert tracer as a percentage of euphotic zone inert tracer change, the mean difference between the sum of the flux components and the change in euphotic zone inert tracer for all runs is 0.2 %. In 96 % of cases the difference between the flux terms and the inert tracer change is less than 1 %, with a maximum difference of 9 % for run Rrr using the Bye (1986) wind stress parametrization (A.5).

A.2.3 Discussion

The greatest percentage differences between the change in inert tracer T_1 and the sum of the flux components is observed when the fluxes are small (of order 10^8 units day^{-1} in magnitude) into the sub-volume. The absolute difference between the change in output inert tracer and the sum of the output flux components for the sub-volume is approximately constant between 10^6 to 10^7 units for all scenarios. As a results when the calculated fluxes are of order 10^8 units day^{-1} the percentage error is quite large.

In all cases, the uncertainty in the flux component terms is small when compared to the uncertainty in the change in euphotic zone inert tracer volume resulting from errors in the calculation of the eddy position (Section A.4).

A.3 Validity of the Richardson number parametrization

The Richardson number parametrization of vertical turbulent mixing used in the eddy model is considered to be robust for values of the Richardson number greater than 1 (Chapter 3). The parametrization was calibrated using observations of the Richardson number above a critical value of 0.25. However, previous studies investigating the Richardson number dependence of turbulent mixing have suggested that at values of the Richardson number approaching the critical value turbulent mixing is enhanced to a greater degree than the parametrization in this thesis would allow (Soloview et al., 2001; Peters et al., 1995). There were relatively few observations in the Richardson number range 0.25 to 1 used in calibrating the parametrization in this thesis. Hence, both the lack of observations of Richardson number less than 1 and the findings from previous studies suggested the lower Richardson number limit of 1 for the parametrization in this thesis (Chapter 3).

Here we consider the typical range of Richardson numbers that are generated by the eddy model to assess whether the application of the parametrization described in this thesis is valid.

A.3.1 Method

The Richardson number (Ri) was calculated from the temperature, salinity, u and v velocities using the equations described in Chapter 3 for each model output step. The minimum value of the Richardson number occurring in the model depth layers around the euphotic depth (between model depth levels 11 and 14) over a fixed model sub-volume (as described above, Figure A.2) was determined. In this thesis only the fluxes of inert tracer into the euphotic zone are considered. Hence, here we consider only the values of the Richardson number which would be used in determining the turbulent diffusivity at the model euphotic depth.

The numbers of grid cells, within the defined volume, where the Richardson number was less than 1 and where the Richardson number was less than 0.25 were also determined.

A.3.2 Results

The minimum Richardson number drops below 1 during scenario Rrr on six occasions when using the standard wind stress parametrization and on three occasions when using the Bye (1986) wind stress parametrization out of a total of 36 model outputs (Figure A.6). The minimum Richardson number remains above 0.25 in all cases (Figure A.6). For all cases where the minimum Richardson number in the model sub-volume is less than 1, the percentage of grid cells where the Richardson number is less than 1 is below 0.1 % of the total number of grid cells considered.

A.3.3 Discussion

In all cases the Richardson numbers calculated from the model output in the volume around the model euphotic depth are above the minimum critical Richardson number of 0.25 used when calibrating the parametrization. This would suggest that in all cases the model Richardson number is super-critical and that there are likely to be no periods of sustained high vertical mixing (Chapter 5). On the few occasions when the minimum Richardson number in the depth layers around the model euphotic depth drops below 1 this only occurs in a small (< 1 %) percentage of the model volume. On these few instances where the model Richardson number drops below 1, the mixing parametrization used in his thesis may underestimate the value of the turbulent diffusivity. This would suggest that the diffusive flux calculated may be slightly underestimated in scenario Rrr. However, for the vast majority of cases the Richardson number parametrization used in the eddy model is appropriate for use with range of Richardson numbers produced by the model.

A.4 Estimating the eddy centre

The calculation of euphotic zone flux by first order differencing the inert tracer T_1 volumes in a model sub-domain defined dynamically relative to the centre of the eddy (Chapter 5) assumes that the calculated eddy centre is in the same place relative to the eddy periphery at each model output. Due to the use of a full Coriolis implementation the eddy moves within the model domain throughout the duration of the simulation (Chapter 4). Estimating the position of the eddy centre by fitting to a Martin and Richards (2001) velocity profile gives an exact position for the eddy centre (Chapter 5). However, for calculating the fluxes in the eddy diagnostic zones this is mapped onto the 1 km resolution model grid which results in a rounding of the eddy centre coordinates to the nearest kilometre (Chapter 5).

The horizontal distribution of inert tracer T_1 in the euphotic zone of the eddy model shows a high degree of spatial heterogeneity, with the position of patches of inert tracer changing from day to day. For example, in Figure A.7, a large quantity of inert tracer originally approximately in the centre of the eddy (day 74) moves due to the eddy circulation to the east of zone 1 (day 75) and then back to the centre (day 76). This would suggest that uncertainties in the positioning of the eddy centre combined with spatial heterogeneity of the inert tracer may lead to a degree of uncertainty in the estimations of mean euphotic zone fluxes in the diagnostic zones.

Here we estimate the magnitude of the uncertainty in the euphotic zone inert tracer T_1 fluxes that arise from rounding errors when positioning the centre of the eddy on the model grid.

A.4.1 Method

In order to estimate the uncertainty in inert tracer T_1 flux associated with the positioning of the eddy centre a series of nine points forming a 3x3 km box centred on the estimated eddy centre position were taken (Figure A.8) for each daily model output of all the model runs (Chapter 4). Nine individual estimates of the volume of inert tracer in the euphotic zone were made, for the three diagnostic zones, for an eddy centred on each of the nine points. The flux into the euphotic zone, for the three diagnostic zones, was calculated by first order differencing successive model outputs. This was done for each of the nine individual 'centres'. Mean and associated standard error of the euphotic zone inert tracer flux was then calculated for the nine individual estimates.

A.4.2 Results

Here we concentrate on the uncertainty in zone 1 as this is the zone showing the greatest heterogeneity of inert tracer. Estimates of the flux of inert tracer T_1 based on the calculation of the eddy centre, as described in Chapter 5, are consistent (within the standard error) with the estimates of flux of inert tracer calculated as a mean of nine individual samples for all runs (Figure A.9 and A.10).

Expressing the calculated standard error as a percentage of the calculated total flux, in 90 % of cases the standard error is less than 10 % of the associated total flux, in 95 % of cases the standard error is less than 20 % of the total flux and in 97 % of cases the standard error is less than 30 % of the total flux. However there are some cases where the standard error is in excess of 100 % of the calculated total flux (Figure A.11).

The highest standard errors for the total inert tracer T_1 fluxes occur when the mean concentration of the inert tracer in the euphotic zone is low. The inert tracer concentration is greater than 0.001 units m^{-3} for 97 % of all cases and greater than 0.005 units m^{-3} for 95 % of all cases. Considering only the cases when the mean concentration of inert tracer in the euphotic zone is greater than 0.001 units m^3 the maximum standard error is 46 % of the associated total flux. Considering only cases where the mean concentration of inert tracer in the euphotic zone is greater than 0.005 units m^3 the maximum standard error is 13 % of the associated volume flux (Figure A.12).

For all cases, the mean of the standard error expressed as a percentage of the total flux is 8 %.

A.4.3 Discussion

The uncertainty associated with the calculated euphotic zone T_1 fluxes arising from inaccuracy of up to 1 km in the positioning of the eddy centre is of order 10 % of calculated flux. Much higher percentage uncertainty figures appear to be associated with cases where the concentration of inert tracer in the euphotic zone is low (less than 0.005 units m^3) and also where the spatial distribution of the tracer highly heterogeneous. For scenario Slc using the standard wind stress parametrization, on day 75 of the simulation, the standard error is 360 % of the calculated inert tracer flux (Figure A.11). In this case, the average concentration of inert tracer within the zone 1 euphotic zone is 0.06 units m^3 which would suggest the standard error should be of order 10 %. However, the circulation of the eddy distorts the inert tracer distribution on day 75 and concentrates the tracer in the eastern side of zone 1 (Figure A.7). This leads to the high calculated uncertainty associated with the flux in zone 1 as displacing the zone by just 1 km moves the boundary into (or out of) the high volume area.

A.5 Vertical viscosity

Though consistent with observations (see Chapter 3), the vertical viscosity used in the eddy model (1 $x10^{-3}$ m^2 s^{-1}) is high compared to what is used in other mixing parametrizations. The Richardson number based vertical mixing parametrizations of Large et al. (1994) and Pacanowski and Philander (1981) both use a constant background vertical viscosity of $1x10^{-4}$ m^2 s^{-1}. Reduced vertical viscosity would be expected to lead to greater downwards diffusion of momentum from the wind-driven mixed layer and potentially to higher shear with associated higher mixing.

Here the impact of reduced vertical viscosity on inert tracer T_1 fluxes is estimated by running the model (described in Chapter 4) using the most variable of the wind forcings (Rrr) with different vertical viscosities.

A.5.1 Method

The model was run using wind forcing Rrr (described in Chapter 4) using both the standard and Bye (1986) wind stress parametrizations, with constant vertical viscosities of 1×10^{-4} (run RrrD4) and 1×10^{-5} m^2 s^{-1} (run RrrD5). Results were collected and compared to the results of running the model with wind forcing Rrr using a constant vertical turbulent viscosity of 1×10^{-3} $m^2 s^{-1}$ as reported in Chapter 5 Model output was processed to calculate fluxes into the euphotic zone for inert tracer T_1 and the size and position of the eddy centre as described in Chapter 5.

A.5.2 Results

A.5.2.1 Eddy physical characteristics

Decreasing the vertical viscosity appears to have little effect on the eddy radius at the euphotic depth and below, with the eddy radius at the euphotic depth and below between 23 to 25 km in all cases (Table A.3). Decreasing the vertical viscosity has the greatest effect on the radius of the eddy at the base of the mixed layer. In this case the standard error is between 2 and 16 km with the radius between 25 to 29 km for both wind stress parametrizations (Table A.3).

As the vertical viscosity decreases the maximum azimuthal velocity of the eddy increases at the euphotic depth by between 3 to 4 cm s^{-1} when using the standard wind stress parametrization and by 1 cm s^{-1} when using the Bye (1986) wind stress parametrization (Table A.4). Minimum azimuthal velocities are constant at the euphotic depth between 16 to 18 cm s^{-1} in all runs for both wind stress parametrizations (Table A.5). Both minimum and maximum azimuthal velocities remain approximately constant at the euphotic depth during the run for both wind stress parametrizations (Table A.4 and A.5).

Mean and standard deviation of the horizontal distance between the eddy centre at 540 m and the eddy centres at the bases of the euphotic zone and mixed-layer increase for both wind stress parametrizations as the vertical viscosity is decreased

(Table A.6). There is also a large increase in the maximum turbulent diffusion coefficient from 1x10^{-4} m^{2}s^{-1} to 1x10^{-2} m^{2}s^{-1} for both wind stress parametrizations as the vertical viscosity is decreased (Table A.6).

A.5.2.2 Fluxes

For all runs and both wind stress parametrizations the fluxes of inert tracer T_1 into the euphotic zone increase as the vertical viscosity is decreased (Table A.7 and A.8). For both wind stress parametrizations the largest increase in flux occurs in zones 1 and 2. Reducing the vertical viscosity to 1x10^{-4} m^{2}s^{-1} (RrrD4) results in an an $\sim$ 50 % increase in mean euphotic zone flux when using the standard wind stress parametrization and an $\sim$ 20 % increase in mean euphotic zone flux when using the Bye (1986) wind stress parametrization in both the zones 1 and 2 (Table A.7 and A.8). Reducing the vertical viscosity to 1x10^{-5} m^{2}s^{-1} (RrrD5) results in the mean euphotic zone flux for the period increasing by $\sim$ 100 % in both zones 1 and 2 when using the standard wind stress parametrization and by $\sim$ 40 % when using the Bye (1986) wind stress parametrization (Table A.7 and A.8).

For all scenarios and both wind stress parametrizations the turbulent diffusive fluxes of inert tracer T_1 into the euphotic zone increase as the vertical viscosity is decreased (Table A.9 and A.10). For both wind stress parametrizations the largest increase in turbulent diffusive flux occurs in zone 1 where mean turbulent diffusive flux increases by up to 60 % as the vertical viscosity is decreased (Table A.9 and A.10). For both wind stress parametrizations the turbulent diffusive fluxes remain approximately equal when the vertical viscosity is decreased (Table A.9 and A.10). The radial distribution of the turbulent diffusive flux shows higher values outside the eddy core (radius $>$ 25 km), for both wind stress parametrizations, which peaks between 25 to 50 km radius as vertical viscosity is reduced (Figure A.13). The mean of the maximum turbulent diffusion coefficient is up to an order of magnitude greater in both reduced viscosity scenarios (RrrD4 and RrrD5) for both wind stress parametrizations compared to scenario Rrr (Table A.11 and A.12).

The advective flux components show the same degree of variability and are of the same order regardless of the vertical viscosity (Table A.13, A.14, A.15 and A.16). In all cases horizontal advective fluxes appear to be small compared to vertical advective fluxes in the zones 1 and 2 with the overall horizontal flux into zone 3 less than 0.008 units m^{-2} day^{-1} in all cases (Table A.13, A.14, A.15 and A.16). Tracer stripe depths appear to be unaffected by decreasing viscosity with mean tracer stripe depths and trend estimates for the period being within 2 m in all cases (Table A.17 and A.18).

A.5.3 Discussion

Eddy radius and azimuthal velocity appear to be most strongly affected by changes in vertical viscosity at the base of the mixed layer (32 m) and relatively unaffected at 540 m depth. Changes in the eddy radius and azimuthal velocity at the depth of the base of the euphotic zone (64 m) as the vertical viscosity is decreased would suggest that the reduction in vertical viscosity is resulting in downwards diffusion of momentum from the wind-driven mixed layer to the base of the euphotic zone. Reducing the vertical viscosity also appears to lead to a more vigorous movement of the eddy centre of rotation. When the vertical viscosity is reduced, for both wind stress parametrizations, the magnitude of the maximum value of the turbulent diffusivity observed and the magnitude of the mean turbulent diffusivities at the euphotic depth are consistent with the occurrence of periods of model convective adjustment (Chapter 5). Convective adjustment may be occurring at the euphotic depth in the reduced viscosity runs as a result of the more vigorous movement of the eddy causing higher density water from the eddy core to be displaced horizontally over lower density surrounding water. Hence the convective adjustment may indicate the presence a sub-mesoscale advective process (Chapter 4).

Peaks in the radial distribution of diffusive fluxes out to 50 km from the eddy centre suggest increased diffusion resulting from increased vertical shears in the reduced viscosity runs. If we consider a snapshot of turbulent diffusivity for day 45 of the runs using both wind stress parametrizations (Figure A.14 and A.15), the spatial distribution of the turbulent diffusivity coefficient is consistent with the radial distribution of the diffusive fluxes (Figure A.13). The enhanced turbulent diffusivity is concentrated around zone 1 in the reduced viscosity runs and increased in magnitude as the viscosity is reduced.

Reducing the vertical viscosity appears to have little effect on vertical advective fluxes. The increased magnitude of the vertical flux components and associated variability is suggestive of a more vigorous internal wave field. However, the insensitivity of the tracer stripe depths to changes in vertical viscosity suggests that there is little if any change in diabatic advective inert tracer T_1 flux.

If we consider the case where the vertical viscosity is reduced by an order of magnitude to 10^{-4} m^2s^{-1} consistent with previous parametrizations (Large et al., 1994; Pacanowski and Philander, 1981) the model shows an additional diffusive flux of inert tracer into the euphotic zone which is greatest within a radius of up to 50 km from the eddy centre. This diffusive flux is increased by ~ 50 % when using the standard wind stress parametrization and by ~ 20 % when using the Bye (1986) wind stress parametrization. The magnitude of the observed turbulent diffusion coefficient during the run suggests that this additional diffusive flux is produced partly by enhanced vertical shear and partly by sub-mesoscale advective processes which are reproduced in the model as a convective mixing.

Scenario	Zone 3	Zone 2	Zone 1
NW	0.028 ± 0.004	-0.024 ± 0.017	0.019 ± 0.029
Scc	0.017 ± 0.009	-0.070 ± 0.035	-0.001 ± 0.156
Slc	-0.002 ± 0.007	-0.141 ± 0.033	-0.007 ± 0.184
Scl	0.003 ± 0.010	-0.150 ± 0.050	-0.004 ± 0.205
Sch	0.035 ± 0.024	0.006 ± 0.035	0.106 ± 0.210
Rcc	0.049 ± 0.007	0.021 ± 0.022	-0.015 ± 0.104
Rrc	0.031 ± 0.034	0.068 ± 0.055	-0.139 ± 0.224
Rrr	0.044 ± 0.044	0.003 ± 0.044	-0.166 ± 0.571

Table A.1: Horizontal diffusive fluxes due to Shapiro filtering of inert tracer T_1 in the euphotic zone (x10^{-5} units m^{-2} day^{-1}) for all runs (Chapter 5) using the standard wind stress parametrization. Values are reported as a mean ± standard error for the whole day 30 to day 75 period. Horizontal diffusion is estimated as described in Section A.1.1.

Scenario	Zone 3	Zone 2	Zone 1
NW	0.000 ± 0.007	-0.044 ± 0.021	0.029 ± 0.027
Scc	0.014 ± 0.006	-0.001 ± 0.033	-0.060 ± 0.133
Slc	-0.011 ± 0.003	-0.047 ± 0.030	-0.059 ± 0.205
Scl	0.034 ± 0.005	-0.070 ± 0.033	-0.048 ± 0.190
Sch	0.007 ± 0.007	-0.041 ± 0.026	-0.107 ± 0.164
Rcc	-0.007 ± 0.008	-0.081 ± 0.028	-0.022 ± 0.113
Rrc	-0.002 ± 0.008	0.026 ± 0.046	-0.031 ± 0.185
Rrr	0.019 ± 0.030	-0.007 ± 0.030	0.100 ± 0.475

Table A.2: Horizontal diffusive fluxes due to Shapiro filtering of inert tracer T_1 into the euphotic zone (x10^{-5} units m^{-2} day^{-1}) for all runs (Chapter 5) using the Bye (1986) wind stress parametrization. Values are reported as a mean ± standard error for the whole day 30 to day 75 period. Horizontal diffusion is estimated as described in Section A.1.1.

Scenario	32 m depth (mixed layer base)	65 m depth (euphotic depth)	540 m depth
Standard wind stress parametrization			
Rrr	24.81 : 25.81 ± 1.81	24.79 : 24.35 ± 0.64	24.67 : 24.53 ± 0.12
RrrD4	29.37 : 25.62 ± 15.74	24.39 : 23.90 ± 0.69	24.75 : 24.57 ± 0.11
RrrD5	27.31 : 25.03 ± 7.71	24.40 : 23.74 ± 3.71	25.08 : 23.13 ± 3.48
Bye (1986) wind stress parametrization			
Rrr	25.10 : 26.95 ± 2.13	24.98 : 24.92 ± 0.51	24.69 : 24.59 ± 0.09
RrrD4	24.99 : 25.91 ± 1.75	24.98 : 24.70 ± 0.40	24.75 : 24.60 ± 0.12
RrrD5	24.99 : 25.94 ± 1.92	24.82 : 25.19 ± 0.75	24.81 : 24.62 ± 0.13

Table A.3: The eddy radius (km), calculated as described in Chapter 5, at three depths; 32 m (the base of mixed layer), 65 m (base of euphotic zone) and 540 m. The radius is reported as day 30 value : day 75 value ± standard error calculated as described in Chapter 5. Results are for all reduced viscosity runs (Rrr viscosity 1x10^{-3} m^{2}s^{-1}, RrrD4 viscosity 1x10^{-4} m^{2}s^{-1}, RrrD5 viscosity 1x10^{-5} m^{2}s^{-1}).

Scenario	32 m depth (mixed layer base)	65 m depth (euphotic depth)	540 m depth
Standard wind stress parametrization			
Rrr	0.32 : 0.32 ± 0.09	0.23 : 0.24 ± 0.03	0.27 : 0.26 ± 0.01
RrrD4	0.39 : 0.35 ± 0.14	0.26 : 0.27 ± 0.04	0.27 : 0.28 ± 0.02
RrrD5	0.39 : 0.30 ± 0.14	0.27 : 0.26 ± 0.05	0.27 : 0.28 ± 0.02
Bye (1986) wind stress parametrization			
Rrr	0.27 : 0.24 ± 0.07	0.21 : 0.20 ± 0.02	0.26 : 0.25 ± 0.00
RrrD4	0.31 : 0.26 ± 0.08	0.22 : 0.19 ± 0.01	0.27 : 0.25 ± 0.01
RrrD5	0.34 : 0.25 ± 0.08	0.22 : 0.21 ± 0.02	0.27 : 0.25 ± 0.01

TABLE A.4: The eddy maximum azimuthal velocity (m s^{-1}) , calculated as described in Chapter 5, at three depths; 32 m (the base of mixed layer), 65 m (base of euphotic zone) and 540 m. The maximum azimuthal velocity is reported as day 30 value : day 75 value ± standard error calculated as described in Chapter 5 Results are for all reduced viscosity runs (Rrr viscosity 1×10^{-3} m^2s^{-1}, RrrD4 viscosity 1×10^{-4} m^2s^{-1}, RrrD5 viscosity 1×10^{-5} m^2s^{-1}).

Scenario	32 m depth (mixed layer base)	65 m depth (euphotic depth)	540 m depth
Standard wind stress parametrization			
Rrr	0.14 : 0.10 ± 0.08	0.18 : 0.18 ± 0.03	0.25 : 0.25 ± 0.01
RrrD4	0.11 : 0.09 ± 0.09	0.17 : 0.18 ± 0.04	0.25 : 0.24 ± 0.01
RrrD5	0.10 : 0.11 ± 0.09	0.17 : 0.16 ± 0.06	0.25 : 0.25 ± 0.02
Bye (1986) wind stress parametrization			
Rrr	0.14 : 0.10 ± 0.07	0.18 : 0.17 ± 0.02	0.25 : 0.25 ± 0.00
RrrD4	0.13 : 0.10 ± 0.07	0.17 : 0.18 ± 0.02	0.25 : 0.24 ± 0.01
RrrD5	0.12 : 0.11 ± 0.06	0.18 : 0.17 ± 0.03	0.25 : 0.25 ± 0.01

TABLE A.5: The eddy minimum azimuthal velocity (m s^{-1}) , calculated as described in Chapter 5, at three depths; 32 m (the base of mixed layer), 65 m (base of euphotic zone) and 540 m. The minimum azimuthal velocity is reported as day 30 value : day 75 value ± standard error calculated as described in section Chapter 5. Results are for all reduced viscosity runs (Rrr viscosity $1\text{x}10^{-3}$ m^2s^{-1}, RrrD4 viscosity $1\text{x}10^{-4}$ m^2s^{-1}, RrrD5 viscosity $1\text{x}10^{-5}$ m^2s^{-1}).

Scenario	32 m depth (mixed layer base)	65 m depth (euphotic depth)	K (m^2s^{-1})
Standard wind stress parametrization			
Rrr	10.34 ± 2.32	4.94 ± 1.51	$9.25x10^{-5}$
RrrD4	15.0 ± 15.7	6.65 ± 1.87	$1.35x10^{-2}$
RrrD5	15.4 ± 17.4	8.3 ± 8.0	$1.21x10^{-2}$
Bye (1986) wind stress parametrization			
Rrr	8.98 ± 2.70	3.39 ± 1.19	$1.07x10^{-4}$
RrrD4	10.8 ± 2.4	3.4 ± 1.4	$1.4x10^{-2}$
RrrD5	10.6 ± 3.0	4.56 ± 1.9	$1.21x10^{-2}$

Table A.6: The horizontal distance of the eddy centre at 32 m and 65 m depth from the eddy centre at 540 m depth (km ± standard deviation). The position of the eddy centres is calculated as described in Chapter 5. The maximum turbulent diffusion coefficient (K) recorded between day 30 and day 75 of the run within a distance of 70 km from the eddy centre (zone 3) at 65 m depth. Results are for all reduced viscosity runs (Rrr viscosity $1x10^{-3}$ m^2s^{-1}, RrrD4 viscosity $1x10^{-4}$ m^2s^{-1}, RrrD5 viscosity $1x10^{-5}$ m^2s^{-1}).

Scenario	Zone 3	Zone 2	Zone 1
Rrr	0.103 ± 0.030	0.105 ± 0.035	0.163 ± 0.160
RrrD4	0.115 :± 0.042	0.327 : -0.043 ± 0.303 (l)	0.243 ± 0.198
RrrD5	0.181 ± 0.041	0.222 ± 0.062	0.321 ± 0.245

TABLE A.7: Fluxes of inert tracer (T_1) into the euphotic zone (units m^{-2} day^{-1}) for all runs using the standard wind stress parametrization. Where the mean flux was estimated by fitting a trend the values are reported as day 30 value : day 75 value ± standard error. The trend fitted is indicated, where (n) is a fit to 1/t and (l) is a fit to t (Chapter 5). Where there was no trend values are reported as mean ± standard error for the whole period. Results are for all reduced viscosity runs (Rrr viscosity 1x10^{-3} m^{2}s^{-1}, RrrD4 viscosity 1x10^{-4} m^{2}s^{-1}, RrrD5 viscosity 1x10^{-5} m^{2}s^{-1}).

Scenario	Zone 3	Zone 2	Zone 1
Rrr	0.176 : 0.015 ± 0.126 (l)	0.225 : 0.007 ± 0.157 (l)	0.220 ± 0.118
RrrD4	0.099 ± 0.022	0.271 : 0.012 ± 0.191 (l)	0.259 ± 0.150
RrrD5	0.197 : 0.055 ± 0.129 (l)	0.311 : 0.030 ± 0.198 (l)	0.305 ± 0.148

TABLE A.8: Fluxes of inert tracer (T_1) into the euphotic zone (units m^{-2} day^{-1}) for all runs using the Bye (1986) wind stress parametrization. Where the mean flux was estimated by fitting a trend the values are reported as day 30 value : day 75 value ± standard error. The trend fitted is indicated, where (n) is a fit to 1/t and (l) is a fit to t (Chapter 5). Where there was no trend values are reported as mean ± standard error for the whole period. Results are for all reduced viscosity runs (Rrr viscosity 1x10^{-3} m^{2}s^{-1}, RrrD4 viscosity 1x10^{-4} m^{2}s^{-1}, RrrD5 viscosity 1x10^{-5} m^{2}s^{-1}).

Scenario	Zone 3	Zone 2	Zone 1
Rrr	0.189 : 0.039 ± 0.037 (n)	0.179 : 0.039 ± 0.044 (n)	0.214 : 0.042 ± 0.077 (n)
RrrD4	0.204 : 0.056 ± 0.026 (n)	0.428 : 0.047 ± 0.027 (n)	0.293 : 0.064 ± 0.128 (n)
RrrD5	0.187 : 0.116 ± 0.032 (n)	0.247 : 0.112 ± 0.057 (n)	0.331 : 0.116 ± 0.073 (n)

Table A.9: Diffusive fluxes of inert tracer (T_1) into the euphotic zone (units m^{-2} day^{-1}) for all runs using the standard wind stress parametrization. Where the mean flux was estimated by fitting a trend the values are reported as day 30 value : day 75 value ± standard error. The trend fitted is indicated, where (n) is a fit to 1/t and (l) is a fit to t (Chapter 5). Where there was no trend values are reported as mean ± standard error for the whole period. Results are for all reduced viscosity runs (Rrr viscosity 1x10^{-3} m^{2}s^{-1}, RrrD4 viscosity 1x10^{-4} m^{2}s^{-1}, RrrD5 viscosity 1x10^{-5} m^{2}s^{-1}).

Scenario	Zone 3	Zone 2	Zone 1
Rrr	0.162 : 0.038 ± 0.032 (n)	0.159 : 0.038 ± 0.040 (n)	0.198 : 0.038 ± 0.078 (n)
RrrD4	0.203 : 0.042 ± 0.015 (n)	0.406 : 0.041 ± 0.036 (n)	0.385 : 0.046 ± 0.101 (n)
RrrD5	0.164 : 0.071 ± 0.029 (n)	0.275 : 0.066 ± 0.047 (n)	0.376 : 0.075 ± 0.105 (n)

Table A.10: Diffusive fluxes of inert tracer (T_1) into the euphotic zone (units m^{-2} day^{-1}) for all runs using the Bye (1986) wind stress parametrization. Where the mean flux was estimated by fitting a trend the values are reported as day 30 value : day 75 value ± standard error. The trend fitted is indicated, where (n) is a fit to 1/t and (l) is a fit to t (Chapter 5). Where there was no trend values are reported as mean ± standard error for the whole period. Results are for all reduced viscosity runs (Rrr viscosity 1x10^{-3} m^{2}s^{-1}, RrrD4 viscosity 1x10^{-4} m^{2}s^{-1}, RrrD5 viscosity 1x10^{-5} m^{2}s^{-1}).

Scenario	Zone 3	Zone 2	Zone 1
Rrr	0.078 : 0.045 ± 0.015 (l)	0.078 : 0.045 ± 0.015 (l)	0.077 : 0.045 ± 0.015 (l)
RrrD4	8.489 : 4.650 ± 2.715 (l)	9.204 : 0.751 ± 2.158 (l)	6.772 : 0.995 ± 1.894 (l)
RrrD5	6.693 ± 0.416	6.131 : 3.233 ± 1.261 (l)	5.406 : 2.196 ± 1.373 (l)

TABLE A.11: Average values of the maximum turbulent eddy diffusivity coefficient (x10^{-3} m^2s^{-1}) recorded in each zone for all runs using the standard wind stress parametrization. Where the mean was estimated by fitting a trend the values are reported as day 30 value : day 75 value ± standard error. The trend fitted is indicated, where (n) is a fit to 1/t and (l) is a fit to t (Chapter 5). Where there was no trend values are reported as mean ± standard error for the whole period. Results are for all reduced viscosity runs (Rrr viscosity 1x10^{-3} m^2s^{-1}, RrrD4 viscosity 1x10^{-4} m^2s^{-1}, RrrD5 viscosity 1x10^{-5} m^2s^{-1}).

Scenario	Zone 3	Zone 2	Zone 1
Rrr	0.085 : 0.031 ± 0.021 (l)	0.085 : 0.031 ± 0.021 (l)	0.085 : 0.031 ± 0.021 (l)
RrrD4	10.651 : 4.07 ± 2.485 (l)	10.651 : 4.07 ± 2.485 (l)	8.934 : 2.858 ± 2.137 (l)
RrrD5	6.554 ± 0.356	6.978 : 4.710 ± 1.896 (l)	6.883 : 3.493 ± 1.691 (l)

TABLE A.12: Average values of the maximum turbulent eddy diffusivity coefficient (x10^{-3} m^2s^{-1}) recorded in each zone for all runs using the Bye (1986) wind stress parametrization. Where the mean was estimated by fitting a trend the values are reported as day 30 value : day 75 value ± standard error. The trend fitted is indicated, where (n) is a fit to 1/t and (l) is a fit to t (Chapter 5). Where there was no trend values are reported as mean ± standard error for the whole period. Results are for all reduced viscosity runs (Rrr viscosity 1x10^{-3} m^2s^{-1}, RrrD4 viscosity 1x10^{-4} m^2s^{-1}, RrrD5 viscosity 1x10^{-5} m^2s^{-1}).

Scenario	Zone 3	Zone 2	Zone 1
Rrr	0.006 ± 0.002	-0.003 ± 0.002	-0.029 ± 0.041
RrrD4	-0.001 ± 0.002	-0.006 ± 0.003	0.018 ± 0.062
RrrD5	0.001 ± 0.005	-0.010 ± 0.005	-0.059 ± 0.064

Table A.13: Horizontal advective fluxes of inert tracer (T_1) into the euphotic zone (units m^{-2} day^{-1}) for all runs using the standard wind stress parametrization. Where the mean flux was estimated by fitting a trend the values are reported as day 30 value : day 75 value ± standard error. The trend fitted is indicated, where (n) is a fit to 1/t and (l) is a fit to t (Chapter 5). Where there was no trend values are reported as mean ± standard error for the whole period. Results are for all reduced viscosity runs (Rrr viscosity 1x10^{-3} m^{2}s^{-1}, RrrD4 viscosity 1x10^{-4} m^{2}s^{-1}, RrrD5 viscosity 1x10^{-5} m^{2}s^{-1}).

Scenario	Zone 3	Zone 2	Zone 1
Rrr	0.002 ± 0.028	0.063 ± 0.031	0.574 ± 0.125
RrrD4	0.015 0.038	0.090 ± 0.042	0.601 ± 0.174
RrrD5	0.045 0.037	0.131 ± 0.052	0.680 ± 0.217

Table A.14: Vertical advective fluxes of inert tracer (T_1) into the euphotic zone (units m^{-2} day^{-1}) for all runs using the standard wind stress parametrization. Where the mean flux was estimated by fitting a trend the values are reported as day 30 value : day 75 value ± standard error. The trend fitted is indicated, where (n) is a fit to 1/t and (l) is a fit to t (Chapter 5). Where there was no trend values are reported as mean ± standard error for the whole period. Results are for all reduced viscosity runs (Rrr viscosity 1x10^{-3} m^{2}s^{-1}, RrrD4 viscosity 1x10^{-4} m^{2}s^{-1}, RrrD5 viscosity 1x10^{-5} m^{2}s^{-1}).

Scenario	Zone 3	Zone 2	Zone 1
Rrr	0.002 ± 0.001	0.002 : -0.005 ± 0.005 (l)	-0.016 ± 0.029
RrrD4	-0.003 ± 0.000	-0.001 ± 0.001	0.008 ± 0.035
RrrD5	-0.005 : 0.007 ± 0.010 (l)	-0.002 ± 0.002	-0.009 ± 0.042

TABLE A.15: Horizontal advective fluxes of inert tracer (T_1) into the euphotic zone (units m^{-2} day^{-1}) for all runs using the Bye (1986) wind stress parametrization. Where the mean flux was estimated by fitting a trend the values are reported as day 30 value : day 75 value ± standard error. The trend fitted is indicated, where (n) is a fit to 1/t and (l) is a fit to t (Chapter 5). Where there was no trend values are reported as mean ± standard error for the whole period. Results are for all reduced viscosity runs (Rrr viscosity 1x10^{-3} m^{2}s^{-1}, RrrD4 viscosity 1x10^{-4} m^{2}s^{-1}, RrrD5 viscosity 1x10^{-5} m^{2}s^{-1}).

Scenario	Zone 3	Zone 2	Zone 1
Rrr	0.008 ± 0.018	0.055 ± 0.021	0.414 ± 0.090
RrrD4	0.017 ± 0.020	0.053 ± 0.026	0.270 ± 0.118
RrrD5	0.016 ± 0.017	0.061 ± 0.026	0.341 ± 0.125

TABLE A.16: Vertical advective fluxes of inert tracer (T_1) into the euphotic zone (units m^{-2} day^{-1}) for all runs using the Bye (1986) wind stress parametrization. Where the mean flux was estimated by fitting a trend the values are reported as day 30 value : day 75 value ± standard error. The trend fitted is indicated, where (n) is a fit to 1/t and (l) is a fit to t (Chapter 5). Where there was no trend values are reported as mean ± standard error for the whole period. Results are for all reduced viscosity runs (Rrr viscosity 1x10^{-3} m^{2}s^{-1}, RrrD4 viscosity 1x10^{-4} m^{2}s^{-1}, RrrD5 viscosity 1x10^{-5} m^{2}s^{-1}).

Scenario	Zone 3	Zone 2	Zone 1
Rrr	64.72 : 61.68 ± 0.30 (n)	64.55 : 61.11 ± 0.28 (n)	62.77 : 57.28 ± 0.99 (n)
RrrD4	65.39 : 61.36 ± 0.32 (n)	65.11 : 60.25 ± 0.38 (n)	63.45 : 57.51 ± 1.18 (n)
RrrD5	66.05 : 59.29 ± 0.28 (l)	66.12 : 58.92 ± 0.28 (n)	64.13 : 58.04 ± 1.15 (n)

Table A.17: Mean depth of inert tracer stripe (T_2) for all runs using the standard wind stress parametrization. Where the mean depth was estimated by fitting a trend the values are reported as day 30 value : day 75 value ± standard error. The trend fitted is indicated, where (n) is a fit to 1/t and (l) is a fit to t (Chapter 5). Where there was no trend values are reported as mean ± standard error for the whole period. Results are for all reduced viscosity runs (Rrr viscosity 1x10^{-3} m^{2}s^{-1}, RrrD4 viscosity 1x10^{-4} m^{2}s^{-1}, RrrD5 viscosity 1x10^{-5} m^{2}s^{-1}).

Scenario	Zone 3	Zone 2	Zone 1
Rrr	64.86 : 61.88 ± 0.22 (n)	64.59 : 59.98 ± 0.24 (n)	62.73 : 52.63 ± 0.79 (n)
RrrD4	65.02 : 61.75 ± 0.22 (n)	64.63 : 58.87 ± 0.28 (n)	62.36 : 51.44 ± 1.07 (n)
RrrD5	65.76 : 59.66 ± 0.18 (l)	65.60 : 57.21 ± 0.17 (n)	63.62 : 52.52 ± 1.05 (n)

Table A.18: Mean depth of inert tracer stripe (T_2) for all runs using the Bye (1986) wind stress parametrization. Where the mean depth was estimated by fitting a trend the values are reported as day 30 value : day 75 value ± standard error. The trend fitted is indicated, where (n) is a fit to 1/t and (l) is a fit to t (Chapter 5). Where there was no trend values are reported as mean ± standard error for the whole period. Results are for all reduced viscosity runs (Rrr viscosity 1x10^{-3} m^{2}s^{-1}, RrrD4 viscosity 1x10^{-4} m^{2}s^{-1}, RrrD5 viscosity 1x10^{-5} m^{2}s^{-1}).

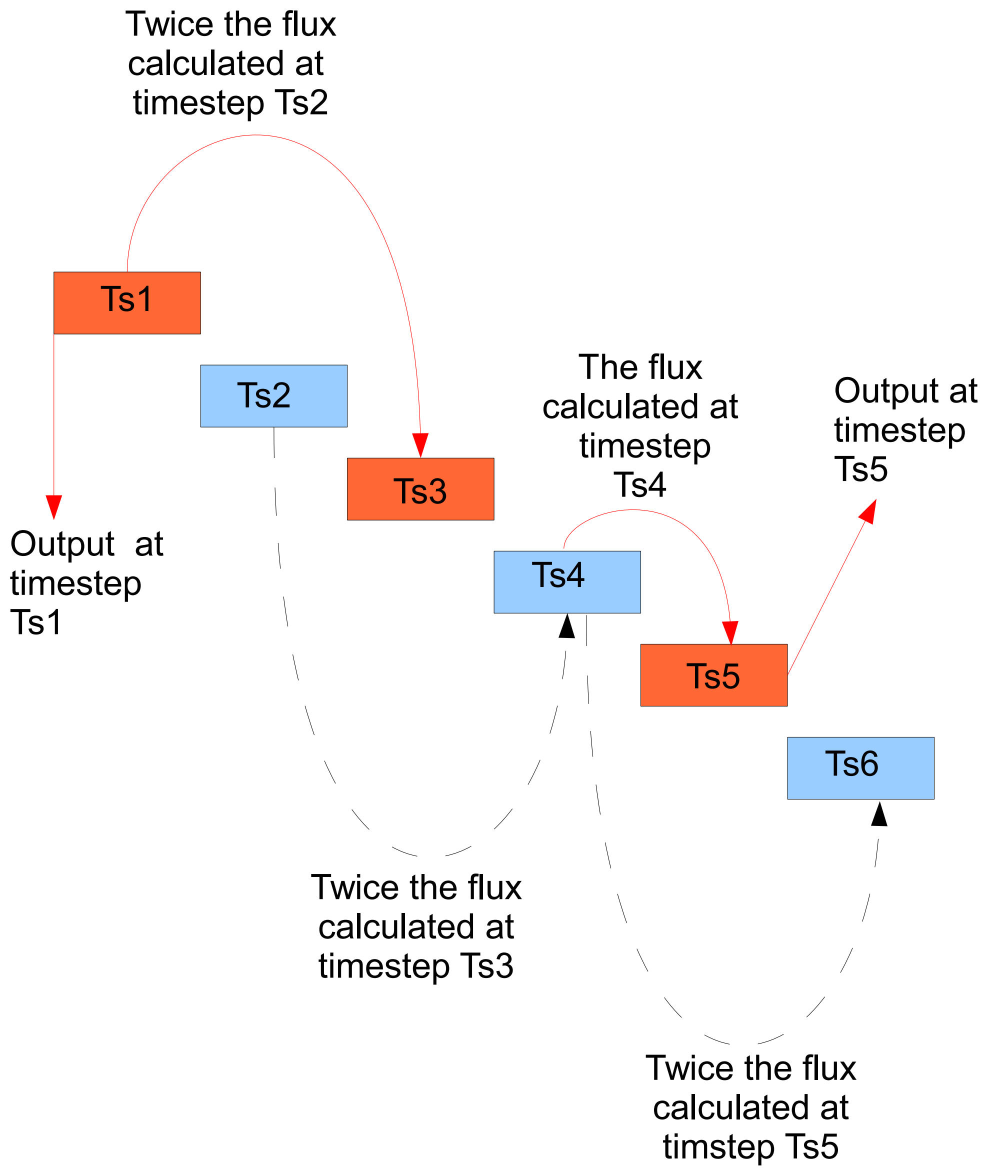

FIGURE A.1: Cartoon showing an idealised leapfrog time-step scheme. Consisting of a single fixed volume cell, the model runs for six time intervals from time-step Ts1 to time-step Ts6. Tracer concentrations are output at time-steps Ts1 and Ts5. The model advances from time-step Ts2 to time-step Ts3 by adding twice the tracer flux calculated at Ts2 to the tracer concentration at Ts1. Ts4 is an Euler forward time-step where the model advances from Ts4 to Ts5 by adding the tracer flux calculated at Ts4 to the tracer concentration at Ts4.

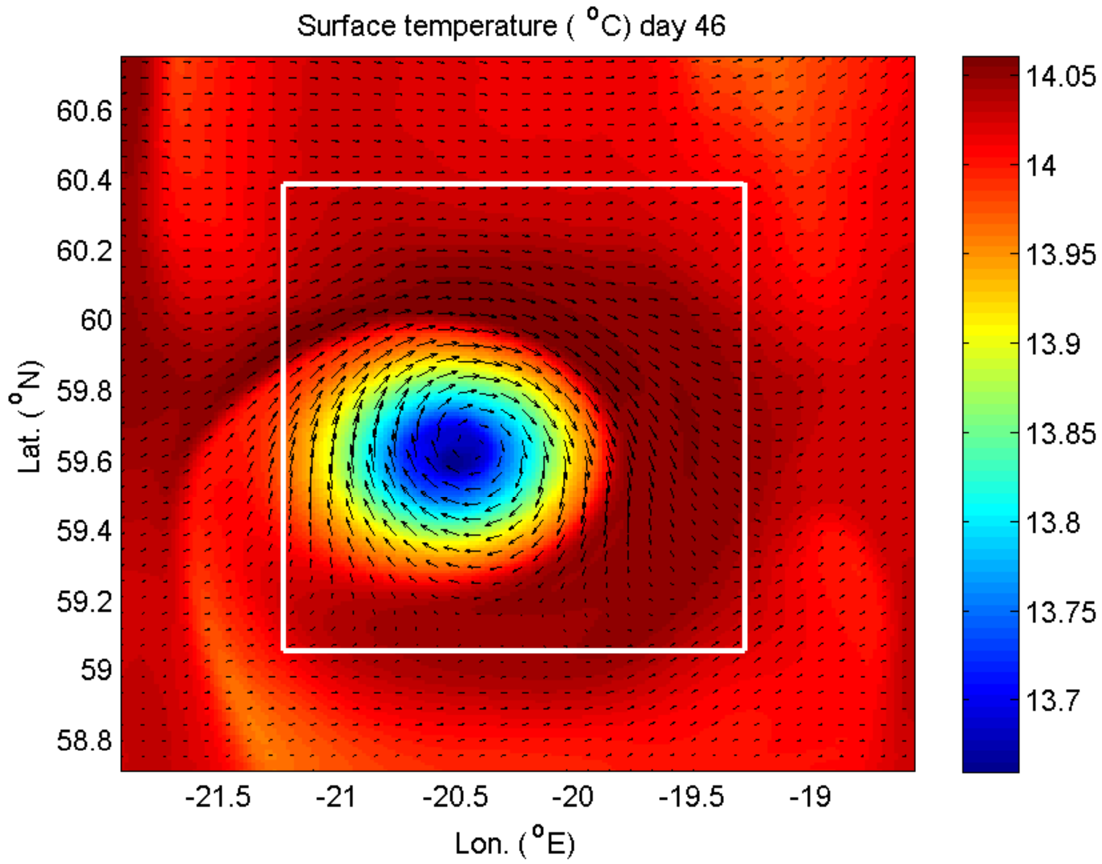

FIGURE A.2: The position of the sub-volume of the model domain used when comparing the fluxes calculated by first order differencing the change in output inert tracer volume in the euphotic zone to the sum of the output model flux components. Arrows indicate the direction of the eddy circulation.

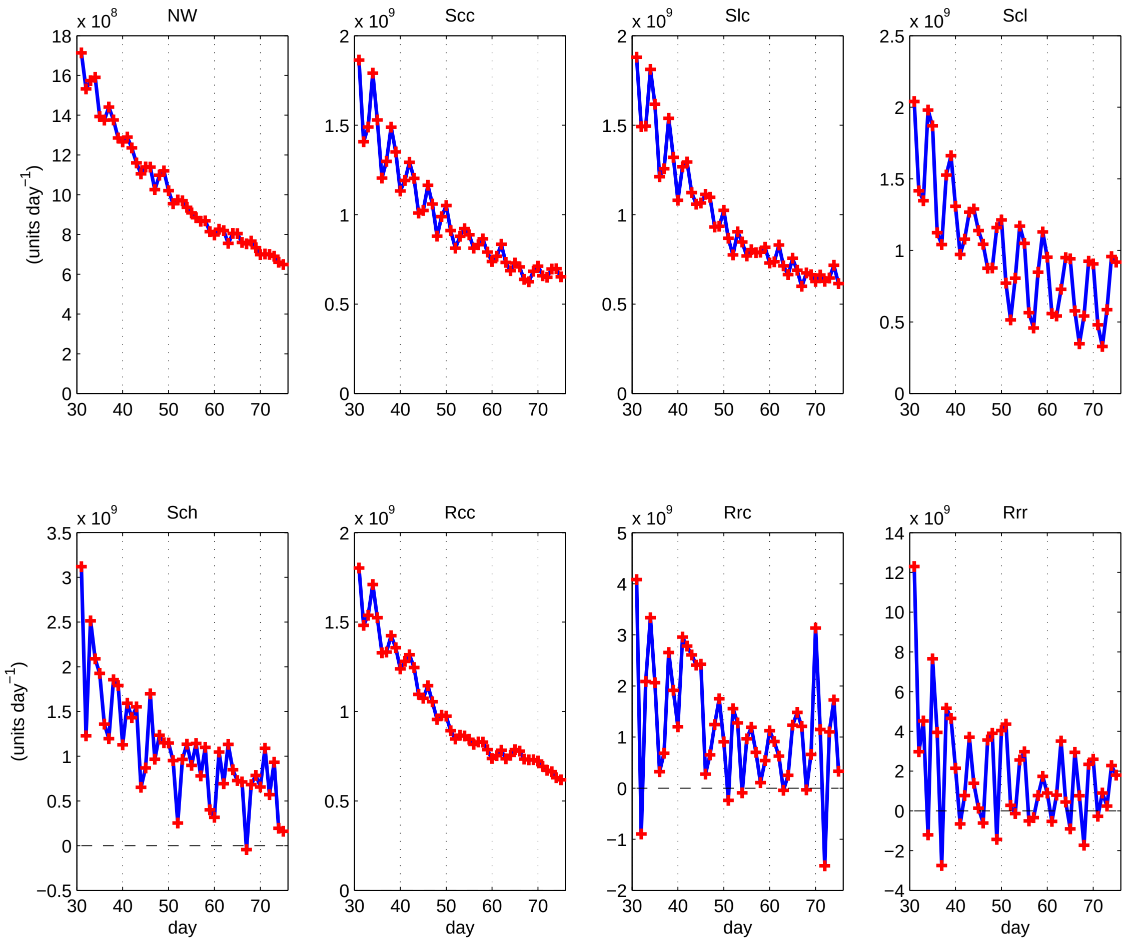

FIGURE A.3: Fluxes into the model sub-volume (see Figure A.2) calculated by first order differencing the change in output inert tracer volume in the euphotic zone (blue line) and from the sum of the output model flux components (red crosses). Results plotted for all runs using the standard wind stress parametrization. Note the different scales on the y-axes. Zero flux is indicated as a dashed black line where appropriate.

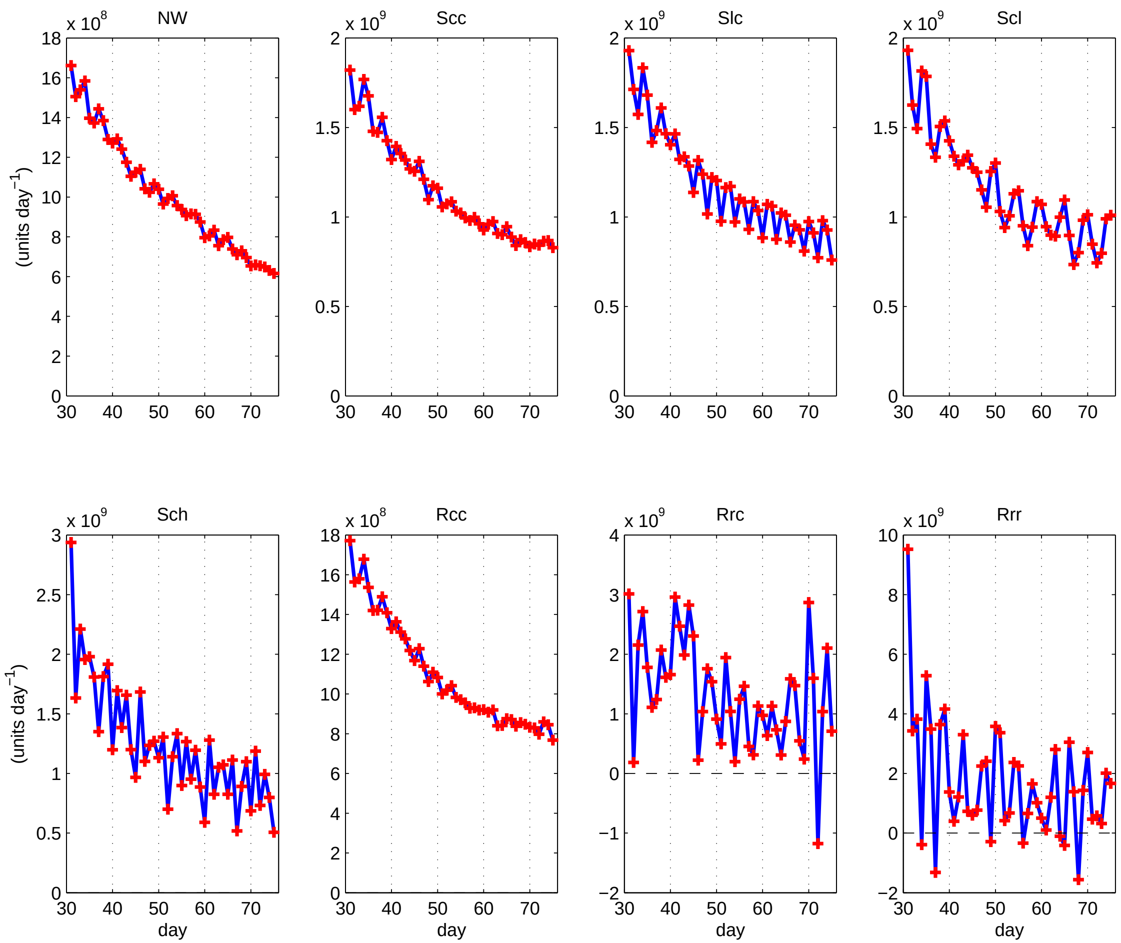

FIGURE A.4: Fluxes into the model sub-volume (see Figure A.2) calculated by first order differencing the change in output inert tracer volume in the euphotic zone (blue line) and from the sum of the output model flux components (red crosses). Results plotted for all runs using the Bye (1986) wind stress parametrization. Note the different scales on the y-axes. Zero flux is indicated as a dashed black line where appropriate.

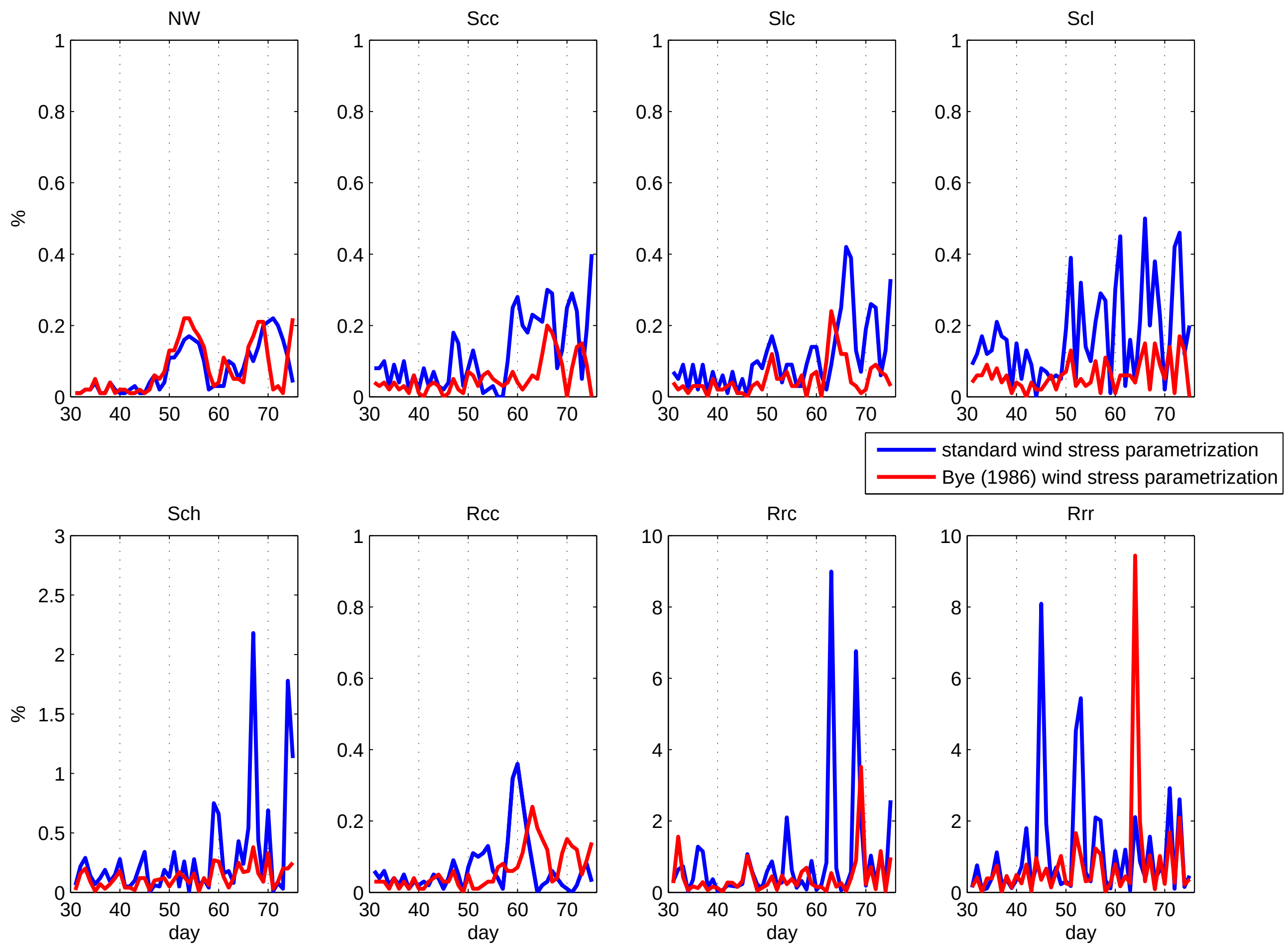

FIGURE A.5: The difference between fluxes into the model sub-volume (see Figure A.2) calculated by first order differencing the change in output inert tracer volume in the euphotic zone and from the sum of the output model flux components expressed as a percentage of the change in euphotic zone inert tracer volume. Results plotted for all runs using both wind stress parametrizations. Note the different scales on the y-axis.

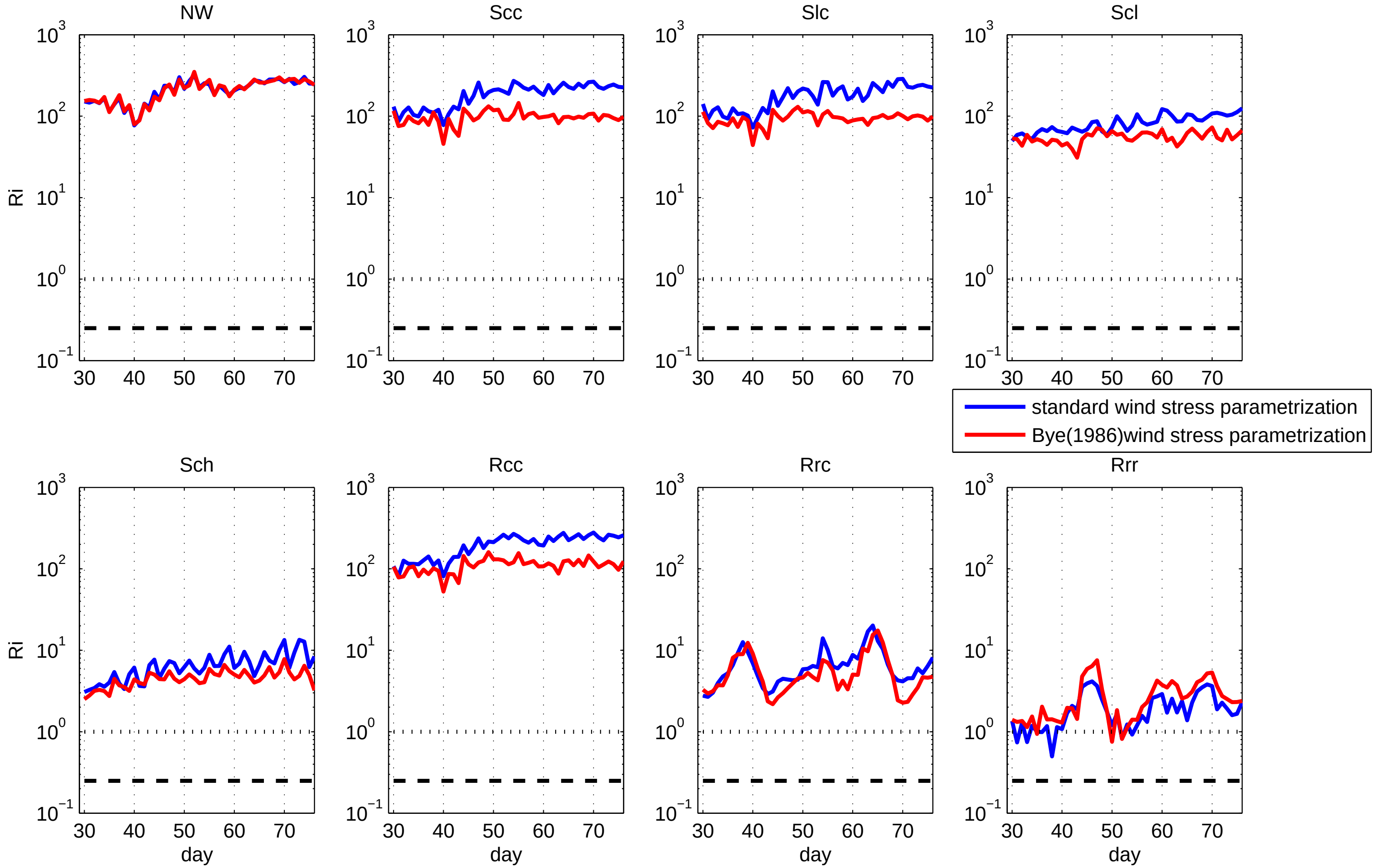

FIGURE A.6: The minimum value of the Richardson number (Ri) calculated at each model output step for all model runs using both wind stress parametrizations. Ri was calculated for model depth layers around the euphotic depth in the model sub-volume described in Section A.2 (see Figure A.2). Values of Ri=1 (fine black dashed line) and Ri=0.25 (thick black dashed line) are marked on each plot.

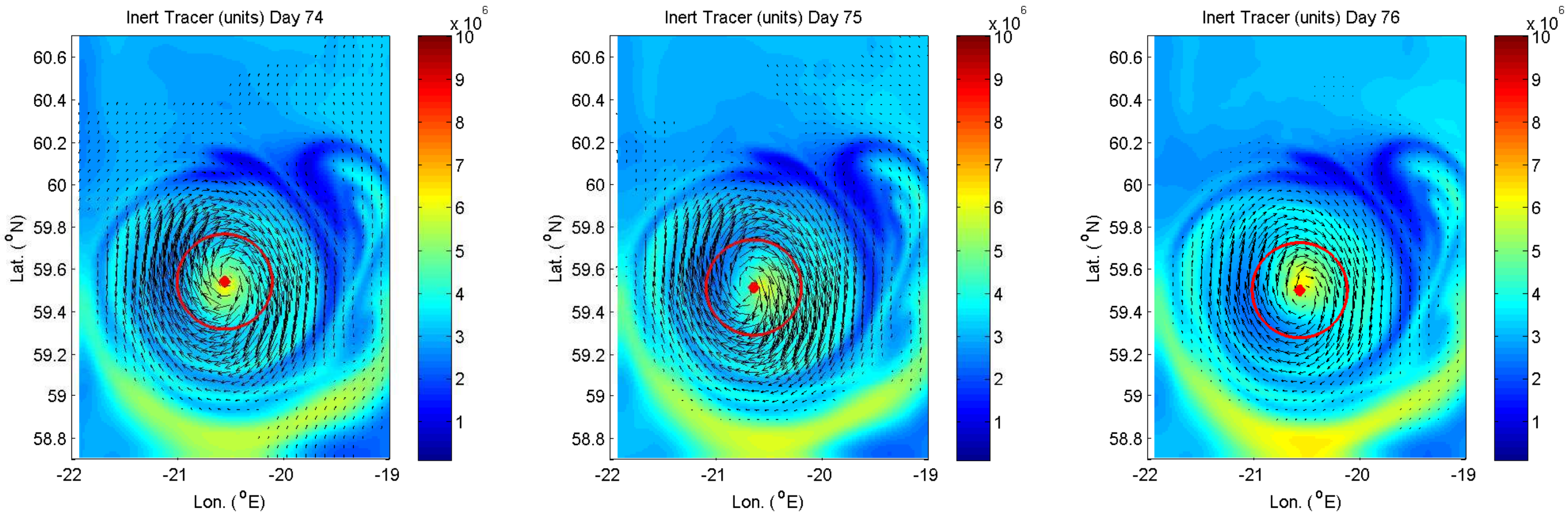

FIGURE A.7: The quantity of inert tracer in the euphotic zone (units) for days 74, 75 and, 76 of run Slc using the standard wind stress parametrization. The boundary of zone 1, radius 25 km, calculated as described in Chapter 5 is marked in red.

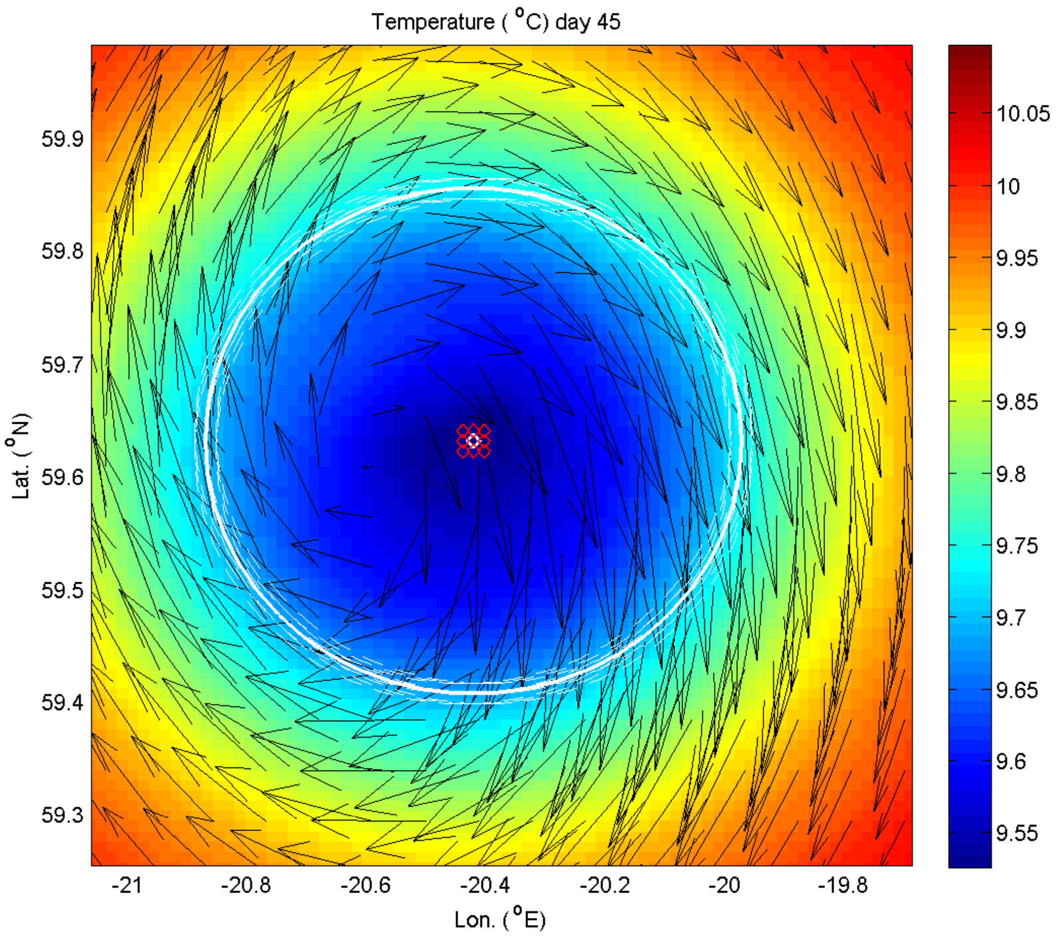

FIGURE A.8: An eddy model temperature field for the base of the euphotic zone showing the nine point 3x3 km box used in estimating the effect of eddy centre position uncertainty on diagnosed fluxes. The centre of the eddy, calculated as described in Chapter 5, is marked as a white diamond and zone 1 (25 km radius) a solid white circle. Zone 1 areas associated with the remaining eight points are marked as dashed white circles.

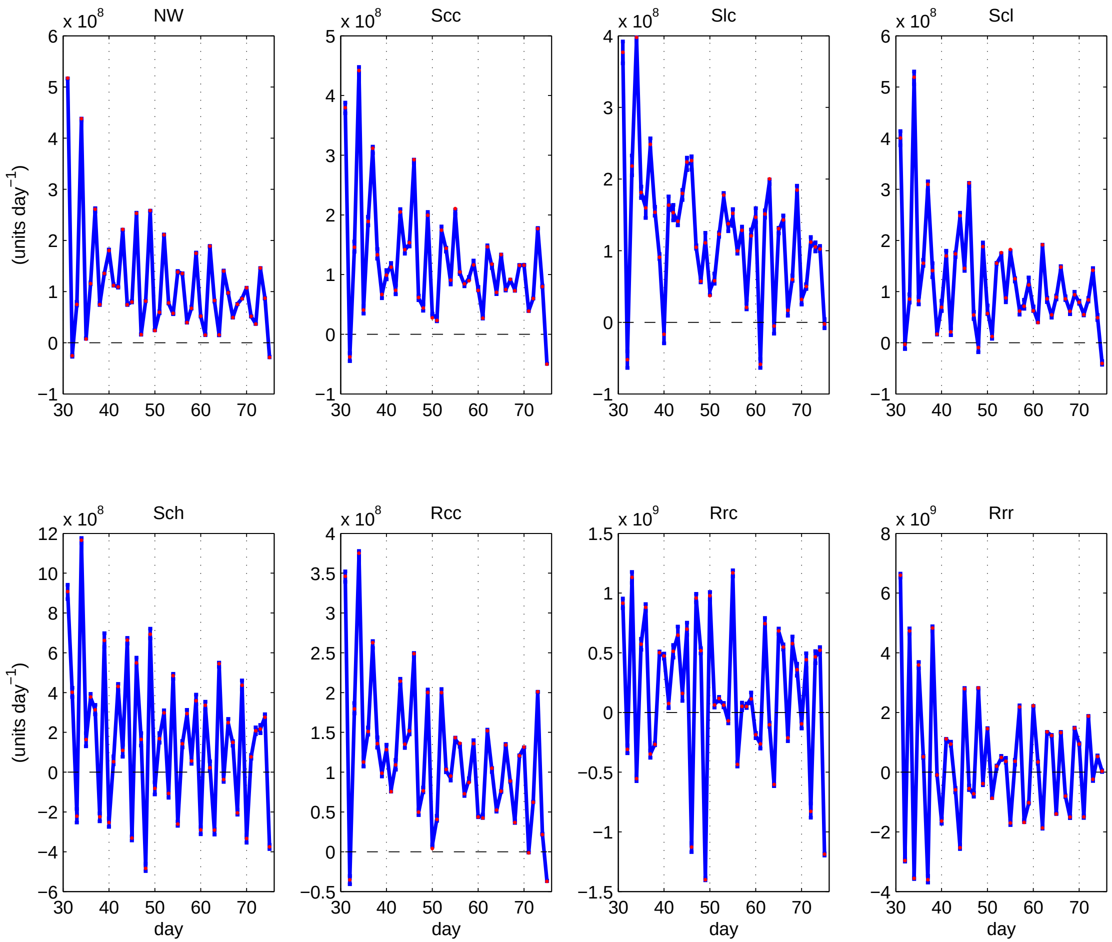

FIGURE A.9: Flux of inert tracer (T_1) into zone 1 estimated as a mean of nine sample points shown in Figure A.8 (blue line with standard error errorbars) for all runs using the standard wind stress parametrization. Fluxes of inert tracer calculated as described in Chapter 5 from a single point at the eddy centre are marked as red spots. Note the different scales on the y-axes. Zero flux is indicated as a dashed black line where appropriate.

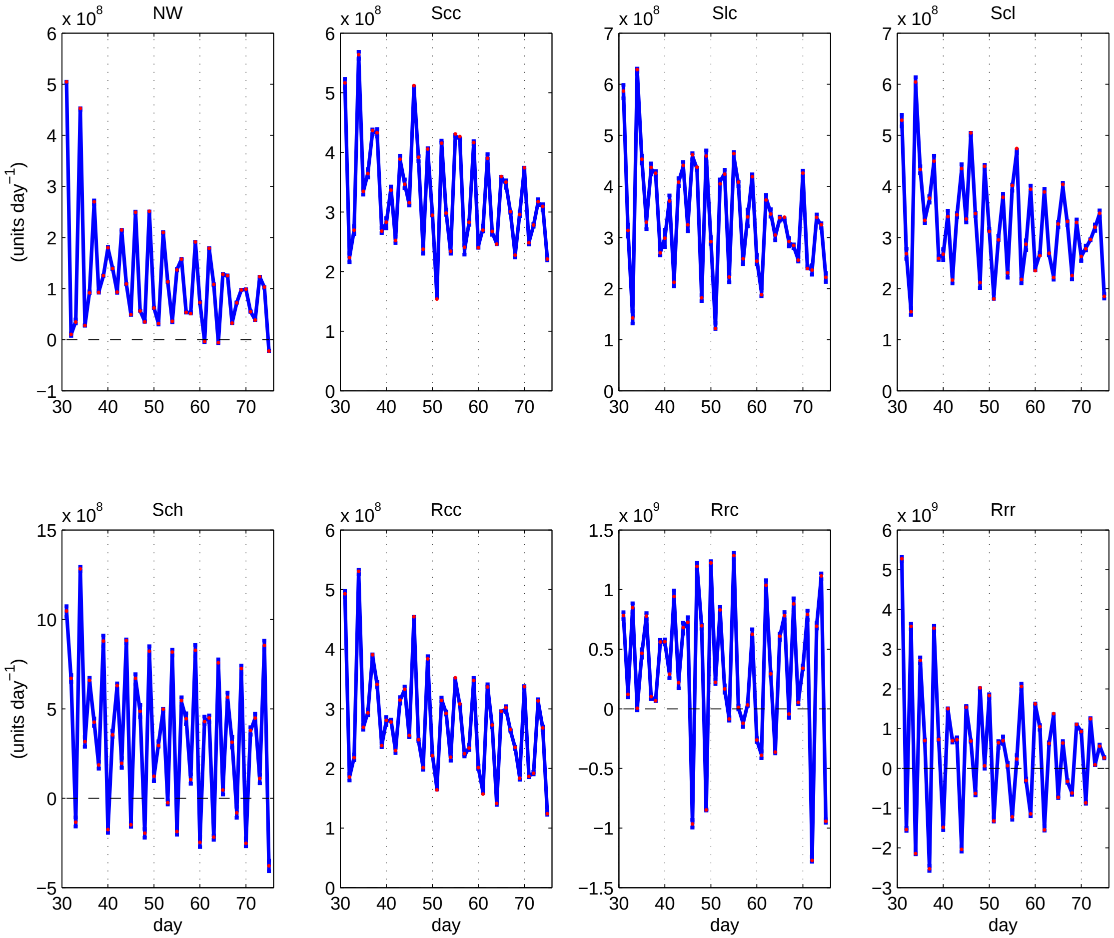

FIGURE A.10: Flux of inert tracer (T_1) into zone 1 estimated as a mean of nine sample points shown in Figure A.8 (blue line with standard error errorbars) for all runs using the Bye (1986) wind stress parametrization. Fluxes of inert tracer calculated as described in Chapter 5 from a single point at the eddy centre are marked as red spots. Note the different scales on the y-axes. Zero flux is indicated as a dashed black line where appropriate.

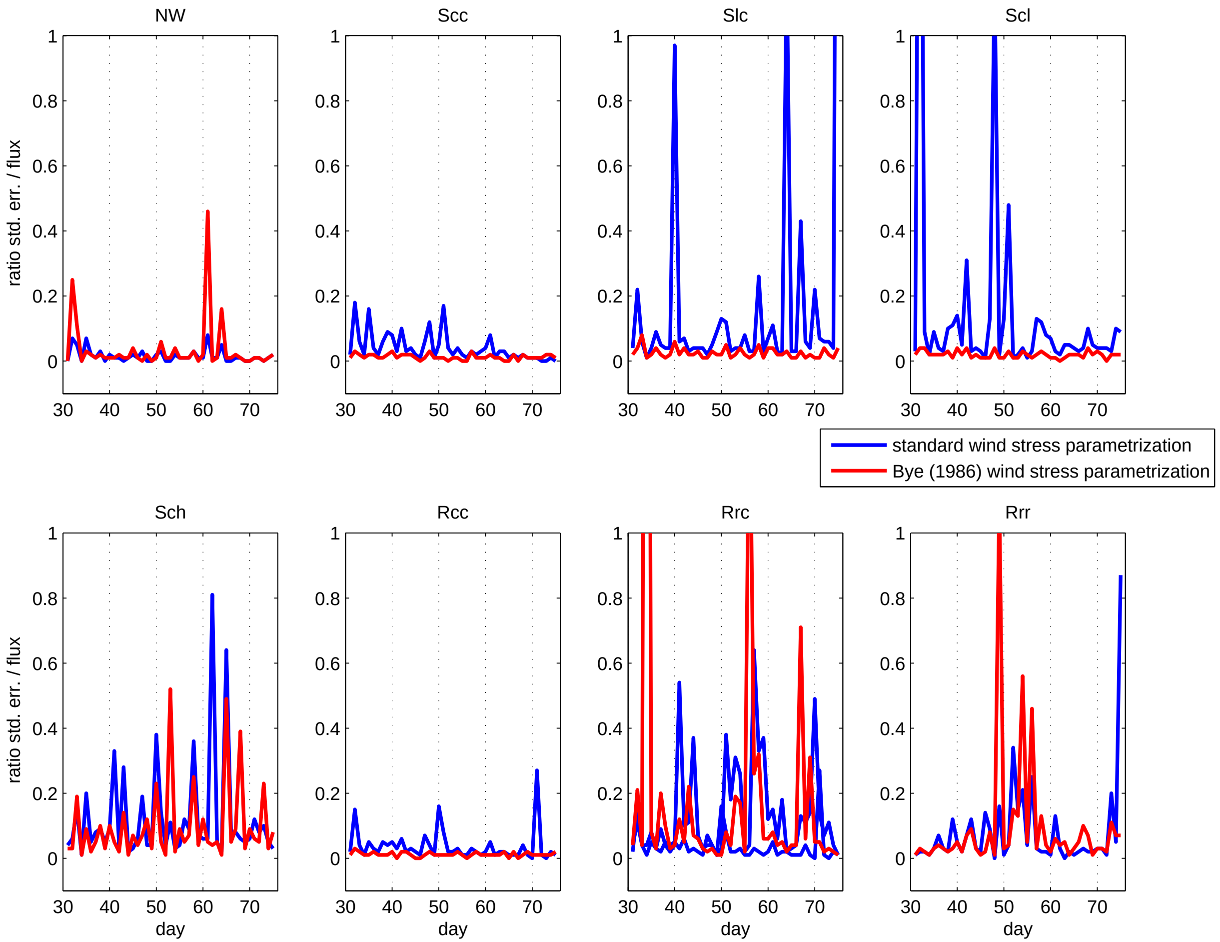

FIGURE A.11: Ratio of standard error to total euphotic zone inert tracer flux for zone 1 calculated from nine sample points shown in Figure A.8 for all runs using both wind stress parametrizations. The Bye (1986) wind stress parametrization in shown in red and the standard wind stress parametrization in blue.

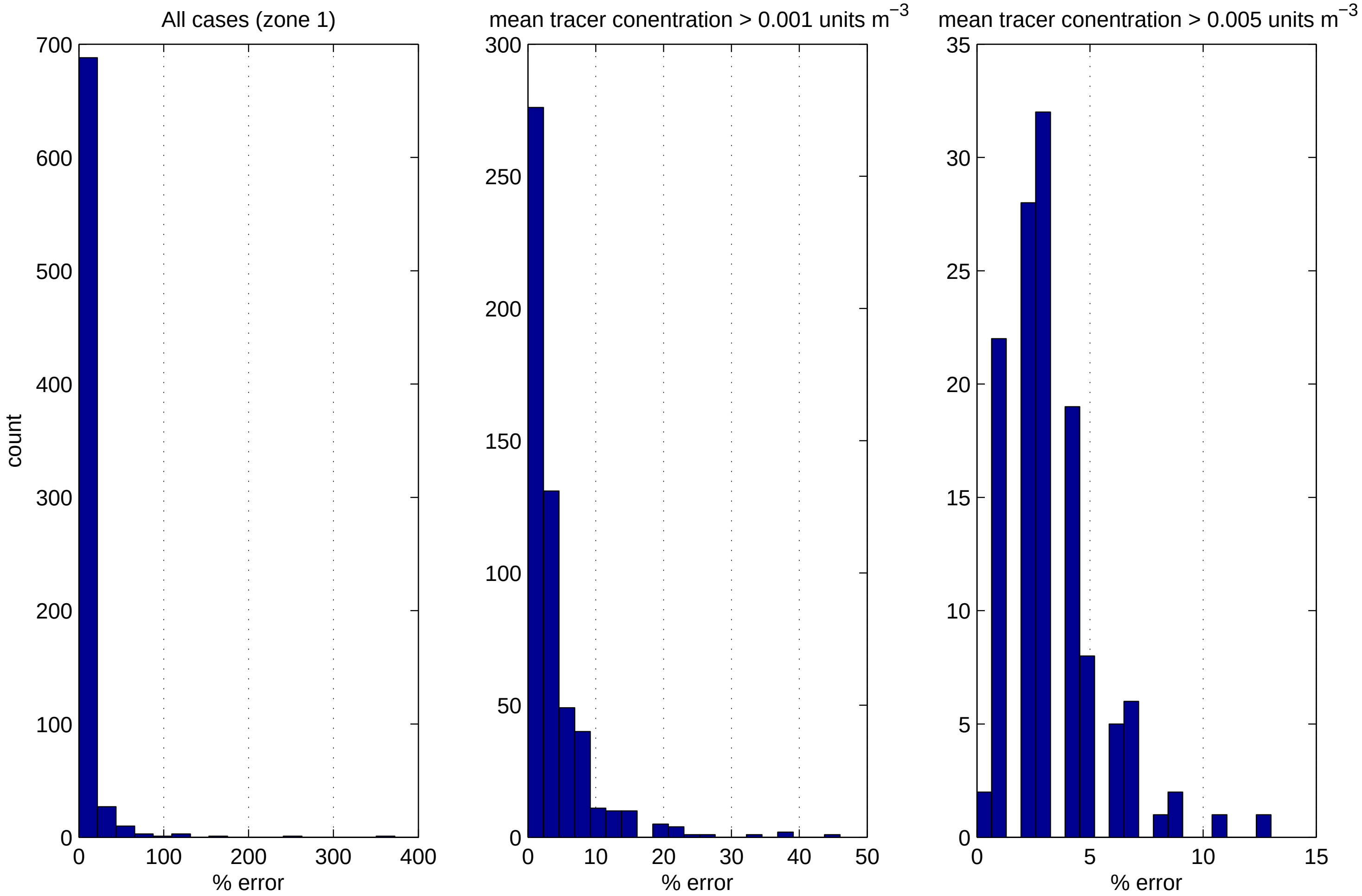

FIGURE A.12: Histogram of the ratio of standard error to total euphotic zone flux for zone 1 calculated from nine sample points, shown in Figure A.8. For all cases (left), for only those cases where mean tracer concentration is greater than 0.001 units m^{-3} (centre), and for only those cases where mean tracer concentration is greater than 0.005 units m^{-3} (right).

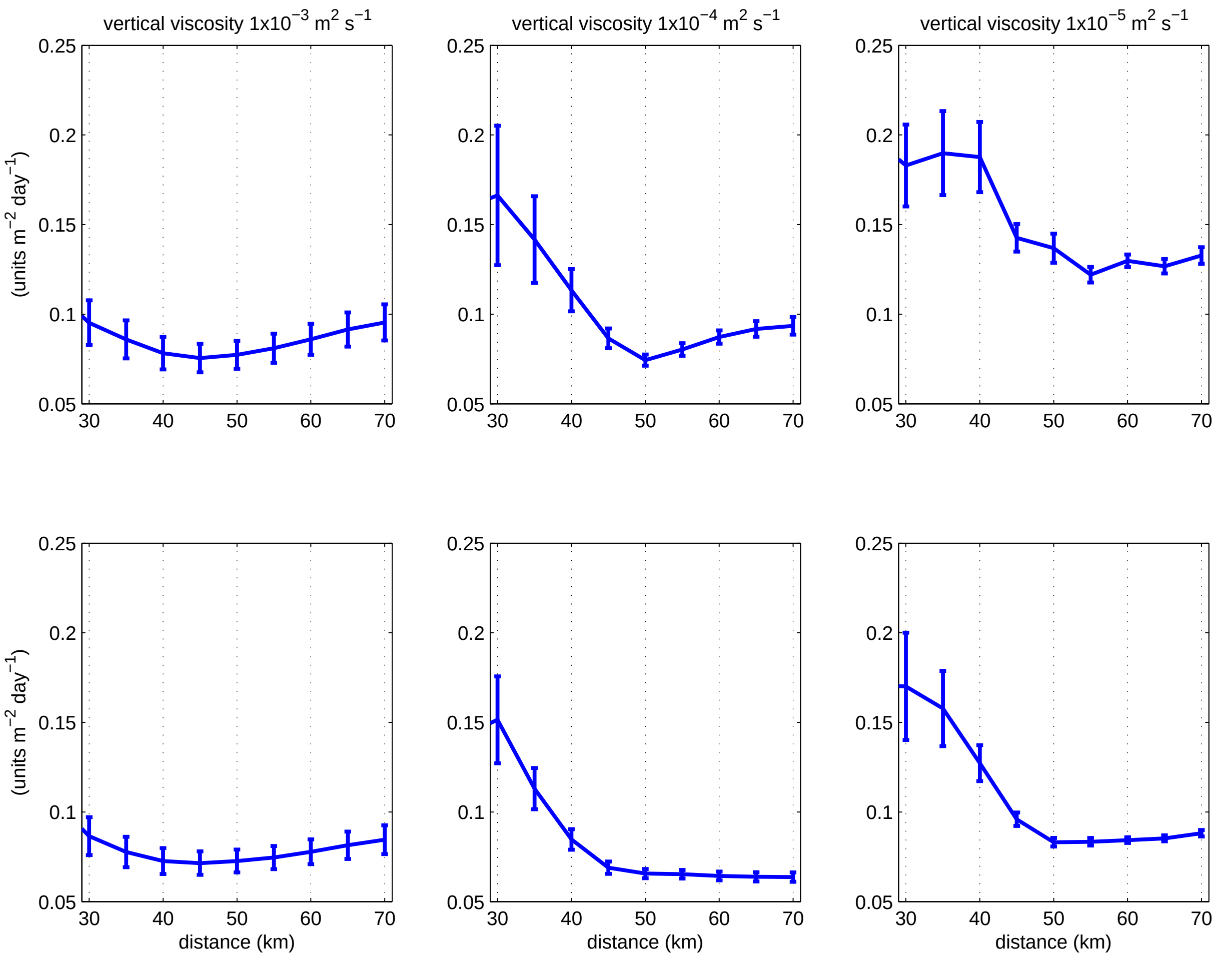

FIGURE A.13: Radial distribution of the mean diffusive fluxes of inert tracer (T_1) into the euphotic zone (units m^{-2} day^{-1}) for all runs for the period from day 30 to day 75 of the run. Results from runs using the standard wind stress parametrization are in the top three panels, results from runs using the Bye (1986) wind stress parametrization are in the bottom three panels. Error bars show ± standard error to the mean.

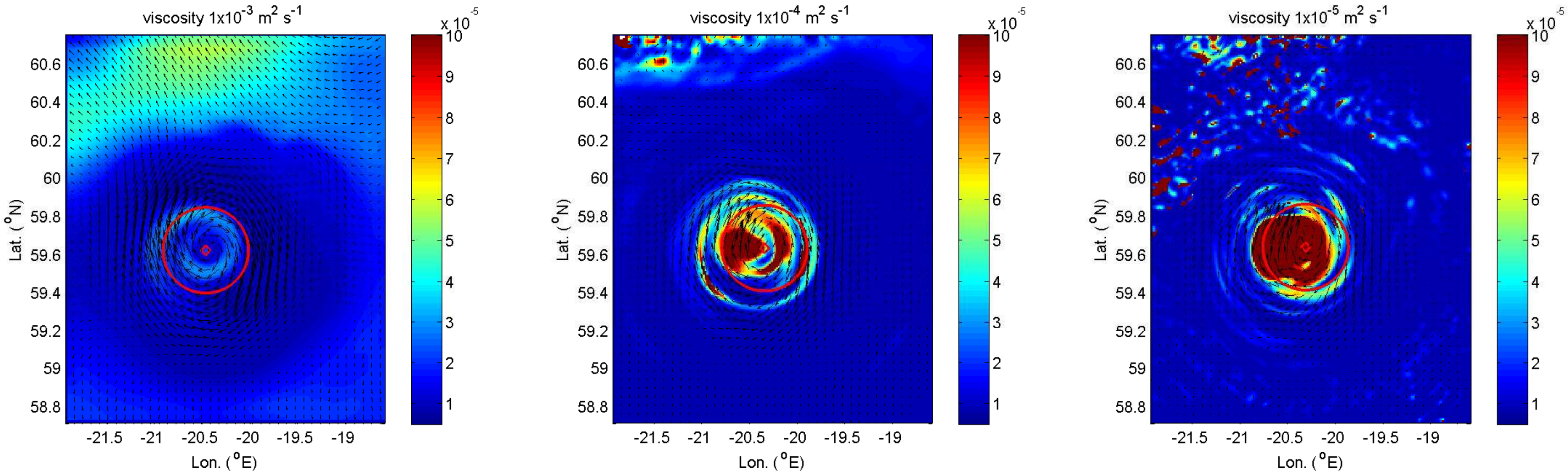

FIGURE A.14: Turbulent eddy diffusivity (K) for the base of the euphotic zone on day 45 of the model run. Runs carried out using wind forcing Rrr and the standard wind stress parametrization with vertical viscosities of 1x10^{-3} m^{2}s^{-1}, 1x10^{-4} m^{2}s^{-1} and 1x10^{-5} m^{2}s^{-1}. The area of zone 1 (radius 25km) is marked as a red circle.

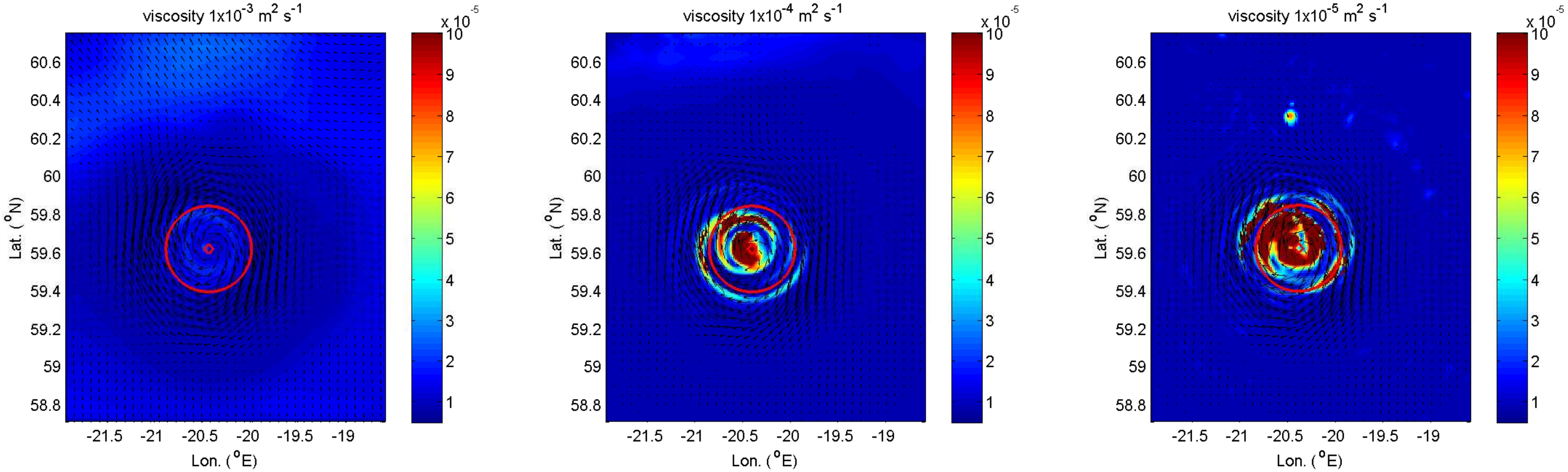

FIGURE A.15: Turbulent eddy diffusivity (K) for the base of the euphotic zone on day 45 of the model run. Runs carried out using wind forcing Rrr and the Bye (1986) wind stress parametrization, with vertical viscosities of 1x10^{-3} m^2s^{-1}, 1x10^{-4} m^2s^{-1} and 1x10^{-5} m^2s^{-1}. The area of zone 1 (radius 25km) is marked as a red circle.

Bibliography

Alford, M. and Pinkel, R. (2000), 'Observations of overturning in the thermocline: The context of ocean mixing', *Journal Of Physical Oceanography* **30**(10), 805–832.

Allen, J. (2007), Cruise report no. 23 RSS Discovery cruise 321 24th Jul-23 Aug 2007. Biophysical interactions in the Iceland Basin 2007, Technical report, National Oceanography Centre, Southampton.

Allen, J., Brown, L., Saunders, R., Moore, M., Mustard, A., Fielding, S., Lucas, M., Rixen, M., Savidge, G., Henson, S. and Mayor, D. (2005), 'Diatom carbon export enhanced by silicate upwelling in the Northeast Atlantic', *Nature* **437**, 728–732.

Baker, M. and Gibson, C. (1987), 'Sampling turbulence in the stratified ocean-statistical consequences of strong intermittency', *Journal Of Physical Oceanography* **17**(10), 1817–1836.

Blayo, E. and Debreu, L. (2005), 'Revisiting open boundary conditions from the point of view of characteristic variables', *Ocean Modelling* **9**(9-10), 231–252.

Boccaletti, G., Ferrari, R. and Fox-Kemper, B. (2007), 'Mixed layer instabilities and restratification', *Journal Of Physical Oceanography* **37**, 2228–2250.

Boyd, P., Jickells, T., Law, C., Blain, S., Boyle, E., Buesseler, K., Coale, K., Cullen, J., de Baar, H., Follows, M., Harvey, M., Lancelot, C., Levasseur, M., Owens, N., Pollard, R., Rivkin, R., Sarmiento, J., Schoemann, V., Smetacek, V., Takeda, S., Tsuda, A., Turner, S. and Watson, A. (2007), 'Mesoscale iron enrichment experiments 1993-2005: Synthesis and future directions', *Science* **315**, 612–167, doi: 10.1126/science.1131669.

Brundage, W. and Dugan, J. (1986), 'Observations of an anticyclonic eddy of 18 °c water in the Sargasso Sea', *Journal Of Physical Oceanography* **16**, 717–727.

Bryden, H. and Nurser, A. (2003), 'Effects of strait mixing on ocean stratification', *Journal Of Physical Oceanography* **33**(8), 1870–1872.

Burkill, P. (2006), Cruise report, no. 9 RRS Discovery cruise 306, 23 jun-6 jul 2006. pelagic biogeochemistry of the PAP site., Technical report, National Oceanography Centre, Southampton.

Bye, J. (1986), 'Momentum exchange at the sea surface by wind stress and understress', *Quaterly Journal Of The Royal Meterological Society* **112**, 501–510.

Carlson, C., Ducklow, H. and Michaels, A. (1994), 'Annual flux of dissolved organic-carbon from the euphotic zone in the Northwestern Sargasso Sea', *Nature* **371**(6496), 405–408.

Chang, Y. S., Xu, X., Özgökmen, T. M., Chassignet, E. P., Peters, H. and Fischer, P. F. (2005), 'Comparison of gravity current mixing parameterizations and calibration using a high-resolution 3D nonhydrostatic spectral element model', *Ocean Modelling* **10**(3-4), 342–368.

Chapman, D. (1985), 'Numerical traetment of cross-shelf open boundaries in a barotropic costal ocean model', *Journal Of Physical Oceanography* **15**(10), 1060–1075.

Courant, R., Friedrichs, K. and Lewy, H. (1967), 'On the partial difference equations of mathematical physics', *IBM Journal of Research and Development* **11**(2), 215–234.

D'Asaro, E. (1985), 'Upper ocean temperature structure, inertial currents, and Richardson Numbers observed during strong meteorological forcing', *Journal Of Physical Oceanography* **15**, 943–962.

De Silva, I., Brant, A., Montenegro, L. and Fernando, H. (1999), 'Gradient Richardson Number measurements in a stratified shear layer', *Dynamics Of Atmospheres And Oceans* **30**, 47–63.

Dewey, R. and Crawford, W. (1988), 'Bottom stress estimates from vertical dissipation rate profiles on the continental shelf', *Journal Of Physical Oceanography* **18**(8), 1167–1177.

Dillon, T. (1982), 'Vertical overturns-a comparison of Thorpe and Ozmidov length scales', *Journal Of Geophysical Research-Oceans* **87**(NC12), 9601–9613.

Dugdake, R. and Goering, J. (1967), 'Uptake of new and regenerated forms of nitrogen in primary productivity', *Limnology And Oceanography* **12**(2), 196–206.

Dukowicz, J. and Smith, R. (1994), 'Implicit free-surface method for the Bryan-Cox-Semtner ocean model.', *Journal Of Geophysical Research-Oceans* **99**, 7991–8014.

Eden, C. (2007), 'Eddy length scales in the North Atlantic Ocean', *Journal Of Geophysical Research-Oceans* **112**, C06004, doi:10.1029/2006JC003901.

Eden, C. and Dietze, H. (2009), 'Effects of mesoscale eddy/wind interactions on biological new production and eddy kinetic energy', *Journal Of Geophysical Research-Oceans* **114**, C05023, doi:10.1029/2008JC005129.

Emery, W. and Thomson, R. (1997), *Data Analysis Methods in Physical Oceanography*, Elsevier, Amsterdam, The Netherlands.

Fung, I., Meyn, S., Tegen, I., Doney, S., John, J. and Bishop, J. (2000), 'Iron supply and demand in the upper ocean', *Global Biogeochemical Cycles* **14**, 281–295.

Garcia-Soto, G., Pingree, R. and Valdés, L. (2002), 'Navidad development in the Southern Bay of Biscay: Climate change and swoddy structure from remote sensing and in situ measurements', *Journal Of Geophysical Research-Oceans* **107 (C8)**, 3118, 10.1029/2001JC001012.

Garrett, C. (2001), 'What is the "near-inertial" band and why is it different from the rest of the internal wave spectrum?', *Journal Of Physical Oceanography* **31**(10), 962–971.

Garrett, C. and Munk, W. (1979), 'Internal waves in the ocean', *Annual Review Of Fluid Mechanics* **11**, 339–369.

Garrett, C. and St. Laurent, L. (2002), 'Aspects of deep ocean mixing', *Journal Of Oceanography* **58**(10), 11–24.

Gill, A. (1982), *Atmosphere-Ocean Dynamics*, Academic Press, London, United Kingdom.

Gregg, M. (1989), 'Scaling turbulent dissipation in the thermocline', *Journal Of Geophysical Research-Oceans* **94**(C7), 9689–9698.

Gregg, M. (1999), 'Uncertainties and limitations in measuring epsilon and chi(tau)', *Journal Of Atmospheric And Oceanic Technology* **16**(11), 1483–1490.

Gregg, M., D'Asro, E., Shay, T. and Larson, N. (1986), 'Observations of persistent mixing and near-inertial internal waves', *Journal Of Physical Oceanography* **16**, 856–885.

Gregg, M. and Sanford, T. (1980), ‘Signatures of mixing from the Bermuda Slope, the Sargasso Sea and the Gulf Stream’, *Journal Of Physical Oceanography* **10**(10), 105–127.

Gregg, M. and Sanford, T. (1988), ‘The dependence of turbulent dissipation on stratification in a diffusively stable thermocline’, *Journal Of Geophysical Research-Oceans* **93**(NC12), 12381–12392.

Gregg, M., Sanford, T. and Winkel, D. (2003), ‘Reduced mixing from the breaking of internal waves in equatorial waters’, *Nature* **422**, 513–515.

Hansard, P., Landing, W., Measures, C. and Voelker, B. (2009), ‘Dissolved iron(II) in the Pacific Ocean: Measurements from the PO2 and P16N CLIVAR/CO2 repeat hydrography expeditions nutrients and SPM’, *Deep-Sea Research Part I-Oceanographic Research Papers* **56**, 1117–1129.

Hibiya, T. and Nagasawa, M. (2004), ‘Latitudinal dependence of diapycnal diffusivity in the thermocline estimated using a finescale parameterization’, *Geophysical Research Letters* **31**, L01301, doi:10.1029/2003GL017998.

Hibiya, T., Nagasawa, M. and Niwa, Y. (2007), ‘Latitudinal dependence of diapycnal diffusivity in the thermocline observed using a microstructure profiler.’, *Geophysical Research Letters* **34**, L24602, doi:10.1029/2007GL032323.

Hoskins, B. and Bretherton, F. (1972), ‘Atmospheric frontogenesis models: Mathematical formulation and solution’, *Journal Of The Atmospheric Sciences* **29**, 11–37.

Hoskins, B. and Hodges, K. (2002), ‘New perspectives on the Northern Hemisphere winter storm tracks’, *Journal Of The Atmospheric Sciences* **59**, 1041–1061.

Howarth, M. and Souza, A. (2005), ‘Reynolds stress observations in continental shelf seas’, *Deep-Sea Research Part II-Topical Studies In Oceanography* **52**(9-10), 1075–1086.

Jackson, L., Hallberg, R. and Legg, S. (2008), ‘A parameterization of shear-driven turbulence for ocean climate models’, *Journal Of Physical Oceanography* **38**, 1033–1053.

Jenkins, W. (1988), ‘Nitrate flux into the euphotic zone near Bemuda’, *Nature* **331**(6156), 521–523.

Jensen, T. (1998), 'Open boundary conditions in stratified ocean models', *Journal Of Marine Systems* **16**, 297–322.

Jickells, T., Liss, P., Broadgatea, W., Turner, S., Kettle, A., Read, J., Baker, J., Cardenas, L., Carsea, F., Hamren-Larssen, M., Spokes, L., Steinke, M., Thompson, A., Watson, A., Archer, S., Bellerby, R., Law, C., Nightingale, P., Liddicoat, M., Widdicombe, C., Bowie, A., Gilpin, L., Moncoiffé, G., Savidge, G., Preston, T., Hadziabdic, P., Frost, T., Upstill-Goddard, R., Pedrós-Alió, C., Simó, R., Jackson, A., Allen, A. and DeGrandpre, M. (2008), 'A lagrangian biogeochemical study of an eddy in the Northeast Atlantic', *Progress In Oceanography* **76**(3), 366–398.

Johnson, H. and Garrett, C. (2004), 'Effects of noise on thorpe scales and run lengths', *Journal Of Physical Oceanography* **34**(11), 2359–2372.

Johnson, K., Gordon, R. and Coale, K. (1997), 'What controls dissolved iron concentrations in the world ocean ?', *Marine Chemistry* **57**, 137–161.

Jones, J. (1973), 'Vertical mixing in the Equatorial Undercurrent', *Journal Of Physical Oceanography* **3**, 286–295.

Kalnay, E., Kanamitsu, M., Kistler, R., Collins, W., Deaven, D., Gandin, L., Iredell, M., Saha, S., White, G., Woollen, J., Zhu, Y., Leetmaa, A., Reynolds, R., Chelliah, M., Ebisuzaki, W., Higgins, W., Janowiak, J., Mo, K., Ropelewski, C., Wang, J., Jenne, R. and Joseph, D. (1996), 'The NCEP/NCAR 40-year reanalysis project', *Bulletin of the American Meteorological Society* **77**, 437–470.

Kara, A., Rochford, P. and Hurlburt, H. (2000), 'An optimal definition for ocean mixed layer depth', *Journal Of Geophysical Research-Oceans* **105**(C7), 16803–16821.

Kasajima, Y., Olsson, K., Johannessen, T., Messias, M., Jeansson, E., Bellerby, R. and Skjelvan, I. (2006), 'A submesoscale coherent eddy in the Greenland Sea in 2003', *Journal Of Geophysical Research-Oceans* **111**, C07013, doi:10.1029/2005JC003130.

Killworth, P., Webb, D., Stainforth, D. and Paterson, S. (1991), 'The development of a free-surface Bryan-Cox-Semtner ocean model', *Journal Of Physical Oceanography* **21**, 1333–1348.

Kim, D., Lee, K., Choi, S., Kang, H., Zhang, J. and Chang, Y. (2005), 'Determination of diapycnal diffusion rates in the upper thermocline in the North Atlantic Ocean using sulfur hexafluoride', *Journal Of Geophysical Research-Oceans* **110**(C10).

Klein, P. and Lapeyre, G. (2009), 'The oceanic vertical pump induced by mesoscale turbulence', *Annual Review Of Marine Science* **1**, 351–375.

Kunze, E. (1985), 'Near-inertial wave propagation in geostrophic shear', *Journal Of Physical Oceanography* **15**(10), 554–656.

Kunze, E. and Sanford, T. (1996), 'Abyssal mixing: Where it is not', *Journal Of Physical Oceanography* **26**(10), 2286–2296.

Lapeyre, G. and Klein, P. (2006), 'Impact of the small-scale elongated filaments on the oceanic vertical pump', *Journal Of Marine Research* **64**(6), 835–851.

Large, W., McWilliams, J. and Doney, S. (1994), 'Oceanic vertical mixing-a review and a model with a nonlocal boundary-layer parameterization', *Reviews Of Geophysics* **32**(4), 363–403.

Large, W. and Pond, S. (1981), 'Open ocean momentum flux measurements in moderate to strong winds', *Journal Of Physical Oceanography* **11**(11), 324–336.

Law, C., Martin, A., Liddicoat, M., Watson, A., Richards, K. and Woodward, E. (2001), 'A lagrangian SF6 tracer study of an anticyclonic eddy in the North Atlantic: patch evolution, vertical mixing and nutrient supply to the mixed layer', *Deep-Sea Research Part II-Topical Studies In Oceanography* **48**(4-5), 705–724.

Law, C., Watson, A., Liddicoat, M. and Stanton, T. (1998), 'Sulphur hexafluoride as a tracer of biogeochemical and physical processes in an open-ocean iron fertilisation experiment.', *Deep-Sea Research Part II-Topical Studies In Oceanography* **45**(4-5), 977–994.

Ledwell, J., McGillicuddy Jr, D. and Anderson, L. (2008), 'Nutrient flux into an intense deep chlorophyll layer in a mode-water eddy', *Deep-Sea Research Part II-Topical Studies In Oceanography* **55**(6766), 1139–1160.

Ledwell, J., Montgomery, E., Polzin, K., St Laurent, L., Schmitt, R. and Toole, J. (2000), 'Evidence for enhanced mixing over rough topography in the abyssal ocean', *Nature* **403**(6766), 179–182.

Ledwell, J., Watson, A. and Law, C. (1998), 'Mixing of a tracer in the pycnocline', *Journal Of Geophysical Research-Oceans* **103**(C10), 21449–21529.

Legg, S. and Marshall, J. (1993), 'A heton model of the spreading phase of Open-Ocean deep convection', *Journal of Physical Oceanography* **23**, 1040–1056.

Lermusiaux, P. (1997), Error Subspace Data Assimilation Methods for Ocean Field Estimation: Theory, Validation and Applications, PhD thesis, Harvard University, Cambridge, Massachusetts.

Lévy, M., Klein, P. and Ben Jelloul, M. (2009), 'New production stimulated by high frequency winds in a turbulent mesoscale eddy field', *Geophysical Research Letters* **36**, L16603, doi:10.1029/2009GL039490.

Lévy, M., Klein, P. and Treguier, A. (2001), 'Impact of sub-mesoscale physics on production and subduction of phytoplankton in an oligotrophic regime', *Journal Of Marine Research* **59**, 535–565.

Lévy, M., Memery, L. and Madec, G. (1998), 'The onset of a bloom after deep winter convection in the Northwestern Mediterranean Sea: mesoscale process study with a primitive equation model', *Journal Of Marine Systems* **16**, 7–21.

Lewis, M., Harrison, W., Oakey, N., Herbert, D. and Platt, T. (1986), 'Vertical nitrate fluxes in the oligotrophic ocean', *Science* **234**(4778), 870–873.

Lilly, J. and Rhines, P. (2002), 'Coherent eddies in the Labrador Sea observed from a mooring', *Journal Of Physical Oceanography* **32**, 585–598.

Lozovatsky, I., Roget, E., Fernando, H., Figueroa, M. and Shapovalov, S. (2006), 'Sheared turbulence in a weakly stratified upper ocean', *Deep-Sea Research Part I-Oceanographic Research Papers* **53**(25-26), 387–407.

Lu, Y. and Lueck, R. (1999), 'Using a broadband adcp in a tidal channel. part ii: Turbulence', *Journal Of Atmospheric And Oceanic Technology* **16**(11), 1568–1579.

Lueck, R., Wolk, F. and Yamazaki, H. (2002), 'Oceanic velocity microstructure measurements in the 20th century', *Journal Of Oceanography* **58**(1), 153–174.

Luther III, G. and Wu, J. (1997), 'What controls dissolved iron concentrations in the world ocean ?-a comment', *Marine Chemistry* **57**, 173–179.

MacKinnon, J. and Winters, K. (2005), 'Subtropical catastrophe: Significant loss of low mode tidal energy at 28.9°', *Geophysical Research Letters* **32**, L15605, doi:10.1029/2005GL023376.

Mahadevan, A. (2006), 'Modeling vertical motions at ocean fronts: Are nonhydrostatc effects relevant at submesoscales ?', *Ocean Modelling* **14**(3-4), 222–240.

Mahadevan, A. and Tandon, A. (2006), 'An analysis of mechanisms for submesoscale vertical motion at ocean fronts', *Ocean Modelling* **14**(3-4), 241–256.

Mahadevan, A., Thomas, L. and Tandon, A. (2008), 'Comment on "eddy/wind interactions stimulate extraordinary mid-ocean plankton blooms"', *Science* **320**, 448b.

Marmorino, G. (1987), 'Observations of small-scale mixing processes in the seasonal thermocline. part ii: Wave breaking', *Journal Of Physical Oceanography* **17**(3), 1348–1355.

Marshall, J., Hill, C., Perelman, L. and Adcroft, A. (1997), 'Hydrostatic, quasi-hydrostatic, and nonhydrostatic ocean modeling', *Journal Of Geophysical Research-Oceans* **102**, 5733–5752.

Marshall, J. and Schott, F. (1999), 'Open-ocean convection: Observations, theory, and models', *Reviews Of Geophysics* **37**(1), 1–64.

Martin, A. (2005), 'The kaleidoscope ocean', *Philosophical Transactions Of The Royal Society A* **363**, 2873–2890.

Martin, A. and Pondaven, P. (2003), 'On estimates for the vertical nitrate flux due to eddy pumping', *Journal Of Geophysical Research* **108 (C11)**, doi:10.1029/2003JC001841.

Martin, A. and Richards, K. (2001), 'Mechanisms for vertical nutrient transport within a North Atlantic mesoscale eddy', *Deep-Sea Research Part II-Topical Studies In Oceanography* **48**(4-5), 757–773.

Martin, A., Wade, I., Richards, K. and Heywood, K. (1998), 'The PRIME eddy', *Journal Of Marine Research* **56**(2), 439–462.

McDowell, S. and Rossby, H. (1978), 'Mediterranean water-intense mesoscale eddy off Bahamas', *Science* **202**(4372), 1085–1087.

McGillicuddy, D., Anderson, L., Bates, N., Bibby, T., Buesseler, K., Carlson, C., Davis, C., Ewart, C., Falkowski, P., Goldthwait, S., Hansell, D., Jenkins, W., Johnson, R., Kosnyrev, V., Ledwell, J., Li, Q., Siegel, D. and Steinberg, D. (2007), 'Eddy/wind interactions stimulate extraordinary mid-ocean plankton blooms', *Science* **316**(5827), 1021–1026.

McGillicuddy, D., Anderson, L., Doney, S. and Maltrud, M. (2003), 'Eddy-driven sources and sinks of nutrients in the upper ocean: Results from a 0.1 degrees resolution model of the North Atlantic', *Global Biogeochemical Cycles* **17**(2), doi:10.1029/2002GB001987.

McGillicuddy, D., Johnson, R., Siegel, D., Michaels, A., Bates, N. and Knap, A. (1999), 'Mesoscale variations of biogeochemical properties in the Sargasso Sea', *Journal Of Geophysical Research-Oceans* **104**(C6), 13381–13394.

McGillicuddy, D., Ledwell, J. and Anderson, L. (2008), 'Response to comment on "eddy/wind interactions stimulate extraordinary mid-ocean plankton blooms"', *Science* **320**, 448c.

McGillicuddy, D. and Robinson, A. (1997), 'Eddy-induced nutrient supply and new production in the Sargasso Sea', *Deep-Sea Research Part I-Oceanographic Research Papers* **44**(8), 1427–1450.

McGillicuddy, D., Robinson, A., Siegel, D., Jannasch, H., Johnson, R., Dickeys, T., McNeil, J., Michaels, A. and Knap, A. (1998), 'Influence of mesoscale eddies on new production in the Sargasso Sea', *Nature* **394**(6690), 263–266.

McNeil, J., Jannasch, H., Dickey, T., McGillicuddy, D., Brzezinski, M. and Sakamoto, C. (1999), 'New chemical, bio-optical and physical observations of upper ocean response to the passage of a mesoscale eddy off Bermuda', *Journal Of Geophysical Research-Oceans* **104**(C7), 15537–15548.

McWilliams, J. (1985), 'Submesoscale, coherent vortices in the ocean', *Reviews Of Geophysics* **23 (2)**, 165–182.

Molemaker, M. and Dijkstra, H. (2000), 'Stability of a cold core eddy in the presence of convection: Hydrostatic versus nonhydrostatic modeling', *Journal Of Physical Oceanography* **30**(3), 475–494.

Molemaker, M., McWilliams, J. and Yavneh, I. (2005), 'Baroclinic instability and loss of balance', *Journal Of Physical Oceanography* **35**, 1505–1517.

Monin, A. and Yaglom, A. (1971), *Statistical Fluid Mechanics*, Vol. 1, The MIT Press, Cambridge, Massachusetts and London, England.

Moum, J., Gregg, M., Lien, R. and Carr, M. (1995), 'Comparison of turbulence kinetic-energy dissipation rate estimates from 2 ocean microstructure profilers', *Journal Of Atmospheric And Oceanic Technology* **12**(2), 346–366.

Moum, J., Lien, R., Perlin, A., Nash, J., Gregg, M. and Wiles, P. (2009), 'Sea surface cooling at the Equator by subsurface mixing in tropical instability waves', *Nature Geoscience* **2**, 761–765.

Munk, W. (1966), 'Abyssal recipes', *Deep-Sea Research* **13**, 707–730.

Munk, W. and Anderson, E. (1948), 'Notes on a theory of the thermocline', *Journal Of Marine Research* **3**, 267–295.

Munk, W. and Wunsch, C. (1998), 'Abyssal recipes ii: energetics of tidal and wind mixing', *Deep-Sea Research Part I-Oceanographic Research Papers* **45**(12), 1977–2010.

Nagai, T., Tandon, A., Yamazaki, H. and Doubell, M. (2009), 'Evidence of enhanced turbulent dissipation in the frontogenetic Kuroshio Font thermocline', *Geophysical Research Letters* **36**, L12609, doi:10.1029/2009GL038832.

Naveira Garabato, A. (2008), Cruise report, no. 35 RRS James Cook cruise 29 01 Nov-22 Dec 2008 SOFine cruise report: Southern Ocean Finestructure, Technical report, National Oceanography Centre, Southampton.

Naveira Garabato, A., Polzin, K., King, B., Heywood, K. and Visbeck, M. (2004), 'Widespread intense turbulent mixing in the Southern Ocean', *Science* **303**, 210–212.

Nielsdóttir, M., Moore, C., Sanders, R., Hinz, D. and Achterberg, E. (2009), 'Iron limitation of the postbloom phytoplankton communities in the Iceland Basin', *Global Biogeochemical Cycles* **23**, GB3001, doi:10.1029/2008GB003410.

Niiler, P. and Kraus, E. (1977), One-dimensional models of the upper ocean, *in* E. Kraus, ed., 'Modelling and Prediction of the Upper Layers of the Ocean.', Pergamon, pp. 143–172.

Oakey, N. (1982), 'Determination of the rate of dissipation of turbulent energy from simultaneous temperature and shear microstructure measurements', *Journal Of Physical Oceanography* **12**(3), 256–271.

Oliger, J. and Sundstrom, A. (1978), 'Theoretical and practical aspects of some initial boundary value problems in fluid dynamics', *SIAM Journal On Applied Mathematics* **35**, 419–446.

Oliver, K., Eldevik, T., Stevens, D. and Watson, A. (2008), 'A Greenland Sea perspective on the dynamics of postconvective eddies', *Journal Of Physical Oceanography* **38**, 2755–2771.

Orlanski, I. (1976), 'A simple boundary condition for unbounded hyperbolic flows', *Journal Of Computational Physics* **21**, 251–269.

Osborn, T. (1980), 'Estimates of the local rate of vertical diffusion from dissipation measurements.', *Journal Of Physical Oceanography* **10**, 83–89.

Oschlies, A. (2001), 'Model-derived estimates of new production: New results point towards lower values', *Deep-Sea Research Part I-Oceanographic Research Papers* **48**(10), 2173–2197.

Oschlies, A. (2002*a*), 'Can eddies make ocean deserts bloom?', *Global Biogeochemical Cycles* **16**(4), doi:10.1029/2001GB001830.

Oschlies, A. (2002*b*), 'Nutrient supply to the surface waters of the North Atlantic: A model study', *Journal Of Geophysical Research-Oceans* **107**(C5).

Oschlies, A. and Garcon, V. (1998), 'Eddy-induced enhancement of primary production in a model of the North Atlantic Ocean', *Nature* **394**(6690), 266–269.

Pacanowski, R. and Philander, S. (1981), 'Parameterization of vertical mixing in numerical-models of tropical oceans', *Journal Of Physical Oceanography* **11**(11), 1443–1451.

Paillet, J. (1999), 'Central water vortices of the Eastern North Atlantic', *Journal Of Physical Oceanography* **29**, 2487–2503.

Paillet, J., Le Cann, B., Carton, X., Morel, Y. and Serpette, A. (2002), 'Dynamics and evolution of a northern meddy', *Journal Of Physical Oceanography* **32**, 55–79.

Park, Y., Fuda, J., Durand, I. and Naveira Garabato, A. (2008), 'Internal tides and vertical mixing over the Kerguelen Plateau', *Deep-Sea Research Part II-Topical Studies In Oceanography* **55**(6766), 582–593.

Pelegri, J. and Csanady, G. (1994), 'Diapycnal mixing in western boundary currents', *Journal Of Geophysical Research-Oceans* **99 (C9)**, 18275–18304.

Peters, H., Gregg, M. and Sanford, T. (1991), 'Equatorial and Off-Equatorial fine-scale and large scale shear variability at 140 W.', *Journal Of Geophysical Research-Oceans* **99, C9**, 16913–16928.

Peters, H., Gregg, M. and Sanford, T. (1995), 'On the parameterization of Equatorial turbulence: Effect of fine-scale variations below the range of the diurnal cycle', *Journal Of Geophysical Research-Oceans* **100 (C9)**(C9), 18333–18348.

Peters, H., Gregg, M. and Toole, J. (1988), 'On the parameterization of Equatorial turbulence', *Journal Of Geophysical Research-Oceans* **93, C2**, 1199–1218.

Pingree, R. (1996), 'A shallow subtropical subducting westward propagating eddy (swesty)', *Philosophical Transactions Of The Royal Society A* **354 (1710)**, 979–1026.

Pingree, R. and le Cann, B. (1992), 'Three anticyclonic slope water oceanic eddies (SWODDIES) in the Southern Bay of Biscay in 1990', *Deep-Sea Research Part I-Oceanographic Research Papers* **39**, 1147–1175.

Pollard, R. and Regier, L. (1992), 'Vorticity and vertical circulation at an ocean front', *Journal Of Physical Oceanography* **22**(3), 609–625.

Polzin, K. (1996), 'Statistics of the Richardson Number: Mixing models and finestructure.', *Journal Of Physical Oceanography* **26**(6), 1409–1425.

Polzin, K., Toole, J., Ledwell, J. and Schmitt, R. (1997), 'Spatial variability of turbulent mixing in the abyssal ocean', *Science* **276**(5309), 93–96.

Polzin, K., Toole, J. and Schmitt, R. (1995), 'Finescale parameterizations of turbulent dissipation', *Journal Of Physical Oceanography* **25**(3), 306–328.

Popova, E., Coward, A., Nurser, G., de Cuevas, B., Fasham, M. and Anderson, T. (2006), 'Mechanisms controlling primary and new production in a global ecosystem model-part i: Validation of the biological simulation', *Ocean Science Discussions* **2**, 249–266.

Popova, E., Lozano, C., Srokosz, M., Fasham, M., Haley, P. and Robinson, A. (2002), 'Coupled 3d physical and biological modelling of the mesoscale variability observed in the North-East Atlantic in spring 1997: biological processes', *Deep-Sea Research Part I-Oceanographic Research Papers* **49**(10), 1741–1768.

Popova, E. and Srokosz, M. (2009), 'Modelling the ecosystem dynamics at the Iceland-Faeroes Front: Biophysical interactions', *Journal Of Marine Systems* pp. 182–196.

Prandke, H. (2007), Measurement of small scale turbulence-data processing, dissipation rate computation, and error discussion, Presentation, ISW Wassermesstechnik, Petersdorf.

Prandke, H. (2008*a*), 'Microstructure velocity shear probe PNS'. **URL:** *http://www.isw-wasser.com/product6.htm*

Prandke, H. (2008*b*), 'The MSS free-fall profiler'. **URL:** *http://www.isw-wasser.com/product1.htm*

Prandke, H. (2008*c*), MSSpro microstructure data evaluation tool user manual, Technical report, ISW Wassermesstechnik, Petersdorf.

Prandke, H. and Stips, A. (1998), 'Test measurements with an operational microstructure-turbulence profiler: Detection limit of dissipation rates', *Aquatic ScienceS* **60**(3), 191–209.

Press, W., Flannery, B., Teukolsky, S. and Vetterling, W. (1989), *Numerical Recipes, The Art of Scientific Computing (FORTRAN Version)*, Cambridge University Press, Cambridge.

Reverdin, G., Gascard, J., LeCann, B., Prieur, L., Assenbaum, M. and Lherminier, P. (2009), 'A long lasting mode water vortex in the Northeast Atlantic Ocean', *Journal Of Physical Oceanography* **39**, 536–558.

Richardson, P. (1993), 'A census of eddies observed in North-Atlantic SOFAR float data', *Progress In Oceanography* **31**(1), 1–50.

Rippeth, T., Simpson, J., Williams, E. and Inall, M. (2003), 'Measurement of the rates of production and dissipation of turbulent kinetic energy in an energetic tidal flow: Red Wharf Bay revisited', *Journal Of Physical Oceanography* **33**(9), 1889–1901.

Rippeth, T., Wiles, P., Palmer, M., Sharples, J. and Tweddle, J. (2009), 'The diapcynal nutrient flux and shear-induced diapcynal mixing in the seasonally stratified western Irish Sea', *Continental Shelf Research* **29**, 1580–1587.

Robinson, A. (1966), 'An investigation into the wind as the cause of equatorial undercurrent', *Journal Of Marine Research* **24**, 179–204.

Roget, E., Lozovatsky, I., Sanchez, X. and Figueroa, M. (2006), 'Microstructure measurements in natural waters: Methodology and applications', *Progress In Oceanography* **70**(2-4), 126–148.

Sanders, R., Brown, L., Henson, S. and Lucas, L. (2005), 'New production in the Irminger Basin during 2002', *Journal Of Marine Systems* **55**, 291–310.

Sarmiento, J., Gruber, N. and Sundermann, J. (2006), *Ocean Biogeochemical Dynamics*, Princeton University Press, Princeton and Oxford.

Schultz Tokos, K. and Rossby, T. (1991), 'Kinematics and dynamics of a Mediterranean salt lense', *Journal Of Physical Oceanography* **21**, 879–892.

Shapiro, R. (1971), 'The use of linear filtering as a parameterization of atmospheric diffusion', *Journal Of The Atmospheric Sciences* **28**, 523–531.

Shapiro, R. (1975), 'Linear filtering', *Mathematics Of Computation* **29**, 1094–1097.

Smith, S. (1980), 'Wind stress and heat flux over the ocean in gale force winds', *Journal Of Physical Oceanography* **10**, 709–726.

Sod, G. (1985), *Numerical Methods in Fluid Dynamics Initial and Initial Boundary-Value Problems*, Cambridge University Press, Cambridge.

Soloview, A., Lukas, R. and Hacker, P. (2001), 'An approach to parameterization of the oceanic turbulent boundary layer in the Western Pacific warm pool', *Journal Of Geophysical Research-Oceans* **106, C3**, 4421–4435.

Spall, M. and Robinson, A. (1989), 'A new open ocean, hybrid coordinate primitive equation model', *Mathematics And Computers In Simulation* **31**, 241–269.

Stansfield, K., Garrett, C. and Dewey, R. (2001), 'The probability distribution of the Thorpe displacement within overturns in Juan de Fuca Strait', *Journal Of Physical Oceanography* **31**(12), 3421–3434.

Stips, A. (2005), Dissipation measurement, *in* H. Baumert, J. Simpson and J. Sundermann, eds, 'Marine Turbulence: Theories, Observations, and Models. Results of the CARTUM Project', Cambridge University Press, pp. 115–126.

Sweeney, E., Jr., M., D. and Buesseler, K. (2003), 'Biogeochemical impacts due to mesoscale eddy activity in the Sargasso Sea as measured at the Bermuda Atlantic Time-series study (BATS)', *Deep-Sea Research Part II-Topical Studies In Oceanography* **50**, 3017–3039.

Temam, R. and Tribbia, J. (2003), 'Open boundary conditions for the Primitive and Boussinesq equations', *Journal Of The Atmospheric Sciences* **60**, 2647–2660.

Tennekes, H. and Lumley, J. (1972), *A First Course in Turbulence*, The MIT Press, Cambridge, Massachusetts and London, England.

Thomas, L. and Lee, C. (2005), 'Intensification of ocean fronts by down-front winds', *Journal Of Physical Oceanography* **35**, 1086–1102.

Thorpe, S. (1977), 'Turbulence and mixing in a Scottish loch', *Philosophical Transactions of the Royal Society of London. Series A* **286**(1334), 125–181.

Thorpe, S. (2004), 'Recent developments in the study of ocean turbulence', *Annual Review Of Earth And Planetary Sciences* **32**, 91–109.

Thorpe, S. (2005), *The Turbulent Ocean*, Cambridge University Press, Cambridge, United Kingdom.

Toole, J. and Schmitt, R. (1987), 'Small-scale structures in the north-west Atlantic sub-tropical front', *Nature* **347**(3), 47–49.

Turner, J. (1973), *Buoyancy effects in fluids*, Cambridge University Press, Cambridge, United Kingdom.

UNESCO (1980), 'Background papers and supporting data on the international equation of state of seawater', *UNESCO Technical Papers in Marine Science* **38**, 192.

Van Gastel, P. and Pelegri, J. (2004), 'Estimates of gradient Richardson Numbers from vertically smoothed data in the Gulf Stream region', *Scientia Marina* **68(4)**(6), 459–482.

Webb, D., Coward, A., de Cuevas, B. and Gwilliam, C. (1997), 'A multiprocessor ocean general circulation model using message passing', *Journal Of Atmospheric And Oceanic Technology* **14**(1), 175–183.

Welch, P. (1967), 'The use of Fast Fourier Transform for the estimation of power spectra: A method based on time averaging over short, modified periodograms.', *IEEE Transactions On Audio And Electroacoustics* **AU15**(2), 70–73.

Willett, C., Leben, R. and Lavin, M. (2006), 'Eddies and tropical instability waves in the Eastern tropical Pacific: A review', *Progress In Oceanography* **69**(2-4), 218–238.

Williams, R. and Follows, M. (2003), Physical transport of nutrients and the maintenance of biological production, *in* M. Fasham, ed., 'Ocean Biogeochemistry: The role of the ocean carbon cycle in global change', Springer, pp. 19–51.

Williams, R., McLean, A. and Follows, M. (2000), 'Estimating the convective supply of nitrate and implied variability in export production over the North Atlantic', *Global Biogeochemical Cycles* **14(4)**, 1299–1313.

Winkel, D., Gregg, M. and Sanford, T. (2002), 'Patterns of shear and turbulence across the Florida Current', *Journal Of Physical Oceanography* **32**, 3269–3285.

Yamazaki, H. and Osborn, T. (1990), 'Dissipation estimates for stratified turbulence', *Journal Of Geophysical Research-Oceans* **95**(C6), 9739–9744.

Yelland, M., Moat, B., Taylor, P., Pascal, R., Hutchings, J. and Cornell, V. (1998), 'Wind stress measurements from the open ocean corrected for airflow distortion by the ship', *Journal Of Physical Oceanography* **28**, 1511–1526.

Yelland, M. and Taylor, P. (1996), 'Wind stress measurements from the open ocean', *Journal Of Physical Oceanography* **26**, 541–558.

Yu, Z. and Schopf, P. (1997), 'Vertical eddy mixing in the tropical upper ocean: Its influence on zonal currents', *Journal Of Physical Oceanography* **27**, 1447–1458.

Zantopp, R. and Leaman, K. (1982), 'Gulf of Cadiz water observed in a thermocline eddy in the Western North Atlantic', *Journal Of Geophysical Research-Oceans* **87 (C3)**, 1927–1934.

Zhou, W. (2002), 'An alternative leapfrog scheme for surface gravity wave equations', *Journal Of Atmospheric And Oceanic Technology* **19**, 1415–1423.